Ultracold Collisions and Fundamental Physics with Strontium

by

Sebastian Blatt

Mag. rer. nat., Leopold-Franzens-Universität Innsbruck. 2005

A thesis submitted to the

Faculty of the Graduate School of the

University of Colorado in partial fulfillment

of the requirement for the degree of

Doctor of Philosophy

Department of Physics

2011

This thesis entitled:

Ultracold Collisions and Fundamental Physics with Strontium

written by Sebastian Blatt

has been approved for the Department of Physics

_____

Jun Ye

_____

Deborah Jin

Date ___May 26, 2011___

The final copy of this thesis has been examined by the signatories, and we find that both the content and the form meet acceptable presentation standards of scholarly work in the above mentioned discipline.

Blatt, Sebastian (Ph. D., Physics)

Ultracold Collisions and Fundamental Physics with Strontium

Thesis directed by Professor Adjoint Jun Ye

The success of strontium-based optical lattice clocks in the last five years has led to a recommendation by BIPM of strontium as a future standard of frequency and time. Due to the excellent agreement between three international labs, the strontium optical clock transition is the best agreed-upon optical frequency to date. We use the international optical clock data to limit present-day drift of fundamental constants and their coupling to the ambient gravitational potential. Strontium lattice clocks are still making rapid progress and promise a large signal-to-noise improvement over single-ion-based frequency standards by employing $\mathcal{O}(10^4)$ atoms. Reaching quantum-projection-noise limited measurement requires a careful study and control of the many-body interactions in the system. We measure interactions between ultracold fermions at the 10^{-17} level and relate them to s-wave collisions due to a loss of indistinguishability during the spectroscopic process. This new understanding of the many-body effects will increase the precision of current optical lattice clock systems and can lead to the accuracy level that has so far been pioneered only in single particle (trapped ion) systems. A second generation strontium system is used to control ultracold interactions in an otherwise ideal gas of bosonic ^{88}Sr via the optical Feshbach resonance effect. These new measurement and control capabilities pave the way to reach atomic shot-noise limited optical clock performance without detrimental effects from large atom numbers.

für Irina

Acknowledgments

I joined the strontium gang in November of 2004 and have stayed with them through a diploma thesis and all of graduate school. I would like to thank both Jun and Rudi Grimm for making that first year possible. During my first visit to the lab, I was awed that anybody could know and understand the function of every little piece in that huge pile of lasers, optics, electronics, cables, instruments, and vacuum hardware. I was amazed that almost half of the lab was supposed to be for a single experiment, and really wanted to learn how to build something like that myself.

Luckily, it turned out that the Sr experiment was large enough to require many people to actually run it and I learned something from each of them. Working with a lot of smart people in *really* cramped spaces until the early morning hours let me appreciate the value of teamwork. Without being able to rely on everyone knowing their part of the experiment very well and keeping it running, none of the work over the years would have been possible. Jun's enthusiasm for physics and his willingness to consider even our craziest ideas still amazes me. I would like to thank Jun for showing us that combining superior technical skill with broad interest and enthusiasm leads to many new ideas and great results. The importance of free pizza, a coffee machine, and large amounts of grilled meats cannot be overstated either.

Even when I first joined, Marty Boyd and Andrew Ludlow let me play with all of the expensive stuff right away. Knowing that I was handling the only laser diode left in the lab and that it cost more than I earned in four months was a great motivator. Over many

all of this possible. I would not be here without you. Thanks also to my brothers, Florian & Christian, my grandparents Gerda, Edith & Otto, and my parents-in-law, Bernadette and Hubert, for all they have done to support my wife and myself over the years.

My wife Irina has the greatest patience of all.

Thank you for being there and especially for being there when the going gets tough.

CONTENTS

LIST OF TABLES

LIST OF FIGURES

Introduction

PRECISION spectroscopy of electronic transitions in atomic systems has led to many technological advances over the last decades. Atomic transition frequencies have become the most accurately measured physical quantities, which has led to the redefinition of the second in terms of the ^{133}Cs hyperfine transition frequency. Development of more accurate atomic frequency standards based on optical transitions has sped up greatly with the invention of the femtosecond optical frequency comb. These lasers emit a coherent train of laser pulses at radio frequency repetition rates which provides a coherent link between the optical and radio frequency domains. Absolute frequency measurements of optical transition frequencies with these devices has become routine over the last decade. Most optical standards are based on narrow intercombination lines available in two-valence-electron systems such as neutral alkaline earth atoms. This work focuses on experiments related to such an optical frequency standard using neutral ^{87}Sr trapped in an optical lattice.

The optical lattice clock entered the scientific scene in 2005 with work on ^{87}Sr by Hidetoshi Katori's group at the university of Tokyo [1], our group at JILA [2], and Pierre Lemonde's group at LNE-SYRTE in Paris [3]. Since then, several other groups have realized optical lattice based frequency standards such as fermionic ^{171}Yb [4] and bosonic ^{88}Sr [5, 6]. Their widespread use in laboratories across the world has made optical lattice clocks very well-characterized precision measurement systems. The ^{87}Sr standard in particular has been accepted as a secondary frequency standard by the Bureau International des Poids et Mésures

(BIPM). The main reason for this choice is the excellent global agreement on the absolute value of the optical transition frequency in the Sr lattice clock. In fact, the $^1S_0$-$^3P_0$ transition frequency in neutral ^{87}Sr at $429,228,004,229,873.65(37)$ Hz [7] is the best agreed-upon optical frequency there is [8].

An optical lattice clock consists of ultracold atoms trapped in an optical lattice at a *magic* wavelength where the trapping potential is matched for both clock states. The atoms are interrogated using a highly frequency-stable spectroscopy laser tuned to a narrow clock transition. The spectroscopy laser is frequency-stabilized to the transition frequency on timescales of a few seconds by recreating a new sample and repeating the experiment roughly once per second. This approach combines the advantages of trapped ion clocks with the large signal-to-noise (S/N) achieved in an atomic beam based frequency standard by creating an array of identical microtraps that are interrogated concurrently.

Optical lattice clock systems have already exceeded ion clocks in terms of measurement precision, although their accuracies have not yet reached the levels demonstrated in NIST's ion-trap frequency standards. Current lattice clock accuracies are limited by two effects. The first is due to the influence of the room temperature blackbody radiation (BBR), which produces an AC Stark shift of the clock transition. This purely single particle effect limits all state-of-the-art optical and rf frequency standards, and its uncertainty increases with decreasing clock transition frequency. Uncertainty in the BBR shift will be reduced with technical advances in controlling the sample environment. The second limiting effect arises from clock frequency shifts related to the atomic density. Understanding and control of these shifts is much more interesting and challenging. The main conceptual challenge remains a clear understanding of the intricacies of the underlying many-body system dynamics. Characterizing and controlling these dynamics will allow even larger S/N gains and should result in lattice clock systems with unprecedented precision and accuracy.

This thesis is split into three parts. We will describe the experimental setup of the ^{87}Sr standard only briefly; by now, there are many excellent reviews on how such a standard is

built. We will provide references to the relevant PhD theses and papers. An important aspect in understanding the spectroscopic process of atoms trapped in a deep optical lattice are their motional degrees of freedom. We will investigate the resulting spectroscopic features in detail. The spectroscopic process is complicated by the fact that $\mathcal{O}(10)$ atoms occupy a typical lattice site. Even though ^{87}Sr is fermionic, the atoms will experience interactions because of their necessarily different motional state. We relate these fundamental motional inhomogeneities to an inhomogeneous excitation process which allows fermionic s-wave interactions. These interactions modify the spectroscopic lineshapes and introduce small but important frequency shifts at the 10^{-16} level. A detailed understanding of the many-body interactions at this level leads to the counterintuitive idea of suppressing the interactions by increasing their magnitude. As a demonstration of the high level of understanding gained since 2005, we will use the unprecedented agreement between all of the groups working on ^{87}Sr to investigate physics beyond the standard model. What can we say about cosmological problems like the variation of fundamental constants? Finally, we will investigate whether it is possible to manipulate the interactions in an alkaline-earth based many-body system using laser light. Magnetic-field-induced scattering resonances do not exist in the spinless ground state of alkaline earth atoms. We experimentally demonstrate that the Optical Feshbach Resonance effect can be useful in manipulating the interactions in these systems.

The work presented here is a summary and extension of the work presented in Refs. [8–10]. At this point, a complete survey of the experimental setup and all important effects influencing the operation of an optical lattice clock has grown far beyond the scope of a single thesis or review article. Related publications and theses about our system and other optical lattice clocks are listed in Appendix C.

THE ^{87}SR FREQUENCY STANDARD

I**N** this chapter, we will give a brief summary of the operation of a ^{87}Sr optical lattice clock. This overview summarizes many important experimental procedures and tools and detailed descriptions can be found in the papers and theses cited. Also see the list of theses and papers in Appendix C, especially Refs. [11–14].

1.1. Lattice clock overview

Preparing the atomic sample. Strontium is an alkaline earth, a two-electron system with corresponding singlet and triplet states, as shown in Fig. 1.1. The main transition is the 30 MHz wide $5s^2\ ^1$S$_0$-$5s6p\ ^1$P$_1$ transition at 461 nm which is used in all current experiments to load a magneto-optical trap (blue MOT) from a Zeeman-slowed atomic beam from an effusive oven. A sketch of the vacuum chamber with beam directions is shown in Fig. 1.2. In this way, depending on the Sr isotope used, $10^6 - 10^8$ atoms are trapped and cooled to mK temperatures. The MOT transition is not completely closed and roughly one in 10^5 atoms leaks to the metastable $5s5p\ ^3$P$_2$ via $5s4d\ ^1$D$_2$. Since the ^{3}P$_2$ state has a magnetic dipole moment, those atoms are not lost from the magneto-optical trap, but remain trapped in the quadrupole field [15–17]. To prepare a ground state sample, a repumping scheme must be used. There are several excited triplet states that will decay back to ^{1}S$_0$ via $5s5p\ ^3$P$_1$ and all of them have been used. In our lab, two lasers on the $5s5p\ ^3$P$_0 - 5s6s\ ^3$S$_1$ and

$5s5p\ ^3P_2 - 5s6s\ ^3S_1$ are continuously interacting with the atoms while they are cycling on $^1S_0$-$^1P_1$ in the blue MOT [11, 18].
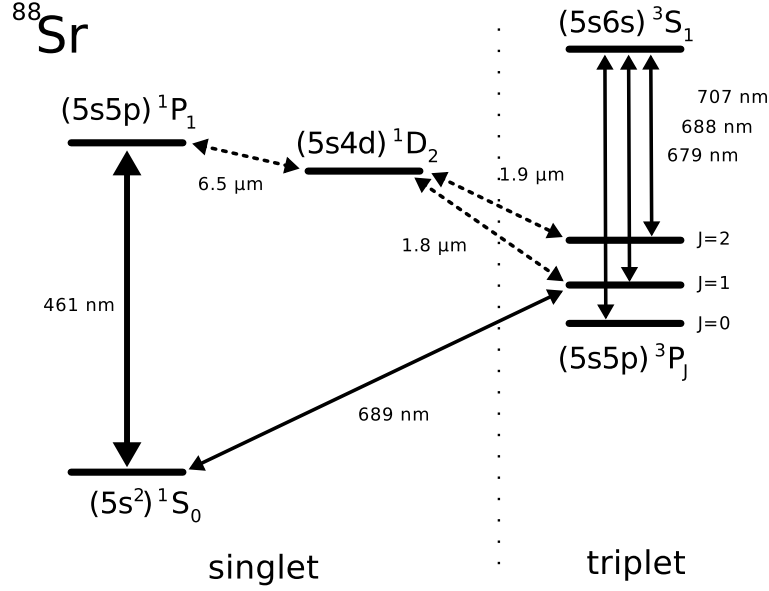
Figure 1.1.: Electronic level diagram of strontium, excluding hyperfine structure. Note that the clock transition $^1S_0$-$^3P_0$ only exists in ^{87}Sr due to the hyperfine interaction. In the bosonic isotopes, is has to be induced by a magnetic field.

After the blue MOT has been loaded with atoms for several hundred ms, the magnetic field gradient is reduced drastically, the blue light is switched off and atoms are loaded into a second stage magneto-optical trap (red MOT) operating on the 7.5 kHz wide $5s^2\ ^1S_0 - 5s5p\ ^3P_1$ transition at 689 nm. The narrow linewidth allows cooling down to the recoil limit of several hundred nK [18, 19], and in the presence of hyperfine structure, the red MOT dynamics require a second laser [20]. Typically, the atoms are cooled to $1-3\ \mu$K after about 200 ms of cooling at the end of the red MOT stage.

Magic wavelength optical lattice. The remaining atoms are then transferred into an optical lattice formed by a vertically oriented, retro-reflected laser beam, as sketched in Fig. 1.3. The individual microtraps are the pancake-shaped high-intensity regions of the standing wave. The atoms are further cooled with Doppler cooling in the transverse directions as well as sideband cooling along the lattice axis. Typically, 10^3-10^4 atoms remain
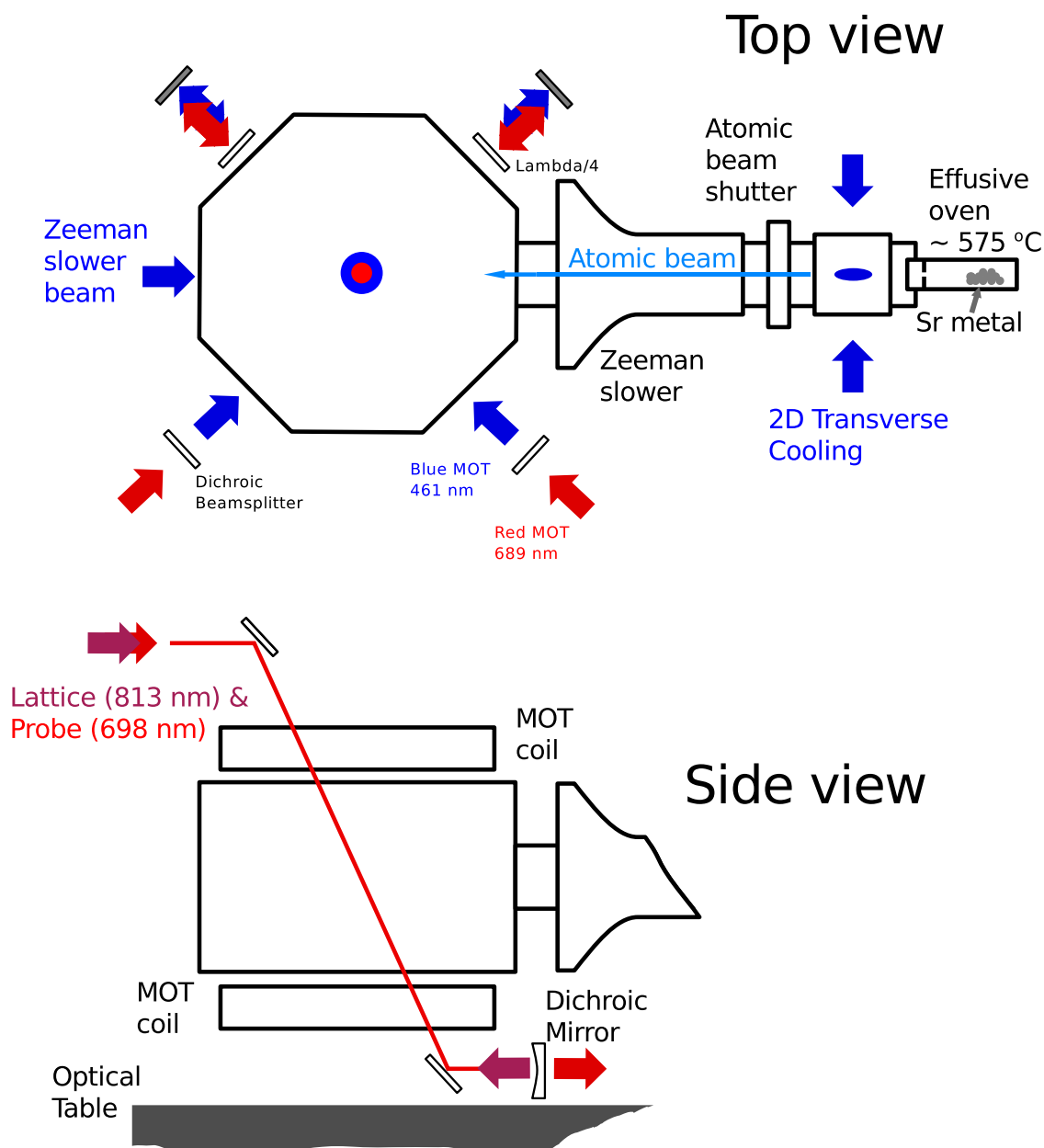
Figure 1.2.: Sketch of the vacuum system. The atoms emerge from an effusive oven at
∼575 °C and are collimated with two retroreflected transverse cooling beams. The resulting
atomic beam is slowed in a Zeeman slower and the beam enters the vacuum chamber. Three
retroreflected beams at 461 nm form a MOT at the chamber center. The magnetic field
gradient is reduced and three retroreflected red beams at 689 nm form another MOT.
The red MOT is overlapped with the retroreflected lattice beam entering from the top
of the chamber. The probe beam at 698 nm is overlapped with the lattice, but is not
retroreflected. Typical lattice lifetimes are ∼1 s.

at temperatures of 1 μK (2 μK) along (transverse to) the lattice axis. The lattice wavelength is set to the *magic wavelength* at 813.4208(5) nm for the $5s5p\ ^1S_0 - 5s5p\ ^3P_0$ clock transition in ^{87}Sr [21], where the AC Stark shift for the ground $^1S_0$ and excited $^3P_0$ clock states are equal to first order. The clock transition at 698 nm is allowed only in the fermionic isotope through hyperfine mixing of $^3P_1$ into the $^3P_0$ state [22], but can be induced by a large magnetic field in bosonic alkaline earths as well [5, 6, 23, 24].
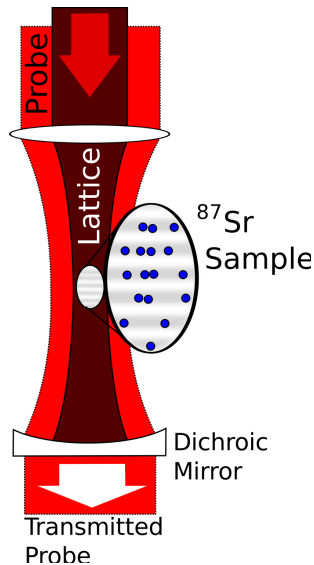
Figure 1.3.: The optical lattice is formed by a retroreflected beam at 813 nm. The retrore-flector is a curved dichroic mirror that transmits the probe light at 698 nm to avoid standing wave effects in the spectroscopy.

Spectroscopy. In the one-dimensional magic wavelength optical lattice, spectroscopy is performed by copropagating the spectroscopy laser along the lattice axis (see Fig. 1.3). In this way, spectroscopic information is obtained in the Lamb-Dicke regime, where motional effects only appear in vibrational sidebands, well separated from the electronic carrier transition [25, 26]. The clock laser frequency is then stabilized to the clock transition frequency. On short time scales, the clock laser obtains its frequency stability from a lock to a high-quality-factor optical cavity [27] (see Fig. 1.4) since information from the atomic sample only arrives at rate given by the experimental cycle time of $\sim$ 1 s. The spectroscopy laser typically interacts with the atoms for 80 ms, resulting in a duty cycle of $\sim$10%. The stabilized clock laser references

an octave spanning optical frequency comb [13].

Absolute frequency measurement. The optical frequency comb serves as a distribution center that makes the clock laser frequency stability available at other optical and microwave frequencies (see Fig. 1.4). To measure the absolute frequency of our Sr standard, we use a stabilized optical fiber link between our lab and the NIST Time and Frequency division [28]. The absolute frequency reference is provided by a hydrogen maser referenced to the primary Cs standard. The maser references an RF oscillator, which is used to modulate the amplitude of a telecom laser. The laser light is transferred to our lab, where the amplitude modulation frequency is detected and compared against the optical frequency comb. In this way, the absolute frequency of the Sr clock transition can be measured.

Direct optical comparisons. The quality of the RF frequency transfer method is limited by how well the hydrogen maser can be referenced to the primary Cs standard (NIST F-1). To compare other optical clocks at NIST to Sr, we use a direct optical frequency transfer method [28, 29]. Another telecom laser is phase-locked directly to the frequency comb in our lab. The laser light is then directly transferred via the optical fiber link. At NIST, the light is beat against another octave-spanning optical frequency comb which serves as the optical frequency distribution center at NIST [30]. In this way, we measure frequency ratios between Sr and other optical standards with high precision [12, 31].

1.2. Current ^{87}Sr error budget

Any frequency standard needs to be evaluated carefully for systematic effects that influence its accuracy. Using the direct optical-to-optical comparison scheme outlined in the previous section, systematic effects can be studied by modulating one clock's parameters between two settings while continuously comparing against the other clock.

An example of a systematic effect is the optical lattice wavelength. The sensitivity of the clock transition frequency to the optical lattice wavelength in the vicinity of the magic wavelength can be tested in this way, and a conservative estimate of the lattice wavelength
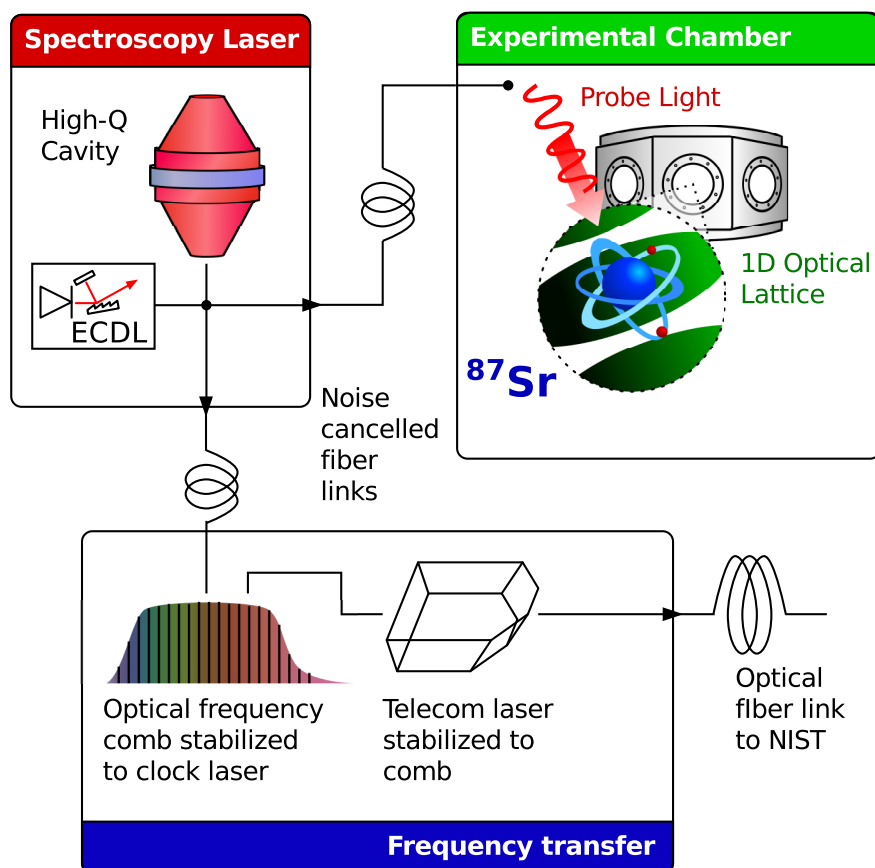
Figure 1.4.: Spectroscopic information from the atoms at the center of the vacuum chamber is used to tune the spectroscopy laser on timescales of the experimental duty cycle. The laser itself is stabilized to a highly mechanically-stable optical cavity on short timescales. The spectroscopy laser stabilizes a self-referenced optical frequency comb. The comb references other lasers, such as a telecom laser that is used to transmit the spectroscopy laser's stability to NIST for optical clock comparisons. The optical clock layout at NIST is similar and another frequency comb is used to compare the telecom laser's optical phase to the respective optical clock. The optical length of all fiber links is stabilized.

stability allows putting an uncertainty on the final result. In principle, such an uncertainty could also be arrived at by calculating the sensitivity of the spectroscopy to variability in the lattice wavelength. As far as possible, it is important not to rely on such estimates since one can never be sure that the calculation has taken all important effects into account. For this reason, all systematic effects should be experimentally tested. Ideally, every parameter contributing to the experimental result should be varied individually. Evaluating a full uncertainty budget thus requires many iterations of the optical clock experiment and any change to the experimental layout requires the reevaluation of systematic effects.

In Tab. 1.1, we show the uncertainty budget from the last full evaluation of the JILA [87]Sr clock against the primary US frequency standard, NIST F-1 . Ref. [7] includes a very thorough investigation of all systematic effects that influence such a measurement. The paper is a good example of the metrological procedure required to claim uncertainties below the Hz level in an optical frequency measurement. A full discussion is beyond the scope of this introduction, but we highlight the effects that limit state-of-the-art optical frequency standards below.

The first two entries of Tab. 1.1 describe shifts of the clock transition frequency with respect to the lattice intensity. The third entry describes the AC Stark shift of the clock transition frequency with respect to the ambient room-temperature blackbody radiation (BBR). The next two entries describe sensitivity of the clock transition with respect to the magnetic field. The seventh entry characterizes the shift of the clock transition with respect to the atomic density in the optical lattice. The next entry is a conservative estimate of spectroscopic lineshape modification due to imperfect nuclear-spin polarization. The servo error estimate bounds the effect of possible integrator offsets in the digital servo that stabilizes the clock laser to the atomic transition. Due to the tight confinement along the optical lattice axis, the second order Doppler effect is very small.

The total [87]Sr optical clock systematic uncertainty is much smaller than the uncertainty in the calibration of the intermediate hydrogen maser used to compare Sr versus the Cs fountain, since the Sr error budget was measured in a direct optical-to-optical comparison

Contributor	Correction (10^{-16})	Uncertainty (10^{-16})
Lattice Stark (scalar/tensor)	-6.5	0.5
Lattice hyperpolarizability	0.1	0.1
BBR Stark	54.0	1.0
AC Stark (probe)	0.15	0.1
1st order Zeeman	0.2	0.2
2nd order Zeeman	0.36	0.04
Density	3.8	0.5
Line pulling	0	0.2
Servo error	0	0.5
2nd order Doppler	0	$\ll 0.01$
Sr systematics total	52.11	1.36
Maser calibration	-4393.7	8.5
Gravitational shift	12.5	1.0
Total	-4329.1	8.66
$\nu_{\text{Sr}} - \nu_0$	73.65 Hz	0.37 Hz

Table 1.1.: ^{87}Sr error budget from Ref. [7].

against the NIST Ca optical clock. The large discrepancy between the quality of rf frequency measurements and direct optical comparisons is a strong indicator of why a future redefinition of the second in terms of an optical standard is being pursued.

Another effect that will become more and more important as remote optical frequency standards are compared is the gravitational red shift. Our lab at JILA and the NIST Time & Frequency division are separated by 3.5 km and a height difference of 11.3(2) m between the Sr clock and the Cs fountain has been estimated by GPS receivers in each building. The height difference by itself introduces a frequency correction on the 10^{-15} level. However, the uncertainty in the red shift correction not only includes the mere height difference but also an upper limit on the "transverse" variation in the gravitational field from the nearby mountains. The gravitational potential also fluctuates in time and these effects will become more and more important as optical clock comparisons become more accurate or are performed over longer distances. The red shift uncertainty here includes an estimate of the gravitational isosurface variation between JILA and NIST at the 10 cm level using the National Geodetic Survey markers next to either lab [7].

The largest systematic effects related to the atomic system are the AC Stark shifts induced by the room-temperature BBR and transition frequency shifts when the atomic density is varied. Those two shifts are also the conceptually most worrying and interesting effects. In Cs fountains, these effects appear at much larger magnitude, but with the increase in optical clock accuracy, all state-of-the-art optical standards are becoming limited by the same effects.

The BBR correction was first introduced by W. Itano [32] and since then, atomic frequency standards have been defined at zero temperature. The correction here is based on theoretical calculations of the clock state polarizabilities at the BBR wavelengths [33]. Half of its uncertainty comes from insufficient knowledge of these polarizabilities, the other half is experimental. Even though the temperature of the vacuum chamber is measured in multiple spots and rolling corrections are applied, the metallic vacuum chamber is not a black body. For these reasons, the BBR shift in optical clocks has received much attention in the last few years [34, 35]. Work on measuring the shift experimentally is under way in many labs, but

any such measurement requires a specialized setup [36] and there are no experimental results so far. Nevertheless, the BBR is a pure single-particle effect and will be understood and controlled with a technical solution involving a temperature-controlled environment similar to the ones employed in Cs fountain clocks.

The next largest uncertainty are clock frequency shifts related to the atomic density. These effects are intellectually much more challenging and interesting since they can potentially compromise both precision and accuracy. For this reason, recent work in our lab has focused on understanding and controlling these shifts. The density shift is an intrinsically many-body effect arising from atomic interactions. Its appearance is especially surprising since the atoms are at temperatures of ~ 1 μK and s-wave interactions should be suppressed by the Pauli exclusion principle. The density shift will be discussed in detail in Chapter 3. To understand its origin, however, we need to understand the spectroscopic process in considerable detail.

Chapter 2

LASER SPECTROSCOPY OF LATTICE-TRAPPED ATOMS

LASER spectroscopy of tightly confined atoms has been investigated in the context of ion traps for more than three decades [25, 26]. The key advantage of trapping particles for laser interrogation is signal-to-noise (S/N) gain by extending the coherent light-atom interaction time. However, the atom needs to be tightly trapped with respect to the interrogating wavelength to suppress contamination of the signal by the atomic motion. In addition, the trapping potential needs to be the same for ground and excited state coupled by the spectroscopy light to avoid coupling the motional and spectroscopic degrees of freedom.

The same advantageous spectroscopic conditions as for ion traps can now be achieved for neutral atoms by trapping them in a tight optical lattice. The theoretical description of the spectroscopic process still applies, but has to be modified to account for the conditions in optical lattices.

The second, and much more important, difference between ion trap and optical lattice spectroscopy is that spectroscopy in optical lattices allows interrogating many sites of the lattice simultaneously. The lattice can act as an array of identical microtraps and thus the S/N is in principle enhanced by a factor of $\sqrt{N}$, where N is the overall number of atoms interrogated. If, additionally, the particles in different lattice sites can be entangled, one can

hope to increase the spectroscopic S/N by another factor proportional to $\sqrt{N}$.

For these reasons, high-resolution spectroscopy in optical lattices has been investigated actively over the last decade, mostly based on the "magic wavelength lattice clock" proposal [37, 38] building on parallel ideas for applications in cavity QED experiments [39]. First ^{87}Sr spectroscopy results were available shortly thereafter [1, 40, 41]. The first systematic investigation of high-resolution ^{87}Sr spectroscopy for application in an optical atomic clock was published in 2006 [2], followed by similar results from the Paris [3] and Tokyo [42] groups. Soon after, we used the same system to achieve the highest quality factor in any kind of coherent spectroscopy [43].

To achieve higher resolutions and to make use of the full enhancement factor due to N, the spectroscopic process must be investigated in deeper detail. The main obstacle to high-resolution spectroscopy was overcome by using the magic wavelength lattice [21], and the Paris group verified that higher order polarizability contributions are small [44]. Next, the effect of the hyperfine interaction on spectroscopy was investigated in detail [22], leading to spin-polarized operation of the lattice clock used in all groups today [7, 42, 45].

Soon after, it became obvious that the number of atoms trapped in an individual lattice site is an important factor in spectroscopy. A significant systematic shift of the optical frequency with number of atoms per lattice site was first observed in direct optical clock comparisons [31]. These comparisons still used simultaneous spin polarization to $m_F = \pm 9/2$, but the density shift persisted even with a single spin species [46]. The dominant role of Rabi frequency inhomogeneity due to populating different transverse motional states was described qualitatively as due to inhomogeneity-induced s-wave interactions [9], which led to several theoretical models trying to describe the underlying effect [47–50].

The importance of understanding the interactions in a many-body system for clock spectroscopy using more than one particle was highlighted recently by demonstrating that density shifts can be suppressed if the interparticle interactions are increased by placing the particles in a two-dimensional optical lattice [51].

In this Chapter, we will introduce the framework for understanding the optical lattice

spectroscopy and introduce optical sideband spectroscopy as an important tool to understand the system parameters. With these methods, we will proceed to model collisions between ultracold fermions and understand the density shift as arising from system inhomogeneities.

The framework for understanding spectroscopy of trapped particles builds on the results available from laser spectroscopy of ions trapped in RF traps. The main ideas have been developed early on and have been described in many theses from our lab [11, 12, 14] and the Paris group [52–54]. The main parameter to understand spectroscopy of tightly bound particles is the Lamb-Dicke parameter [26]

$$\eta = \nu_{\text{rec}}^p / \nu_{\text{trap}}, \tag{2.1}$$

given by the ratio of probe light recoil frequency $\nu_{\text{rec}}^p = h/(2m\lambda_p^2)$ to trapping frequency ν_{trap}, where λ_p is the probe light wavelength and m is the mass of the particle. In the limit $\eta \ll 1$, the particle's motional wave function has a small extent with respect to the probing wavelength and the probing process will not change the motional state of the particle. This limit is called the *Lamb-Dicke regime* and the process is very similar to what happens in Mössbauer spectroscopy: the particle is so tightly bound that the recoil from absorption and reemission of a probe photon gets absorbed by the crystal lattice (the optical lattice here).

2.1. Carrier and Sideband Transitions

The response of a particle to the probing light in the dipole approximation is given by the Rabi frequency

$$\Omega \propto \langle \psi_f | e^{i \boldsymbol{k}_p \cdot \boldsymbol{x}} | \psi_i \rangle, \tag{2.2}$$

between initial and final motional state $|\psi_i\rangle$ and $|\psi_f\rangle$, and we assumed the probe to be a plane wave with wave vector $\boldsymbol{k}_p = 2\pi/\lambda_p \hat{\boldsymbol{k}}_p$, and $\boldsymbol{x}$ is the position operator of the particle. The Lamb-Dicke approximation consists of expanding the matrix element in orders of $\boldsymbol{k}_p \cdot \langle \boldsymbol{x} \rangle$:

$$\Omega \equiv \Omega_0 \left[\langle \psi_f | \psi_i \rangle + i \boldsymbol{k}_p \cdot \langle \psi_f | \boldsymbol{x} | \psi_i \rangle + \ldots \right]. \tag{2.3}$$

If we assume three-dimensional harmonic confinement with trap frequencies (ν_x, ν_y, ν_z) and initial (final) trap state $|\boldsymbol{n}\rangle = |n_x, n_y, n_z\rangle$ ($|\boldsymbol{m}\rangle = |m_x, m_y, m_z\rangle$), this expansion can be summed up analytically and reduces to the well-known expression [25, 26, 55]

$$
\begin{aligned}
\Omega_{\boldsymbol{m}\leftarrow\boldsymbol{n}} &= \Omega_0 \prod_{j\in\{x,y,z\}} \langle m_j | e^{i\eta_j(\hat{a}_j + \hat{a}_j^\dagger)} | n_j \rangle \\
&= \Omega_0 \prod_{j\in\{x,y,z\}} e^{-\eta_j^2/2} \sqrt{\frac{n_j^<!}{(n_j^< + \Delta n_j)!}} (i\eta_j)^{\Delta n_j} L_{n_j^<}^{\Delta n_j}(\eta_j^2),
\end{aligned}
\tag{2.4}
$$

where $\hat{a}_j$ ($\hat{a}_j^\dagger$) are bosonic annihilation (creation) operators, $n_j^< = \min(n_j, m_j)$, $\Delta n_j = |n_j - m_j|$, L_n^α is a generalized Laguerre polynomial, and the η_j are the per-axis Lamb-Dicke parameters

$$
\eta_j \equiv (\hat{\boldsymbol{k}}_p \cdot \hat{\boldsymbol{x}}_j) k_p a_j / \sqrt{2} = (\hat{\boldsymbol{k}}_p \cdot \hat{\boldsymbol{x}}_j) \nu_{\text{rec}}^p / \nu_j = (\hat{\boldsymbol{k}}_p \cdot \hat{\boldsymbol{x}}_j) \sqrt{\frac{h}{2m\lambda_p^2\nu_j}},
\tag{2.5}
$$

for oscillator length $2\pi a_j \equiv \sqrt{h/(m\nu_j)}$, and trap axis direction $\hat{x}_j$. In most of the following, we are interested in the carrier transition

$$
\Omega_c(\boldsymbol{n}) \equiv \Omega_{\boldsymbol{n}\leftarrow\boldsymbol{n}} = \Omega_0 \prod_j e^{-\eta_j^2/2} L_{n_j}(\eta_j^2),
\tag{2.6}
$$

where the motional state is unchanged. However, the first blue (red) sideband, where one motional quantum is added (removed) is also of interest (change in quantum number assumed along $\hat{z}$ here)

$$
\begin{aligned}
\Omega_{\text{bsb}}(\boldsymbol{n}) &\equiv \Omega_{(n_x, n_y, n_z+1)\leftarrow\boldsymbol{n}} = \Omega_c(\boldsymbol{n}) \frac{i\eta_z}{\sqrt{n_z+1}} \frac{L_{n_z}^1(\eta_z^2)}{L_{n_z}(\eta_z^2)} \\
\Omega_{\text{rsb}}(\boldsymbol{n}) &\equiv \Omega_{(n_x, n_y, n_z-1)\leftarrow\boldsymbol{n}} \stackrel{n_z \geq 0}{=} \Omega_c(\boldsymbol{n}) \frac{i\eta_z}{\sqrt{n_z}} \frac{L_{n_z-1}^1(\eta_z^2)}{L_{n_z}(\eta_z^2)},
\end{aligned}
\tag{2.7}
$$

In the Lamb-Dicke regime, we can expand the Laguerre polynomials in orders of η_j to simplify the expressions

$$
\begin{aligned}
\Omega_c(\boldsymbol{n}) &= \Omega_0 \prod_j e^{-\eta_j^2/2} [1 - n_j \eta_j^2] \\
\Omega_{\text{rsb}}(\boldsymbol{n}) &= \Omega_c(\boldsymbol{n}) i\eta_z \sqrt{n_z} \left[1 + \frac{n_z}{2}\eta_z^2\right] \\
\Omega_{\text{bsb}}(\boldsymbol{n}) &= \Omega_c(\boldsymbol{n}) i\eta_z \sqrt{n_z+1} \left[1 + \frac{n_z+1}{2}\eta_z^2\right].
\end{aligned}
\tag{2.8}
$$

Remarks

- The red sideband does not exist if the particle is in the ground state initially, consistent with the original expression in terms of $\hat{a}_j$ and $\hat{a}_j^\dagger$.

- The first order sideband Rabi frequencies Ω_{rsb} and Ω_{bsb} are $90°$ out of phase with the carrier frequency Ω_c.

- The atomic response always depends on the initial motional state $|\boldsymbol{n}\rangle$ of the particle and decreases with increasing $|\boldsymbol{n}|$.

- The atomic response distributes among all target states $|\boldsymbol{m}\rangle$ such that $|\Omega_0|^{-2} \sum_{\boldsymbol{m}} |\Omega_{\boldsymbol{m} \leftarrow \boldsymbol{n}}|^2 = \prod_j \sum_{m_j} \langle n_j | e^{-i\boldsymbol{k}_p \cdot \boldsymbol{x}^\dagger} | m_j \rangle \langle m_j | e^{i\boldsymbol{k}_p \cdot \boldsymbol{x}} | n_j \rangle = \prod_j \langle n_j | n_j \rangle = 1$.

2.2. Spectra for a harmonic trap

Using the results from the last Section, we can discuss the absorption spectrum of a harmonically trapped particle. The spectrum will be dominated by the carrier transition at the base frequency. The first sideband transitions are detuned from the carrier by the energy added or removed due to the extra motional quantum (or phonon). Here, the extra detuning is given by $+\nu_z$ ($-\nu_z$) for the blue (red) sideband. If ν_z is larger than the power-broadened carrier linewidth Ω_c and the natural linewidth of the carrier transition, the system is said to be in the resolved sideband regime. The first blue and red sideband transitions produce spectral features that are well separated from the carrier transition and addressable by tuning the spectroscopy laser to the corresponding detuning $\pm\nu_z$ from the carrier.

In the following, we will limit our discussion to completely coherent population dynamics, and neglect all decoherence processes. In this regime, we can describe the response of an ensemble of particles as mixture of single particles. In the absence of decoherence, each particle responds to the spectroscopy light according to its carrier and sideband Rabi frequencies. In the resolved sideband regime, the relative phases of carrier and sideband Rabi frequencies

can also be neglected and the excited state population at time t can be written as

$$
\begin{aligned}
p_e(n_z, \Delta, t) = {} & \frac{|\Omega_{\mathrm{rsb}}(n_z)|^2}{|\Omega_{\mathrm{rsb}}(n_z)|^2 + (\Delta + \nu_z)^2} \sin^2 \left[\sqrt{|\Omega_{\mathrm{rsb}}(n_z)|^2 + (\Delta + \nu_z)^2} \frac{t}{2} \right] \\
& + \frac{|\Omega_c(n_z)|^2}{|\Omega_c(n_z)|^2 + \Delta^2} \sin^2 \left[\sqrt{|\Omega_c(n_z)|^2 + \Delta^2} \frac{t}{2} \right] \\
& + \frac{|\Omega_{\mathrm{bsb}}(n_z)|^2}{|\Omega_{\mathrm{bsb}}(n_z)|^2 + (\Delta - \nu_z)^2} \sin^2 \left[\sqrt{|\Omega_{\mathrm{bsb}}(n_z)|^2 + (\Delta - \nu_z)^2} \frac{t}{2} \right]
\end{aligned}
\tag{2.9}
$$

For a thermal mixture in a truncated harmonic oscillator, we find the thermally averaged excited state population

$$
P_e(T_z, \Delta, t) = \frac{1 - q_z}{1 - q_z^{1+N_z}} \sum_{n_z=0}^{N_z} q_z^{n_z} p_e(n_z, \Delta, t),
\tag{2.10}
$$

with Boltzmann factor $q_z = \exp(-\frac{h\nu_z}{k_B T_z})$ and maximal quantum number N_z.

An example spectrum of p_e with respect to Δ for a particle in the $n_z = 1$ state of a harmonic trap probed along the $\hat{z}$ direction is shown in Fig. 2.1(a). First order blue and red motional sidebands appear detuned by the trap frequency from the central carrier transition. We have assumed negligible transition linewidth, resulting in the sinc^2 sidelobes around carrier and sidebands. Note that the sidebands are only suppressed with respect to the carrier because the sideband Rabi frequencies are attenuated by η_z, and $\Omega_{\mathrm{bsb}}^2 / \Omega_{\mathrm{rsb}}^2 \simeq 1 + 1/n_z$. In a completely homogeneous system, the Rabi flopping on the sidebands has the same contrast as the carrier.

In panel (b) of the same figure, we added a slight inhomogeneity to the system by assuming a thermal distribution truncated at $N_z = 6$ and plot the thermally averaged excited state population for $T_z = 3~\mu\mathrm{K}$. Note that the inhomogeneity reduces the initial rise of the sidebands, with respect to the carrier. The difference in the excited state fraction dynamics is small as long as the exposure time is short. This can be seen in panels (c) and (d) which compare the carrier Rabi flopping for the two cases (a) and (b). The Rabi frequency inhomogeneity in (b) and (d) causes decay and revival of the Rabi flopping contrast in panel (d). Even with the added inhomogeneity, we can thus always find an exposure time – experimental conditions permitting – where the carrier or the sidebands have full contrast.

(a) Pure state $n_z = 1$.

(b) Thermal average at $T_z = 3$ μK, $N_z = 6$.

(c) Pure state $n_z = 1$.

(d) Thermal average at $T_z = 3$ μK, $N_z = 6$.
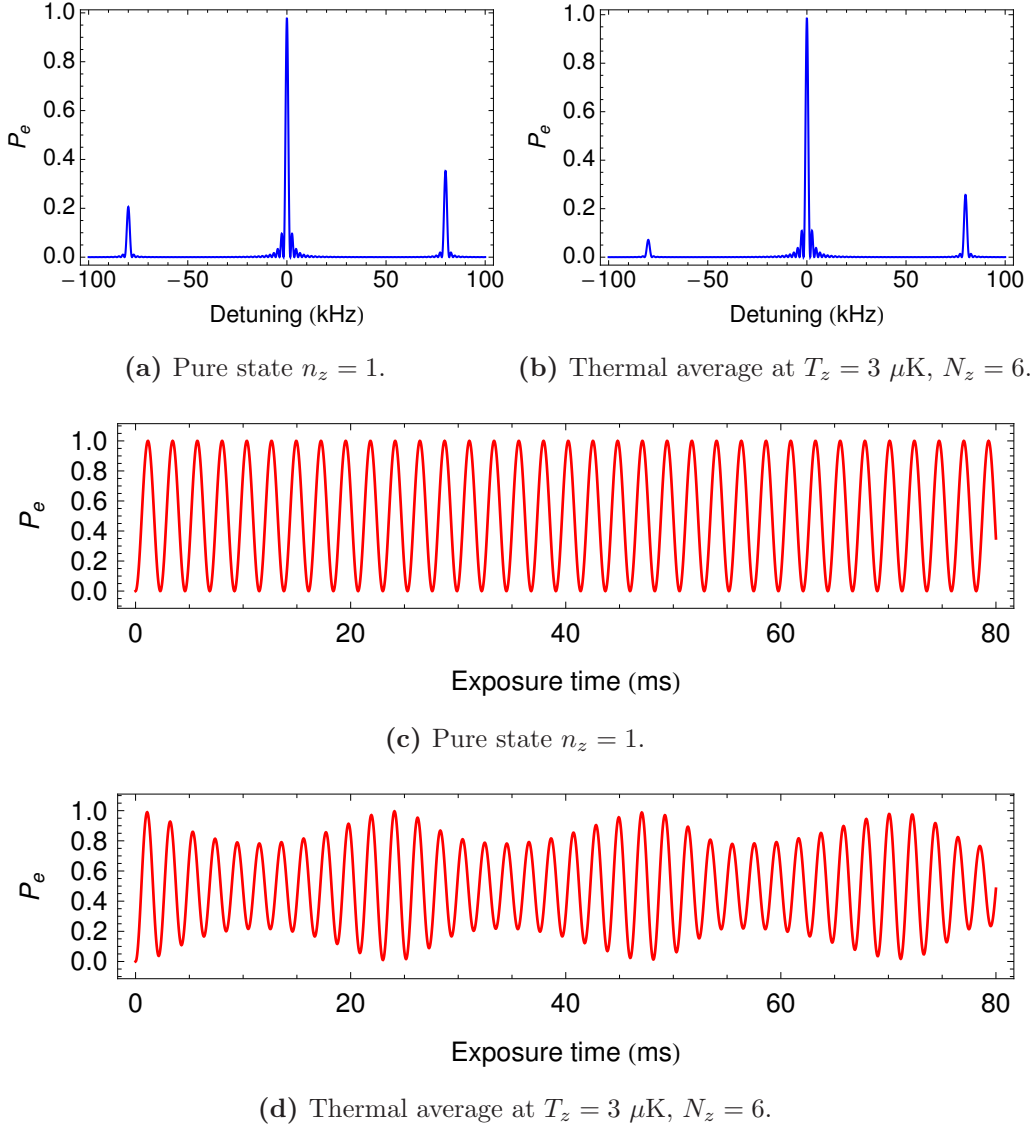
Figure 2.1.: Example absorption spectrum of a harmonically bound particle. The trap frequency $\nu_z = 80$ kHz and the Lamb-Dicke parameter $\eta_z = 0.3$, and the harmonically bound particle is probed purely along z. Natural linewidth is neglected and $\Omega_0 = 1$ kHz. The exposure time t is set to $t^{-1} = \Omega_0 e^{-\eta_z^2/2}$ to produce a π pulse on the carrier for $n_z = 0$ in panels (a) and (b). Panels (c) and (d) show coherent carrier Rabi flopping over 80 ms corresponding to the situations in (a) and (b).

The situation shown in panels (b) and (d) corresponds to typical parameters used in the optical lattice clock experiment. The simulated data, however, does not at all look like what is seen in the experiment. The maximal carrier contrast is 90% and the sidebands never reach the excited state fraction observed in the carrier. The imbalance between red and blue sideband is always present as well. Clearly, there is more inhomogeneity in the experiment than we have assumed so far.

2.3. 1D Optical Lattice Potential

To find a more realistic description of the inhomogeneity of the vertical one-dimensional lattice system, we need to look at the trapping potential more carefully. In the following, we assume a one-dimensional magic-wavelength optical lattice formed by a retro-reflected laser beam. The crucial role of atomic polarizability, the effects pertaining to lattice polarization and magnetic field, and the effect of nuclear structure on spectroscopy will be completely omitted. For more information on these effects refer to the detailed explanations in Refs. [11].

For our purposes, imagine a conservative trapping potential that is exactly the same for both clock states. In this Section, we would like to exhibit the effect of the motional degrees of freedom on spectroscopy in the context of Eq. 2.2. The material here summarizes and extends previous discussions in Refs. [9, 11, 14, 51–54, 56].

In this spirit, we approximate the optical lattice potential around its focal point as

$$U(\boldsymbol{x}) = U(x, y, z) = -U_0 e^{-2r^2/w_0^2} \cos^2 \kappa z, \tag{2.11}$$

where w_0 is the Gaussian waist of the retro-reflected beam, and $\kappa = 2\pi/\lambda$ is the wavevector of the beam for the magic wavelength $\lambda = 813.43$ nm. The trap depth U_0 is given by the time-averaged laser power P and the dynamic AC polarizability at the lattice wavelength $\alpha(\lambda)$ as

$$U_0 = \frac{4P}{\pi \epsilon_0 c w_0^2} \alpha(\lambda). \tag{2.12}$$

Experimentally, P, w_0, and $\alpha(\lambda)$ are hard to know accurately enough. Instead, knowledge about the trap geometry is usually inferred from measured trap frequencies under the as-

sumption of the overall form of Eq. 2.11. To understand this relation clearly, the potential has to be understood in more detail.

If we neglect gravity for now, U has the form of a periodic potential and is cylindrically symmetric around z. Atoms are trapped in the anti-nodes of the periodic potential and are thus confined longitudinally on the order of $\lambda/2$. The transverse confinement along r is much weaker, since the waist w_0 of an optical beam is typically much larger than λ. We conclude that the aspect ratio $(\propto w_0/\lambda)$ of a microtrap will be large. Even if we had allowed the Gaussian beam waist to vary with z, the shape of adjacent microtraps would be very similar, as long as only pancakes within the Rayleigh range $z_R = \pi w_0^2/\lambda$ are populated. Since the number of similar pancakes $\propto z_R/\lambda \propto (w_0/\lambda)^2$, it scales as the aspect ratio squared. From these simple arguments, we conclude that it is reasonable to think of atoms trapped in identical pancake-shaped microtraps. For each microtrap, we can calculate longitudinal and transverse trapping frequencies which can then be compared to the spectroscopically measured results.

2.4. Tunneling in the WKB approximation

A complication to the simple picture above is that the potential is periodic in z which allows tunneling between different microtraps. The tunneling rate gives each microtrap level a finite energy width. For shallow lattices, tunneling can dominate the system dynamics and we cannot speak of isolated microtraps anymore. As a first estimate, we will try to use the WKB approximation to describe the tunneling rates in fairly deep lattices that are typical for optical clock experiments.

In the semi-classical WKB approximation, the tunneling rate is given by a collision attempt rate with the potential wall and a tunneling amplitude that exponentially decays with the wall height and width (see e.g. Ref. [57]). For $U(z) = U_0(1 - \cos^2 \kappa z)$, we find a tunneling rate

$$\Gamma_{\mathrm{WKB}} = \frac{E_{\mathrm{rec}}}{\hbar} \frac{\sqrt{E/E_{\mathrm{rec}}}}{\xi_0} \exp\left[-2\sqrt{\frac{U_0}{E_{\mathrm{rec}}}} \int_{\xi_0}^{\pi-\xi_0} d\xi \sqrt{1 - \frac{E}{U_0} - \cos^2 \xi}\right], \qquad (2.13)$$

with lattice recoil energy $E_{rec} \equiv h^2/(2m\lambda^2) \simeq h \times 3.47$ kHz and atomic mass $m = 87$ amu. We use the dimensionless excursion $\xi = \kappa z$, and the classical turning point is given by $\xi_0 = \arccos\sqrt{1 - E/U_0}$ with $\xi_0 \in [0, \pi/2]$. Numerical results for a lattice depth $U_0 = 120 E_{rec}$ are shown as the solid red curve in Fig. 2.2. This trap depth is a typical value for our optical clock experiments and would correspond to a longitudinal trap frequency of $\sim$75 kHz. The tunneling lifetimes predicted from $1/\Gamma_{WKB}$ are basically infinite unless the particle is very highly excited. For reference, the black dashed line indicates a tunneling rate of 1 s^{-1} for ^{87}Sr in the magic wavelength lattice.
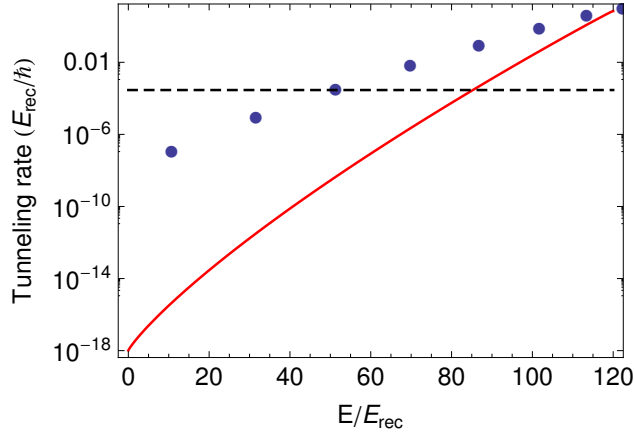
Figure 2.2.: WKB approximation to the tunneling rate in a $\cos^2$ lattice (red solid curve) versus full band structure calculation (blue circles) in a 120 recoil deep lattice. The black dashed line indicates a tunneling rate of 1 s^{-1} for the ^{87}Sr magic wavelength lattice. The WKB approximation fails to describe tunneling in the infinite lattice because only two adjacent sites were included.

The blue circles in Fig. 2.2 show the tunneling rates calculated using the full lattice band structure for an infinite lattice. Even for the relatively deep lattice used here, the WKB approximation clearly underestimates the tunneling rate in a periodic potential with many sites. Including the periodicity correctly is hard, since the transverse and longitudinal potentials are multiplied instead of added in the Schrödinger equation and thus do not allow separable solutions.

2.5. Lattice Band Structure

To treat tunneling to all orders, we need to think of the potential as an array of longitudinal lattices, one for each transverse motional quantum state. This picture is supported by the following argument: because the microtrap aspect ratio is large (typically $\gg 50$), we can think of the transverse motional dynamics as much slower than the longitudinal dynamics. This separation of time scales means that tunneling happens instantaneously on the transverse time scale. For the same reason, there are also many more transverse than longitudinal quantum states occupied at a given temperature. This means that we can think of the transverse degrees of freedom as a classical parameter that parametrizes the quantum mechanical degree of freedom along the longitudinal direction. For this reason, tunneling events that change the transverse quantum number are not important since such a change will not influence the system dynamics drastically.

To understand the longitudinal tunneling dynamics, we consider r as a classical parameter that simply scales the trap depth and focus on describing the longitudinal problem. A detailed derivation [14] shows that the one-dimensional longitudinal Schrödinger equation reduces to the Mathieu equation

$$\frac{d^2\phi}{d\xi^2} + (a - 2q\cos 2\xi)\phi = 0, \tag{2.14}$$

for the longitudinal spatial wave function $\phi(\xi)$, with $\xi = \kappa z$. The Mathieu parameters

$$\begin{aligned} q &= \frac{U_0(r)}{4E_{\text{rec}}}, \\ a &= \frac{E}{E_{\text{rec}}} - 2q, \end{aligned} \tag{2.15}$$

describe the kinetic energy E and the trap depth $U_0(r)$. The Mathieu equation only has stable solutions for certain combinations of a and q and stability diagrams can be found in standard mathematical works [58], works on ion traps [59], or in the context of band theory [60]. A plot of $a + 2q$ versus $4q$ is shown in Fig. 2.3 and directly shows the evolution of the energy structure from isolated harmonic oscillator levels to broad energy bands with decreasing trap depth from infinity.
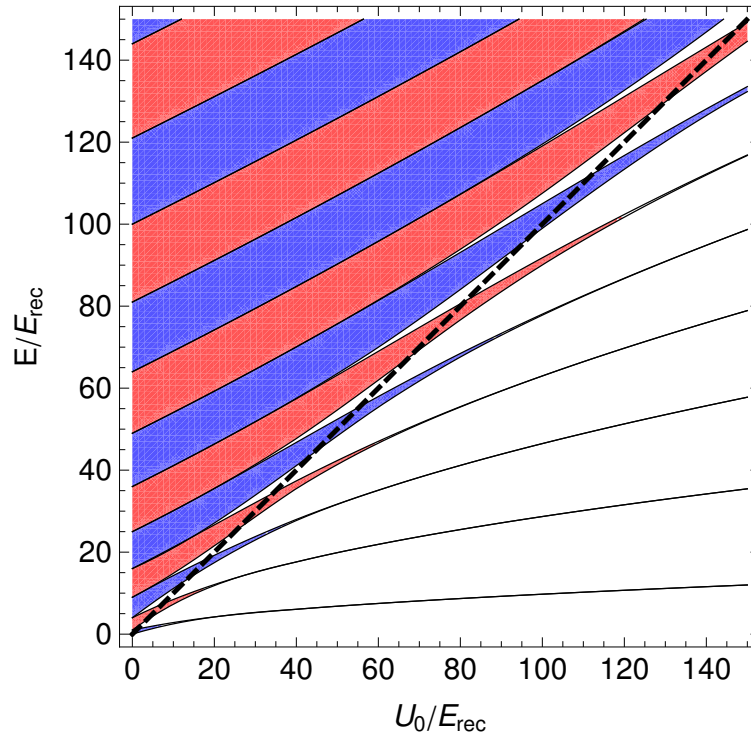
Figure 2.3.: Band structure of the infinite one-dimensional optical lattice without gravity plotted as allowed kinetic energy E versus trap depth U_0 in recoil units. Bands with odd (even) band index n are shown in blue (red). The dashed line indicates the lattice depth $E = U_0$.

A spatial wavefunction basis (Wannier basis) that is localized at the position of each microtrap can be constructed and for small band width and band index n, the Wannier wave functions for lattice site m can be written in terms of the Mathieu equation's standard solutions [14]

$$w_n^m(\xi) = \sqrt{\frac{2}{\pi}} \Theta_m(\xi) \, ce_n(\xi), \tag{2.16}$$

where

$$\Theta_m(\xi) = \begin{cases} 1 & \xi \in [m\pi, (m+1)\pi) \\ 0 & \text{else} \end{cases} \tag{2.17}$$

is the supporting function of the m-th lattice site. In this approximation, matrix elements in the Wannier functions can be easily calculated, for example to estimate lattice heating rates [14]. However, the approximation is based on completely isolated sites and is applicable only for low band index n in a deep lattice. To estimate, for instance, the effects of tunneling, we need to use a numerical method to generate more realistic Wannier states that also apply to shallower lattices. A useful method is based on representing the Schrödinger equation in momentum space, since the potential term will then couple only two specific momenta to the particle momentum. We rewrite the periodic Schrödinger equation as[1]

$$H = \frac{\hbar^2 \hat{k}^2}{2m} + \frac{U_0}{2}[1 - \cos 2\kappa\hat{z}], \tag{2.18}$$

In a plane wave basis $\langle x|k \rangle \propto e^{ikz}$, the periodicity in the potential transforms into coupling only two other momenta to a given momentum k:

$$H|k\rangle = \left(\frac{\hbar^2 k^2}{2m} + \frac{U_0}{2}\right)|k\rangle - \frac{U_0}{4}(|k + 2\kappa\rangle + |k - 2\kappa\rangle). \tag{2.19}$$

The periodicity of the potential leads to periodic Bloch waves $|n, q\rangle$ as the eigenfunctions of this operator. Here, the dimensionless quasimomentum q is limited to the first Brillouin zone $\kappa q \in (-\kappa, \kappa]$ and n indexes the band structure as above. We let q be a fixed value within the first Brillouin zone, and transfer Eq. 2.18 into a plane wave basis parametrized by q. We

---

[1]Many references describe the application of Bloch's theorem and the Wannier basis to optical lattices. This summary is based on [56, 61–64].

can omit odd multiples of κ in the basis, since they are not coupled by Eq. 2.19. We let

$$\langle \xi | j, q \rangle \propto e^{i(2j+q)\xi}, \tag{2.20}$$

with integer j, and we truncate the basis such that $-J \leq j \leq J$. This choice is equivalent to treating a system of $2J+1$ lattice sites with periodic boundary conditions. As above, we use the dimensionless position $\xi \equiv \kappa z$. In this basis, the Hamiltonian matrix (in units of the recoil energy) is sparse and has tridiagonal structure [56, 62]

$$H(q) = \frac{u}{2} I_{2J+1} + \begin{pmatrix} (-2J+q)^2 & -\frac{u}{4} & & & & & \\ -\frac{u}{4} & (-2J+2+q)^2 & -\frac{u}{4} & & & & \\ & -\frac{u}{4} & \ddots & \ddots & & & \\ & & \ddots & \ddots & \ddots & & \\ & & & \ddots & \ddots & -\frac{u}{4} & \\ & & & & -\frac{u}{4} & (2J-2+q)^2 & -\frac{u}{4} \\ & & & & & -\frac{u}{4} & (2J+q)^2 \end{pmatrix}, \tag{2.21}$$

where $u \equiv U_0/E_{\rm rec}$ and I_{2J+1} is the $(2J+1)$-dimensional identity matrix. Diagonalizing $H(q)$ numerically gives a set of $(2J+1)$ real q-dependent eigenvector coefficients $c_j^n(q)$ which are normalized to

$$\sum_{j=-J}^{J} [c_j^n(q)]^2 = 1, \tag{2.22}$$

as well as the q-dependent eigenenergies $E_n(q)$. Here, n indexes the band structure and the eigenvectors are sorted according to their eigenvalue. The band structure for $u = 120$ is shown in Fig. 2.4(a). There are seven trapped bands, and all but the two highest are very flat, indicating well-separated microtraps.

To quantify the tunneling rates with respect to trap depth, we calculate the band widths as the difference between the $q = 0$ and the $q = 1$ energy structure in Fig. 2.4(b). The tunneling rate is given by the inverse of the band width. For the magic wavelength lattice, the recoil frequency is $h/(2m\lambda^2) \simeq 3.47$ kHz, so that a bandwidth of $2.9 \times 10^{-4} E_{\rm rec}$ would correspond to a tunneling rate of 1 s^{-1}. Even at typical trap depths of $120 E_{\rm rec}$, tunneling

(a) Band structure for $U_0 = 120 E_{\text{rec}}$. The dashed line indicates U_0.
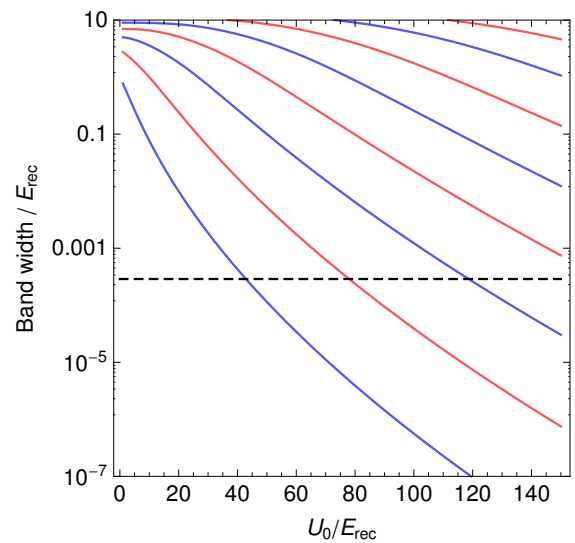
(b) Band widths as a function of U_0. The dashed line indicates a tunneling rate of 1 s^{-1} at $E_{\text{rec}} = h \times 3.47$ kHz.

Figure 2.4.: Quasimomentum-resolved band structure calculations from diagonalization of Eq. 2.21 with $J = 30$.

can be significant if the particles are in higher longitudinal bands or are highly excited in the transverse direction (reducing the effective lattice depth).

It is instructive to also calculate the tunneling rates from a Wannier function perspective. The Bloch vectors in the truncated plane wave basis used here are

$$\langle \xi | n, q \rangle = \frac{1}{\sqrt{\pi}} \sum_{j=-J}^{J} c_j^n(q) e^{i(2j+q)\xi}, \tag{2.23}$$

which are normalized over $[-\pi, \pi] \ni \xi$. If we choose a sufficiently dense set of quasimomenta $q_k \in (-1, 1]$, the Wannier function for lattice site m can be represented as

$$w_n^m(\xi) = \frac{1}{\sqrt{N}} \sum_{k=1}^{N} e^{-iq\pi m} \langle \xi | n, q \rangle. \tag{2.24}$$

The prefactor makes the resulting Wannier function site-normalized.

Figure 2.5 shows the site-localized Wannier functions (solid blue), the Mathieu function approximation (dotted red), and the harmonic oscillator approximation (dotted green) for all trapped bands in a $120E_{\text{rec}}$ lattice. The agreement between Wannier function and Mathieu function is almost perfect within a lattice site, even for the high-lying bands with finite width. The harmonic oscillator approximation shows discrepancies even in the $n = 2$ band. The Mathieu functions are periodic in the lattice spacing and the Wannier functions are localized in each site. However, the localization of the Wannier functions is so good that the cut-off Mathieu function approximation in Eq. 2.16 is almost perfect (see right hand side plots). Although the harmonic oscillator functions could be improved by simple first-order perturbation theory in the anharmonic z^4 term, we recommend the cut-off Mathieu functions for any site-local calculation at this lattice depth since they are readily available in mathematical packages.[2]

In the tight-binding approximation [64], the tunneling dynamics can be described by particles hopping from site to site and the band width is determined by a single tunneling matrix element

$$\mathcal{J}_n \simeq - \int_{-\infty}^{\infty} dx \, [w_n^m(x)]^* H w_n^{m+1}(x). \tag{2.25}$$

---

[2]For instance, as the `MathieuC` function in Mathematica.
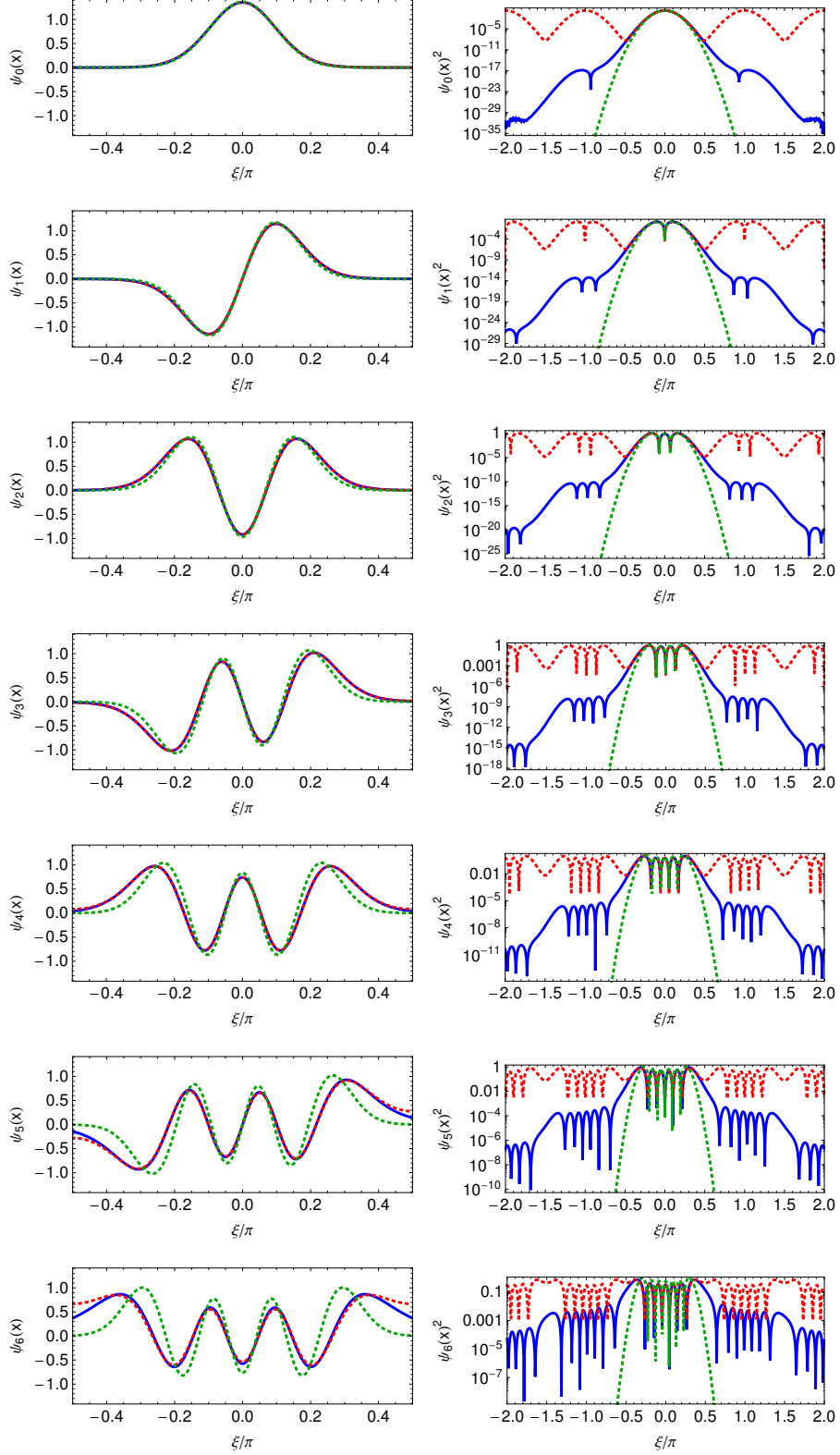
Figure 2.5.: Wannier functions (solid blue), periodic Mathieu functions (dotted red), and harmonic oscillator wave functions (dotted green) for the $120E_{\text{rec}}$ lattice and all trapped bands $n = 0$ to 6.

Within the validity of the tight-binding approximation, the relation between $\mathcal{J}$ and the band width (or tunneling rate) is given by

$$4\mathcal{J}_n = E_n(q=1) - E_n(q=0), \tag{2.26}$$

and from Eqs. 2.23 one can show that calculation of $\mathcal{J}$ in the numerical eigenvalues reduces to a simple integral over the complex unit circle

$$\mathcal{J}_n = -\frac{1}{N}\sum_{k=1}^{N} E_n(q_k)e^{i\pi q_k} \simeq -\int_{-1}^{1} dq E_n(q)e^{i\pi q} = -2\int_{0}^{1} dq E_n(q)\cos\pi q. \tag{2.27}$$

2.6. Adiabatic Wannier-Stark ladder

So far, we have neglected gravity in the description of the optical lattice potential and especially in the models used to describe the tunneling rates. Suppression of tunneling in optical lattice clocks has been a concern from the very beginning. To prevent the atoms from tunneling while the clock laser is interacting, two steps were taken. As we have seen in the last section, the lattices for optical clocks are typically fairly deep ($> 100E_{\text{rec}}$). In addition, the lattice is oriented along gravity, which breaks the symmetry between lattice sites.

This effect is fairly simple to understand: the energy shift between lattice sites due to gravity is given by

$$\Delta_g \equiv \frac{mg}{\kappa} \simeq 0.79\ E_{\text{rec}}, \tag{2.28}$$

for gravitational acceleration $g \simeq 9.81$ m/s^2. If this energy splitting is larger than the lattice bandwidth (without gravity), energy levels in neighboring sites are no longer degenerate and the band width becomes suppressed. Each band n separates into individual states in isolated lattice sites. Since the acceleration is uniform along the lattice, the new energy states are evenly split by Δ_g and this structure is called a Wannier-Stark ladder.

Tunneling from a higher-lying state in the Wannier-Stark ladder to a lower-lying state becomes exponentially suppressed with the ratio of Δ_g over the original bandwidth Γ_n. If the mismatch becomes large enough, such that Δ_g becomes on the order of the interband splitting, resonant tunneling can be allowed from a lower-lying Wannier-Stark ladder to a

higher lying one. As we will see, this is not an issue in deep optical lattices and we only have to consider tunneling within an isolated ladder.

The new eigenstates that describe particles in isolated sites can be easily obtained within the tight-binding approximation. The Wannier-Stark states are given by superpositions of the original Wannier states [64]

$$\psi_n^\ell(\xi) = \frac{1}{\sqrt{M}} \sum_{m=-M}^{M} z_n^m w_n^m(\xi),\tag{2.29}$$

where ℓ is the new Wannier-Stark site index. The new energy levels can be obtained by diagonalizing the tridiagonal Hamiltonian matrix in the Wannier states

$$H_n' = \varepsilon_n I_{2M+1} + \begin{pmatrix} V_{-M} & -\mathcal{J}_n & & & & & \\ -\mathcal{J}_n & V_{-M+1} & -\mathcal{J}_n & & & & \\ & -\mathcal{J}_n & \ddots & \ddots & & & \\ & & \ddots & \ddots & \ddots & & \\ & & & \ddots & \ddots & -\mathcal{J}_n & \\ & & & & -\mathcal{J}_n & V_{M-1} & -\mathcal{J}_n \\ & & & & & -\mathcal{J}_n & V_M \end{pmatrix},\tag{2.30}$$

where $V_m = m\Delta_g/E_{\rm rec}$ and $\varepsilon_n = \int dx [w_0^n(x)]^* H w_0^n(x)$.

However, calculating the tunneling lifetimes of the new Wannier-Stark states is hard. A numerically involved method is based on calculating the poles of a scattering matrix [63]. None of the work available treats the transverse potential, and tunneling in the vertical one-dimensional optical lattice remains hard to calculate accurately.

Following the arguments in Section 2.3, we will treat the transverse coordinate as a classical parameter that adiabatically follows the longitudinal dynamics since any longitudinal tunneling event is much faster than the transverse oscillation time. For these reasons, we model the full potential as an "adiabatic" Wannier-Stark ladder and disallow any change in r during a tunneling event.

A plot of the adiabatic band structure is shown in Fig. 2.6(a), where the infinite lattice energies and their band widths are shown as a function of r/w_0, where the radial trap profile

is modeled by replacing $U_0 \mapsto U_0 e^{-2r^2/w_0^2}$. None of the lower-lying bands become very wide, unless we go to large radii $r \sim w_0$. For transverse temperatures T, the thermally averaged radius is given by

$$\rho_{\text{rms}}^2 \equiv \langle \rho^2 \rangle \simeq \frac{\int_0^\infty d\rho \rho^3 \exp\left[-\frac{2U_0}{k_B T}\rho^2\right]}{\int_0^\infty d\rho \rho \exp\left[-\frac{2U_0}{k_B T}\rho^2\right]} = \frac{k_B T}{2U_0} \simeq 3.0 \times \left(\frac{T}{\mu K}\right)\left(\frac{U_0}{E_{\text{rec}}}\right)^{-1} \tag{2.31}$$

with $\rho \equiv r/w_0$, and $k_B \times 1~\mu K \simeq 6.0~E_{\text{rec}}$. Typical transverse temperatures are $2 - 4~\mu K$, resulting in $\rho_{\text{rms}} \simeq 0.2 - 0.3$. Longitudinal temperatures can be as low as $1~\mu K$, when the sample is laser-cooled in the optical lattice. In this regime, the lowest bands are not significantly broadened, but their energy is strongly dependent on ρ.

The longitudinal Wannier states are thus parametrized by ρ and we can find a tunneling rate for each band and each transverse position. A thermal average over ρ will give an order-of-magnitude estimate for the tunneling rate. Since we do not have a full model for the tunneling, we give upper and lower bounds on the thermally averaged tunneling rate from the following considerations.

An upper bound on the tunneling rate is given by the lattice band structure in the absence of gravity. Fig. 2.6(b) shows the radially varying tunneling rate without gravity as solid colored lines. A lower bound on the tunneling rate is given by the WKB approximation Eq. (2.13), since it completely neglects the effect of many sites, but handles the shape $\cos^2$ shape of the longitudinal potential. The results from the WKB calculation are shown as the dotted colored lines in Fig. 2.6(b). The dashed black line indicates Δ_g. A full model for the tunneling rate should smoothly interpolate between the WKB expression (valid for $\Gamma \ll \Delta_g$) and the lattice structure without gravity (valid for $\Gamma \gg \Delta_g$).

A thermal average over the radial coordinate is shown in panel (c). Note that the first three longitudinal bands have a bandwidth that is always much smaller than Δ_g, indicating that tunneling is negligible even in a thermal sample. For typical lattice depths and longitudinal temperatures of $1~\mu K$, more than 99% of the population resides in the lowest longitudinal band. We conclude that tunneling is not an issue in a vertical one-dimensional lattice at temperatures of a few μK.
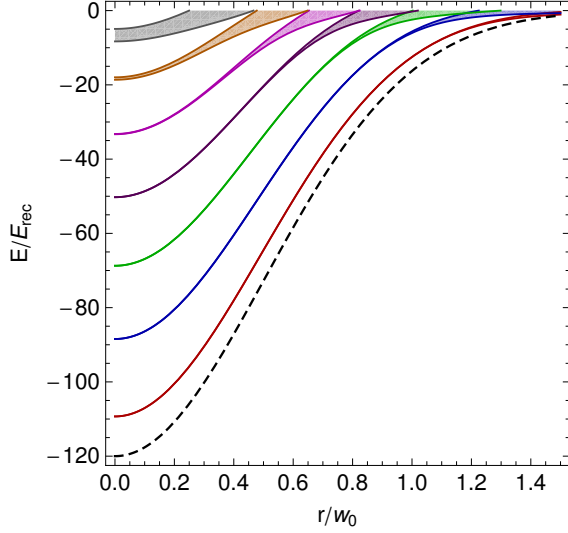
(a) Radial energy structure and band widths without gravity. The dashed line indicates the adiabatic longitudinal lattice depth as the transverse coordinate r varies.
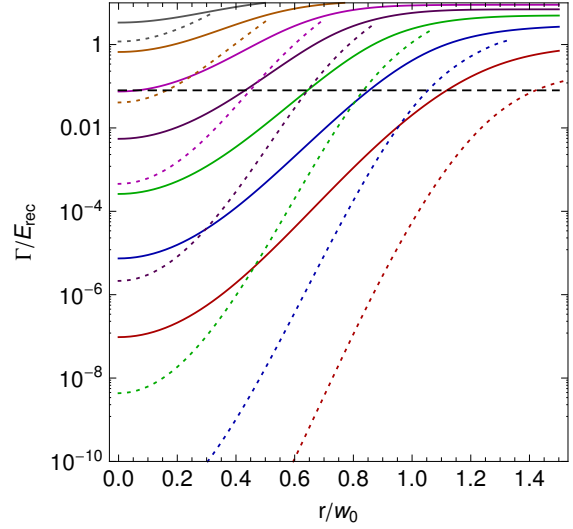
(b) Radial band widths without gravity (solid lines) and WKB tunneling rate (dotted lines). The dashed line indicates the gravitational energy shift $\simeq 0.79 E_{\rm rec}$ between lattice sites for a fully vertical lattice.
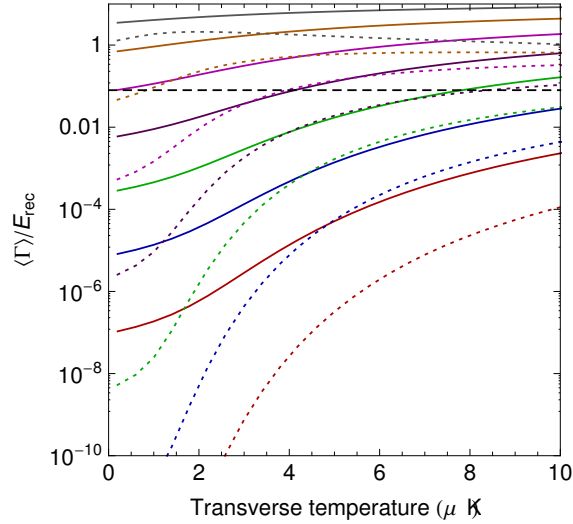
(c) Thermal average over radial direction of panel (b). The full trap depth is $U_0/k_B \simeq 20~\mu$K.

Figure 2.6.: Adiabatic longitudinal band structure in a transverse Gaussian beam potential $U_0 \mapsto U_0 e^{-2r^2/w_0^2}$, with $U_0 = 120 E_{\rm rec}$. The tunneling rate in the Wannier-Stark lattice should interpolate between the band structure without gravity and the WKB tunneling around the gravitational splitting between lattice sites.

Note that transitions between neighboring Wannier-Stark states can also be driven by the spectroscopy laser [56], but that the amplitude of these transitions becomes negligible already at lattice depths of a few recoil. Recent experimental work shows control of tunneling dynamics in a Wannier-Stark ladder by probing these transitions, but at lattice depths of $\leq 4E_{\mathrm{rec}}$ [65].

2.7. Single-site potential

As shown in the last section, we can ignore tunneling dynamics in the vertical one-dimensional lattice. However, the lattice band structure is still important, since the energies of the Wannier-Stark states are given by the lattice without gravity. In this Section, we will develop a simplified model of the single-site potential to finally describe the optical sideband spectra we observed.

We approximate the lattice potential Eq. 2.11 around an antinode of the $\cos^2$ term up to second order in r and fourth order in z

$$U(z,r) \simeq U_0 \left(-1 + \kappa^2 z^2 + \frac{2}{w_0^2} r^2 - \frac{\kappa^4}{3} z^4 - \frac{2\kappa^2}{w_0^2} z^2 r^2 \right), \qquad (2.32)$$

where the gravitational shift is absorbed into an offset of the z coordinate. Treating the quartic distortion and the r-z coupling term in first order perturbation theory for harmonic oscillator states $|\boldsymbol{n}\rangle$ gives an energy spectrum

$$E_{\boldsymbol{n}}/h = \nu_z(n_z+1/2)+\nu_r(n_x+n_y+1)-\frac{\nu_{\mathrm{rec}}}{2}(n_z^2+n_z+1)-\nu_{\mathrm{rec}}\frac{\nu_r}{\nu_z}(n_x+n_y+1)(n_z+1/2), \quad (2.33)$$

with recoil frequency $\nu_{\mathrm{rec}} = E_{\mathrm{rec}}/h$ and longitudinal and transverse trap frequencies

$$\begin{aligned} \nu_z &= 2\nu_{\mathrm{rec}}\sqrt{\frac{U_0}{E_{\mathrm{rec}}}} \\ \nu_r &= \sqrt{\frac{U_0}{m\pi^2 w_0^2}}. \end{aligned} \qquad (2.34)$$

Measuring both trap frequencies determines the trap parameters U_0 and w_0 completely. The

number of states in the trap is approximately given by $N_z N_r^2$, with

$$N_z \simeq \frac{U_0}{h\nu_z} = \sqrt{\frac{U_0}{4E_{\text{rec}}}},$$

$$N_r \simeq N_z \frac{\nu_z}{\nu_r}. \tag{2.35}$$

Typical values in our experiment are $\nu_z \simeq 80$ kHz and $\nu_r \simeq 450$ Hz, giving N_z $(N_r) \simeq$ 6(1000). As shown in the last Section, the longitudinal trap frequency changes with the radial coordinate. Here, this relation is encapsulated in the $r^2 z^2$ coupling term. The frequency gap between longitudinal states is

$$\gamma_z(\boldsymbol{n}) \equiv (E_{n_x,n_y,n_z+1} - E_{n_x,n_y,n_z})/h = \nu_z - \nu_{\text{rec}}(n_z + 1) - \nu_{\text{rec}}\frac{\nu_r}{\nu_z}(n_x + n_y + 1). \tag{2.36}$$

We will use the single-site approximation in the next Section to describe the spectral features in absorption spectroscopy of particles trapped in the one-dimensional optical lattice.

2.8. Sideband spectra in a one-dimensional optical lattice

We finally arrived at the important quantity $\gamma_z(\boldsymbol{n})$ that describes the spectroscopic features in a one-dimensional optical lattice and can model the equivalent of the harmonic confinement features in Fig. 2.1. Two example absorption spectra are shown in Fig. 2.7.

The first spectrum (red squares) represents a sample loaded directly from the $^1\text{S}_0$-$^3\text{P}_1$ MOT into the optical lattice without any further cooling. The second spectrum (blue circles) represents the same situation, but with longitudinal sideband cooling and transverse Doppler cooling applied to the sample before spectroscopy. Several features are evident. As in Fig. 2.1, there is a central sharp carrier transition as well as a red and a blue first order sideband. The relative height of the blue and red sideband is an indication of the temperature along the probe direction (see Section 2.2). However, the sidebands are not symmetric, but slope towards the carrier, while maintaining a sharper edge that faces away from the carrier.

In this Section, we will build a detailed model of the spectroscopic features in Fig. 2.7 to extract important system parameters such as longitudinal and transverse temperatures by
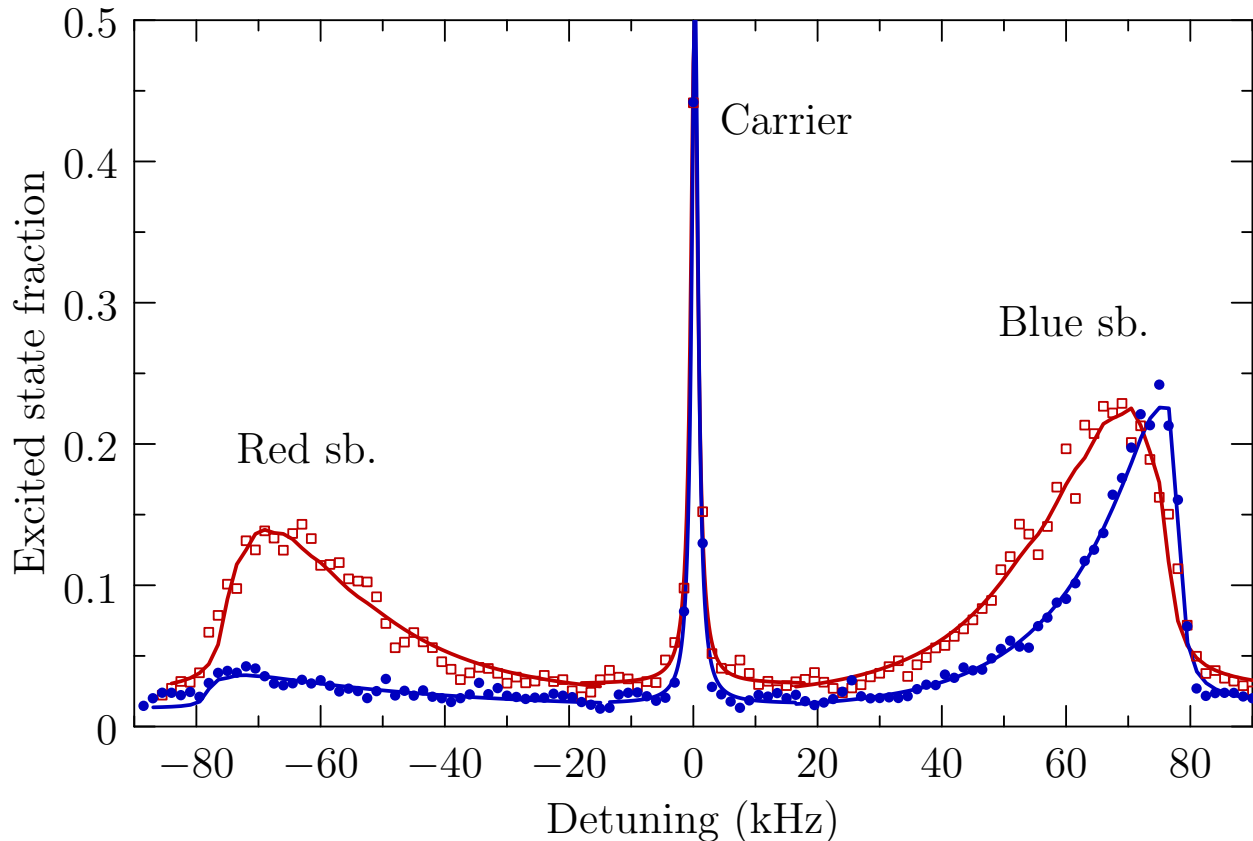
Figure 2.7.: Example absorption spectra in the one-dimensional optical lattice probed along the lattice axis with a Rabi pulse time of 80 ms. Three features are evident: a central carrier transition, where the longitudinal motional state n_z is unchanged, and a red (blue) sideband where n_z is reduced (increased) by one. The data points in red represent a sample loaded from the $^1S_0$-$^3P_1$ MOT. Data points in blue show the change in the spectral features after the sample is cooled in-trap using longitudinal sideband cooling and transverse Doppler cooling. Fits to the data (solid lines) are based on the single-site expansion of the lattice potential.

fit. Based on the model, we will also be able to explain spectroscopy on the carrier transition in detail.

The sideband features can be well understood in the single-site potential picture derived in the previous Section. From Eq. 2.36, we see that the first-order longitudinal sidebands $n_z \to n_z \pm 1$ will appear at different detunings from the carrier for each n_z. In addition, each longitudinal sideband depends on its radial state through the $r^2 z^2$ coupling term. Even if only the $n_z = 0$ state is populated, the sideband spectrum will not be Lorentzian as in a harmonic trap, but will be smeared out towards the carrier since $\gamma_z(\boldsymbol{n})$ decreases with increasing n_r. The sharp sideband edge indicates the highest $\gamma_z(\boldsymbol{n})$ at the lowest $\boldsymbol{n}$ in the sample. The position of the sharp edge thus lets us determine $\gamma_z(n_x = n_y = n_z = 0) = \nu_z - \nu_{\text{rec}}$ precisely.

Since the sidebands are still well separated from the carrier, we will derive a lineshape expression valid for the blue sideband first. Similar to Eq. 2.10, we assume a thermal distribution with transverse temperature T_r and find the thermally averaged excited state population for the n_z-component of the ℓ-th order longitudinal sideband as

$$
P_e^\ell(n_z, T_r, \Delta, t) = \left(\frac{1 - q_r}{1 - q_r^{1+N_r}} \right)^2 \sum_{n_x=0}^{N_r} \sum_{n_y=0}^{N_r} q_r^{n_x} q_r^{n_y} \times
$$
$$
\frac{|\Omega_\ell(\boldsymbol{n})|^2}{|\Omega_\ell(\boldsymbol{n})|^2 + [\Delta - \ell\gamma_z(\boldsymbol{n})]^2} \sin^2 \sqrt{|\Omega_\ell(\boldsymbol{n})|^2 + [\Delta - \ell\gamma_z(\boldsymbol{n})]^2} \frac{t}{2},
$$

(2.37)

with radial Boltzmann factor $q_r \equiv \exp(-h\nu_r/k_B T_r)$. Since there are many Rabi frequencies $\Omega_\ell(\boldsymbol{n})$ contributing to the sum, we simplify the problem by cycle-averaging the time dependent Rabi oscillations and set $\sin^2(\cdot) \mapsto 1/2$.

To allow for experimental imperfections, we allow for a slight angular mismatch $\Delta\theta$ between the probe pointing $\hat{\boldsymbol{k}}_p$ and the lattice direction $\hat{\boldsymbol{z}}$ and for this discussion, we choose the $\hat{\boldsymbol{x}}$ and $\hat{\boldsymbol{y}}$ axes in the radially-isotropic harmonic confinement such that

$$
\hat{\boldsymbol{k}}_p \simeq k_p[\hat{\boldsymbol{z}} + \frac{\Delta\theta}{2}(\hat{\boldsymbol{x}} + \hat{\boldsymbol{y}})].
$$

(2.38)

The transverse extent of the probe beam is large and can be approximated by a cylindrically symmetric function with respect to the net probe direction $\hat{\boldsymbol{k}}_p$. The extent of the probe beam w_p is generally chosen to be much larger than the trap waist w_0. The resulting Rabi

frequency from Eq. 2.2 is

$$\Omega(\boldsymbol{n}) = \Omega_0 \langle \boldsymbol{n} | e^{i\boldsymbol{k}_p \cdot \boldsymbol{x}} [1 + \mathcal{O}(a_r^2/w_p^2)] | \boldsymbol{n} \rangle, \tag{2.39}$$

with transverse oscillator length $2\pi a_r \equiv \sqrt{h/(m\nu_r)}$. For typical parameters, $a_r^2/w_p^2 \simeq 10^{-4}$, and we conclude that the transverse shape of a cylindrically symmetric probe beam with large cross section cannot influence the spectroscopic results. The Lamb-Dicke parameters become

$$\eta_z = \frac{1}{\lambda_p} \sqrt{\frac{h}{2m\nu_z}}$$
$$\eta_x = \eta_y = \eta_r = \frac{\Delta\theta}{2\lambda_p} \sqrt{\frac{h}{2m\nu_r}}. \tag{2.40}$$

Since the mismatch $\Delta\theta$ is assumed to be small, we can approximate the Laguerre polynomials in the Rabi frequency as in Eq. 2.8 and find a carrier Rabi frequency

$$\Omega_c(\boldsymbol{n}) \simeq \left[\Omega_0 \prod_j e^{-\eta_j^2/2} \right] (1 - n_z \eta_z^2)[1 - (n_x + n_y)\eta_r^2] \tag{2.41}$$

and blue (red) first-order longitudinal sideband Rabi frequencies

$$\Omega_{\text{bsb}}(\boldsymbol{n}) = \Omega_c(\boldsymbol{n}) i\eta_z \sqrt{n_z} \left(1 + \frac{n_z}{2}\eta_z^2 \right),$$
$$\Omega_{\text{rsb}}(\boldsymbol{n}) = \Omega_c(\boldsymbol{n}) i\eta_z \sqrt{n_z + 1} \left(1 + \frac{n_z + 1}{2}\eta_z^2 \right). \tag{2.42}$$

Note that with the symmetric misalignment choice $\eta_x = \eta_y \equiv \eta_r$ and that all transverse motional quantum numbers appear as the combination $n_x + n_y$ in Eq. 2.38. If we introduce a radial quantum number n_r and a corresponding degeneracy factor $n_r + 1$, we can collapse one of the sums in the equation and find the time averaged and radially averaged excited state population for the carrier $\ell = 0$ and blue (red) sideband $\ell = +1$ (-1):

$$\langle P_e^\ell(n_z, T_r, \Delta) \rangle_t \simeq \frac{1}{2} \left(\frac{1 - q_r}{1 - q_r^{1+N_r}} \right)^2 \sum_{n_r=0}^{N_r} \frac{(n_r + 1)q_r^{n_r}\Omega_c(n_z, n_r)^2 f_\ell(n_z)}{\Omega_c(n_z, n_r)^2 f_\ell(n_z) + [\Delta - \ell\gamma_z(n_z, n_r)]^2}, \tag{2.43}$$

where we neglected fourth order terms in η_z in

$$f_\ell(n_z) = \begin{cases} \eta_z^2(n_z + 1) & \ell = -1 \\ 1 & \ell = 0 \\ \eta_z^2 n_z & \ell = +1 \end{cases} \tag{2.44}$$

On the shallow sideband slope, $(\Delta/\gamma_z \ll 1)$, the sum can be simplified further by realizing that its main contribution arises from the term where $\Delta = \ell\gamma_z(n_z, n_r)$, which leads to a relationship

$$n_r + 1 \simeq -\frac{\nu_z}{\nu_{\rm rec}\nu_r}[\Delta - \tilde{\gamma}_z(n_z)], \tag{2.45}$$

between radial quantum number and base longitudinal frequency gap $\tilde{\gamma}_z(n_z) \equiv \nu_z - \nu_{\rm rec}(n_z + 1)$. If we approximate the radial sum by this main term, we find a simple functional form

$$\sigma_{\rm bsb}^{n_z}(\Delta) \equiv \langle P_e^{\rm bsb}(n_z, T_r, \Delta)\rangle_t \propto \left(1 - \frac{\Delta}{\tilde{\gamma}_z(n_z)}\right) e^{-\alpha[1-\Delta/\tilde{\gamma}_z(n_z)]}\Theta[\tilde{\gamma}_z(n_z) - \Delta], \tag{2.46}$$

with $\alpha \equiv [\tilde{\gamma}_z(n_z)/\nu_{\rm rec}](h\nu_z/k_B T_r)$. The applicability of this approximation is ensured by cutting off the the line shape at $\Delta = \tilde{\gamma}_z(n_z)$ with the Heaviside function Θ. For the relevant parameters, this lineshape can be approximately area-normalized to three significant figures with a prefactor $\alpha^2/\tilde{\gamma}_z(n_z)$.

The longitudinal trap anharmonicity produces a blue sideband for each n_z at a different detuning. Assuming a thermal distribution in z with temperature T_z, we can describe the full blue sideband shape as a Boltzmann-weighted superposition of area-normalized components

$$\sigma_{\rm bsb}(\Delta) \equiv \left(\sum_{n_z=0}^{N_z} e^{-E_{n_z}/k_B T_z}\right)^{-1} \sum_{n_z=0}^{N_z} e^{-E_{n_z}/k_B T_z}\sigma_{\rm bsb}^{n_z}(\Delta), \tag{2.47}$$

where the longitudinal energy $E_{n_z}/h = \nu_z(n_z+1/2) - \nu_{\rm rec}/2(n_z^2+n_z+1)$ includes the quartic distortion of the longitudinal trap as an approximation to the full lattice band structure in Section 2.5. The red sideband lineshape is derived analogously.

A nonparametric method to extract the longitudinal temperature T_z from sideband spectra can be derived by comparing the integrated areas underneath the first order blue and red sidebands. Regardless of the details of the component lineshapes σ^{n_z}, the only difference between the red and blue sidebands is that the Boltzmann weights are shifted according to $n_z \mapsto n_z + 1$. Since $n_z = 0$ does not contribute to the red sideband, the ratio of sideband areas is

$$\frac{\int d\Delta\, \sigma_{\rm rsb}(\Delta)}{\int d\Delta\, \sigma_{\rm bsb}(\Delta)} = \frac{\sum_{n_z=1}^{N_z} e^{-E_{n_z}/k_B T_z}}{\sum_{n_z=0}^{N_z} e^{-E_{n_z}/k_B T_z}} = 1 - \frac{e^{-E_0/k_B T_z}}{\sum_{n_z=0}^{N_z} e^{-E_{n_z}/k_B T_z}}. \tag{2.48}$$

After extracting ν_z from the sharp sideband edge, and given a calibration measurement of ν_r and ν_z for a particular lattice laser power and waist, we can calculate the energy structure E_{n_z} as shown previously. With this information, Eq. 2.48 can be solved numerically for T_z. Note that comparing the sideband peak heights is generally not accurate since power-broadening of the underlying individual components is dependent on the motional state through $\Omega(\boldsymbol{n})$.

The fits (solid lines) in Fig. 2.7 are based on fitting the sideband lineshapes using Eq. 2.47. However, the underlying functional form for $\sigma_{\mathrm{bsb}}^{n_z}(\Delta)$ does not use the main-term approximation in Eq. 2.46. For most applications, Eq. 2.46 is sufficient and easy to implement in a fitting routine to extract the transverse temperature T_r from longitudinal spectra after fixing T_z to the number extracted from the sideband area ratio. Note that the sideband lineshape is not very sensitive to the value of η_r^2 and thus $\Delta\theta$ because the main term approximation describes the overall shape fairly accurately and η_r^2 appears only in $\Omega_c(n_z, n_r)$, which cancels in the main term.

2.9. Carrier spectroscopy and effective misalignment

We have seen in the last Section that the sideband shapes are fairly insensitive to a possible effective misalignment $\Delta\theta$ between the probe beam and the lattice axis. However, it is clear that $\Delta\theta$ would introduce Rabi frequency inhomogeneity through Eq. 2.41.

Describing the carrier spectroscopy for non-zero $\Delta\theta$ leads to simpler formulas if we rotate the coordinate system such that the inhomogeneity is along a particular trap axis, say

$$\boldsymbol{k}_p \simeq k_p(\hat{z} + \Delta\theta\hat{x}), \tag{2.49}$$

such that $\eta_x = \frac{\Delta\theta}{\lambda_p}\sqrt{\frac{h}{2m\nu_r}}$, and $\eta_y = 0$. For a particular n_z, we retain the time dependence in Eq. 2.43, set $\ell = 0$, and let $N_r \to \infty$:

$$P_e^c(n_z, \Delta, t) = (1 - q_x) \sum_{n_x=0}^{\infty} q_x^{n_x} \frac{\Omega_c(n_z, n_x)^2}{\Omega_c(n_z, n_x)^2 + \Delta^2} \sin^2\left(\sqrt{\Omega_c(n_z, n_x)^2 + \Delta^2}\frac{t}{2}\right). \tag{2.50}$$

This expression can be directly fit to carrier lineshapes and Rabi flopping data. However, for our purposes, it is instructive to expand the Rabi frequencies in terms of η_x^2 to exhibit a

simple dependence on the misalignment $\Delta\theta$. Care must be taken with expanding the Rabi frequencies but leaving the sinusoidal behavior unchanged, and we find

$$
\begin{aligned}
\frac{\Omega_c(n_z, n_x)^2}{\Omega_c(n_z, n_x)^2 + \Delta^2} &\sin^2\left(\sqrt{\Omega_c(n_z, n_x)^2 + \Delta^2}\frac{t}{2}\right) \\
&\simeq \left[1 - 2n_x\eta_x^2\frac{\Delta^2}{\Omega_c(n_z)^2 + \Delta^2}\right]\sin^2\left[\sqrt{\Omega_c(n_z)^2 + \Delta^2}\left(1 - \frac{\Omega_c(n_z)^2}{\Omega_c(n_z)^2 + \Delta^2}n_x\eta_x^2\right)\frac{t}{2}\right].
\end{aligned}
\tag{2.51}
$$

To describe carrier Rabi flopping in a simple fashion adequate for a fitting routine, we set $\Delta = 0$. In this case, we obtain

$$
\begin{aligned}
P_e^c(n_z, t) &= \sum_{n_x=0}^{\infty}(1 - q_x)q_x^{n_x}\sin^2[\phi(n_z)(1 - \eta_x^2 n_x)/2] \\
&= \frac{1}{2} + \frac{1 - q_x}{2}\frac{q_x\cos[\phi(n_z)(1 - \eta_x^2)] - \cos\phi(n_z)}{1 + q_x^2 - 2q_x\cos\phi(n_z)\eta_x^2},
\end{aligned}
\tag{2.52}
$$

with

$$
\phi(n_z) \equiv \Omega_0 e^{-\eta_x^2/2}e^{-\eta_z^2/2}L_{n_z}(\eta_z^2)t.
\tag{2.53}
$$

If more than one longitudinal state n_z is occupied, a Boltzmann-weighted superposition of Eq. 2.52 is used as before. For zero misalignment $\eta_x \to 0$, Eq. 2.52 reduces to completely coherent Rabi flopping $\sin^2\phi(n_z)/2$. In the presence of misalignment, the Rabi fringes dephase to $1/2$ because the n_x dependence introduces many different Rabi frequencies. With higher transverse temperature T_r, more transverse states n_x will contribute, and the Rabi frequency inhomogeneity increases. Larger misalignment angle $\Delta\theta$ increases the inhomogeneity in a similar way, by introducing a larger change in Rabi frequency for the same n_x. Note that the dephasing of the oscillations is a completely coherent process and that rephasing of the oscillations still occurs. However, because many n_x contribute, the revivals will take many seconds.

Experimentally, we obtain the excited state fraction by first measuring the population in the ground state by recording fluorescence on $^1S_0$-$^1P_1$. This process is destructive and removes the ground state atoms from the lattice. After the measurement pulse, the excited state population is repumped back to the ground state via $^3P_1$. These atoms are then measured again by fluorescence detection. The experimentally measured excited state fraction is given by the ratio of excited state fluorescence counts over the sum of ground and excited

state counts. The repump efficiency $\beta \leq 1$ can vary, which causes dephasing of the Rabi flopping to $\beta/(\beta + 1)$ instead of $1/2$.

Figure 2.8 shows the effect of transverse temperature and misalignment angle on the carrier Rabi flopping. The top panel shows the excited state fraction as a function of Rabi pulse time for sample temperatures of 1 μK (blue circles) and 3 μK (red squares), as determined from sideband spectra and time-of-flight expansion. The Rabi oscillations are visible for about 10 cycles in the cold sample, but decay quickly after 5-6 cycles in the hotter sample. The data is fit with Eq. 2.53 and we obtain $\Omega_0 = 59$ Hz and 76 Hz, respectively. Both fits result in a misalignment angle $\Delta\theta \simeq 10$ mrad.

In the lower panel, $\Delta\theta$ is increased by misaligning the probe beam with respect to the lattice axis and the effect on the visibility is even more drastic than when increasing the temperature. Fits with Eq. 2.53 give $\Omega_0 = 55$ Hz and $\Delta\theta = 10$ mrad for the least misaligned case (blue circles). A fit to the red squares results in $\Omega_0 = 56$ Hz and $\Delta\theta = 17$ mrad, consistent with a geometrical estimate of $\Delta\theta$. For the largest misalignment (green triangles), the small η_x^2 approximation used in deriving Eq. 2.53 starts to break down and the fit looks much worse. However, the fit still predicts $\Delta\theta = 40$ mrad, again consistent with the geometrical estimate.

Each data point in the figure is obtained by scanning out a full carrier spectrum for a given pulse time and measuring the central fringe height. An example spectrum fit with Eq. 2.50 is shown in Fig. 2.9 for a probe time of 1.7 ms. In this case, the temperature is allowed to vary when fixing the misalignment to 10 mrad from Fig. 2.8. The resulting temperatures $T_z = T_r = 2.1(2)$ μK agrees well with the sideband method and time-of-flight expansion.

In our experimental apparatus, even in the experimentally best aligned case, the carrier spectroscopy data is consistent with a misalignment angle $\Delta\theta \simeq 10$ mrad. From geometrical estimates, the alignment precision should be much be better than that. The angle $\Delta\theta$ should be interpreted as an *effective* misalignment that is due to the geometrical overlap between the probe wave vector and the lattice shape. Both probe and lattice beams pass through the same optical elements after being combined on a dichroic beamsplitter. The main suspect for
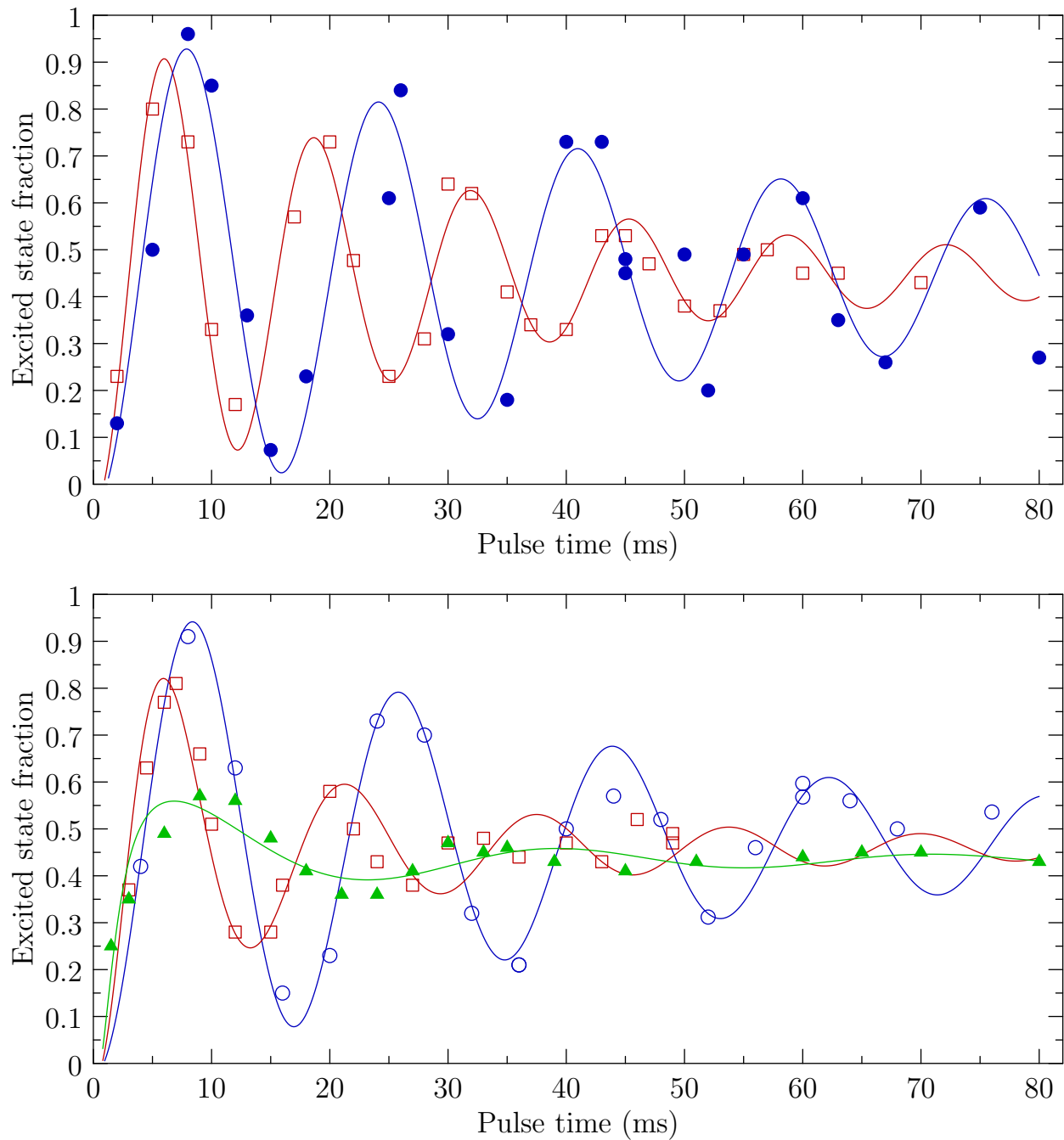
Figure 2.8.: Carrier Rabi flopping as the central peak excited state fraction in a lineshape scan for varying Rabi pulse time. The top panel shows the faster dephasing with an increase in temperature from 1 μK (blue circles) to 3 μK (red squares). The bottom panel shows similar behavior with an intentionally misaligned probe beam, where the blue circles correspond to the most well aligned case (see text).
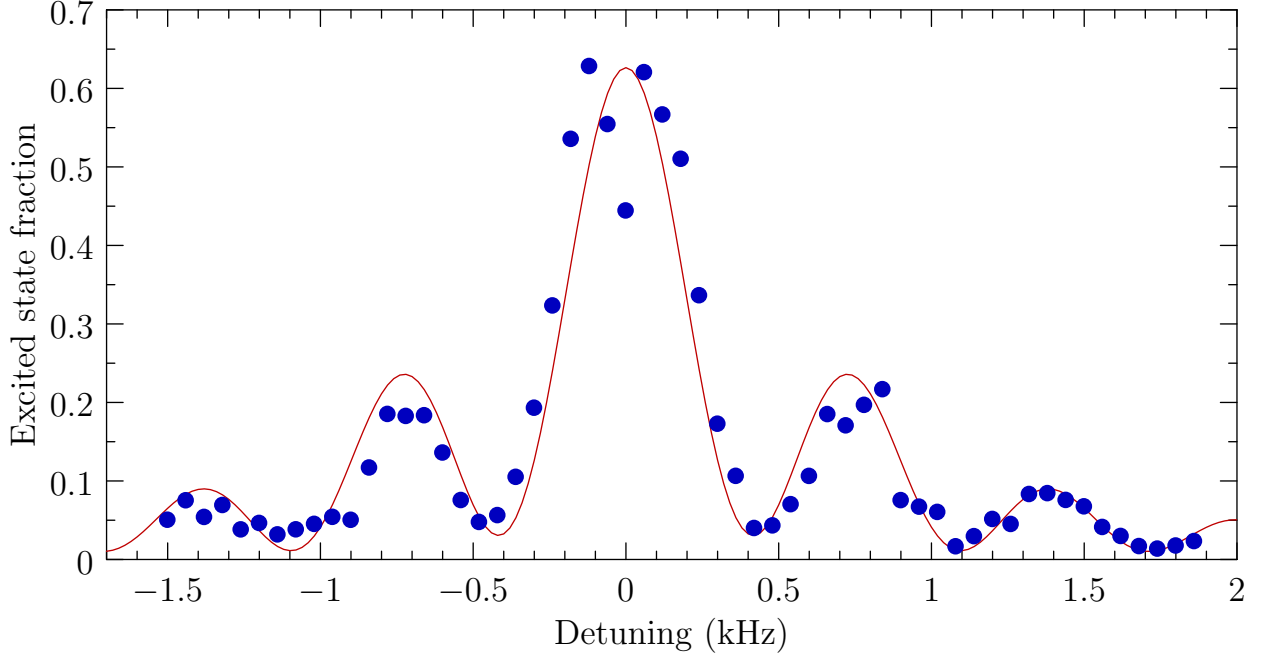
Figure 2.9.: Carrier line shape for the best-aligned case. The data (blue circles) are fit with Eq. 2.50 and the temperature is allowed to vary while fixing $\Delta\theta = 10$ mrad.

introducing the effective angular mismatch are aberrations caused by the vacuum viewports that both the probe and lattice beams traverse.

As we have seen above, the main result of both effective misalignment and temperature is to increase the inhomogeneity in Rabi frequencies. Note, however, that the inhomogeneity discussed here is Rabi frequency inhomogeneity due to variation of the atomic response to a perfectly homogeneous optical field over the small extent of a single lattice site. To characterize these kinds of effects in a source-independent way, we define a single-site mean Rabi frequency $\bar{\Omega}$ and an rms spread $\Delta\Omega$ by

$$
\begin{aligned}
\bar{\Omega} &= \sum_{n_x, n_z} w(n_x) w(n_z) \Omega(n_x, n_z), \\
\Delta\Omega &= \sqrt{\sum_{n_x, n_z} w(n_x) w(n_z) \Omega(n_x, n_z)^2 - \bar{\Omega}^2},
\end{aligned}
\tag{2.54}
$$

using the appropriately normalized Boltzmann weights w. The ratio $\Delta\Omega/\bar{\Omega}$ characterizes the single-site inhomogeneity in a dimensionless way and we plot results for temperature and misalignment induced inhomogeneity in Fig. 2.10. Typical values for this experiment are

0.05-0.4 for the misalignment angles determined from the data in Fig. 2.8.
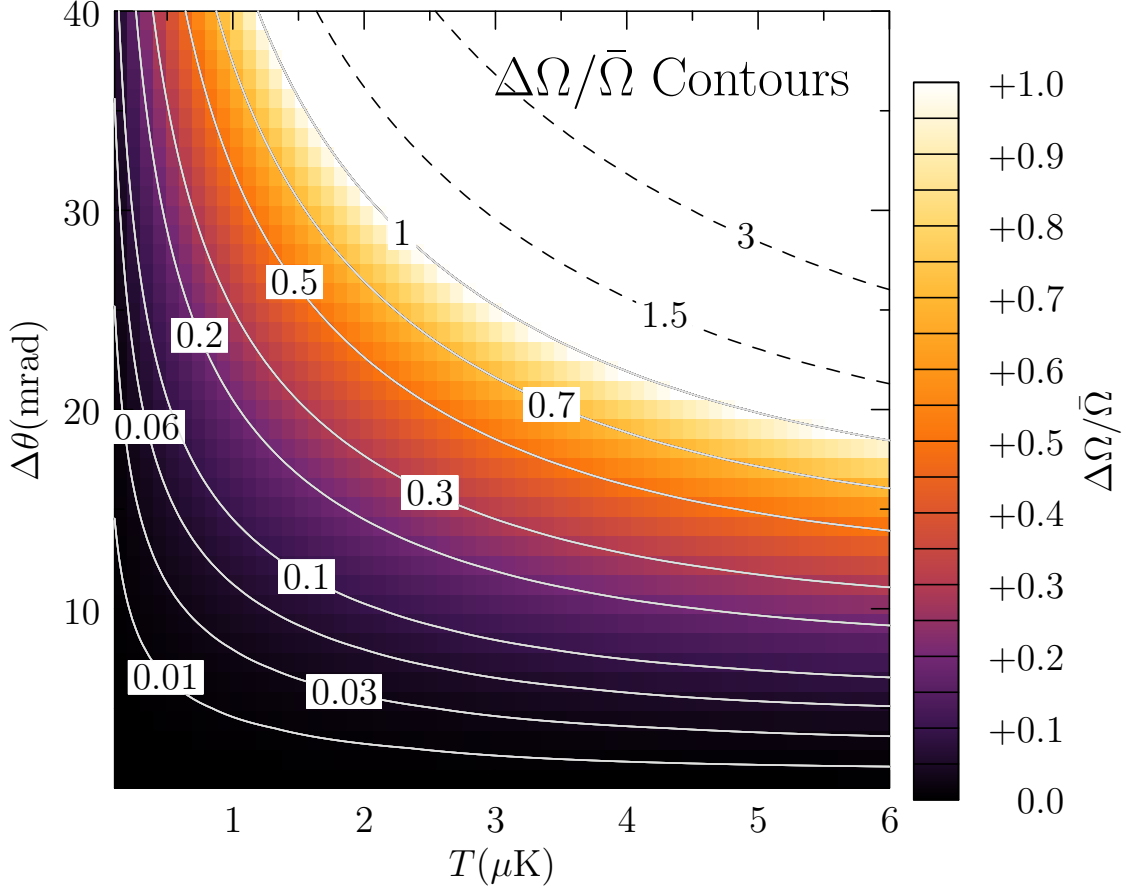
Figure 2.10.: Contour plot of the single-site Rabi frequency inhomogeneity parameter $\Delta\Omega/\bar{\Omega}$ when assuming an effective misalignment $\Delta\theta$ along x and a homogeneous sample temperature $T_z = T_r = T$. The dashed contours indicate points where $\bar{\Omega}$ becomes smaller than $\Delta\Omega$, because the transverse Laguerre polynomials in the Rabi frequency expression can become negative for sufficiently large n_x.

To summarize: we have shown how optical spectroscopy of carrier and motional sideband transitions in a vertical one-dimensional optical lattice can be used to extract important system parameters. We have determined the full potential from measurement of sideband frequencies, extracted information about the kinetic energy in all directions, and found a way to characterize the single-site Rabi frequency inhomogeneity.

The inhomogeneity characterization in terms of $\Delta\Omega/\bar{\Omega}$ is useful because it allows a general discussion of inhomogeneity-induced effects. In particular, we will extensively use the inhomogeneity parameter to characterize inhomogeneity-induced optical clock shifts in the next Chapter.

Ultracold Collisions in Lattice Spectroscopy

WE have seen in the previous Chapter that spectroscopy of many particles can enhance the signal-to-noise of the measurement by using many atoms simultaneously to measure a spectroscopic feature. A major limitation to making the particles evolve equally under the influence of the spectroscopy laser is that their response depends on the individual atom's motional state. This simple fact is in principle unavoidable if using fermionic particles since their motional state cannot be the same if there is more than one particle per site.

The main reason for using fermionic particles for clock spectroscopy is that interactions between identical particles (they only differ in their spatial wavefunction) are suppressed by the Pauli exclusion principle. The suggestion of building an optical clock using Fermions arose because one of the main limitations to the Cs frequency standard are interaction-induced clock frequency shifts during the Ramsey dark time. In a Cs fountain clock, the atoms are prepared in a MOT and then are launched upwards through a microwave cavity where the first Ramsey pulse takes place. The atomic cloud slows under the influence of gravity and falls back down through the same microwave cavity and a second Ramsey pulse interacts with the atoms. The problem is that that the Cs atoms interact during this whole sequence. In contrast, in an optical lattice clock, the atoms are confined to the sites of an optical lattice

and their motional state is an eigenstate of the trapping potential. The thought is then that the Pauli exclusion principle should prevent the egregious clock frequency shifts that limit the Cs fountain clock accuracy.

With the increasing performance of the Sr optical lattice clock, in particular after reaching accuracies below 10^{-15}, our experiments have shown that the above picture is too simple. When the single-site occupation number is varied by loading more or less atoms into the optical lattice, we have found that the optical clock frequency experiences a shift proportional to the atomic density.

How can we reconcile this experimental fact with the Pauli exclusion principle? Remember that the Pauli exclusion principle only holds for indistinguishable particles. The Sr atoms in our experiments are optically pumped into a single spin state and their electronic state is prepared in either $^1S_0$ or $^3P_0$. This means that the particles are initially indistinguishable in their internal degrees of freedom. However, because their external degrees of freedom are distinguishable (they are in different motional states), they react to a perfectly homogeneous spectroscopic excitation in an inhomogeneous way. If we consider two atoms in different motional states, their Rabi frequency will be slightly different. This difference makes their evolution on the Bloch sphere different and the atoms slowly become distinguishable as the spectroscopic excitation progresses. As soon as they are not completely indistinguishable anymore, they are allowed to interact. This interrogation-induced distinguishability is fundamental to the spectroscopic process and will lead to density-dependent clock frequency shifts.

Our experimental data [9, 46] has led to multiple theoretical models that try to relate the underlying interactions to the spectroscopic results [47–50]. We will present an introduction to the many-body model developed by A. Rey and co-workers [47], since its generality allows specialization to all other published models. The understanding gained from applying the model to explain the experimental data has led to rapid progress in understanding and controlling the density shifts in both our Sr system and NIST's Yb lattice clock [4], although the underlying interaction mechanics are very dependent on the atomic species

and the particulars of the system under consideration. The model has been generalized to bosonic atoms [66] and predicts the paradoxical fact that density shifts can be suppressed by increasing the interaction energy in a two-dimensional optical lattice. This suppression has also been experimentally verified [51, 67] and work on measuring more of the important interaction parameters is in progress.

Here, we will limit the discussion to the results obtained in a one-dimensional optical lattice and present a general introduction to modeling the loss of indistinguishability and its influence on spectroscopic lineshapes in Rabi spectroscopy.

3.1. Experimental procedure and results

For this experiment, all atoms were initially prepared in the same nuclear spin state and the excited electronic state $^3P_0$. The remaining ground state atoms were removed from the lattice by scattering blue light on the $^1S_0$-$^3P_1$ transition. This preselection via the spectroscopy light results in a slightly more homogeneous sample by removing atoms with very different Rabi frequencies.

The atoms are prepared in either one of the $m_F = \pm 9/2$ magnetic sublevels in the presence of a small bias magnetic field, resulting in a splitting of about 250 Hz between the $\pm 9/2$ transitions. The spectroscopy light propagates along the lattice axis and is linearly polarized along the magnetic field axis and the lattice polarization [22]. To initialize the stabilization procedure, the polarization alternates between $\pm 9/2$ on every cycle and a spectroscopic trace that contains both transitions is built up by scanning the detuning inwards from the outer edges of both spectra. Each half of the initial spectrum is fit with a model lineshape and its center, maximal amplitude and FWHM are extracted.

The clock laser is then frequency-stabilized to the clock transition; the stabilization procedure is shown schematically in Fig. 3.1. The sample is polarized to $\pm 9/2$ alternating every two experimental cycles. Two points on each component lineshape are measured by detuning the clock laser by η FWHM from the component center. The choice of η determines

the final ground state fraction P_g targeted during each interrogation. Four values of P_g are obtained at the four lock points indicated by the green circles in Fig. 3.1 for $\eta = 0.5$. The four values are fed into two separate digital servos that estimate the component line centers. The estimate for line width and peak excited state fraction are assumed to be constant. The servos adjust the detuning steps such that all four lock points have equal P_g when measured.

The clock transition frequency is then *defined* by the average of the two component line center estimates. In this way, the atomic response stabilizes the noisy clock laser to the atomic reference and makes the clock frequency first-order insensitive against any m_F-antisymmetric systematic effects such as a varying bias field.
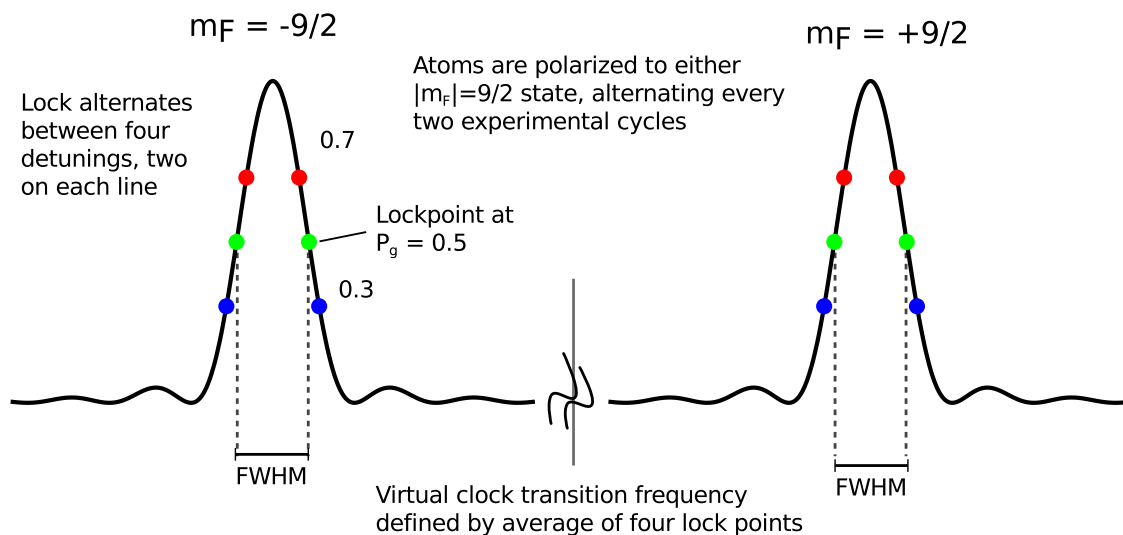
Figure 3.1.: The clock laser is stabilized to a spectroscopic lineshape by alternatively probing at a negative or positive detuning and comparing the final ground state fraction. The sample is alternately polarized into $m_F = \pm 9/2$ every two cycles. A separate servo for each case equalizes the final ground state fraction. A virtual clock transition frequency is defined by the average of both servoed line centers.

As we discussed in the introduction to this Chapter, the density-related clock frequency shifts considered here arise from interactions between the atoms during the spectroscopic pulse. The shifts are quite small (10^{-16} level) and a lot of averaging is necessary to determine their magnitude accurately. The shifts were measured by modulating the atomic density

every 30 s for an experimental cycle time of ~1 s which corresponds to a locking duty cycle of ~4 s. The (virtual) Sr clock frequency was continuously compared against the NIST Ca standard over the optical fiber link [31, 46] and the difference between consecutive segments of low and high density clock frequency data was averaged over long time scales.

By varying η, the locking point on the lineshape was varied. When scanning η in fine enough steps, the measurement determines the differential line shape asymmetry between low and high density settings. It is important to note that the value of m_F is assumed to have no influence on the component lineshapes. Both clock states have no electronic spin ($J = 0$) and the only difference between different magnetic sublevels is the orientation of the nuclear spin with respect to the bias field. The collision process is determined by the interaction of the electron shells. Because of the full outer electronic shells in the spinless states, the coupling between electronic spin and nuclear spin is extremely weak and it is very unlikely that a collision event induces a nuclear spin flip. For these reasons, the value of m_F should have no influence on the scattering process and all component lineshapes look the same.

The experiment was performed over a range of locking points η and for two sample temperatures. Each setting of η required at least a full day of continuous averaging against the Ca standard. The resulting clock frequency shift data [46] at the reference density $\rho_0 = 1 \times 10^{11}$ cm^{-3} is shown in Fig. 3.2. We note two features: (1) the magnitude of the clock frequency shift decreases with locking points closer to the peak of the line profile; (2) the magnitude of the shift increases with increasing temperature.

In the remainder of this Chapter, we will develop a model that describes the spectroscopic response of N particles in the presence of interactions. Using the N-particle model, we can then make predictions about the relative influence of interactions and Rabi frequency inhomogeneity on the lineshapes.
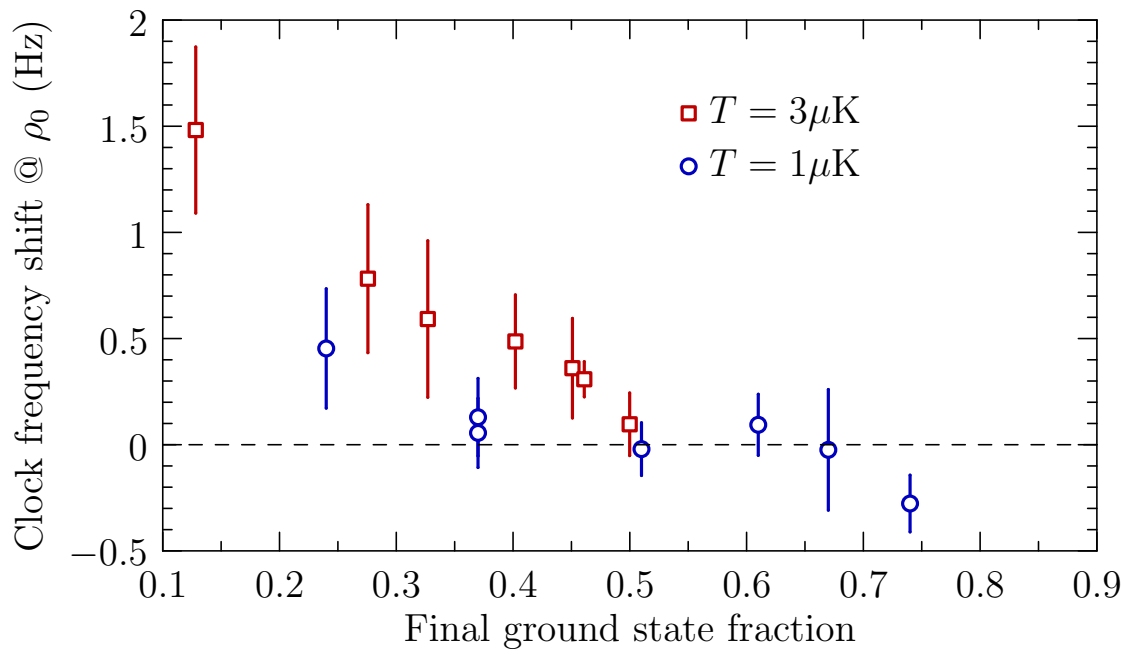
Figure 3.2.: Clock frequency shift [46] as a function of locking point on the spectroscopic lineshape when varying the single-site density. The shift decreases when locking closer to the top of the peak and the shift increases for higher sample temperature. The data are scaled to the reference density $\rho_0 = 1 \times 10^{11}$ cm^{-3}.

3.2. Spin model

In this Section, we will derive an N-particle pseudo-spin model that can be used to describe the spectroscopic process within a single lattice site. The derivation here is based on the theory by A. Rey [47], which can be extended to bosonic atoms [66] and has been successfully used to model the s-wave collisional dynamics in our system for both one- and two-dimensional optical lattices [51, 67]. More recently, the theory has also been adapted to describe p-wave collisions in a Yb optical lattice clock [68].

For nuclear-spin-polarized fermionic atoms in a single-site, the general description requires a fully many-body Hamiltonian [47]

$$
\begin{aligned}
H = \sum_{\alpha \in \{e,g\}} \int d^3r \ \hat{\Psi}_\alpha^\dagger \left[-\frac{1}{2m} \nabla^2 + V(\boldsymbol{r}) \right] \hat{\Psi}_\alpha \\
+ \frac{\hbar \omega_{eg}}{2} \int d^3r \ (\hat{\rho}_e - \hat{\rho}_g) - \frac{\hbar \Omega}{2} \int d^3r \ \left[\hat{\Psi}_e^\dagger e^{-i(\omega_L t - \boldsymbol{k} \cdot \boldsymbol{r})} \hat{\Psi}_g + \ \text{h.c.} \right] \\
+ u_{eg}^- \int d^3r \ \hat{\rho}_e \hat{\rho}_g,
\end{aligned}
\tag{3.1}
$$

that includes both ground (g) and excited (e) electronic states. Here, the field operator $\hat{\Psi}_\alpha^\dagger$ creates a fermion in electronic state α, and the density operator $\rho_\alpha \equiv \hat{\Psi}_\alpha^\dagger \hat{\Psi}_\alpha$ measures the atomic density in state α. The first term describes the kinetic energy within the single-site potential V, which we assume to be the same for both electronic states. The second and third terms describe the energy splitting $\hbar \omega_{eg}$ and the bare Rabi frequency coupling Ω_0 between the clock states with laser frequency ω_L. Here, Ω_0 is defined as the Rabi frequency in the absence of any motional effects. The final term introduces the fermionic s-wave interactions between ground and excited state atoms via $u_{eg}^- = 4\pi \hbar^2 a_{eg}^-/m$. The singlet scattering length a_{eg}^- describes the energy shift of two atoms in an antisymmetric superposition of electronic states. For bosonic atoms, more interaction terms would need to be included [66].

To specialize H to the situation at hand, we expand the field operators in terms of fermionic creation (annihilation) operators $c_{\alpha,\boldsymbol{n}}^\dagger$ ($\hat{c}_{\alpha,\boldsymbol{n}}$) that create (destroy) a particle in electronic state α and motional state $\boldsymbol{n}$. We find

$$
\hat{\Psi}_\alpha = \sum_{\boldsymbol{n}} \hat{c}_{\alpha,\boldsymbol{n}} \phi_{\boldsymbol{n}}(\boldsymbol{r}),
\tag{3.2}
$$

using motional state eigenfunctions $\phi_{\boldsymbol{n}}$. In Chapter 2, we found that the longitudinal motional wavefunctions are well described by the cut-off Mathieu functions and that the transverse degrees of freedom can be modeled as a degenerate two-dimensional harmonic oscillator. We assume separable wave functions along the trap axes $\hat{\boldsymbol{x}}_i$ and write

$$\phi_{\boldsymbol{n}}(\boldsymbol{r}) = \prod_i \psi_{n_i}(x_i), \tag{3.3}$$

An important limitation to the applicability of this operator expansion is that we have assumed particles to be in particular motional eigenstates. The eigenenergy picture is not necessarily valid when considering spectroscopic time scales shorter than typical trap oscillation periods. Here, a typical spectroscopy time scale is 80 ms and a typical longitudinal (transverse) oscillation period is 12 μs (2 ms). For time scales $\sim$2 ms, we cannot consider the atoms to be in a transverse motional eigenstate and wavepackets of many motional states would have to be considered. In this regime, any inhomogeneity-induced collisions should also be suppressed which can be explained by a local picture. The atoms are effectively confined to a volume determined by their velocity and the spectroscopy pulse time. If this volume is significantly smaller than the trapping volume, the excitation process becomes more homogeneous. No collisions can occur since the atoms cannot travel far enough to encounter collision partners that have been excited in a slightly different way. Here, we will focus on long pulse times, use motional eigenstates and neglect to describe such effects. However, these effects would become important when trying to describe Ramsey spectroscopy with short pulse times such that interactions only have to be considered during the Ramsey dark time.

Using the operator expansion, we find a simplified Hamiltonian under the rotating wave approximation in a rotating frame at the laser frequency ω_L

$$\begin{aligned}
H = &- \hbar\delta \sum_{\boldsymbol{n}} \hat{c}_{e,\boldsymbol{n}}^\dagger \hat{c}_{e,\boldsymbol{n}} + \sum_{\alpha,\boldsymbol{n}} E_{\boldsymbol{n}} \hat{c}_{\alpha,\boldsymbol{n}}^\dagger \hat{c}_{\alpha,\boldsymbol{n}} - \sum_{\boldsymbol{n}} \frac{\hbar\Omega_{\boldsymbol{n}}}{2} \left(\hat{c}_{g,\boldsymbol{n}}^\dagger \hat{c}_{e,\boldsymbol{n}} + \text{ h.c.} \right) \\
&+ u_{eg}^- \sum_{\boldsymbol{n}^1,\boldsymbol{n}^2,\boldsymbol{n}^3,\boldsymbol{n}^4} A_{\boldsymbol{n}^1,\boldsymbol{n}^2,\boldsymbol{n}^3,\boldsymbol{n}^4} \, \hat{c}_{e,\boldsymbol{n}^1}^\dagger \hat{c}_{e,\boldsymbol{n}^2} \hat{c}_{g,\boldsymbol{n}^3}^\dagger \hat{c}_{g,\boldsymbol{n}^4},
\end{aligned} \tag{3.4}$$

with laser detuning $\delta \equiv \omega_L - \omega_{eg}$, and motional-state dependent Rabi frequency $\Omega_{\boldsymbol{n}}$ as in Eq. 2.6. The interaction term is proportional to the number of ground and excited state

atoms and the probability amplitude of a given collision process is given by the wave function overlap between the motional states involved

$$A_{\boldsymbol{n}^1,\boldsymbol{n}^2,\boldsymbol{n}^3,\boldsymbol{n}^4} \equiv \prod_i \int_{-\infty}^{\infty} dx_i \ \psi_{n_i^1}^*(x_i)\psi_{n_i^2}(x_i)\psi_{n_i^3}^*(x_i)\psi_{n_i^4}(x_i). \tag{3.5}$$

Since the probability amplitude is an overlap integral over different motional states, we can immediately conclude that the dominant contributions will arise from terms where the $\boldsymbol{n}^j$ are as similar as possible. However, there are still many contributing terms, and it is necessary to simplify the sum considerably. The complexity of the collision term for $N \geq 2$ is the main limitation in modeling the 1D optical lattice. However, a detailed discussion of the assumptions made will lead to a simpler model that contains all other density shift models in the literature as limiting cases [9, 48, 50].

If we require strict energy conservation for elastic collisions, the energy of the creates particles 1 and 3 has to be equal to the destroyed particles 2 and 4. Thus the motional state indices $\boldsymbol{n}^j$ in the interaction term are constrained by

$$E_{\boldsymbol{n}^1} + E_{\boldsymbol{n}^3} = E_{\boldsymbol{n}^2} + E_{\boldsymbol{n}^4}. \tag{3.6}$$

We consider the collision process as a simultaneous motional index conversion

$$\begin{aligned} \boldsymbol{n}^2 &\mapsto \boldsymbol{n}^1, \\ \boldsymbol{n}^4 &\mapsto \boldsymbol{n}^3, \end{aligned} \tag{3.7}$$

and would like to limit the allowed index mappings to simplify the collision term. We make the following assumptions

(i) Although the anharmonicity along the transverse directions is small for typical temperatures, the full trap potential is anharmonic along each axis (see Section 2.7). The anharmonicity suppresses collision processes that conserve energy by changing two quantum by forbidding simultaneous change of two quantum numbers within index vector $\boldsymbol{n}^j$ to conserve energy. In other words, processes, where one particle reduces its motional quantum number and the other particle increases its motional quantum

number according to

$$(n_k^1 = n_k^2 + m \ \wedge \ n_k^4 = n_k^3 - m) \ \forall \ k, m \tag{3.8}$$

are forbidden.

(ii) We assume that the degeneracy in the transverse degrees of freedom is lifted and that there are no accidental degeneracies such that

$$E_{\boldsymbol{n}} \neq E_{\boldsymbol{m}} \ \forall \ \boldsymbol{n}, \boldsymbol{m}. \tag{3.9}$$

Under this assumption, the motional quantum numbers $\boldsymbol{n}$ uniquely determine the energy of a state.

(iii) We assume that only the full motional quantum number vector can be exchanged during a collision. Processes that only swap the motional state along one axis are forbidden.

Within these assumptions, the only allowed collision processes are

$$\begin{aligned} \boldsymbol{n}^2 &= \boldsymbol{n}^1 \ \wedge \ \boldsymbol{n}^4 = \boldsymbol{n}^3, \\ \boldsymbol{n}^2 &= \boldsymbol{n}^3 \ \wedge \ \boldsymbol{n}^4 = \boldsymbol{n}^1, \end{aligned} \tag{3.10}$$

which conserve the number of particles occupying each mode $\boldsymbol{n}$.

Since we consider fermionic particles, initially, there is only particle in each occupied mode. Under our assumptions, this fact does not change during the spectroscopy process which allows us to parametrize the Hamiltonian by a fixed set of motional states. The population dynamics can then be calculated within that set of modes and a final description of a thermal sample can be obtained by thermal averaging over the motional modes considered. We conclude that the drastic simplifications in the collision term are necessary to separate the motional dynamics from the electronic degrees of freedom in the presence of interactions.

The interaction term becomes

$$u_{eg}^- \sum_{\boldsymbol{n} \neq \boldsymbol{m}} \left(A_{\boldsymbol{n},\boldsymbol{n},\boldsymbol{m},\boldsymbol{m}} \ \hat{c}_{e,\boldsymbol{n}}^\dagger \hat{c}_{e,\boldsymbol{n}} \hat{c}_{g,\boldsymbol{m}}^\dagger \hat{c}_{g,\boldsymbol{m}} + A_{\boldsymbol{n},\boldsymbol{m},\boldsymbol{m},\boldsymbol{n}} \ \hat{c}_{e,\boldsymbol{n}}^\dagger \hat{c}_{e,\boldsymbol{m}} \hat{c}_{g,\boldsymbol{m}}^\dagger \hat{c}_{g,\boldsymbol{n}} \right). \tag{3.11}$$

Using the symmetry of A and defining the per-mode number operator $\hat{N}_{\alpha,\boldsymbol{n}} \equiv \hat{c}_{\alpha,\boldsymbol{n}}^\dagger \hat{c}_{\alpha,\boldsymbol{n}}$, we can simplify this term to

$$\frac{u_{eg}^-}{2} \sum_{\boldsymbol{n} \neq \boldsymbol{m}} A_{\boldsymbol{n},\boldsymbol{n},\boldsymbol{m},\boldsymbol{m}} \left(\hat{N}_{e,\boldsymbol{n}} \hat{N}_{g,\boldsymbol{m}} + \hat{N}_{e,\boldsymbol{m}} \hat{N}_{g,\boldsymbol{n}} + \hat{c}_{e,\boldsymbol{n}}^\dagger \hat{c}_{e,\boldsymbol{m}} \hat{c}_{g,\boldsymbol{m}}^\dagger \hat{c}_{g,\boldsymbol{n}} + \hat{c}_{e,\boldsymbol{m}}^\dagger \hat{c}_{e,\boldsymbol{n}} \hat{c}_{g,\boldsymbol{n}}^\dagger \hat{c}_{g,\boldsymbol{m}} \right). \quad (3.12)$$

We introduce a per-mode pseudo-spin operator $\boldsymbol{S}_{\boldsymbol{n}}$ with components

$$\begin{aligned}
S_{\boldsymbol{n}}^1 &\equiv \frac{1}{2}(\hat{c}_{e,\boldsymbol{n}}^\dagger \hat{c}_{g,\boldsymbol{n}} + \hat{c}_{g,\boldsymbol{n}}^\dagger \hat{c}_{e,\boldsymbol{n}}), \\
S_{\boldsymbol{n}}^2 &\equiv \frac{1}{2i}(\hat{c}_{e,\boldsymbol{n}}^\dagger \hat{c}_{g,\boldsymbol{n}} - \hat{c}_{g,\boldsymbol{n}}^\dagger \hat{c}_{e,\boldsymbol{n}}), \\
S_{\boldsymbol{n}}^3 &\equiv \frac{1}{2}(\hat{c}_{e,\boldsymbol{n}}^\dagger \hat{c}_{e,\boldsymbol{n}} - \hat{c}_{g,\boldsymbol{n}}^\dagger \hat{c}_{g,\boldsymbol{n}}) = \frac{1}{2}(\hat{N}_{e,\boldsymbol{n}} - \hat{N}_{g,\boldsymbol{n}}).
\end{aligned} \quad (3.13)$$

Noting that $\hat{N}_{e,\boldsymbol{n}} + \hat{N}_{g,\boldsymbol{n}} = \mathbf{1}$ and using the fermionic anticommutator relations $\hat{c}_{j,\boldsymbol{n}} \hat{c}_{k,\boldsymbol{m}}^\dagger + \hat{c}_{k,\boldsymbol{m}}^\dagger \hat{c}_{j,\boldsymbol{n}} = \delta_{j,k} \delta_{\boldsymbol{n},\boldsymbol{m}}$ we obtain

$$\begin{aligned}
S_{\boldsymbol{n}}^3 S_{\boldsymbol{m}}^3 - \frac{1}{4}\mathbf{1} &= \frac{1}{4}(\hat{N}_{e,\boldsymbol{n}} - \hat{N}_{g,\boldsymbol{n}})(\hat{N}_{e,\boldsymbol{m}} - \hat{N}_{g,\boldsymbol{m}}) - \frac{1}{4}(\hat{N}_{e,\boldsymbol{n}} + \hat{N}_{g,\boldsymbol{n}})(\hat{N}_{e,\boldsymbol{m}} + \hat{N}_{g,\boldsymbol{m}}) \\
&= -\frac{1}{2}(\hat{N}_{e,\boldsymbol{n}} \hat{N}_{g,\boldsymbol{m}} + \hat{N}_{g,\boldsymbol{n}} \hat{N}_{e,\boldsymbol{m}}), \\
S_{\boldsymbol{n}}^1 S_{\boldsymbol{m}}^1 + S_{\boldsymbol{n}}^2 S_{\boldsymbol{m}}^2 &= -\frac{1}{2}(\hat{c}_{e,\boldsymbol{n}}^\dagger \hat{c}_{e,\boldsymbol{m}} \hat{c}_{g,\boldsymbol{m}}^\dagger \hat{c}_{g,\boldsymbol{n}} + \hat{c}_{e,\boldsymbol{m}}^\dagger \hat{c}_{e,\boldsymbol{n}} \hat{c}_{g,\boldsymbol{n}}^\dagger \hat{c}_{g,\boldsymbol{m}}).
\end{aligned} \quad (3.14)$$

This allows us to write the interaction term as a spin-spin interaction in the electronic pseudo-spins

$$-u_{eg}^- \sum_{\boldsymbol{n} \neq \boldsymbol{m}} A_{\boldsymbol{n},\boldsymbol{n},\boldsymbol{m},\boldsymbol{m}}(\boldsymbol{S}_{\boldsymbol{n}} \cdot \boldsymbol{S}_{\boldsymbol{m}} - 1/4). \quad (3.15)$$

Since the motional quantum number distribution is conserved, the kinetic energy term only introduces a constant energy shift

$$\sum_{\alpha,\boldsymbol{n}} E_{\boldsymbol{n}} \hat{c}_{\alpha,\boldsymbol{n}}^\dagger \hat{c}_{\alpha,\boldsymbol{n}} = \sum_{\boldsymbol{n}} E_{\boldsymbol{n}}(\hat{N}_{e,\boldsymbol{n}} + \hat{N}_{g,\boldsymbol{n}}) = \sum_{\boldsymbol{n}} E_{\boldsymbol{n}}, \quad (3.16)$$

and can be omitted.

We finally find a simplified N-particle pseudo-spin Hamiltonian that is parametrized by the initial motional state configuration $\{\boldsymbol{n}^1, \ldots, \boldsymbol{n}^N\}$ under the collision term assumptions given in the above derivation. The Hamiltonian is

$$H/\hbar = -\delta \sum_{\boldsymbol{n}} S_{\boldsymbol{n}}^3 - \sum_{\boldsymbol{n}} \Omega_{\boldsymbol{n}} S_{\boldsymbol{n}}^1 - \sum_{\boldsymbol{n} \neq \boldsymbol{m}} U_{\boldsymbol{n},\boldsymbol{m}}(\boldsymbol{S}_{\boldsymbol{n}} \cdot \boldsymbol{S}_{\boldsymbol{n}} - 1/4), \quad (3.17)$$

with $U_{\boldsymbol{n},\boldsymbol{m}} \equiv u_{eg}^- A_{\boldsymbol{n},\boldsymbol{n},\boldsymbol{m},\boldsymbol{m}}/\hbar$. Note that this Hamiltonian is basically a Heisenberg Hamiltonian used to model spin dynamics in a solid state system:

$$H = -g\mu_B \boldsymbol{B} \cdot \sum_i \boldsymbol{S}_i - \frac{1}{2}J\sum_{\langle i,j\rangle} \boldsymbol{S}_i \cdot \boldsymbol{S}_j. \tag{3.18}$$

Here, the set of occupied motional modes represents the sites of the Heisenberg lattice. The system here has more inhomogeneity than Eq. 3.18, since the "external field" $\boldsymbol{B}$ is site-dependent. In addition, the interaction term J becomes site-dependent and we allow longer-range interactions than between nearest neighbors. However, we can still define a metric of nearness between the motional modes, since the interaction term $U_{\boldsymbol{n},\boldsymbol{m}}$ decays quickly according to $\prod_j |n_j - m_j|^{-1}$ [51]. Hamiltonians of the general form of Eq. 3.17 have been extensively studied in condensed matter physics to calculate the magnetization in solid state materials under the influence of external and internal fields. For instance, a classic paper by Holstein and Primakoff [69] discusses the eigenvalues and solutions of an even more general Hamiltonian than Eq. 3.17 for a large number of sites. The Hamiltonian Eq. 3.17 is also very similar for the one used in describing spectroscopy of nitrogen-vacancy color centers in diamond that couple to a background spin bath [70]. For our purposes, we can simulate the dynamics of Eq. 3.17 directly for small N, since typical atom numbers per site are small. For larger samples, a solid-state type approximation method might become more appropriate.

We can gain a simple understanding of the pseudo-spin dynamics produced by H by letting the Rabi frequencies $\Omega_{\boldsymbol{n}} \mapsto \Omega$ be homogeneous and neglecting the interactions $U_{\boldsymbol{n},\boldsymbol{m}} \mapsto 0$. If we introduce a total spin operator

$$\boldsymbol{S} \equiv \sum_{\boldsymbol{n}} \boldsymbol{S}_{\boldsymbol{n}}, \tag{3.19}$$

we find

$$H/\hbar = -\delta S^3 - \Omega S^1 \equiv -\boldsymbol{V} \cdot \boldsymbol{S}, \tag{3.20}$$

with $\boldsymbol{V} \equiv (\Omega, 0, \delta)^{\top}$. In the Heisenberg picture, the expectation values of the total spin follow

$$\langle \dot{\boldsymbol{S}} \rangle = -i\langle [\boldsymbol{S}, H/\hbar] \rangle. \tag{3.21}$$

Using the commutation relations for the components of angular momentum operators $[S^k, S^\ell] = i\hbar \sum_m \epsilon_{k\ell m} S^m$ [71], we find the equations of motion for an N-particle Bloch vector

$$\langle \dot{\boldsymbol{S}} \rangle = -\boldsymbol{V} \times \langle \boldsymbol{S} \rangle \tag{3.22}$$

which describes a simple rotation of $\langle \boldsymbol{S} \rangle$ around axis $\boldsymbol{V}$. The rotation conserves the length of the Bloch vector $|\langle \boldsymbol{S} \rangle| = N/2$.

The same result is obtained when considering the Hamiltonian in Eq. 3.20 as a sum of N identical single particle Hamiltonians. Each single-particle pseudospin evolves in the same way within its own Bloch sphere and their sum evolves in the same way. If we allow a Rabi frequency inhomogeneity again, each particle will evolve within its on Bloch sphere according to its Rabi frequency $\Omega_{\boldsymbol{n}}$. Each individual evolution is norm-conserving, but the ensemble of Bloch vectors dephases and rephases according to the distribution of Rabi frequencies. Summing the individual Bloch vectors produces a total Bloch vector that exhibits periodic changes in length while it rotates on the total Bloch sphere. These inhomogeneous dynamics are exactly what we derived in Sec. 2.9 and can be qualitatively characterized by the mean $\bar{\Omega} \equiv N^{-1} \sum_{j=1}^N \Omega_{\boldsymbol{n}^j}$ and standard deviation $\Delta\Omega \equiv \left[(N-1)^{-1} \sum_{j=1}^N (\Omega_{\boldsymbol{n}^j} - \bar{\Omega})^2 \right]^{1/2}$ of the Rabi frequency distribution. Note that the Rabi frequency distribution moments here are not defined with respect to a thermal distribution, but with respect to the set of initially populated motional modes under consideration.

If we limit ourselves again to homogeneous Rabi frequencies and homogeneous interactions, another interesting limit of the dynamics can be explored. We let

$$H/\hbar = -\boldsymbol{V} \cdot \boldsymbol{S} - U\boldsymbol{S} \cdot \boldsymbol{S} = -(\boldsymbol{V} - U\boldsymbol{S}) \cdot \boldsymbol{S}. \tag{3.23}$$

The interaction thus acts like an additional external field that depends on the current spin state. If we replace the self-interaction term with the solution for $U = 0$, we obtain

$$H/\hbar \simeq -\boldsymbol{V} \cdot \boldsymbol{S} - U(\boldsymbol{V} \times \langle \boldsymbol{S} \rangle) \cdot \boldsymbol{S}. \tag{3.24}$$

In the Heisenberg picture, this iterative approximation leads to

$$\langle \dot{\boldsymbol{S}} \rangle = -\boldsymbol{V} \times \langle \boldsymbol{S} \rangle - U(\boldsymbol{V} \times \langle \boldsymbol{S} \rangle) \times \langle \boldsymbol{S} \rangle, \tag{3.25}$$

which is known as the Landau-Lifshitz equation for the magnetization of a solid under the influence of an effective magnetic field $\boldsymbol{V}$ in the presence of damping (proportional to U). This equation was first introduced phenomenologically and includes the simplest nonlinear term that leads to damping of the magnetization [72]. The Landau-Lifshitz equation is widely used to model the ferromagnetic response of solids [73, 74]. We conclude that our problem at hand is very similar to what happens in an isolated magnetized domain of a solid when a magnetic field is applied.

Including inhomogeneous interactions makes algebraic calculations significantly more difficult, but for low N, the spin Hamiltonian is still relatively easy to simulate using numerical matrix calculations. Matrix representations of the spin operators are easily obtained by tensor products[1]

$$
\begin{aligned}
S^j_{\boldsymbol{n}^k} &= \underbrace{I_2 \otimes \cdots \otimes I_2}_{k-1} \otimes \frac{1}{2}\, \sigma^j \otimes \underbrace{I_2 \otimes \cdots \otimes I_2}_{N-k} \\
S^j &= \sum_{k=1}^{N} S^j_{\boldsymbol{n}^k}
\end{aligned}
\tag{3.26}
$$

where I_2 is the 2-dimensional identity matrix and σ^j is the j-th Pauli matrix. Using these 2^N-dimensional matrices to represent H makes it immediately obvious that simulating the full evolution of more than a few particles with inhomogeneous Rabi frequencies and interactions is hard. Note that the Hamiltonian should only be used with a pure pseudo-spin polarized initial state

$$
|\psi\rangle_0 = \otimes_{j=1}^{N}|g\rangle \ \text{ or } \ \otimes_{j=1}^{N}|e\rangle,
\tag{3.27}
$$

which guarantees the assumptions about motional mode populations that led to the spin Hamiltonian. In the spin-matrix representation, the polarized states correspond to the first

---

[1]Kronecker products of matrices can be calculated with `kron` in Matlab and `KroneckerProduct` in Mathematica, for example. More optimized object-oriented representations of tensor products can be found in specialized toolkits such as the Matlab Quantum Optics toolbox (`http://qwiki.stanford.edu/index.php/Quantum_Optics_Toolbox`) or C++QED (`http://www.uibk.ac.at/th-physik/qo/research/cppqed.html`)

and last entry in the state vector. The propagator is a simple matrix exponential

$$U(t - t_0) = \exp[-iH/\hbar(t - t_0)] \tag{3.28}$$

and the excited state fraction is given by

$$
\begin{aligned}
P_e &\equiv N^{-1}\langle N_e \rangle = N^{-1}\langle S^3 + \frac{N}{2} I_{2^N} \rangle \\
&= N^{-1}[U(t - t0)\psi_0]^\dagger [S^3 + \frac{N}{2} I_{2^N}][U(t - t0)\psi_0]
\end{aligned} \tag{3.29}
$$

Thermal averaging of P_e is done by averaging results for different sets of initial motional modes $\{n^j\}$ according to their Boltzmann factor $\prod_{j=1}^{N} e^{-E_{n^j}/k_B T}$. To model a realistic sample, we also have to average the results of calculations over a distribution of N over the occupied lattice sites.

3.3. Spin model fit to experimental data

The experimental data in Fig. 3.2 was fit with the N-particle spin model derived in the last Section by A. Rey and coworkers [47]. The result of thermal averaging for $T = 1 \mu K$ ($3 \mu K$) is shown in Fig. 3.3 as the pink (blue) shaded region. The uncertainty in the fit is mostly due to allowing a 10% variation in the pulse area. Each data point consists of at least one full day of averaging against the NIST Ca clock. A conservative estimate of the clock laser intensity variation on long time scales results in an uncertainty of about 10% on the π-pulse condition. For the fits here, the singlet scattering length is set to $a_{eg}^- = 200 \ a_0$, which is consistent with the unitarity limit given by the thermal wavelength

$$
\begin{aligned}
\frac{\lambda_T}{2\pi} &\equiv \hbar/\sqrt{2\pi m_{Sr} k_B (T + T_{zp})} \\
&\simeq 221 \ a_0 \ @ \ T = 3 \ \mu K
\end{aligned} \tag{3.30}
$$

where $T_{zp} \simeq 3.5 \ \mu K$ corresponds to the ground state energy of the single-site potential.

The inset of Fig. 3.3 shows the $1 \ \mu K$ Rabi flopping data from Fig. 2.8 and the dotted purple line corresponds to the fit from the same figure using $\Delta\Omega/\bar{\Omega} = 0.05$. The solid blue curve is a fit using the thermally averaged N-particle model. To match the data when including
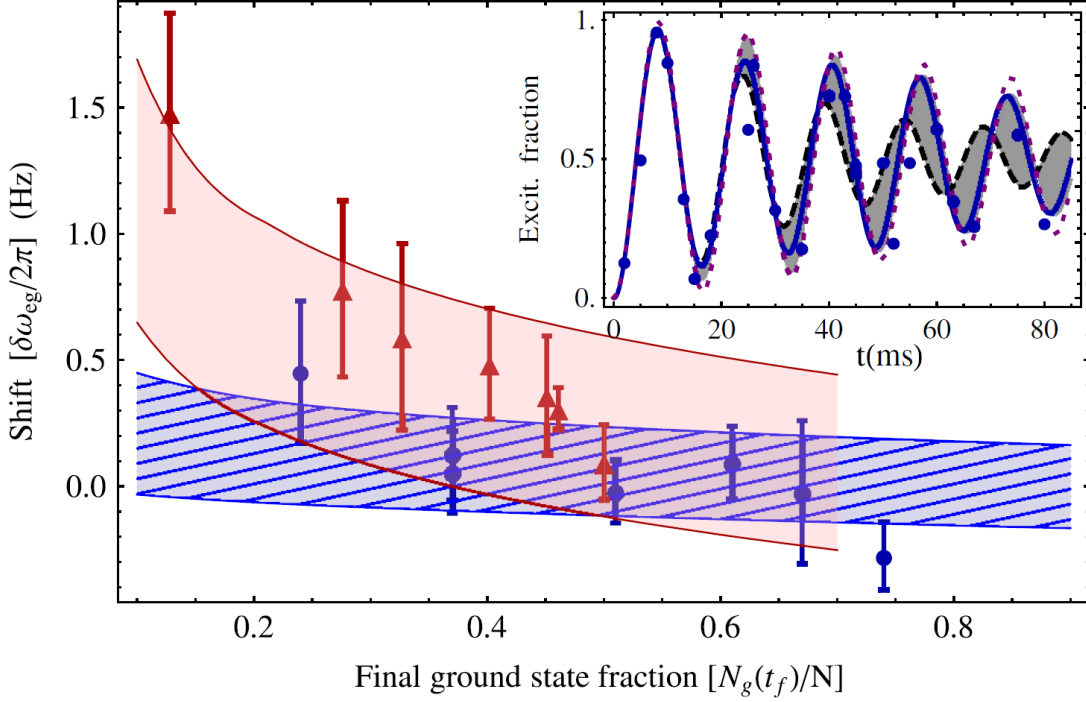
Figure 3.3.: (Figure from Ref. [47]). The shaded regions indicate fits of the experimental data in Fig. 3.2 with the thermally averaged N-particle spin model. The singlet scattering length is set to the unitarity limit $a_{eg}^- = 200\ a_0$ and the uncertainty region results from allowing the π-pulse condition to vary by 10%. The inset also shows a fit of the Rabi flopping data in Fig. 2.8 with the full N-particle spin model. The dashed black curve is the result for setting $a_{eg}^- = 0$ and the solid blue curve is the fit for $a_{eg}^- = 200\ a_0$ when using $\Delta\Omega/\bar{\Omega} = 0.15$. The dotted purple line results when extracting $\Delta\Omega/\bar{\Omega} = 0.05$ from the theory in Sec. 2.9 and setting $a_{eg}^- = 0$.

interactions, the Rabi frequency inhomogeneity has to be increased to $\Delta\Omega/\bar{\Omega} = 0.15$. For comparison, the black dashed curve shows the N-particle model with $\Delta\Omega/\bar{\Omega} = 0.15$ when the interactions are neglected. Note that all three fits agree almost perfectly during the first Rabi cycle, because $\Delta\Omega/\bar{\Omega}$ is still small enough to take several cycles to develop a significant effect.

We conclude that it is necessary to include interactions to fit carrier Rabi flopping in the presence of Rabi frequency inhomogeneity. Note that the agreement between the data and the theoretical model is fair. However, the large amount of averaging necessary to describe the spectroscopy makes it hard to make general statements. In particular, predicting the behavior of the thermally averaged N-particle model from simulations of the 2-particle Hamiltonian are not reliable. Predicting a zero crossing (or no zero crossing) from the two-particle model as a function of locking point is too simplistic.

Even though the optical lattice spectroscopy has been made as clean as possible, the large number of degrees of freedom still requires a full model. Performing optical lattice spectroscopy for optical frequency standards still requires a precise measurement of the density shift. This important systematic *cannot* be neglected, but we will show that the density shift *can* be suppressed by engineering the trapping potential.

3.4. Two particles

Although the two-particle model does not easily generalize to N particles, it is instructive to consider the dynamics for $N = 2$ since several parameter regimes become obvious. The matrix representation of H for $N = 2$ is

$$H/\hbar = \frac{1}{2} \begin{pmatrix} -2\delta & -\Omega_2 & -\Omega_1 & 0 \\ -\Omega_2 & U_{12} & -U_{12} & -\Omega_1 \\ -\Omega_1 & -U_{12} & U_{12} & -\Omega_2 \\ 0 & -\Omega_1 & -\Omega_2 & 2\delta \end{pmatrix} \tag{3.31}$$

where the subscripts j indicate motional modes $\boldsymbol{n}^j$ and we have used $U_{\boldsymbol{n},\boldsymbol{m}} = U_{\boldsymbol{m},\boldsymbol{n}}$. The matrix is written in the tensor product basis $|g_1 g_2\rangle, |g_1 e_2\rangle, |e_1 g_2\rangle, |e_2 e_2\rangle$. We see that the interactions only manifest in the $e - g$ subspace. The tensor basis is the most convenient for numerical calculations, but for our purposes, H becomes much more informative in a singlet and triplet basis of symmetrized and antisymmetrized pseudo-spin superpositions. The basis transformation is defined by

$$P = \begin{pmatrix} 1 & 0 & 0 & 0 \\ 0 & 0 & 0 & 1 \\ 0 & 1/\sqrt{2} & 1/\sqrt{2} & 0 \\ 0 & 1/\sqrt{2} & -1/\sqrt{2} & 0 \end{pmatrix}, \tag{3.32}$$

which rotates the $e - g$ subspace into a symmetric and antisymmetric superposition $|\pm\rangle \equiv (|eg\rangle \pm |ge\rangle)/\sqrt{2}$ and rearranges the Hamiltonian such that the triplet states $|ee\rangle, |gg\rangle, |+\rangle$ (symmetric under particle exchange) form the top left block.

$$\mathcal{H}_2 \equiv \hbar^{-1} P H P^{-1} = \begin{pmatrix} -\delta & 0 & -\bar{\Omega}/\sqrt{2} & \Delta\Omega/\sqrt{2} \\ 0 & \delta & -\bar{\Omega}/\sqrt{2} & -\Delta\Omega/\sqrt{2} \\ -\bar{\Omega}/\sqrt{2} & -\bar{\Omega}/\sqrt{2} & 0 & 0 \\ \Delta\Omega/\sqrt{2} & -\Delta\Omega/\sqrt{2} & 0 & U_{12} \end{pmatrix}, \tag{3.33}$$

where we have defined $\bar{\Omega} \equiv (\Omega_1 + \Omega_2)/2$ and $\Delta\Omega \equiv (\Omega_1 - \Omega_2)/2$. The antisymmetric (under particle exchange) singlet state $|-\rangle$ is the only state that interacts, as shown by U_{12} in the bottom right corner of $\mathcal{H}_2$. This Hamiltonian was first considered in the context of optical clock density shifts in Ref. [48]. As we have seen, it is not general enough to describe thermal averaging over motional modes and sites with $N > 2$. As we will see, it is nevertheless an important conceptual tool to understand the system dynamics.

From Eq. 3.33, we can immediately see that if the system is initially prepared in a pseudo-spin polarized state $|ee\rangle$ or $|gg\rangle$, the induced dynamics will be constrained to the non-interacting triplet manifold unless there is a Rabi frequency inhomogeneity $\Delta\Omega$ that couples to the interacting singlet. Unless there is non-zero Rabi frequency inhomogeneity, the interaction cannot influence the lineshape.

To simulate the influence of nonzero inhomogeneity and interactions for nonzero inhomogeneity and interactions, it is useful to rescale $\mathcal{H}_2$ by $\bar{\Omega}$. Figure 3.4(a) shows the total spin dynamics for $\Delta\Omega/\bar{\Omega} = 0.4$ and $u = U_{12}/\bar{\Omega} = 0.4$ when $\delta/\bar{\Omega}$ is scanned across the resonance. The system is prepared in the $|ee\rangle$ state at the south pole of the Bloch sphere and the evolution of the Bloch vector from $t = 0$ to $t = \pi/\bar{\Omega}$ is shown as a colored trace. The trace colors are interpolated from red $\delta/\bar{\Omega} = -2$ (red detuning) to blue $\delta/\bar{\Omega} = 2$ (blue detuning). The light green trace indicates $\delta = 0$ and we see that even for two particles, the individual Bloch vector dephasing can be significant. Panel (b) shows the resulting spectroscopic line shape for $t = \pi/\bar{\Omega}$: the maximal excited state fraction is attenuated and the spectrum becomes skewed. Switching the sign of u mirrors the lineshape around $\delta = 0$.
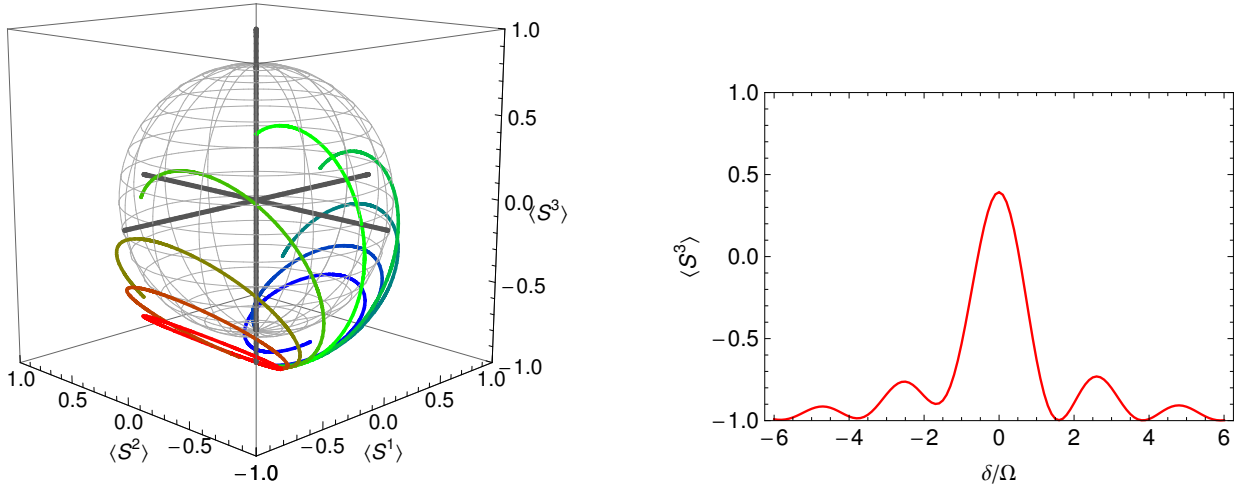
(a) Total spin expectation value $\langle \boldsymbol{S} \rangle$ on Bloch sphere for detuning $\delta/\bar{\Omega} \in (-2, 2)$. Red (blue) traces indicate the evolution of $\langle \boldsymbol{S} \rangle$ for $\bar{\Omega}t \leq \pi$ and negative (positive) values of δ.

(b) Spectrum of $\langle S^3 \rangle$ versus detuning for the same conditions as in panel (a) at $\bar{\Omega}t = \pi$.

Figure 3.4.: Two-particle spin model for $\Delta\Omega/\bar{\Omega} = u = 0.4$, where $\langle S^3 \rangle = -1(+1)$ indicates that both particles are in the ground (excited) state.

The lineshape skewing is very dependent on the interplay of $\Delta\Omega/\bar{\Omega}$, u, and the pulse time. The position of the locking points on the central fringe adds to the complexity. This complex interplay makes it difficult to formulate general descriptions that do not require numerical

simulation. The spectroscopic lineshape parameter-dependence becomes even more complex when considering a Ramsey scheme. Ramsey pulses that are short enough such that interactions can be neglected require a separate description not covered by either the full spin-model or the simpler two-particle model in this Section. In the presence of interactions, a Ramsey sequence can easily be generated by chaining the spin-model propagators (Eq. 3.28). However, even long dark times do not simplify the resulting lineshape parameter dependence significantly.

A full description of the spectroscopic lineshape in the presence of interactions remains a difficult problem as long as all the parameters in H are on similar orders of magnitude. We will show that the description becomes much simpler when the interaction parameter u dominates over all other energy scales in the Hamiltonian.

3.5. Interaction-dominated regime

Another instructive way of looking at the two Hamiltonian is a dressed basis at the mean Rabi frequency $\bar{\Omega}$. The dressed eigenstates can be obtained by diagonalizing $\mathcal{H}_2$ when letting $\Delta\Omega \mapsto 0$. As discussed in the last Section, the triplet manifold becomes decoupled from the singlet state and the triplets are split by twice the effective Rabi frequency $\sqrt{\bar{\Omega}^2 + \delta^2}$. If we label the dressed states by their original triplet labels, we find the situation schematically shown in Fig. 3.5(a). When admitting a small inhomogeneity again, the spin-polarized dressed states $|ee\rangle$ and $|gg\rangle$ can couple to the singlet via $\Delta\Omega$. The singlet $|-\rangle$ is split off from $|+\rangle$ by the interaction energy $U = U_{12}$. Since all energy scales are on similar orders of magnitude, the $\Delta\Omega$-induced dynamics become a detuning-dependent interference pattern between all allowed transitions in the energy diagram. The interference mainly occurs within the central fringe of the spectroscopic lineshape. This complex interplay is exactly why the lineshape and thus the density shift is so parameter-dependent.

The situation simplifies drastically if we allow the interaction energy U to become large with respect to $\bar{\Omega}$ and $\Delta\Omega$. In the small detuning regime $\delta \ll U$, the singlet becomes
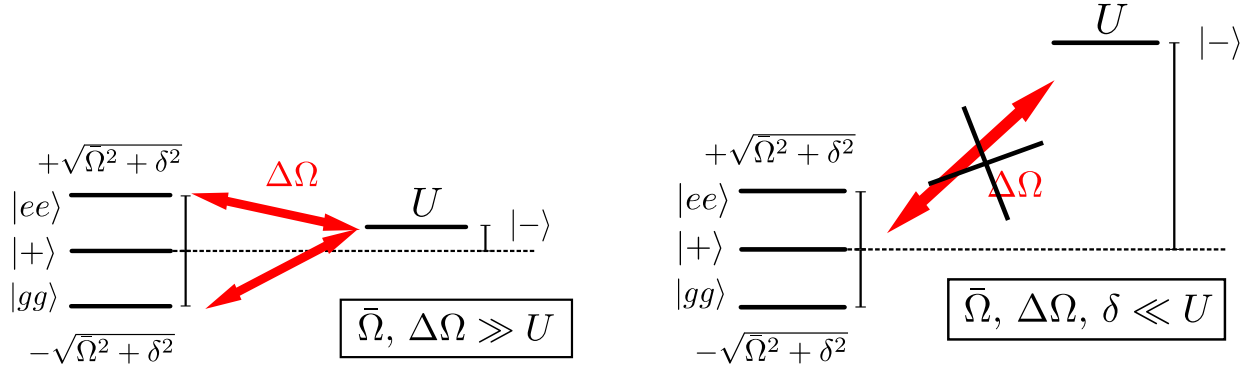
(a) Dressed states and coupling when the interaction $U \ll \bar{\Omega}, \Delta\Omega$ is a perturbation. Transfer between the $\bar{\Omega}$-dressed triplets and the singlet state in the perturbative regime resulting in a modified lineshape.

(b) When U is the largest energy scale, the dressed triplets cannot couple to the singlet and U does not influence the lineshape.
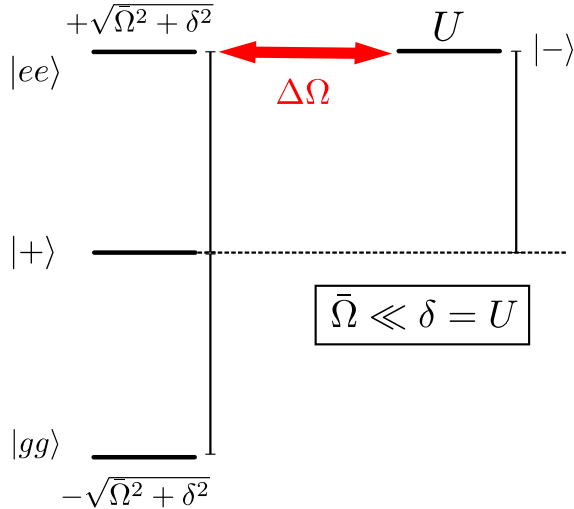
(c) Same as panel (b), but if we detune far enough, resonant transfer with $\Delta\Omega$ between one of the triplets and the singlet results in a spectroscopic feature when $\delta = U$.
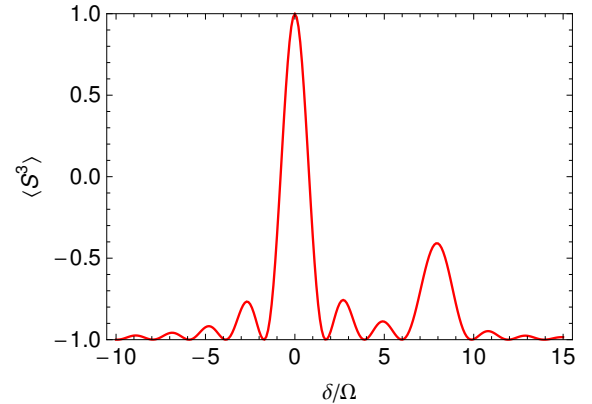
(d) Example spectrum for $N = 2$, $u = 8$, $\Delta\Omega/\bar{\Omega} = 0.4$. The interaction separates into its on spectral feature and does not perturb the carrier spectrum.

Figure 3.5.: Dressed triplet states for $N = 2$ with mean Rabi frequency $\bar{\Omega}$ and singlet state that is separated by the interaction energy U. Panel (a) shows the regime where U is a perturbation on the Rabi dynamics. Panel (b) indicates that a large interaction will suppress transfer to the singlet, and thus suppress effects of U on the lineshape. Panel (c) shows that if $U \gg \bar{\Omega}$, a detuning of $\delta = U$ will produce resonant transfer to the singlet and result in a single well-separated interaction sideband. An example spectrum for case (c) is shown in panel (d).

separated from the triplets by a large energy gap, as shown in Fig. 3.5(b). Transitions between triplets and the singlet are in principle still allowed, but their amplitude becomes strongly suppressed by the energy separation as long as $|U| \gg \Delta\Omega$. In this regime, the coupling between triplets and singlet can be treated perturbatively for small detuning. In other words: the influence of U on the central fringe is suppressed.

However, if we increase the detuning until the triplet splitting matches the singlet energy, resonant transfer between one of the stretched triplets and the singlet becomes allowed. This situation is shown in Fig. 3.5(c). The Rabi frequency inhomogeneity allows transitions to the singlet, even if $\Delta\Omega \ll \bar{\Omega}, U$. The effect on the spectrum is shown in panel (d), where we let $U/\bar{\Omega} = 8$ and $\Delta\Omega/\bar{\Omega} = 0.4$. The central fringe is symmetric and not influenced. At $\delta = U$, a separated interaction sideband appears, corresponding to resonant Rabi flopping between a stretched triplet and the singlet. In this way, larger interactions can suppress the influence of interactions on the relevant parts of the spectroscopic lineshape.

The interaction energy U can be strongly enhanced in a two-dimensional optical lattice where the atoms are confined to the lowest motional state in two axes. The overlap integrals contributing to U become less suppressed and U can become the dominating energy scale in the Rabi flopping dynamics. A density shift suppression by more than an order of magnitude has been shown recently [51] in a two-dimensional optical lattice, and separated interaction sidebands have been observed [67].

These new developments show that the presence of atomic interactions does not necessarily put a hard limit on the number of atoms that can be used to enhance the spectroscopic signal-to-noise ratio. The combination of precision measurement and ultracold many-body systems will allow the future development more precise and also more accurate optical lattice frequency standards.

On the other hand, many new proposals for quantum simulation with alkaline earth atoms will have to rely on manipulation of the internal and external atomic degrees of freedom with high fidelity. The measurement, control, and understanding of the density shift demonstrates

that combining insights from different fields yields a better understanding of all of them. In this spirit, we will apply the high precision of Sr optical lattice clocks to study fundamental physics by using the clock data to put limits on present day variation of fundamental constants in the next Chapter.

Variation of Fundamental Constants

M ANY landmark physical experiments have succeeded in finding new physical phenomena, particles, or forces by testing accepted theories such as Newton's theory of gravitation. The surprising results from such experiments have led to improved theories of physics, such as general relativity. Within the last century, general relativity has become one of the most well-tested physical theories. One of the main driving forces behind high-accuracy tests of general relativity are theories beyond the standard model, because their scope can be experimentally constrained by null results from high-accuracy tests.

Fundamental constants determine the relative scale of different physical forces. For instance, the fine-structure constant α is the coupling constant between electromagnetic fields and matter, and also sets the energy scale of electronic transitions in atoms. Since the equations of physics are parametrized by fundamental constants such as α, a natural question to ask is whether they have to have particular numerical values such as $\alpha = e^2/(4\pi\epsilon_0 \hbar c) \simeq 1/137$, with electron charge e, vacuum permittivity ϵ_0, Planck's constant $h = 2\pi\hbar$, and speed of light c.

Such questions arise in the course of trying to describe all physical forces in a unified way or in modeling the physics of the early universe. The experimental search for variations

in fundamental constants has gained much momentum from an analysis of astronomical data from quasar spectra which indicated a non-zero fractional variation $\delta\alpha/\alpha \sim 10^{-6}$ on cosmological timescales [75], although later analyses showed a much smaller variation [76]. Limits on variation of α on geological timescales have also been extracted from analyses of the natural fission reactor at Oklo [77]. Present-day limits on variations of fundamental constants can be obtained from long-term absolute frequency records of atomic clocks, since atomic transition frequencies are sensitive to fundamental constants such as α. A full review of this subject is beyond the scope of this introduction, but many reviews [78–80] and extensive lecture notes are available [81].

In this Chapter, we will analyze the international frequency record obtained from absolute frequency measurements of ^{87}Sr optical lattice clocks to put limits on present-day drifts in α and the electron-proton mass ratio m_e/m_p [30, 82–85]. We also check the same data for a violation of local position invariance by testing for a coupling of fundamental constants to the solar gravitational potential [30, 86–89].

4.1. Sensitivity constants

The energetic structure of an atom is determined by the interaction between many fundamental particles: quarks form the nucleons and nucleons bond via nuclear forces. The electromagnetic charge Ze of the resulting atomic nucleus determines how many electrons can be bound into electronic shells orbiting the nucleus. Almost all chemistry can then be understood as resulting from the energetic structure of this cloud of electrons. Most of atomic physics and chemistry is based on the fact that the outermost (valence) electrons determine an atom's behavior almost completely. However, their quantized energy structure is of course dependent on the full underlying many-body system.

Modern atomic structure calculations can model the electron cloud ab-initio. The resulting valence electron energy levels relate the wavelengths of spectroscopic transitions in atoms to the underlying physics and especially the fundamental constants. By continual checks

against experimental data across many atomic species, these calculations have become very accurate over the last decades. Because of their accuracy, one can extract the sensitivity of the resulting electronic structure to the value of the underlying fundamental constants.

Assume that we are interested in a dipole-allowed optical transition. In atomic units, the transition frequency can be expressed via the atomic unit of energy, the Hartree energy $E_h \simeq 27.2$ eV which is roughly twice the energy required to dissociate an electron from a proton. The resulting expression for the atomic unit of frequency

$$\omega_{\text{opt}} \propto E_h/\hbar = \alpha^2 \frac{m_e c^2}{\hbar}, \tag{4.1}$$

exhibits the energy scale of electronic transitions as the product of the Compton frequency of the electron $m_e c^2/\hbar$ and α^2.

The notation here is slightly modified from the review article by S. Lea [80] to conform better to the notation used in our paper [8]. There is no standard notation for the sensitivity constants and functions mentioned here. The confusing use of the SI value of the Rydberg cR_∞ to represent variations in frequency units is avoided, especially when talking about frequency variations in the Cs standard. Since it is the current definition of frequency, there can be no frequency variation of the Cs standard. Clock comparisons are either performed against the Cs standard to obtain absolute frequencies or they are not. If they are not, then the result of a clock comparison cannot be represented in SI frequency units. Instead, the result of a clock comparison must be converted to a dimensionless fractional frequency ratio.

Any absolute frequency measurement is a comparison of a frequency ω to the Cs frequency ω_{Cs} and the measurement also returns the *dimensionless* value $\omega/\omega_{\text{Cs}}$. Only with the *definition* 1 s $\equiv 9,192,631,770 \times (2\pi/\omega_{\text{Cs}})$ can such a result be converted to a frequency in SI units, but we emphasize that in reality all such experiments measure dimensionless frequency ratios.

A fractional variation in measured dimensionless fractional frequencies can be expressed as the logarithmic derivative

$$\frac{\delta(\omega/\omega_{\text{Cs}})}{\omega/\omega_{\text{Cs}}} = \partial_t \ln \omega/\omega_{\text{Cs}} = \partial_t \ln \omega - \partial_t \ln \omega_{\text{Cs}}. \tag{4.2}$$

We now write the proportionality factor in Eq. 4.1 as a dimensionless function $F(\{\eta_k\})$, where $\{\eta_k\}$ denominates the set of fundamental constants η_k determining the atomic structure:

$$\omega = F(\{\eta_k\}) \times (\text{units})$$
$$\omega_{\text{Cs}} = F_{\text{Cs}}(\{\eta_k\}) \times (\text{units}).$$
(4.3)

A dimensionless variation in these frequencies is then seen to separate into a variation of F and a variation of the units used in the atomic structure calculation

$$\partial_t \ln \omega = \partial_t \ln F(\{\eta_k\}) + \partial_t \ln (\text{units})$$
$$\partial_t \ln \omega_{\text{Cs}} = \partial_t \ln F_{\text{Cs}}(\{\eta_k\}) + \partial_t \ln (\text{units}).$$
(4.4)

from which we see that the units in the atomic structure calculation do not matter when comparing against the experimental data:

$$\frac{\delta(\omega/\omega_{\text{Cs}})}{\omega/\omega_{\text{Cs}}} = \partial_t \ln \omega - \partial_t \ln \omega_{\text{Cs}} = \partial_t \ln F(\{\eta_k\}) - \partial_t \ln F_{\text{Cs}}(\{\eta_k\}).$$
(4.5)

Any measured fractional frequency variation can thus be directly compared to the sensitivity calculations from the atomic structure calculations (usually done in atomic units).

The numerical variation in atomic structure calculations is fit with a simple model

$$F(\{\eta_k\}) = \text{const} \times \prod_k \eta_k^{c_k},$$
(4.6)

and numerical constants c_k are extracted for the transitions of interest. In this parametrization,

$$\partial_t \ln F(\{\eta_k\}) = \partial_t \sum_k \ln \eta_k^{c_k} = \sum_k c_k \partial_t \ln \eta_k \equiv \sum_k c_k \frac{\delta \eta_k}{\eta_k}.$$
(4.7)

The fractional frequency variation of a species j compared against the Cs standard thus becomes a simple linear combination of the fractional variation of fundamental constants

$$\frac{\delta(\omega_j/\omega_{\text{Cs}})}{\omega_j/\omega_{\text{Cs}}} = \sum_k (c_k^j - c_k^{\text{Cs}}) \frac{\delta \eta_k}{\eta_k}.$$
(4.8)

In this way, we can extract information about $\delta \eta_k/\eta_k$ from absolute frequency measurements since the sensitivity constants c_k are known.

Also note that any other atomic clock comparison producing dimensionless frequency ratios can be checked for variation in fundamental constants via

$$\frac{\delta(\omega_j/\omega_i)}{\omega_j/\omega_i} = \sum_k (c_k^j - c_k^i)\frac{\delta\eta_k}{\eta_k}. \tag{4.9}$$

4.1.1. Sensitivity of the ^{133}Cs clock transition

Which fundamental constants are important for the ^{133}Cs standard based on a hyperfine transition? Hyperfine transition energies are given by the nuclear magnetic moment

$$\mu_{\mathrm{N}} = g_{\mathrm{N}}\mu_p = g_{\mathrm{N}}\frac{e\hbar}{2m_p}, \tag{4.10}$$

with nuclear g-factor g_{N}, nuclear magneton μ_p, and with proton rest mass m_p. A typical atomic energy scale for a hyperfine transition is thus

$$\omega_{\mathrm{hfs}} \propto \alpha^2 \frac{\mu_N}{\mu_B}\frac{m_e c^2}{h} = g_N \frac{m_e}{m_p} \; \mathrm{a.u.}, \tag{4.11}$$

where $\mu_B = e\hbar/(2m_e)$ is the Bohr magneton, and a.u. indicates the atomic unit of frequency $E_h/\hbar$.

The Schmidt model relates g_N to the proton g-factor across many species [78, 80, 90, 91]. If we assume that these relations hold even when the fundamental constants are varying, and that the proton g-factor itself is constant, we can isolate the electron-proton mass ratio m_e/m_p as one of the contributors to the sensitivity function F.

The main contributor to F is the fine structure constant α. For transitions between ground state hyperfine levels, the contribution can be written as $\alpha^2 F_{\mathrm{rel}}(Z\alpha)$, where F_{rel} summarizes relativistic corrections that scale with the nuclear charge Z [80, 87, 91]. Other contributions are small, and we can write

$$\omega_{\mathrm{hfs}} = \mathrm{const} \times \alpha^2 F_{\mathrm{rel}}(Z\alpha)\frac{m_e}{m_p} \; \mathrm{a.u.}, \tag{4.12}$$

such that

$$\partial_t \ln \omega_{\mathrm{hfs}} = \partial_t \ln F_{\mathrm{rel}}(Z\alpha) + \partial_t \ln \frac{m_e}{m_p} + \partial_t \ln \mathrm{a.u.}$$

$$= \left(2 + \frac{\partial \ln F_{\mathrm{rel}}(Z\alpha)}{\partial \ln \alpha} \right) \frac{\delta\alpha}{\alpha} + \frac{\delta(m_e/m_p)}{m_e/m_p} + \partial_t \ln \mathrm{a.u.} \tag{4.13}$$

$$\equiv c_\alpha \frac{\delta\alpha}{\alpha} + c_{m_e/m_p} \frac{\delta(m_e/m_p)}{m_e/m_p} + \partial_t \ln \mathrm{a.u.}$$

For the clock transition in ^{133}Cs, we find [92]

$$c_\alpha^{\mathrm{Cs}} \simeq 2 + 0.83$$

$$c_{m_e/m_p}^{\mathrm{Cs}} = 1, \tag{4.14}$$

where the integral numbers are exact from the analytical powers of α and m_e/m_p given above.

4.1.2. Sensitivity of optical clock transitions

For optical transitions, only the relativistic corrections related to $Z\alpha$ contribute significantly, and we find

$$\omega_{\mathrm{opt}} = \mathrm{const} \times F_{\mathrm{rel}}(Z\alpha) \ \mathrm{a.u.}, \tag{4.15}$$

such that

$$\partial_t \ln \omega_{\mathrm{opt}} = \frac{\partial \ln F_{\mathrm{rel}}(Z\alpha)}{\partial \ln \alpha} \frac{\delta\alpha}{\alpha} + \partial_t \ln \mathrm{a.u.} \equiv c_\alpha \frac{\delta\alpha}{\alpha} + \partial_t \ln \mathrm{a.u.} \tag{4.16}$$

For the ^{87}Sr ^{1}S$_0$-^{3}P$_0$ optical clock transition we find [93]

$$c_\alpha^{\mathrm{Sr}} = 0.06, \tag{4.17}$$

which is comparatively small as shown in Table 4.1.

4.1.3. Sensitivity of ^{87}Sr absolute frequency measurements

In summary, measurements of the absolute frequency of the ^{87}Sr clock transition are sensitive to variation in two fundamental constants: the fine structure constant α and the electron-proton mass ratio m_e/m_p. To shorten the notation in the following, we will write $\mu \equiv m_e/m_p$,

Species	Transition	Wavelength (nm)	c_α
^{87}Sr	^{1}S$_0$-^{3}P$_0$	698	0.062
^{171}Yb	^{1}S$_0$-^{3}P$_0$	578	0.314
^{199}Hg, ^{201}Hg	^{1}S$_0$-^{3}P$_0$	266	0.813
^{27}Al$^+$	^{1}S$_0$-^{3}P$_0$	267	0.008
^{171}Yb$^+$	^{2}S$_{1/2}$-^{2}D$_{3/2}$	436	0.881
^{199}Hg$^+$	^{2}S$_{1/2}$-^{2}D$_{5/2}$	282	-3.191

Table 4.1.: Sensitivity of high-Q optical transitions to variation in α, calculated from Ref. [93].

not to be confused with magnetic moments. We find

$$
\begin{aligned}
\frac{\delta(\omega_{\mathrm{Sr}}/\omega_{\mathrm{Cs}})}{\omega_{\mathrm{Sr}}/\omega_{\mathrm{Cs}}} &= (c_\alpha^{\mathrm{Sr}} - c_\alpha^{\mathrm{Cs}})\frac{\delta\alpha}{\alpha} + (c_\mu^{\mathrm{Sr}} - c_\mu^{\mathrm{Cs}})\frac{\delta\mu}{\mu} \\
&= (0.06 - 2 - 0.83)\frac{\delta\alpha}{\alpha} + (0-1)\frac{\delta\mu}{\mu} \\
&= -2.77\frac{\delta\alpha}{\alpha} - \frac{\delta\mu}{\mu}.
\end{aligned}
\tag{4.18}
$$

Because c_α^{Sr} is small, the absolute frequency measurements of ^{87}Sr are a clean measurement of the ^{133}Cs sensitivity to both α and μ. The ^{87}Sr standard can thus also act as an anchor in comparisons against more sensitive species.

4.2. Global absolute frequency record

In the previous Section, we have shown that absolute frequency measurements can be sensitive to possible variations in fundamental constants. In particular, we are interested in analyzing the absolute frequency record of the ^{87}Sr optical lattice clock for such variations. Figure 4.1 shows all published absolute frequency data from our lab (red), the Paris group (green), and the Tokyo group (blue). The data is referenced to $\nu_0 = 429\,228\,004\,229\,800$ Hz. Vertical 1-σ error bars indicate the total uncertainty in each optical frequency measurement and horizontal error bars show the time period over which the measurement took place.

The last four measurements agree within 1.7 Hz [7, 42, 45, 94], and the agreement between the JILA and Paris data [7, 45, 94] is on the 1×10^{-15} level, which approaches the Cs limit and makes the ^{87}Sr ^{1}S$_0$-^{3}P$_0$ optical clock transition the best agreed-upon optical frequency to date.

Improving the absolute frequency measurement much beyond the uncertainty achieved in our last measurement [7] will be difficult without significant improvements in the Cs standard and the dissemination of derived RF frequencies via hydrogen masers. The last measurement in the graph was performed by remote comparison (see Ch. 1) between the ^{87}Sr standard in our lab and the primary US frequency standard, NIST F-1, at NIST Time and Frequency in Boulder. The measurement resulted in over 48 h of consecutive data, taken over a period of 60 h and was stopped when both Cs and Sr standards were limited by their respective and simultaneous comparison against the intermediate hydrogen maser [7, 12]. Direct comparisons of optical clocks can be performed to much higher levels of accuracy [31] and promise to give much more stringent limits on the variation of fundamental constants [95].

The figure also shows a linear and a sinusoidal fit to the frequency data. The fits were performed by minimizing the weighted sum of errors

$$\chi^2 = \sum_k \frac{[\nu_k - f(t_k, \boldsymbol{p})]^2}{\sigma_{\nu_k}^2 + \sigma_{t_k}^2 [f'(t_k, \boldsymbol{p})]^2} \tag{4.19}$$

over the corresponding parameter vector $\boldsymbol{p}$. The points in the data set and their error bars are denominated by $(t_k \pm \sigma_{t_k}, \nu_k \pm \sigma_{\nu_k})$ and the sum is over the whole data set. Here f is the fitting function to model the variation in the frequency record and f' indicates its partial derivative with respect to the independent variable t. We used a Levenberg-Marquardt algorithm [96] modified by Lybanon's method [97] to find the minimum of χ^2. Quoted parameter errors are 1-σ and were obtained from the Hessian matrix of χ^2 evaluated at the minimum [98]. The parameter uncertainties could be reduced slightly by explicitly including the measurement interval $2\sigma_{t_k}$ as a time average $(2\sigma_{t_k})^{-1} \int_{t_k-\sigma_{t_k}}^{t_k+\sigma_{t_k}} d\tau f(\tau, \boldsymbol{p}) \equiv F(t_k, \boldsymbol{p})$ and fitting the frequency record with F to avoid the significant difficulty of handling errors in the independent variable explicitly and correctly [99].
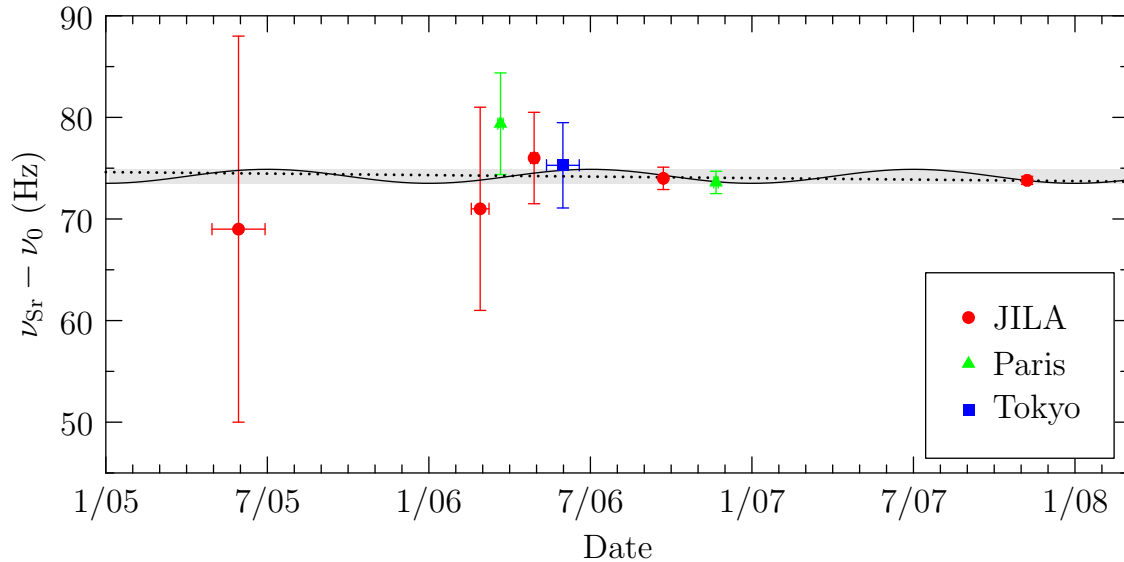
Figure 4.1.: Global absolute frequency measurements of the ^{87}Sr optical lattice clock against the Cs standard from our group, the group at LNE-Syrte in Paris, and the University of Tokyo group. The data is shown with respect to $\nu_0 = 429\ 228\ 004\ 229\ 800$ Hz. A linear fit to the data is shown as a dotted line and a sinusoidal fit is shown as a solid line. Its peak to peak amplitude is indicated by the shaded gray area.

The last four high-accuracy data points determine the fits due to their small error bars. These fits will be used in the following Sections to limit the variation of fundamental constants. The linear fit can be used to check for linear drifts in the fine structure constant and the electron-proton mass ratio (see Sec. 4.3). The sinusoidal fit limits coupling of fundamental constants to the gravitational potential (see Sec. 4.4).

4.3. Linear Drifts

If we assume that fundamental constants have been different at some time in the early universe, the simplest model is that they are changing over time. With present day experiments, we are limited to year-scale time frames. The simplest check we can do is to approximate a

linear variation in time t around the beginning of the measurement period at t_0:

$$\eta_k(t) \simeq \eta_k(t_0) + (\text{drift rate})(t - t_0)$$
$$\frac{\delta\eta_k}{\eta_k} = \frac{(\text{drift rate})}{\eta_k(t_0)}(t - t_0), \tag{4.20}$$

and try to put limits on the fractional drift rate using experimental data. By using absolute frequency measurements of optical standards, we will be able to extract drift rates for α and μ, as shown in Eq. 4.18. We will refer to the fractional drift rates as $\delta\alpha/\alpha$ and $\delta\mu/\mu$ for the rest of this Section, since that is their standard notation. The distinction between the fractional drift rates and more general variations is important since we will allow nonlinear variations in the next Section. Under the assumptions above, we can write Eq. 4.8 as

$$\frac{\delta(\omega_j/\omega_{\text{Cs}})}{\omega_j/\omega_{\text{Cs}}} = \left[(c_\alpha^j - 2.83)\frac{\delta\alpha}{\alpha} - \frac{\delta\mu}{\mu} \right] (t - t_0). \tag{4.21}$$

By fitting a linear function to a frequency record such as in Fig. 4.1, we can extract a fractional frequency drift rate x_j and compare it against the coefficient in Eq. 4.21. However, it is immediately apparent that we cannot extract information about both $\delta\alpha/\alpha$ and $\delta\mu/\mu$ from a single absolute frequency record. Data from at least two different clock species needs to be fit and the resulting set $\{x_j\}$ can then be orthogonalized. By including data from more than two species, we obtain an overdetermined system of linear equations that is solved in a least-squares sense. The least-squares solution and the parameter covariance matrix are obtained by solving the weighted normal equations in matrix form (see e.g. [100]).

To aid in the visualization of the procedure, the experimental fractional drift rates are typically plotted against the numerical sensitivity constants such as in the top panel of Fig. 4.2. Here, we have included absolute frequency data from hydrogen 1S-2S spectroscopy [83, 84], the Yb$^+$ ion clock at PTB [85], the Hg$^+$ ion clock at NIST [30] in addition to our drift rate extracted from Fig. 4.1. Each species has a different sensitivity as indicated by the x-axis. The Cs contribution to each species' sensitivity is shown as a vertical dotted line. We extract drift rates

$$\delta\alpha/\alpha = (-3.3 \pm 3.0) \times 10^{-16}/\text{yr}$$
$$\delta\mu/\mu = (1.6 \pm 1.7) \times 10^{-15}/\text{yr}, \tag{4.22}$$

which agree well with zero at the current level of accuracy.

A detailed visualization of the error in the above result is shown in the bottom panel of Fig. 4.2. Each species contributes a linear constraint

$$x_j - \sigma_{x_j} \leq (c^j_\alpha - 2.83)\frac{\delta\alpha}{\alpha} - \frac{\delta\mu}{\mu} \leq x_j + \sigma_{x_j}, \qquad (4.23)$$

where σ_{x_j} is the 1-σ error bar from the drift rate fit to data as in Fig. 4.1. These linear constraints define a region in the $(\frac{\delta\alpha}{\alpha}, \frac{\delta\mu}{\mu})$ plane that contains the valid values of $\delta\alpha/\alpha$ and $\delta\mu/\mu$ for the measured drift rate $x_j \pm \sigma_{x_j}$. Each region of validity is shown as a color-coded bar in the bottom panel of Fig. 4.2. The intersection of the regions of validity defines an elliptical contour of the reduced χ^2 (shown in white). The quadric shown here is the joint confidence region for $\delta\alpha/\alpha$ and $\delta\mu/\mu$. Its projection onto the axes defines the individual 1-σ confidence intervals for each variable given in Eq. 4.22. Note that the eigenaxes of the error quadric are not along the axes of the plot, indicating that the covariance between $\delta\alpha/\alpha$ and $\delta\mu/\mu$ is significant. The addition of the ^{87}Sr data only reduced the previous uncertainties only by $\sim$15%. Nevertheless, it is important to check for frequency variations across a wide variety of species and systems.

The utility of the bottom half of Fig. 4.2 becomes apparent when discussing the effect of adding results from direct optical clock comparisons to the results shown here. The slope of each confidence region is given by value of $c_\alpha - c^{\text{Cs}}_\alpha$ compared to unity (the Cs sensitivity to $\delta\mu/\mu$). Steeper slopes than the constraint due to Hg$^+$ will not be obtained with current optical clock systems compared to Cs. However, when optical clocks are compared directly, they will contribute constraints on $\delta\alpha/\alpha$ only – as seen from Eqs. 4.9 and 4.16 – but with much higher precision. Adding such a result to the plot amounts to adding a completely vertical region of validity to the plot. Even if the direct optical-to-optical results were only measured with the precision of the absolute frequency measurements, they would immediately put much tighter constraints on both $\delta\alpha/\alpha$ and $\delta\mu/\mu$.

After the Sr studies were completed, preliminary data from the comparison of NIST's Hg$^+$ and Al$^+$ standards became available. This addition puts the current limits on the drift of α
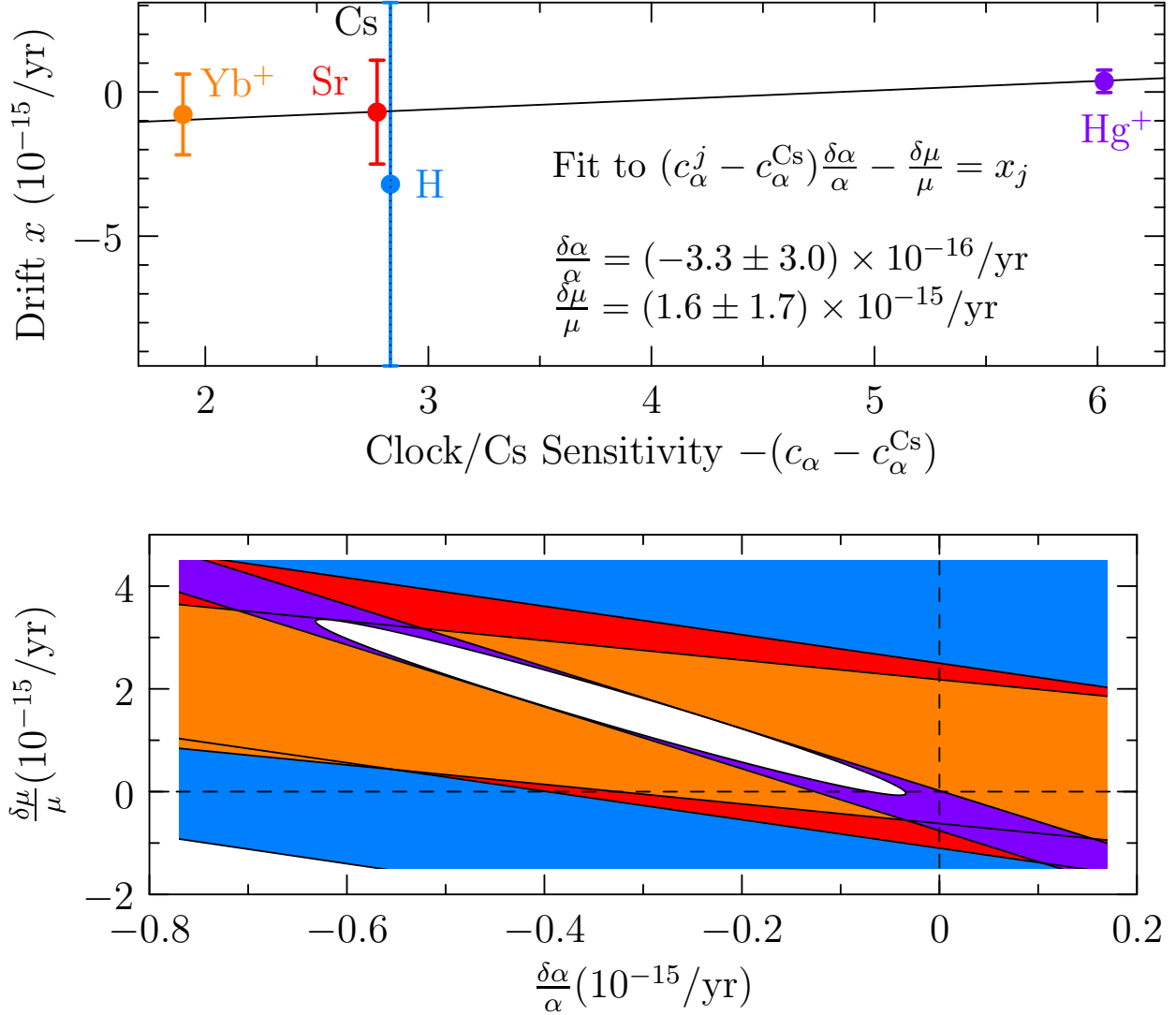
Figure 4.2.: Linear weighted least-squares analysis of optical clock fractional frequency drifts x to extract drift rates $\delta\alpha/\alpha$ and $\delta\mu/\mu$. The top panel shows fractional frequency drift rates with respect to each experiments' sensitivity to variation in α. Other species included are results from hydrogen 1S-2S spectroscopy at MPQ [83], Yb$^+$ ion clock data from PTB [85], and Hg$^+$ ion clock data from NIST [30]. The bottom panel shows the linear constraints contributed by each species as colored regions of validity in the $(\delta\alpha/\alpha, \delta\mu/\mu)$ plane. Their overlap defines a joint 1-σ region of confidence, shown as a white error ellipse. Its projections onto the axes are the 1-σ confidence intervals for $\delta\alpha/\alpha$ and $\delta\mu/\mu$.

and μ at [95]

$$\delta\alpha/\alpha = (-1.6 \pm 2.3) \times 10^{-17}/\text{yr}$$

$$\delta\mu/\mu = (-1.9 \pm 4.0) \times 10^{-16}/\text{yr}.$$

(4.24)

4.4. Gravity

From a heuristic standpoint, there are two simple ideas for the variation of fundamental constants.

"Our universe is changing, and physics was different at different times."

"Our universe is changing, and physics is different in different places."

We investigated the first idea in detail in the last section. What about the second idea? If the physics is really different in spatially separated parts of the universe, what could be the cause? According to general relativity, space is defined by the distribution of masses. Since we are interested in the variation of fundamental constants, we can immediately ask whether they could be coupled to the mass distribution in the universe, which was of course also very different in the early universe than it is now. If that were true, how would such a coupling between fundamental constants and the gravitational potential show up in clock frequency measurements?

4.4.1. Gravitational Potential Variation on Earth

For an earth-bound clock, changes in the ambient gravitational potential can come from different contributors. Here is a list of contributions sorted in terms of magnitude from largest to smallest:

- Relative position of Earth with respect to the Sun.

- Relative position of Jupiter, Saturn, and Venus with respect to Earth.

- Relative position of the Moon with respect to the clock.

Body	Mass (kg)	$r_{\min}$ (m)	$r_{\max}$ (m)	$\Delta U/c^2$
Sun	1.99×10^{30}	1.47×10^{11}	1.52×10^{11}	3.3×10^{-10}
Jupiter	1.90×10^{27}	5.89×10^{11}	9.68×10^{11}	9.4×10^{-13}
Saturn	5.69×10^{26}	1.20×10^{12}	1.66×10^{12}	9.9×10^{-14}
Venus	4.87×10^{24}	3.82×10^{10}	2.61×10^{11}	8.1×10^{-14}
Moon	7.35×10^{22}	3.63×10^{8}	4.06×10^{8}	1.5×10^{-14}
truck	10^4	10	∞	7.43×10^{-25}
graduate student	10^2	0.1	∞	7.43×10^{-25}

Table 4.2.: Peak-to-peak variation in ambient gravitational potential on Earth over one cycle. Astronomical data from Ref. [101].

- Relative position of other planets to Earth

- Gravitational forcing (Earth tides)

- Local moving masses (trucks, trains, etc.)

It might seem surprising at first that the Moon contributes less than Saturn, but a quick order of magnitude estimate can be found from the following argument. Consider the minimal and maximal distances $r_{\min}$ and $r_{\max}$ of the corresponding body of mass m with respect to the clock. We then evaluate the peak-to-peak amplitude of the gravitational potential variation over one cycle

$$\frac{\Delta U}{c^2} = \frac{U(r_{\max}) - U(r_{\min})}{c^2} = -\frac{Gm}{c^2}\left(\frac{1}{r_{\max}} - \frac{1}{r_{\min}}\right), \tag{4.25}$$

with gravitational constant G, and we obtain Tab. 4.2.

For comparison, we also estimate the contributions of Earth tides. Earth is not a rigid body, and "gravitational forcing" (mostly due to the Moon) changes the local elevation with respect to Earth's center periodically. The largest contributions change the local gravitational potential by several ten cm [102]. An upper limit on the gravitational potential variation due to Earth tides is

$$\Delta U/c^2 = (1 \text{ m}) \times g/c^2 \simeq 1.1 \times 10^{-16}, \tag{4.26}$$
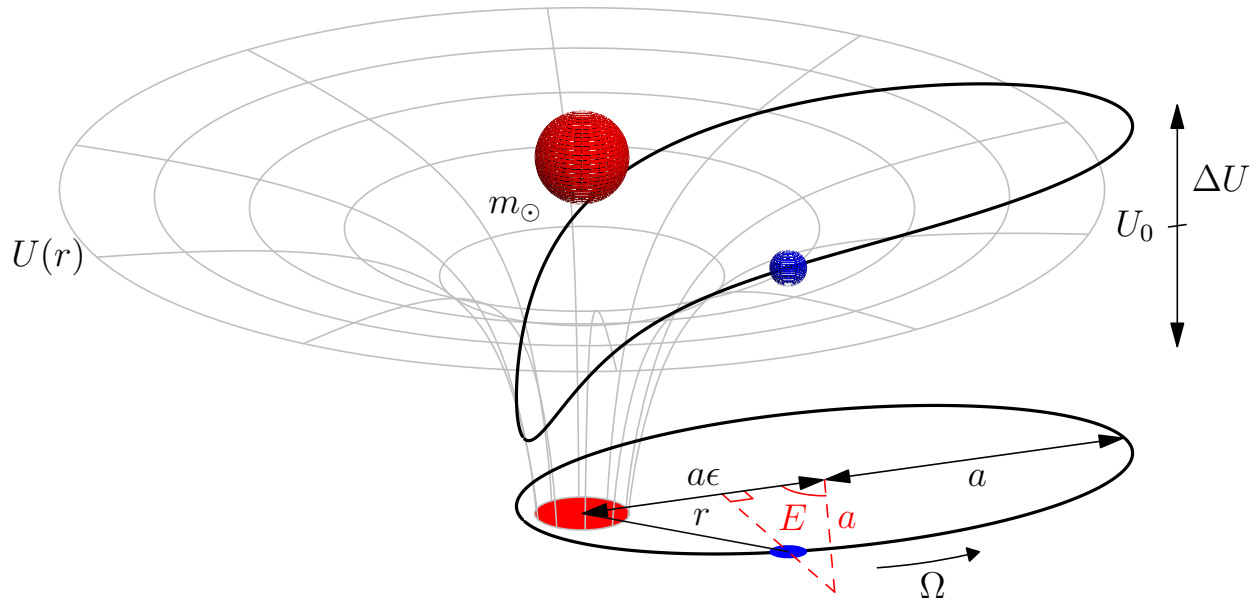
Figure 4.3.: Solar gravitational potential on Earth. Earth (blue) orbits the Sun (red, mass $m_\odot$) on an elliptical orbit with ellipticity ϵ and semimajor axis a. The ellipticity is given by the distance ϵa between the center of the ellipse and the two-body center of mass. The radial distance between Sun and Earth is r and the orbit has a mean angular velocity Ω given by Kepler's third law. The eccentric anomaly E is the angle between the major axis and the orthogonal projection of Earth's position onto a circle with radius a around the center of the ellipse. Earth's orbit is projected onto the solar gravitational potential $U(r)$ and the peak-to-peak gravitational potential variation ΔU as well as the mean solar potential U_0 are indicated.

with local gravitational acceleration $g \simeq 9.81$ m/s^2. In summary, the contribution of the Sun to the ambient gravitational potential variation on Earth is three orders of magnitude larger than all others combined.

Earth travels around the Sun on an elliptical orbit, and high-accuracy models of the trajectory are available [103]. For our purposes, a simple approximation is sufficient. The derivation presented here is based on methods summarized in Ref. [104]. Figure 4.3 shows the geometry of the two-body Sun (red) and Earth (blue) system and indicates the geometric meaning of all variables used in the following derivations.

The solar potential at radial distance $r(t)$ is

$$U(r)/c^2 = -\frac{Gm_\odot}{ac^2}\frac{a}{r} = -\left(\frac{\Omega a}{c}\right)^2 \frac{a}{r}, \tag{4.27}$$

with Sun mass $m_\odot$, the orbit's semimajor axis $a \simeq 1$ au $= 1.496 \times 10^{11}$ m, and Earth's mean angular velocity with respect to the Sun (from Kepler's third law)

$$\Omega \simeq \sqrt{\frac{Gm_\odot}{a^3}} \simeq 2 \times 10^{-7} \text{ s}^{-1}. \tag{4.28}$$

The Earth-Sun orbit r with ellipticity $\epsilon \simeq 0.0167$ is found by solving Kepler's equation

$$\Omega t = E - \epsilon \sin E, \tag{4.29}$$

which relates the *eccentric anomaly*

$$E \equiv \arccos\left(\frac{1 - r/a}{\epsilon}\right) \tag{4.30}$$

to the orbit's elapsed phase since perihelion $M \equiv \Omega t$, also called the *mean anomaly*. From Eq. 4.29, we find that the inverse radial distance is proportional to the derivative of the eccentric anomaly with respect to the elapsed phase

$$\frac{dE}{dM} = \left(\frac{dM}{dE}\right)^{-1} = (1 - \epsilon \cos E)^{-1} = \frac{a}{r}, \tag{4.31}$$

which can be expanded as a power series in the ellipticity [104]

$$\frac{a}{r} = 1 + 2\sum_{n=1}^{\infty} J_n(n\epsilon)\cos nM = 1 + \epsilon \cos M + \mathcal{O}(\epsilon^2). \tag{4.32}$$

To leading order in ϵ, the dimensionless solar gravitational potential on Earth is thus

$$U(t)/c^2 = -(\Omega a/c)^2(1 + \epsilon \cos \Omega t), \tag{4.33}$$

and its variation with respect to the mean potential is

$$\Delta U(t)/c^2 = -(\Omega a/c)^2 \epsilon \cos \Omega t. \tag{4.34}$$

Note again that $t = 0$ indicates the perihelion, where Earth is closest to the Sun, and the solar gravitational potential on Earth is most negative. As shown in Tab. 4.2, the peak-to-peak dimensionless variation is $2\epsilon(\Omega a/c)^2 \simeq 3.3 \times 10^{-10}$.

4.4.2. Gravitational Redshift

One of the reasons for precision measurements using atomic clocks is the study of gravity itself. General relativity predicts that light experiences a frequency shift

$$\frac{\omega}{\omega_{\text{no gravity}}} = \frac{1}{\sqrt{1 - 2u}} \tag{4.35}$$

directly given by the dimensionless ambient gravitational potential $u \equiv U/c^2$. Clocks tick faster the deeper they are bound in a gravitational well. As we have seen in the previous section, even the solar gravitational potential on Earth's surface is neither temporally nor spatially stable. As Earth moves around the sun, the potential experiences shifts on the order of 3×10^{-10}, which means that an optical atomic clock at 429 THz base frequency runs about 140 kHz differently in January (perihelion) than in July (aphelion).

This number is of course meaningless, because clock measurements always involve comparison against a reference, i.e. we need to compare a redshifted frequency ω' at $u + \delta u$ to the base frequency ω at u:

$$\frac{\omega' - \omega}{\omega} = \frac{\delta u}{1 - 2u} + \mathcal{O}(\delta u^2) \simeq \delta u. \tag{4.36}$$

A clock comparison is thus directly sensitive to the differential gravitational potential.

The important point here is that the spatial separation between clocks matters. A difference in elevation close to Earth's surface incurs a frequency shift of 1×10^{-16} m^{-1}. Our absolute frequency measurements against the Cs standard at NIST had to take these effects into account, as the elevation difference between the labs is (12.5 ± 1.0) m. In light of how much the elevation in Earth's potential matters for clock measurements, the agreement between our measurements and the Paris results at the 1×10^{-15} level becomes even more impressive: Paris' mean elevation above sea level is 35 m, Boulder's is 1655 m, leading to a redshift of 1.77×10^{-13} due to Earth's gravitational potential.

The agreement between JILA and Paris thus is two orders of magnitude better than their relative redshifts. This fact points to an important component of international clock comparisons: they must be referenced to a common gravitational isosurface. For this purpose,

international clock comparisons (and the Global Positioning System) are referenced to a model isosurface called the geoid. A good introduction to international timekeeping and the geoid is Ref. [105]. Each of the ^{87}Sr absolute frequency measurements were performed against local RF standards that were individually referenced to the geoid. In this way, the absolute frequencies between Boulder, Paris, and Tokyo become comparable without having to worry about the local gravitational potential up to the specified accuracy of the local RF standard.

4.4.3. Gravitational Coupling

As a simple model, we will assume that a fundamental constant η couples to the ambient gravitational potential U in a dimensionless fashion via a coupling constant k_η, i.e.

$$\frac{\delta\eta}{\eta} = k_\eta \frac{\Delta U}{c^2}. \tag{4.37}$$

Inserting this assumption into Eq. 4.9, we find that a clock comparison experiment should be sensitive to such coupling, since

$$\frac{\delta(\omega_j/\omega_i)}{\omega_j/\omega_i} = \sum_\eta (c_\eta^j - c_\eta^i) k_\eta \frac{\Delta U}{c^2}. \tag{4.38}$$

Using the orbital expansion from Sec. 4.4.1 and assuming an absolute frequency measurement of an optical clock (Eq. 4.16), we find a sinusoidal fractional frequency variation

$$\frac{\delta(\omega_j/\omega_{\mathrm{Cs}})}{\omega_j/\omega_{\mathrm{Cs}}} = -[(c_\alpha^j - 2.83)k_\alpha - k_\mu]\frac{\Omega^2 a^2}{c^2}\epsilon \cos\Omega t. \tag{4.39}$$

Note that both frequency and phase of the sinusoidal variation are fixed by the orbital mechanics. As in Sec. 4.3, we have a situation where the only free parameter in the fit is the amplitude of the effect. The sinusoidal fit in Fig. 4.1 gives an amplitude of

$$y_{\mathrm{Sr}} = (-1.9 \pm 3.5) \times 10^{-15}, \tag{4.40}$$

where the frequency of the fit was fixed at $\Omega = 1.991317 \times 10^{-7}$ s^{-1} and the phase was fixed such that an antinode of the sinusoid coincides with the 2005 perihelion on January

2, 01:00 (UTC). The fitted amplitude is negative, and the Sr data anticorrelates with the gravitational potential. The fit is again mostly determined by the last three high-accuracy data points from the JILA and Paris groups.

As before, data from one species cannot determine limits on the individual coupling constants k_η and we again need to orthogonalize similar data from multiple species. There is even less data available for this kind of analysis than for the linear variation since a good limit on the sinusoidal variation requires many data points over the course of a single oscillation period. The only other species that have been analyzed for annual variations are the NIST Hg$^+$ ion clock [30] and a NIST hydrogen maser array [89]. By correcting a sign error in Ref. [30] when applying Eq. 2 in the subsequent paragraph (corrected in Ref. [106]), we find the constraint from the Hg$^+$ clock data as

$$y_{\text{Hg}^+} = (0.7 \pm 1.2) \times 10^{-15}. \tag{4.41}$$

The sign of the constraint for the hydrogen maser data is derived from the averaged fit in Fig. 3 of Ref. [89]:

$$y_{\text{H-maser}} = (0.03 \pm 0.47) \times 10^{-15}. \tag{4.42}$$

Note that the hydrogen maser is also sensitive to variation in the light (up or down) quark mass m_q divided by the strong interaction coupling constant Λ_{QCD} [92]. We write the sensitivity constant for the H-maser as $c_q = 0.109$ [92] and the corresponding coupling constant to the gravitational potential as k_q.

We divide the measured amplitudes y_j by the peak-to-peak gravitational variation $u_0 = 2(\Omega a/c)^2 \epsilon = 3.3 \times 10^{-10}$. Together with the sensitivity equations, the measured values y_j/u_0 and their uncertainties form a system of linear constraints

$$
\begin{aligned}
y_{\text{Sr}}/u_0 &= 2.77 \; k_\alpha + \; k_\mu, \\
y_{\text{Hg}^+}/u_0 &= 6.03 \; k_\alpha + \; k_\mu, \\
y_{\text{H-maser}}/u_0 &= 0.83 \; k_\alpha + \; 0.109 \; k_q.
\end{aligned}
\tag{4.43}
$$

We can again use weighted linear regression [100] to find the coefficients k_η and their uncer-

tainties as

$$k_\alpha = (2.5 \pm 3.1) \times 10^{-6}$$

$$k_\mu = (-1.3 \pm 1.7) \times 10^{-5} \tag{4.44}$$

$$k_q = (-1.9 \pm 2.7) \times 10^{-5}.$$

To aid with the visualization of this procedure, we write Eq. 4.43 in the general form

$$y_j/u_0 = c_\alpha^j k_\alpha + c_\mu^j k_\mu + c_q^j k_q, \tag{4.45}$$

and divide by c_α to obtain

$$\frac{y_j}{c_\alpha^j u_0} = k_\alpha + d_\mu^j k_\mu + d_q^j k_q, \tag{4.46}$$

where we defined new numerical prefactors $d_\mu \equiv c_\mu^j/c_\alpha^j$ and $d_q^j \equiv c_q^j/c_\alpha^j$. We now interpret this equation as a linear function in the variables d_μ and d_q, and interpret the experimental data for the left hand side as measurements of this linear function with the unknown parameters k_α, k_μ, and k_q.

The resulting graph is shown in Fig. 4.4. The linear function in d_q and d_μ defines a plane. Since there are only three data points, the linear regression is not strictly necessary, but it immediately generalizes to the addition of more species and returns the correct error estimates for the fit parameters. The value of the plane at $d_\mu = 0$, $d_q = 0$ is k_α and its gradient along the d_μ (d_q) axis is k_μ (k_q).

The combination of maser data with optical clock data could be questioned, since hydrogen masers are not frequency-stable and have long-term nonlinear drifts. However, the addition of the maser data only pivots the fitted plane around the Sr-Hg$^+$ axis and influences neither the value nor the error bar of k_α and k_μ.

In conclusion, we find that α, $\mu = m_e/m_p$, and $m_q/\Lambda_{\mathrm{QCD}}$ do not couple to the ambient gravitational potential at the current level of accuracy ($\sim 10^{-15}$). These results will continue to improve with more data becoming available from direct optical clock comparisons. Experiments that test the weak equivalence principle also be analyzed to test for the gravitational coupling discussed in this Section, but such analyses are much less direct [107, 108]. Recently, a suggestion has been put forward that views atom interferometry as a clock experiment at

j	c_α^j	k_α	$+d_\mu^j k_\mu$	$+d_q^j k_q$	$= y_j/(c_\alpha^j u)$
Sr	2.77	k_α	$+0.36k_\mu$		$= (-2.1 \pm 3.2) \times 10^{-6}$
Hg$^+$	6.03	k_α	$+0.17k_\mu$		$= (3.5 \pm 6.0) \times 10^{-7}$
H-maser	0.83	k_α		$+0.13k_q$	$= (1 \pm 17) \times 10^{-7}$
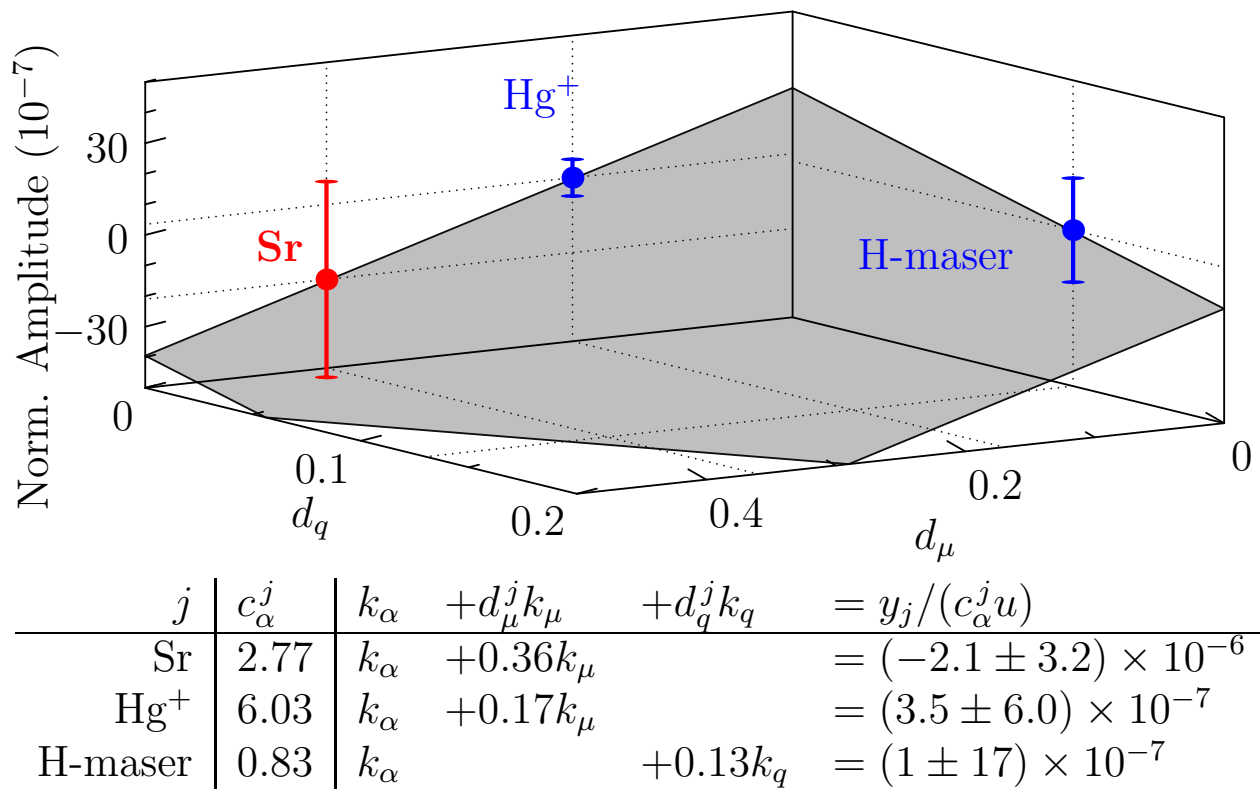
Figure 4.4.: Graphical representation of linear regression to extract the gravitational coupling constants.

the atomic Compton frequency [109, 110], with correspondingly low fractional uncertainty. This interpretation is much-disputed [111, 112] and clock experiments remain the most direct way of investigating gravity [113].

Chapter 5

OPTICAL FESHBACH RESONANCE IN ^{88}SR

SCATTERING resonances in ultracold atomic gases [114, 115] allow control of atomic interactions and have been used very successfully over the last decade to study many novel phenomena. The underlying phenomenon is the magnetically controlled Feshbach resonance (MFR) which arises from coupling of the free particle states to a bound molecular state. Such scattering resonances were studied first by Ugo Fano [116, 117] and Herman Feshbach [118].

MFR is schematically shown in Fig. 5.1(a). Different hyperfine structure states in the electronic ground state manifold of an alkali metal atom lead to multiple molecular ground state potentials. Their relative energies can be tuned by an external magnetic field. If atoms are initially prepared in a given hyperfine structure state (the open channel), and a bound state in a different molecular ground state potential (the closed channel) becomes degenerate with the free particle threshold, a scattering resonance arises, and the free particle scattering phase shift can be modified. Because the bound molecular state is in the ground electronic manifold, it is long-lived and the molecular coupling does not introduce loss. In the zero collision energy limit, the scattering process is completely determined by a real s-wave scattering length.[1] In the vicinity of the resonance, the scattering length diverges

---

[1] A complete discussion of scattering theory relevant to collisions in ultracold atomic gases is beyond the scope of this work, but an excellent summary can be found in Ref. [119]. A good overview on quantum degenerate gases is Ref. [120]. The main review paper for Feshbach resonances in ultracold gases is Ref. [121].

and the achievable change in scattering length is only limited by secondary processes such as three-body collisions [121].

These dispersive changes in scattering length have allowed exquisite control and led to the realization of few-body quantum states [122, 123], and the study of strongly correlated systems [124, 125]. These resonances have played a leading role in building atomic systems that model simple condensed matter systems and have become the dominant experimental tool to tune many-body interactions in atomic physics experiments [121].

With the success of ultracold gases of alkaline earth atoms in recent years for precision measurements (see previous Chapters), many interesting proposals for quantum simulation of many-body systems have been put forward [126–128]. However, magnetically induced Feshbach resonances do not exist in the spinless electronic ground state of these systems since there are no molecular potentials available that can be strongly coupled by experimentally feasible magnetic fields. Instead, the coupling field has to be at optical frequencies and the coupled molecular potential is an excited molecular state. The coupled molecular bound state can now decay via spontaneous emission and the resulting decoherence rate is the most important factor to consider in understanding the resulting Optical Feshbach Resonance (OFR) [121, 129, 130]. The experimental situation is shown in Fig. 5.1(b), which describes a photoassociation (PA) experiment [131] where a PA laser couples free particles to a bound state in a metastable molecular potential. On resonance, molecules are formed which can decay to free particles with high kinetic energy or deeply bound ground state molecules. Once a molecule has formed, it is considered lost from the experiment. In a PA experiment, the laser is tuned across the resonance and atomic loss spectra are measured. If the PA laser is detuned from molecular resonance, the scattering phase shift can still be modified, just as for a magnetic Feshbach resonance. However, the molecular loss limits the achievable scattering length modification. In a dressed state picture [see Fig. 5.1(c)], the OFR looks very similar to the MFR. The closed channel can be tuned with respect to the open channel by either a magnetic field or the laser detuning. The tuning changes the interatomic distance (the Condon point) at which the open and closed channels become resonantly coupled. The
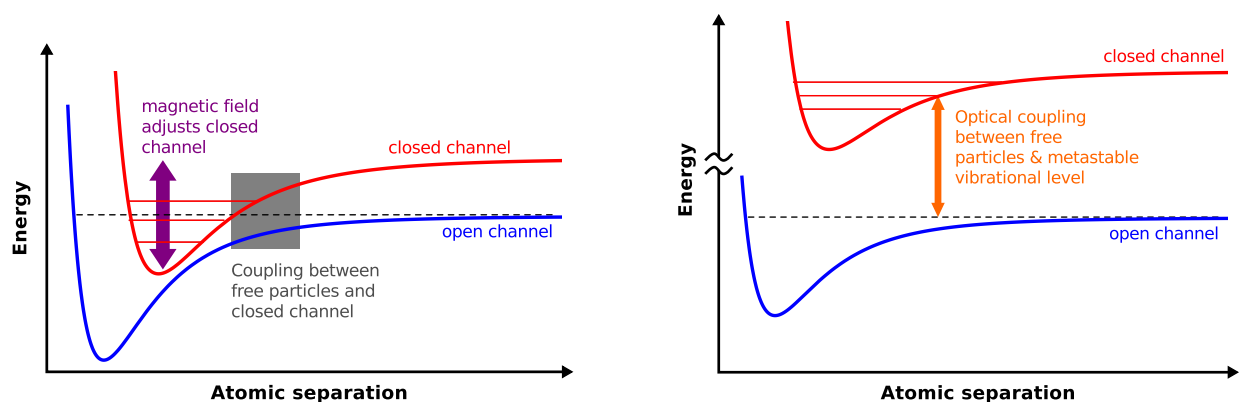
(a) Magnetic Feshbach resonance (MFR) between molecular potentials in the electronic ground state.

(b) Optical Feshbach resonance (OFR) between electronic ground state potential (open channel) and metastable molecular potential (closed channel that decays).
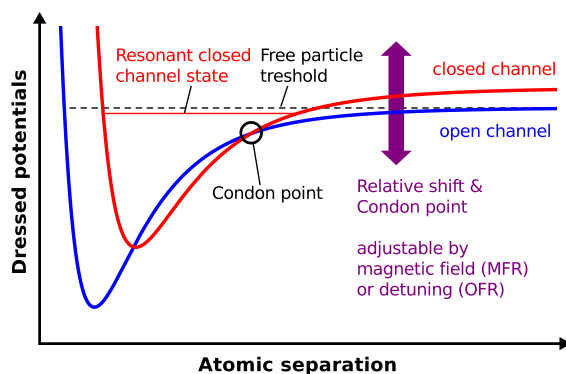
(c) Dressed potential for either magnetic or optical Feshbach resonance. The Condon point R_C indicates the interatomic separation around which the resonant interaction is localized.

Figure 5.1.: Magnetic and optical Feshbach resonances arising from coupled molecular potentials. The coupling is adjustable by either the magnitude of an external magnetic field (MFR) or the detuning of a photoassociation laser (OFR). A resonance appears when the free particle energy becomes resonant with a state in the closed channel. The only conceptual difference is that the OFR closed channel introduces decay when a metastable molecule is formed and subsequently dissociates.

only conceptual difference between OFR and MFR is that OFRs have intrinsic loss given by the natural radiative decay of the metastable molecules and that the OFR strength can be tuned independently by adjusting the PA laser intensity.

The OFR effect was first observed in alkali atoms [132–135] but was not found useful due to large inelastic losses. Much narrower optical intercombination lines are available in alkaline earth atoms and are predicted to overcome this loss problem [136]. These predictions in combination with our group's study on narrow line photoassociation in ^{88}Sr [137] stimulated work on the OFR effect in thermal and quantum degenerate gases of Yb [138, 139].

In our experiment, we worked with bosonic ^{88}Sr, which has a small background s-wave scattering length of $a_{\mathrm{bg}} \simeq -1.4a_0$ [140, 141], with the Bohr radius a_0. The sample is trapped in an optical dipole trap at temperatures of several μK. In this regime, s-wave scattering dominates, but the small a_{bg} makes the sample effectively non-interacting on experimental timescales. In combination with the simple electronic structure, this makes ^{88}Sr an ideal test bench for the OFR effect. For these reasons, we can specialize the general theory to negligible background scattering which simplifies the treatment considerably.

We will first introduce the general theoretical background for describing the OFR effect in both degenerate and thermal gases. Based on the general theory, we will develop the formalism used to describe a single, isolated OFR. Care is taken to make the formalism applicable to the regime where s-wave scattering dominates, but where particles collide at non-zero collision energies. Extraction of the relevant OFR parameters from experimental data such as PA loss spectra requires a careful modeling of the sample dynamics in the presence of interactions. While analytic treatments can highlight important limiting cases, a Monte-Carlo simulation of the sample is required to model the interaction dynamics accurately. Using these methods we are equipped to model the sample dynamics under the influence of the OFR effect in a universal way and predict the requirements for applying OFR in a quantum degenerate gas. Our results will be directly applicable to experiments with quantum degenerate gases of Sr, which have become available in the last two years [142, 143].

5.1. Complex scattering length, S-matrix, collision cross sections & rates

We introduce the necessary notation for describing the OFR effect, based on Refs. [119, 121, 130, 144]. We will use the energy-dependent complex scattering length definition adopted in Ref. [145]

$$\alpha(k) \equiv a(k) - ib(k) \equiv -\frac{\tan \eta_{00}(k)}{k} \tag{5.1}$$

to describe collisions for small but non-zero collision energy in the thermal regime where s-wave scattering dominates, but the finite collision momentum matters. Here, a ($-b$) is the real (imaginary) part of α and $\eta_{00}(k)$ is the complex s-wave scattering phase shift describing both elastic and inelastic components of the scattering process. Molecule formation is considered an inelastic process that removes the collision partners from the sample completely. The collision energy $E \equiv \hbar^2 k^2/(2\mu)$ is related to the relative momentum[2] (mass) $\hbar k$ (μ) of a collision pair and for our purposes, $\mu = m_{\mathrm{Sr}}/2$ with the atomic mass m_{Sr}. The scattering length can be related to the s-wave scattering matrix $S_{00}(k)$ via

$$S_{00}(k) = e^{2i\eta_{00}(k)} \Leftrightarrow \alpha(k) = \frac{1}{ik}\frac{1 - S_{00}(k)}{1 + S_{00}(k)}. \tag{5.2}$$

For collisions between identical bosons, the elastic and inelastic collision cross sections are related to the S matrix via [119, 121]

$$\sigma_{\mathrm{el}}(k) \equiv 2\frac{\pi}{k^2}|1 - S_{00}(k)|^2,$$
$$\sigma_{\mathrm{in}}(k) \equiv 2\frac{\pi}{k^2}(1 - |S_{00}(k)|)^2. \tag{5.3}$$

Note that the cross sections for nonzero k are not simply related to the squares of a and b, but that

$$\sigma_{\mathrm{el}}(k) = 8\pi|\alpha(k)|^2 f(k)^2,$$
$$\sigma_{\mathrm{in}}(k) = \frac{8\pi}{k}b(k)f(k), \tag{5.4}$$

---

[2]Note that here and in the literature, both k and $\hbar k$ are referred to as the relative collision momentum.

with

$$f(k) \equiv \frac{1}{1 + k^2 |\alpha(k)|^2 + 2kb(k)}. \tag{5.5}$$

The function f encapsulates the unitarity limit for both elastic and inelastic processes with $0 < f(k) < 1$ and $f(k) \to 1$ as $k \to 0$.

These collision cross sections are related to the likelihood of a collision event with relative velocity $v_{\rm rel} \equiv \hbar k / \mu$ occurring, in the sense that

$$P_c(|\boldsymbol{v}_i - \boldsymbol{v}_j|) = \sigma(|\boldsymbol{v}_i - \boldsymbol{v}_j|)|\boldsymbol{v}_i - \boldsymbol{v}_j| \frac{\Delta t}{V_c}, \tag{5.6}$$

is the probability of a collision event happening between particles i and j with velocities $\boldsymbol{v}$ within an arbitrary collision volume V_c and time interval Δt, as long as $P_c \ll 1$. From the probabilistic interpretation of the collision cross sections, we can derive differential equations that describe the collision processes. Let V be the trap volume containing a sample of N identical bosons. We subdivide V into collision volumes such that $V = M V_c$, and we choose M such that the average number of atoms within each collision volume

$$N_{\rm occ} = \frac{1}{M} \sum_{i=1}^{M} N_i \tag{5.7}$$

is small ($N_{\rm occ} \ll 1$). The number of particles influenced within a collision volume by collision events during a sufficiently small Δt is then given by a sum over distinguishable collision pairs

$$\Delta N_i = -2 \sum_{k=1}^{N_i} \sum_{\ell=1}^{k-1} P_c(|\boldsymbol{v}_k - \boldsymbol{v}_\ell|) \tag{5.8}$$

where the factor of 2 arises from the fact that two particles are influenced by each collision event. For elastic collisions, this means that two particles change their velocity directions. For the inelastic processes considered here, two particles are lost from the sample per collision event. If we take the average of Eq. 5.8 over all collision volumes, we find the change in average occupation number

$$\Delta N_{\rm occ} \equiv \langle \Delta N_i \rangle_i = -2 \left\langle \sum_{k=1}^{N_i} \sum_{\ell=1}^{k-1} P_c(|\boldsymbol{v}_k - \boldsymbol{v}_\ell|) \right\rangle_i$$
$$\simeq -2 \frac{\Delta t}{V_c} \left\langle \frac{N_i(N_i - 1)}{2} \right\rangle_i \langle \sigma(v_{\rm rel}) v_{\rm rel} \rangle_T , \tag{5.9}$$

where $\langle\cdot\rangle_T$ indicates a thermal average at temperature T over the relative velocity distribution within the sample. The factor $N_i(N_i-1)/2$ stands for the number of distinguishable collision pairs considered in the sum. For small N_{occ}, the collision volume particle number N_i is distributed as a Poisson distribution and we use

$$\langle N_i^2 \rangle - \langle N_i \rangle^2 = \langle N_i \rangle = N_{\mathrm{occ}} \Rightarrow \langle N_i(N_i - 1) \rangle = N_{\mathrm{occ}}^2 \tag{5.10}$$

to find the average occupation number change due to inelastic collisions as

$$\frac{\Delta N_{\mathrm{occ}}}{\Delta t} = -\frac{N_{\mathrm{occ}}^2}{V_c} \langle \sigma_{\mathrm{in}}(v_{\mathrm{rel}}) v_{\mathrm{rel}} \rangle_T. \tag{5.11}$$

We define the mean density $\bar{n} \equiv N_{\mathrm{occ}}/V_c$, let $\Delta t \to 0$ and obtain the mean density evolution due to inelastic collisions

$$\dot{\bar{n}} = -\langle \sigma_{\mathrm{in}}(v_{\mathrm{rel}}) v_{\mathrm{rel}} \rangle_T \, \bar{n}^2 \equiv -\langle K_{\mathrm{in}} \rangle_T \, \bar{n}^2. \tag{5.12}$$

The above derivation lets us define inelastic and elastic collision rate constants

$$\begin{aligned} K_{\mathrm{in}}(k) &\equiv \frac{\hbar k}{\mu} \sigma_{\mathrm{in}}(k), \\ K_{\mathrm{el}}(k) &\equiv \frac{\hbar k}{\mu} \sigma_{\mathrm{el}}(k), \end{aligned} \tag{5.13}$$

where the rate K_{in} is defined as the factor multiplying the density squared in the density loss equation and K_{el} is defined analogously. Note that the ratio of elastic to inelastic collisions at a given collision energy

$$\frac{K_{\mathrm{el}}(k)}{K_{\mathrm{in}}(k)} = \frac{\sigma_{\mathrm{el}}(k)}{\sigma_{\mathrm{in}}(k)} = \frac{|1 - S_{00}(k)|^2}{1 - |S_{00}(k)|^2} = \frac{k|\alpha(k)|^2}{b(k)} [1 + k^2|\alpha(k)|^2 + 2kb(k)] \tag{5.14}$$

tends to zero as $k \to 0$.

Note that the discussion in this Section has been a completely general discussion of elastic and inelastic processes due to an energy-dependent complex scattering length and that no approximations have been made.

5.2. OFR as an isolated decaying Feshbach resonance

In the previous Section, we introduced a treatment of s-wave scattering under a complex scattering length. Complex scattering lengths have been successfully used to describe scat-

tering resonances with loss, i.e. problems where free particles are coupled to a decaying bound state. The Optical Feshbach Resonance is just such a case, where the bound state is a metastable molecular level that decays spontaneously into free particles in the ground electronic state.

For an isolated OFR, Bohn and Julienne [130] derive an S-matrix

$$S_{00}(k) = \frac{E/\hbar + \Delta + i[\gamma - \Gamma_s(k)]/2}{E/\hbar + \Delta + i[\gamma + \Gamma_s(k)]/2} e^{2i\eta_{00}(k)}, \tag{5.15}$$

where Δ is the laser detuning from molecular resonance[3], γ is the intrinsic molecular decay rate, and

$$\Gamma_s(k) \equiv 2k\ell_{\rm opt}(k)\gamma_m, \tag{5.16}$$

is the laser-induced stimulated molecular linewidth in terms of the natural molecular linewidth $\gamma_m = 2\gamma_a$, where γ_a is the natural linewidth of the atomic transition. The strength parameter $\ell_{\rm opt}(k)$ has dimensions of length and thus is called the *optical length*. It can be expressed in terms of molecular parameters and the driving laser intensity I as [136, 144]

$$\ell_{\rm opt}(k) = \frac{\lambda_a^3}{16\pi c} \frac{|\langle n|E\rangle|^2}{k} I, \tag{5.17}$$

where λ_a is the atomic transition wavelength, and c is the speed of light. The molecular Franck-Condon factor $|\langle n|E\rangle|^2$ describes the wave-function overlap between the free particle state with collision energy E and the bound molecular state wave function $|n\rangle$. For small collision energies, the Wigner-threshold law predicts that $|\langle n|E\rangle|^2 \propto k$ and thus $\ell_{\rm opt}$ should be a very weak function of k. We have verified numerically that the Wigner-threshold law holds for Sr collisions beneath $E/k_B = 10$ μK, by comparing the isolated resonance formulas against a full coupled-channels calculation [146]. Typical temperatures in our experiment are $\sim$3 μK, and we will neglect the dependence of $\ell_{\rm opt}$ on k in the following. The optical length is also independent of the oscillator strength of the underlying atomic transition and

---

[3]The molecular detuning definition here includes the I-dependent AC Stark shift of the molecular line to simplify the present discussion. We will derive a more complete description of the molecular detuning Δ later.

thus becomes a general parameter to compare the strength of molecular resonances across species.

In Eq. 5.15, we have allowed for extra molecular loss beyond the radiative decay, such that $\gamma > \gamma_m$. We combine Eqs. 5.13, 5.15, and 5.16, neglecting the small background phase shift η_{00}, and find expressions for the elastic and inelastic collision rates for an isolated resonance:

$$K_{\mathrm{in}}(k) = \frac{2h}{\mu} \frac{\ell_{\mathrm{eff}}}{(\Delta + E/\hbar)^2/\gamma^2 + (1 + 2k\ell_{\mathrm{eff}})^2/4}$$

$$K_{\mathrm{el}}(k) \simeq 2k\ell_{\mathrm{eff}} K_{\mathrm{in}}(k), \tag{5.18}$$

where we have defined an *effective optical length*

$$\ell_{\mathrm{eff}} = \frac{\gamma_m}{\gamma} \ell_{\mathrm{opt}}, \tag{5.19}$$

that describes the OFR strength in the presence of extra molecular decay. The factor $2k\ell_{\mathrm{eff}}$ in the denominator accounts for power broadening of the molecular response. The simple relationship $K_{\mathrm{el}}/K_{\mathrm{in}} = 2k\ell_{\mathrm{eff}}$ between elastic and inelastic collision rates only holds when we can neglect the background scattering length a_{bg}. This relationship simplifies the discussion drastically and we can define a small intensity regime, where

$$\ell_{\mathrm{eff}} \ll \frac{1}{2\langle k \rangle_T} = \frac{\hbar}{2} \sqrt{\frac{\pi}{8\mu k_B T}}, \tag{5.20}$$

for a three-dimensional Maxwell-Boltzmann distribution at temperature T. In this limit, elastic collisions and power broadening can be neglected. The system dynamics can then be described completely by two-body inelastic loss processes with collision rate

$$K_{\mathrm{in}} \to \frac{2h}{\mu} \frac{\ell_{\mathrm{eff}}}{(\Delta + E/\hbar)^2/\gamma^2 + 1/4}, \tag{5.21}$$

which scales linearly with ℓ_{eff}. A typical scale for inelastic collision rates in this regime can be obtained by setting the detuning term to zero:

$$K_{\mathrm{in}} \sim \frac{8h\ell_{\mathrm{eff}}}{\mu} \simeq (3.8 \times 10^{-12} \text{ cm}^3/\text{s}) \times \left(\frac{\ell_{\mathrm{eff}}}{a_0}\right), \tag{5.22}$$

at $\mu = m_{\mathrm{Sr}}/2 = 44$ amu. The inelastic collision rate is still dependent on the relative momentum through the relative energy denominator. Measuring the inelastic loss rate in a PA experiment with small intensities over long timescales thus allows a clean measurement of the line strength factor ℓ_{eff}/I for a given molecular resonance.

5.3. Photoassociative Spectroscopy

We studied the photoassociative loss experimentally for three PA resonances in the excited $^1S_0 - {}^3P_1\ 0_u$ potential of Sr_2. The ground state molecular potential ($^1S_0 - {}^1S_0\ 0_g$) and the excited molecular potential are shown in Fig. 5.2 with respect to the internuclear distance. The PA laser couples two colliding ground state atoms to a high-lying vibrational state in the metastable excited potential. The vibrational levels are labeled as negative numbers n counting from the free particle threshold.
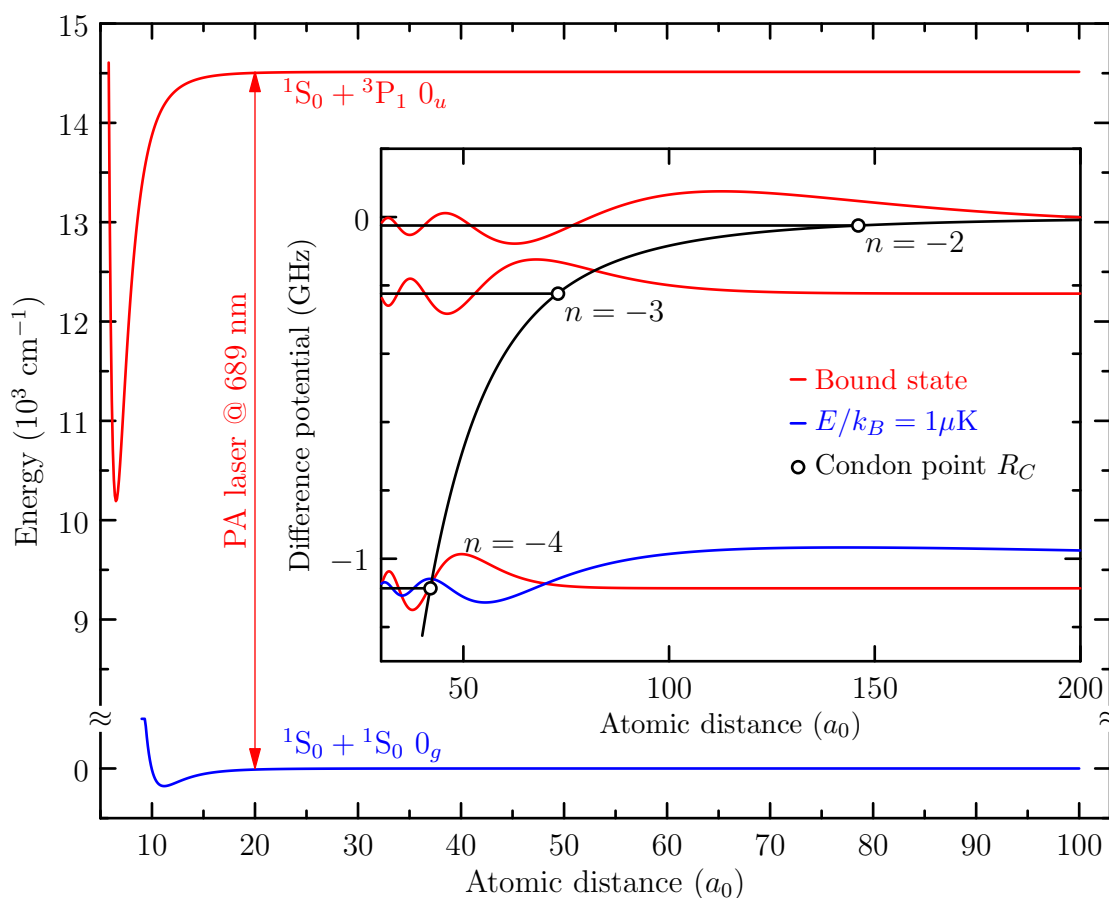
Figure 5.2.: Molecular potentials coupled by a PA laser. The inset shows the difference potential after subtracting the optical frequency. A free particle wave function is indicated in solid blue and bound vibrational wave functions for the vibrational levels of interest are shown in red. Note that the Condon points are at large interatomic distance.

The inset of the figure shows the difference between ground and excited molecular poten-

tials after subtracting the optical frequency. We investigated the $n = -2, -3$, and -4 levels, close to the free particle threshold and thus at relatively small red detuning from the free particle atomic transition. The metastable molecules in these vibrational states are loosely bound and the Condon points for photoassociation are situated at large interatomic distances of $(40 - 150) \times a_0$. For this reason, the Franck-Condon factor determining the optical length is not very dependent on the details of the short range molecular potential and a relatively accurate calculation is based on knowledge of the long-range dispersion coefficients [144]. A representative free particle wave function at a collision energy of $E/k_B = 1$ μK is shown in solid blue and bound state wave functions are overlaid in solid red. The Franck-Condon factor and thus ℓ_{opt} is determined by the overlap integral of these wave functions [144].

For small ℓ_{opt}, the effect of tuning the PA laser across a vibrational resonance is relative-momentum-dependent particle loss (see previous Section). Representative PA loss spectra for small ℓ_{opt} are shown in Fig. 5.3. Here, the fractional atom loss is shown as a function of PA laser detuning from the atomic transition after the PA laser interacted with the trapped sample for $\tau_{\mathrm{PA}} = 200$ ms. Note that the PA intensity is adjusted to compensate for the individual line strength such that the overall loss is comparable. Atomic densities for all spectra were similar $\sim 5 \times 10^{11}$ cm^{-3} and the number of photons scattered per atom off the atomic transition $\tau_{\mathrm{PA}} \Gamma_{\mathrm{sc}} \ll 1$. The spectra look very similar, and we will find in the following Sections that similar values of the optical length ℓ_{opt} describe all three spectra shown.

We will develop a model to extract the optical length and the center frequency of the PA lineshapes for a thermal gas of ^{88}Sr. To obtain this data, we need a model of the density distribution in the optical trap that does not assume thermal equilibrium. We will discuss the trapping geometry and then derive a more general description for the density evolution than Eq. 5.12. Integrating the density over the trap volume then provides us with a model for the atom number evolution with time which we can use to fit the PA spectra in Fig. 5.3.
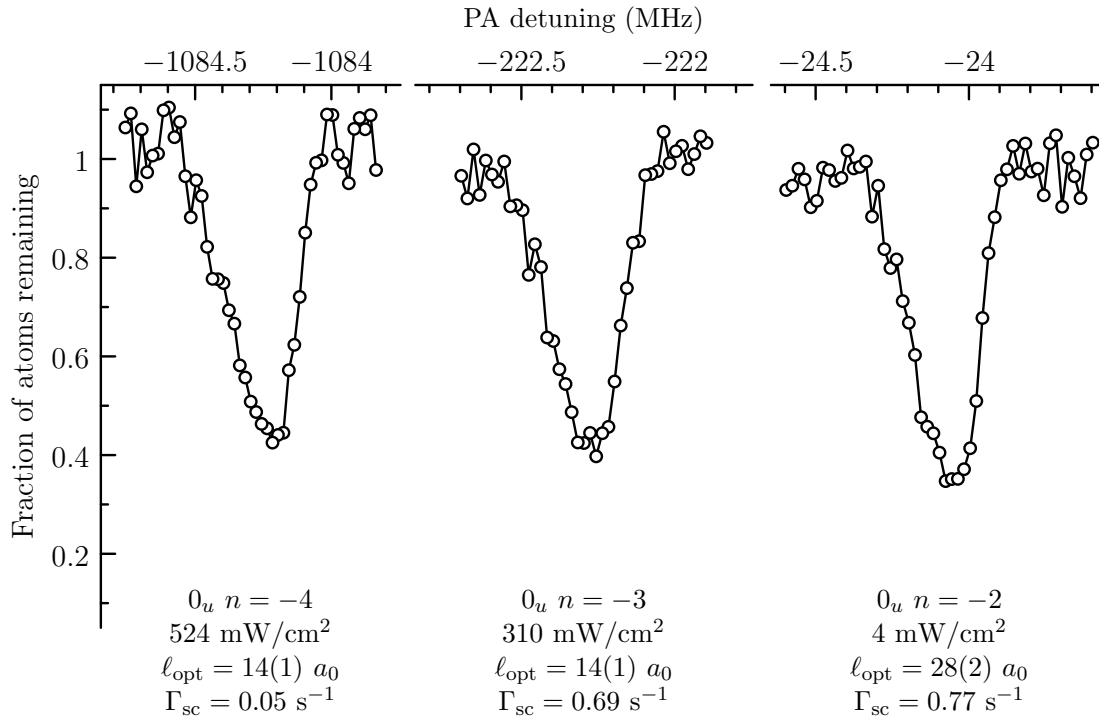
Figure 5.3.: PA loss spectra in the small optical length regime for three vibrational levels. The PA laser interacted with the atoms for 200 ms at the indicated PA laser intensity, which has been adjusted to obtain similar optical length ℓ_{opt}. The scattering rate from the atomic transition Γ_{sc} is kept small such that atomic scattering does not influence the atomic density significantly.

5.4. Experimental Setup

This section gives a brief overview of the third generation Sr apparatus (Sr3) and summarizes some of our experiences with the various components used.

5.4.1. Vacuum system & magnetic coils

An overview drawing of the apparatus is shown in Fig. 5.4 and in the following, capital letters in parentheses refer to the labeled parts of the figure. The atomic beam source is a conventional effusive oven design. The oven is heated from outside the vacuum with ceramic clamshell heaters and the whole assembly is wrapped in high-temperature ceramic heat insulation. The oven temperature is controlled by commercial process controllers with feedback from high-temperature thermocouples. To prevent vacuum part corrosion due to heat cycling, the front end of the oven is machined from a single piece of 316 stainless steel with thick walls (A). A microtube oven nozzle [147, 148] drops in from the front and is held in place by two ventilated screws. We thank F. Schreck of the University of Innsbruck for sending us the microtube material. The tubes are made of 304 stainless steel tubes with 200 μm inner diameter (ID). The tubes are acid-etched to 8 mm length and stacked in a pressure-fit U-shaped holder. The oven front end is welded to a 45° elbow (B) that lets the back end of the oven hang down and prevents solid Sr from migrating towards the nozzle. The elbow and the back end of the oven are connected by a Conflat flange with a Ni gasket (C). The back end is a simple cup filled with natural abundance Sr metal (D) that is water-cooled with a cooling block in the very back (E). The water-cooling allows relatively rapid cooling of the oven from operating temperature to room temperature with $1/e$ time constant ~2.5 h. The back (front) end is typically heated to 575 °C (625 °C). The 50 °C temperature differential combined with the 45° bend seems to have been enough to prevent nozzle clogging for the last 3 yr of operation.

This design produces an atomic beam that separates into a collimated part (collimation given by the opening angle of the individual tubes) and a diffuse part (given by the opening
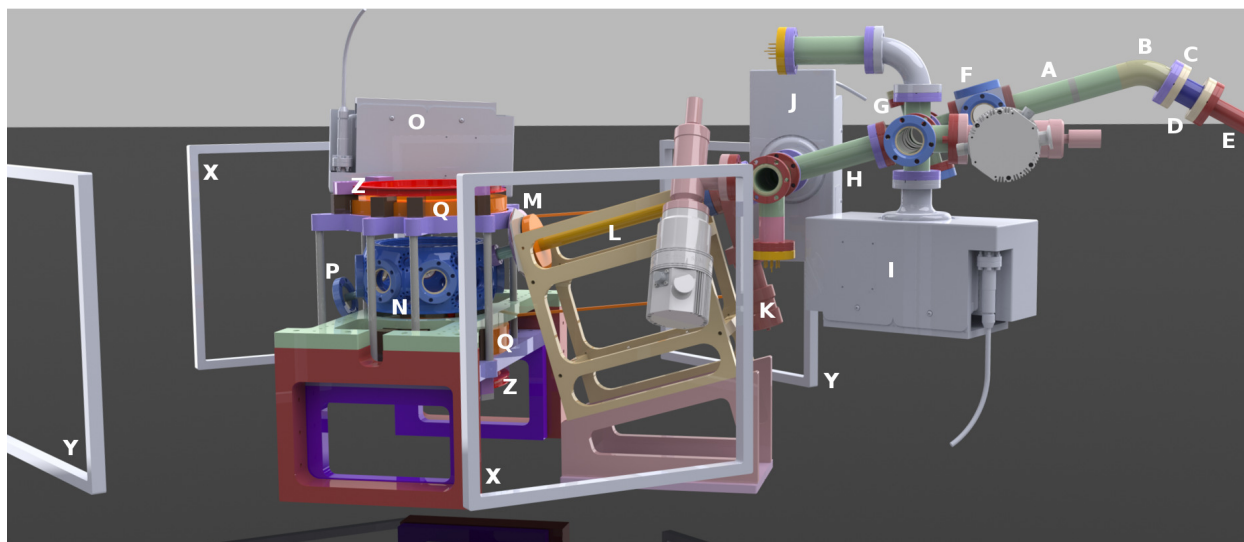
Figure 5.4.: Sr3 vacuum system including magnetic coils without optics and electronics. The parts labeled are described in the main text.

angle of the full nozzle diameter) [147, 149–151]. The major advantage of the microchannel nozzle is that it saves a lot of source material by not transmitting as many atoms with large transverse velocities that cannot be collimated easily even with transverse laser cooling.

The beam passes through a vacuum cube (F) containing a UHV compatible magnetically-coupled rotary feedthrough with a U-shaped attachment, driven by a stepper motor. This setup acts as an atomic beam shutter by rotating the arms of the U into the atomic beam path. In our experiments so far, however, we have not found it necessary to shutter the beam. The rotary shutter was implemented as a replacement for the previously-used in-vacuum Uniblitz shutter. These shutters have been used in earlier Sr experiments because they allow full shuttering of both the atomic beam and oven BBR radiation on time scales < 1 ms. These shutters are notorious for failing catastrophically and are not compatible with vacuum levels below 10^{-9} Torr, since they require in-vacuum electrical connections to a resin-enclosed driving coil. A typical failure mode is that the shutter blades crash into one another and a part of the blade or driving mechanism breaks off. If that happens, the vacuum system will be contaminated with carbohydrates (it smells of burned plastic) and has to be cleaned and rebaked from scratch. Use of these shutter systems is not recommended.

The beam passes through another six-way cross (G) which is used for transverse cooling. The beam is collimated (and steered) by two retroreflected horizontal and vertical beams at 461 nm and about -10 MHz detuning from $^1S_0$-$^1P_1$. The collimated beam then passes through a 5 inch long differential pumping tube with 1/4 inch ID between the oven and the Zeeman slower regions (H). Both oven and Zeeman slower regions are pumped with Varian StarCell 40 l/s ion pumps (I,J) and typical Zeeman slower region pressures can reach 10^{-10} Torr. The system contains ion gauges in the oven, Zeeman slower, and main chamber regions. These are typically turned off and the pressure is estimated from the ion pump currents continuously monitored with a Keithley precision voltmeter. The beam then passes through a pneumatic all-metal gate valve (K) that separates the Zeeman slower tube and the main chamber from the oven region.

The Zeeman slower (L) is 25 cm long and separated into two coils with opposite current directions (not shown in figure). This design reduces the amount of wire that has to be used and results in a much reduced resistive heat load. The design also allows using laser detunings much closer to the atomic resonance. The zero-field detuning is ~ -640 MHz, which can be obtained with high efficiency by using an AOM around 300 MHz before doubling. Choosing a relatively low AOM frequency and shifting the frequency in the infrared decreases the loss drastically compared to using a low-efficiency and hard-to-align 1 GHz AOM at 461 nm. Even though the resistive heat load is small, the Zeeman slower is wound on a water cooled tube that encloses the actual vacuum tube. The coil design was optimized by an adaptive algorithm that varied the number of transverse and longitudinal layers of wire for each coil to obtain the ideal field shape. Another water-cooled magnetic coil (M) is positioned at the end of the Zeeman slower which allows compensating for the residual longitudinal magnetic field due to the Zeeman slower at the center of the vacuum chamber. All coils are driven by constant-current power supplies stable to 10^{-3} that are always on [typical currents are $(1-3)$ A].

The slowed atomic beam (design longitudinal velocity 40 m/s) then enters the main chamber (N) which is pumped with another 40 l/s ion pump (O). Main chamber pressures are in

the low 10^{-10} Torr to high 10^{-11} Torr regime. Unfortunately, the initial design did not include additional Ti:sublimation pumps and the main chamber pressure would rise over the course of the day to $(5-8) \times 10^{-10}$. The oven load was reduced to negligible levels by encapsulating the differential pumping tube region in a shaped aluminum block (not shown in figure) that is cooled by a Fisher Scientific ethylene-glycol circulating chiller to -20 °C. Water-ice buildup is manageable with good thermal insulation and the low humidity in Boulder. Typical lifetimes in the magnetically trapped $^3P_2$ state are $3-5$ s. This lifetime is limited by outgassing of the surfaces in the main chamber. An improved main chamber vacuum design using two 125 l/s ion pumps and two Ti:sublimation pumps is being implemented. Accounting for the increased main chamber surface area, the increase in ion pump speed alone should increase the pumping speed at the center of the main chamber by a factor of 6.

The main chamber (N) is a Kimball spherical octagon made of 316 stainless steel and the large 6 1/2 inch viewports are oriented vertically. To prevent losing access to the eight 2 3/4 inch viewports, the Zeeman slower was tilted upwards and is connected to one of the sixteen 1 1/3 inch viewports. The viewport directly across from the atomic beam (P) is made of UV grade sapphire and heated to 150 °C to prevent formation of a metal film on the viewport. The heater is switched off during red MOT and dipole trap operation to prevent stray magnetic fields from influencing the atoms. The Zeeman slower laser beam (with a typical power of 30 mW) enters through the sapphire viewport and its collimation is optimized to maximize loading of the atoms into the blue MOT. The blue MOT, red MOT and crossed dipole traps are slightly offset from the Zeeman slower path and we have not observed any effect of shuttering the atomic beam on our experiments so far.

The blue MOT is formed by three retroreflected laser beams at 461 nm, with typical beam diameters of 11 mm, powers of ~ 2 mW per beam, and detuning of -40 MHz from the $^1S_0$-$^3P_1$ transition. The magnetic field gradient is 50 Gauss/cm and is produced by a pair of anti-Helmholtz coils (Q) that are driven by a feedback-stabilized constant voltage power supply. The current is measured with a Hall probe and feedback is applied to two parallel water-cooled MOSFETS. The large reverse breakdown voltage (Zener voltage 500 V) allows

shutting off the $\sim$10 mH coil pair within 250 μs with a PI based servo. The fast shutoff time is necessary to switch the magnetic field gradient to 3 Gauss/cm for loading into the second stage MOT. Residual magnetic fields at the center of the chamber are compensated by three feedback-stabilized pairs of magnetic coils (X, Y, Z). The horizontal coil pairs (X, Y) are removed by 65 cm from the chamber center to prevent limiting the optical access and they allow compensation of magnetic fields up to several Gauss.

5.4.2. Blue laser & repumps

A schematic view of the laser beams and magnetic coils relevant to the blue MOT from the top of the vacuum chamber is shown in the central part of Fig. 5.5. The blue light for Zeeman slower and blue MOT is generated by second-harmonic generation (SHG) from infrared light at 921.723 nm, as depicted in the top left inset of the figure.

Diode laser & Tapered Amplifiers. The infrared laser is an AR-coated diode by Eagleyard[4] in a Littman external cavity geometry. We use a JILA laser controller (Jan Hall's highly stable current controller, JILA standard temperature controllers for base and diode mount) to drive the laser diode. Typically, diodes are mounted in Thorlabs collimation tubes and are collimated with aspheres. The C230TME-B aspheric lens works well with most IR laser diodes. Gratings are typically Edmund ruled gold gratings (1200 lines/mm) for IR wavelengths and Optometrics blazed holographic gratings (1200 or 1800 lines/mm) for red wavelengths. The feedback mirror is held in a JILA mirror mount and we use a small Thorlabs AE0203D04F piezoelectric transducer (PZT) to tune the horizontal mirror tilt. We use a reasonably mechanically stable but very versatile mechanical design that holds the diode, grating, and feedback mirror, originally designed by T. Ido. The diode head is temperature-stabilized with a thermoelectric cooler (TEC) and typical diode temperatures are in the range of $16 - 30$ °C. The lower limit is set by the yearly humidity cycle in Boulder, where the dew point can reach $\sim$16 °C in August. The diode mount baseplate is separately temperature-stabilized with a resistive heater to $\sim$5 °C higher than both room temperature

---

[4]Eagleyard AR-coated ridge waveguide laser model number EYP-RWE-0940-08000-0750-SOT01-0000.
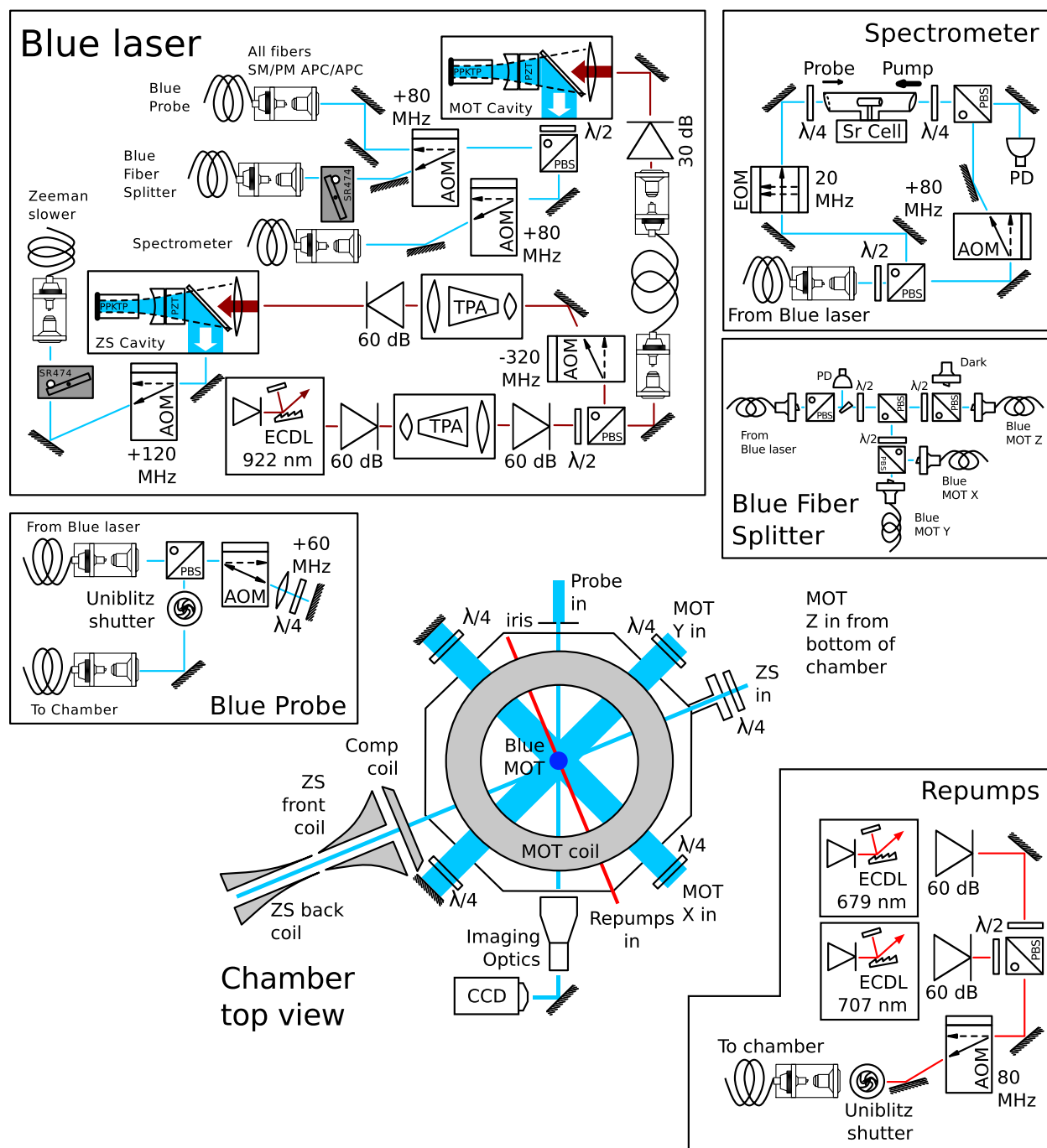
Figure 5.5.: Schematic overview of the 461 nm blue laser system for cooling and trapping. See the main text for details. The central part of the figure shows a schematic top view of the vacuum system, magnetic coils, and laser beams for the blue MOT. The top left part of the figure shows the blue light generation, distribution, and spectroscopic lock using saturated absorption. The bottom right inset shows the repump lasers necessary for blue MOT operation.

and diode head. The laser assembly sits in a simple enclosure and the beam exits through an AR-coated microscope slide or commercial laser window. We use cylindrical lenses mounted in cage systems to optimize the transverse beam shape. We typically use 60 dB of optical isolation on our diode laser setups to prevent optical feedback issues. The Conoptics isolators we use do not have μ-metal shielding, which makes them very magnetic, but also lot cheaper. Zero-order waveplates for any wavelength can be obtained from Tower Optical with short lead times.

The laser injects a 1.5 W Eagleyard tapered amplifier (TPA) chip in a custom mechanical flexure mount (the original version was designed by K.-K. Ni). A TPA is a semiconductor gain medium that widens adiabatically along the horizontal axis from input to output side. The reason for this design is that it can generate large output power while circumventing optical damage to the gain medium by keeping the laser intensity constant. The downside of this approach is that the output beam shape of a typical TPA chip is square and shows vertical stripes in addition to a diffuse background due to amplified spontaneous emission (ASE). The ASE background can be attenuated by coupling the light into a single-mode optical fiber.[5] To make the large optical power useful, it needs to be shaped and collimated. We find that the Thorlabs C230TME-B aspheric lenses also work well for focusing a circular beam into the TPA and collimating the output along the vertical axis. The horizontal axis needs to be carefully collimated with an additional cylindrical lens. Although we have not managed to break a TPA chip with backreflections, we typically tilt the collimating optics and use $30 - 60$ dB of optical isolation as well. To optimize coupling of TPA light into an optical fiber, it helps to mount the collimating cylindrical lens on a linear translation stage.

The TPA output power can fluctuate quite drastically, but this seems to be mostly determined by the chip itself, and only to a lesser degree by the current stability of the power supply. The intensity fluctuations can be servoed out by fast feedback to the TPA current

---

[5]For the optical clock experiment, the broad ASE frequency spectrum in the TPA-amplified optical lattice light can become important, especially in a non-retroreflected lattice. High-efficiency transmissive gratings or a narrow bandwidth optical filter placed before the optical fibers can reduce the ASE problem drastically.

using e.g. a shunt transistor. For the blue laser, we generally intensity-servo the SHG light directly because the SHG process introduces additional kHz-level noise. Although the chip temperature matters, temperature stability is not nearly as critical as for a typical laser diode. For these reasons, we use commercial Thorlabs current and temperature controllers with our TPAs. The temperature controller drives a large-area TEC beneath the TPA mount to keep it stable slightly below room temperature.

Doubling Cavities. The infrared light is frequency-doubled in two linear build-up cavities using periodically-poled potassium titanyl phosphate (PPKTP). The Sr2 system uses a similar cavity design but based on potassium niobate ($KNbO_3$). For a linear cavity design, one crystal surface is coated with a high-reflective coating and forms one of the mirror surfaces of the cavity [152]. The only other optical element necessary is a concave input coupler that is highly reflective at the fundamental and transmissive at the second harmonic which makes such a setup much simpler than the typical bow-tie geometry. Because the crystal itself functions as a cavity mirror, the SHG process has to be temperature-tuned. For $KNbO_3$, the phase-matching temperature is around 150 °C, close to the depoling temperature. In addition, there seem to be no TEC elements that can work at these temperatures and we use a (unipolar) resistive heater instead. One expects better temperature stability and servo bandwidth with a (bipolar) TEC at lower phase-matching temperatures. PPKTP has a phase-matching temperature around 30 °C and high-efficiency SHG in a bow-tie doubler has been demonstrated by the Paris group using a PPKTP crystal by Raicol [52, 153]. This success inspired us (and other groups) to try PPKTP in their doubling systems. Unfortunately, many groups have found that KTP-based SHG is not particularly reliable, mostly because of an effect called gray-tracking [154–158]. This process is widely observed but poorly understood in cw operation, and similar effects in other types of crystals go by the names of GRIIRA (green-induced IR absorption), BLIIRA (blue-induced IR absorption), formation of color centers, etc. The effect is very drastic: initially, the SHG process is very efficient and the SHG mode is a perfect TEM_{00} with high power. Depending on the amount of fundamental power used, the efficiency drops drastically within a few minutes to hours. The

SHG mode starts to show dark striations and eventually, one can observe those dark regions drifting around, which points to fluctuations on thermal timescales. Even with continual readjustments to the crystal temperature, the efficiency keeps dropping until the output becomes useless within a few hours.

Our observations are consistent with findings that gray-tracking is much reduced when operating KTP at higher temperatures [159]. One of the hypotheses for the origin of gray-tracking is that color centers are formed in high-fundamental-intensity regions of the crystal. The color center formation is also temperature dependent and the color centers preferentially absorb the second harmonic. Since the linear buildup cavity contains a standing wave with alternating high- and low-intensity regions, the color center formation should be much more severe than in the bow-tie configuration. Even with a fast temperature servo, these local temperature inhomogeneities cannot be removed which is consistent with the dark striations in the second harmonic mode.

The doubling efficiency can be restored by realigning the cavity such that a different region in the crystal is used in the SHG process. In addition, heating the crystal up to $\sim 100\,°C$ over a full weekend seems to return it to its prior state. Unfortunately, the depoling temperature for PPKTP is around $150\,°C$, and there seems to be no particular advantage in using a high-temperature phase-matched PPKTP crystal over $KNbO_3$. To work with the system at hand, we have added a small translation stage underneath the crystal mount that allows simple adjustments to the cavity alignment. In combination with the overnight heating procedure, the current crystals seem to work. Nevertheless, gray-tracking limits the output power of each doubling cavity to $100 - 120$ mW.

More recently, commercial SHG doubling systems have become available. Many groups have bought the (fairly expensive) Toptica SHG system that seems to produce several hundred mW of 461 nm reliably. Even more recently, NEL has started to sell a fiber-coupled periodically-poled lithium niobate (PP $LiNbO_3$ or PPLN) waveguide doubler for about \$10k [160]. With input powers of ~ 350 mW (IR output power measured by tuning the temperature off resonance), the doubler reliably produces ~ 50 mW of second harmonic

light. We have been using one of these devices for a few months and it seems to be very reliable so far. Unfortunately, only long term use will show whether the doubling efficiency degrades over time. Nevertheless, both the price and the operational simplicity of single-pass doubling over cavity-enhanced SHG makes this a very attractive alternative.

MOT beams. The SHG cavity length is stabilized to the IR laser by modulating the laser current at $\sim$30 MHz. The cavity linewidth is larger than the sideband spacing and we demodulate the IR transmission at the modulation frequency to obtain a Pound-Drever-Hall-like error signal. The cavity input coupler is mounted on a tubular PZT of matched diameter and we apply feedback to the PZT voltage. Once the cavity length is locked, cw blue light is available and is split off from the IR light with a 45° dichroic mirror in front of the input coupler.

The wavelength of the blue light is stabilized to a saturated absorption spectrometer (see top right of Fig. 5.5) based on a Hamamatsu Sr hollow cathode lamp driven by a high-voltage power supply. The probe arm is modulated with an electro-optic modulator (EOM) at $\sim$20 MHz. The pump arm contains an acousto-optic modulator (AOM) that shifts the pump by +80 MHz with respect to the probe. The AOM RF signal is also chopped at $\sim$1 kHz for lock-in detection of the spectroscopic signal. The error signal derived from the lock-in detection allows stabilization of the blue laser wavelength by slow feedback to the IR laser PZT (or current). Once feedback is applied, the blue light at the entry of the spectrometer is now at -40 MHz with respect to the ${}^1S_0$-${}^1P_1$ transition in the Sr cell. Tracing back, the blue light at the exit of the MOT cavity becomes detuned by -120 MHz.

The +80 MHz AOM in front of the optical fiber to the blue fiber splitter makes the blue MOT beams -40 MHz detuned from ${}^1S_0$-${}^1P_1$ in the Sr cell. All optical beams are transferred to the vacuum chamber via single-mode polarization-maintaining (SM/PM) angle-polished (APC/APC) optical fibers. The beams can be switched on fast timescales with AOMs and are shuttered mechanically in addition. The mechanical shutters are necessary to prevent leakthrough into the diffracted AOM order. The human eye is very sensitive to 461 nm, and leakthrough can easily be seen by looking directly into the output of the optical fiber with

the AOM turned off. Even a few photons of 461 nm will affect optical dipole trap lifetimes drastically. The optical cavity length locks are fairly sensitive to acoustical vibrations. For this reason, the blue laser setup was built on a honeycomb breadboard isolated from the optical table by rubber stoppers. This setup provides enough mechanical isolation to step on the optical table without unlocking the cavities. However, placing the fast and very loud Uniblitz mechanical shutters next to the cavities makes the locks oscillate for hundreds of ms, even when not mounting them directly to the blue laser breadboard. The new SRS SR474 shutters do not have a coil-driven blade design, but rely on a torque-balanced bar that swings in front of the shutter opening. The motion of the bar is PID controlled and the shutter speed can be set. We find that fast speeds still introduce vibrations, but that we can mount these shutters on the blue laser breadboard next to the doubling cavities when using one of the slower settings ($\sim$40 ms shutter time).

The beam for the blue MOT is split into three arms using a Schäfter+Kirchhoff cage-mounted free space splitter based on waveplates and polarizing beam cubes. The fiber splitter is a custom design that uses set screws in the fiber holders to point the beams. The splitter is mounted to the optical table in good thermal contact and it is contained in a plastic enclosure. The main advantage of the design is that it (in principle) does not have to be touched after initial alignment. Even though there are no thumb screws in the design, we find that slow mechanical drifts deteriorate the fiber coupling between input and output on long timescales. The transfer efficiency has degraded over the last three years and we have not been able to recover it completely even with careful walks of the set screws. We conclude that a full alignment of these systems is necessary every one or two years. To do that, one needs CCD cameras that can be mounted to the output ports so that the different arms can be aligned simultaneously by turning the set screws systematically. It remains to be seen if this procedure can be done repeatably and without too much time investment. Nevertheless, with the fiber splitters we use for both the blue and red MOT beams, we typically do not have to align the MOT beams at all.

Repumps. As mentioned in Sec. 1.1, we use repumping lasers on the $^3P_2$-$^3S_1$ and $^3P_0$-$^3S_1$

transitions at 707 and 679 nm, respectively. The light is produced by two laser diodes (shown in the bottom right part of Fig. 5.5), similar to the 922 nm laser described above.

Until recently, the only 707 nm diode available was an AR-coated Toptica model. Unfortunately, 707 nm is a window of low efficiency for InGaAs-based laser diodes and even with continual improvements over the last few years this model had low power and was much less frequency-stable than all other diodes we use. Since then, we have switched to the new Hitachi/Opnext HL7001MG diode with higher power and nominal wavelength of 705 nm. This diode seems to be very reliable and is also used in the 698 nm spectroscopy lasers for the optical clock experiments. The 679 nm light is produced by an AR-coated Hitachi/Opnext HL6750MG.

Each day, the wavelength of the repump lasers is set to a particular value on a wavemeter. The lasers are then tuned until we observe the largest enhancement in blue MOT fluorescence. Without further stabilization, the laser wavelength is stable enough for several hours of operation. Both lasers are combined and launched into the same optical fiber. Since enough optical power is available, we form a 1 cm diameter beam from a telescope mounted directly to the vacuum chamber and no alignment is necessary.

Probe beam and absorption imaging. The zeroth order of the MOT AOM is coupled into another fiber and goes to a probe setup closer to the optical chamber (see mid left of Fig. 5.5). The probe beam is used for absorption imaging of the atomic clouds in either the red MOT or the dipole trap. A full overview of this commonly used technique is beyond the scope of this Section, but good technical references to learn about the relevant details are [161–163]. Appendix A summarizes some other relevant considerations.

The probe beam setup uses a double-passed AOM and a fast Uniblitz shutter and enters a final fiber going to the "Probe in" port of the vacuum chamber. The imaging optics are a customized version of the Infinity Photo-Optical K2/SC long working distance microscope. The front lens of the microscope is at ∼16 cm from the atomic cloud. We tested the microscope with transmissive test targets and blue interference-filtered white light (10 nm bandwidth) and recovered imaging resolutions of 4 μm even when including a vacuum viewport (AR

coated as the ones on the vacuum chamber). Due to spatial constraints, the microscope is separated into the imaging lenses and a custom eyepiece mounted to the CCD camera, with a mirror in between.

We use an Andor iKon-M CCD camera with 1024×1024 pixels of 13 μm width. The imaging system magnification corresponds to 2 μm/pixel in the image plane. All our images so far are consistent with the 4 μm test-target resolution. The CCD chip on these cameras can be TEC-cooled to -70 °C without additional water cooling. Electronic noise at these temperatures is drastically reduced, but the cold temperatures require the chip to be in-vacuum. One of the main technical issues in absorption imaging with coherent laser light is fringing induced by interference between optical surfaces in the imaging path. The vacuum window covering the CCD chip is especially susceptible to fringing. The window in our camera is custom AR coated for both 461 nm and 689 nm and the front surface is wedged at 1°. With these precautions, fringing was very significantly reduced versus a camera coated for Rb absorption imaging that we had been using previously. The fringes change very slowly with thermal drifts in the optical surfaces responsible. In principle, the fringe patterns can be recognized and removed using image recognition techniques. We found that we could reduce the residual fringe contrast by a factor of 3-4, but that the technique requires about 30 images taken under the same conditions to work reliably. With the AR coated wedged window, fringing has been much less of an issue.

Absorption images are taken in the camera's "Fast Kinetics" mode that allows splitting the CCD into several regions. Images can be taken in the first region and then shifted to the adjacent region with high speed. The next image can then be taken and the CCD chip is shifted again. In this way, we take three images in quick succession. To prevent contamination of the earlier images in the sequence, two thirds of the CCD chip are masked off with a razor blade on a linear translation stage in a custom part mounted to the front of the camera. A 1 inch diameter Uniblitz shutter is mounted to the front of the razor blade mount and the K2/SC eyepiece mounts to the shutter. The eyepiece also contains a CVI 10 nm bandwidth interference filter centered at 461 nm to reduce stray light contamination.

The filter does not seem to influence the shape of the absorption images we measure.

To initiate taking an absorption image, a dark-field image is taken first and the image is shifted once while the camera shutter is closed. The actual absorption image of the atomic cloud is taken next. The camera shutter opens first ($\sim$8 ms opening time), and the probe shutter opens 3 ms before the probe AOM is gated for 50 μs to obtain the shadow image of the atomic cloud. The probe shutter closes but the camera shutter remains open as the atomic cloud drops away under the influence of gravity and the image is shifted. The probe shutter opens again and the AOM is gated to take the light-field image. Finally, the probe shutter closes, the camera shutter closes, and the full CCD is downloaded from the camera to the imaging program. We use a custom imaging program written in `C++` that processes, displays and stores the images on a file server. Using multithreading techniques, the program can handle the full 1024×1024 pixel images ($\sim$2.5 Mb 16-bit TIFF) at $\sim$1 s experimental cycles.

The double-pass AOM, the fast shutter, and the final fiber in the blue probe setup are used to minimize the effect of leakthrough of blue photons towards the atoms and the imaging system. Leakthrough becomes a problem because of the finite probe shutter opening time and charge builds up for each photon impinging on the CCD. The camera provides a cleaning mode that continuously shifts the CCD chip to remove these charges. This method is not particularly useful in Fast Kinetics mode, however, since it cannot handle charge buildup in between taking partial images. We tested for leakthrough streaking (blue photons hitting the camera while the image is shifted) in between taking the shadow and light-field images by running the imaging sequence without triggering the AOM. With the fast shutter and the double-pass AOM, this effect was reduced to negligible levels.

Another important systematic effect in absorption imaging is forward scattering of blue photons anywhere in the imaging path after the light has interacted with the atomic cloud [162]. We found that this effect can be drastically reduced by irising down the probe beam until only a small region around the atomic cloud is illuminated on the CCD chip.

5.4.3. Red lasers

The laser light for interacting with the $^1S_0$-$^3P_1$ transition is produced by diode lasers at 689 nm. The laser diodes used are Hitachi/Opnext models HL6738MG, AR coated in house. The frequency stability necessary to interact with the 7.5 kHz wide intercombination line is derived from the Sr2 master laser described in Refs. [11, 12]. The top left part of Fig. 5.6 shows a schematic overview of this setup. The red master laser (dotted inset) is another diode in Littman geometry that is stabilized to a high-finesse reference cavity and a saturated absorption spectrometer (similar to the blue spectrometer above) based on a heated Sr cell filled with Ar buffer gas [11]. For our purposes, we extract a laser beam from the master laser that is at -40 MHz detuning with respect to $^1S_0$-$^3P_1$ in the Sr cell. In the Figure, α denotes the laser used for the $^1S_0$-$^3P_1$ MOT, and β is used for the photoassociation experiment. The MOT light is delivered to the vacuum chamber by another Schäfter+Kirchhoff fiber splitter (see middle right of the Figure) that also supports a second arm for a stirring laser in ^{87}Sr. For both α and β, we form an optical beat note with the master light and phase-lock each laser by fast feedback to the laser diode current. For long-term stability, slow feedback to the laser PZT actuator is also applied.

The local oscillator frequency for each phase-lock can then be tuned to set the detunings of each laser. The red MOT in ^{88}Sr requires only a single laser, but its detuning needs to change from a broadband modulation to a single frequency [11, 18]. We use the following scheme to transfer atoms from the blue MOT to the red MOT. As the light from Zeeman slower, blue MOT beams, and repump lasers is turned off with AOMs and mechanical shutters, the MOT field gradient is switched from 50 Gauss/cm to 3 Gauss/cm. The gradient is kept constant for 80 ms and then is ramped linearly to 10 Gauss/cm within 125 ms and kept at this value for another 56 ms. At the end of this sequence, the magnetic field gradient and the red light are switched off and atoms are loaded into the optical dipole trap. Residual magnetic fields are zeroed by three pairs of compensation coils (see Figure).

As the magnetic field gradient switches from 50 Gauss/cm to 3 Gauss/cm, α light is applied to the atoms and the α local oscillator is modulated to cover the Doppler-broadened velocity
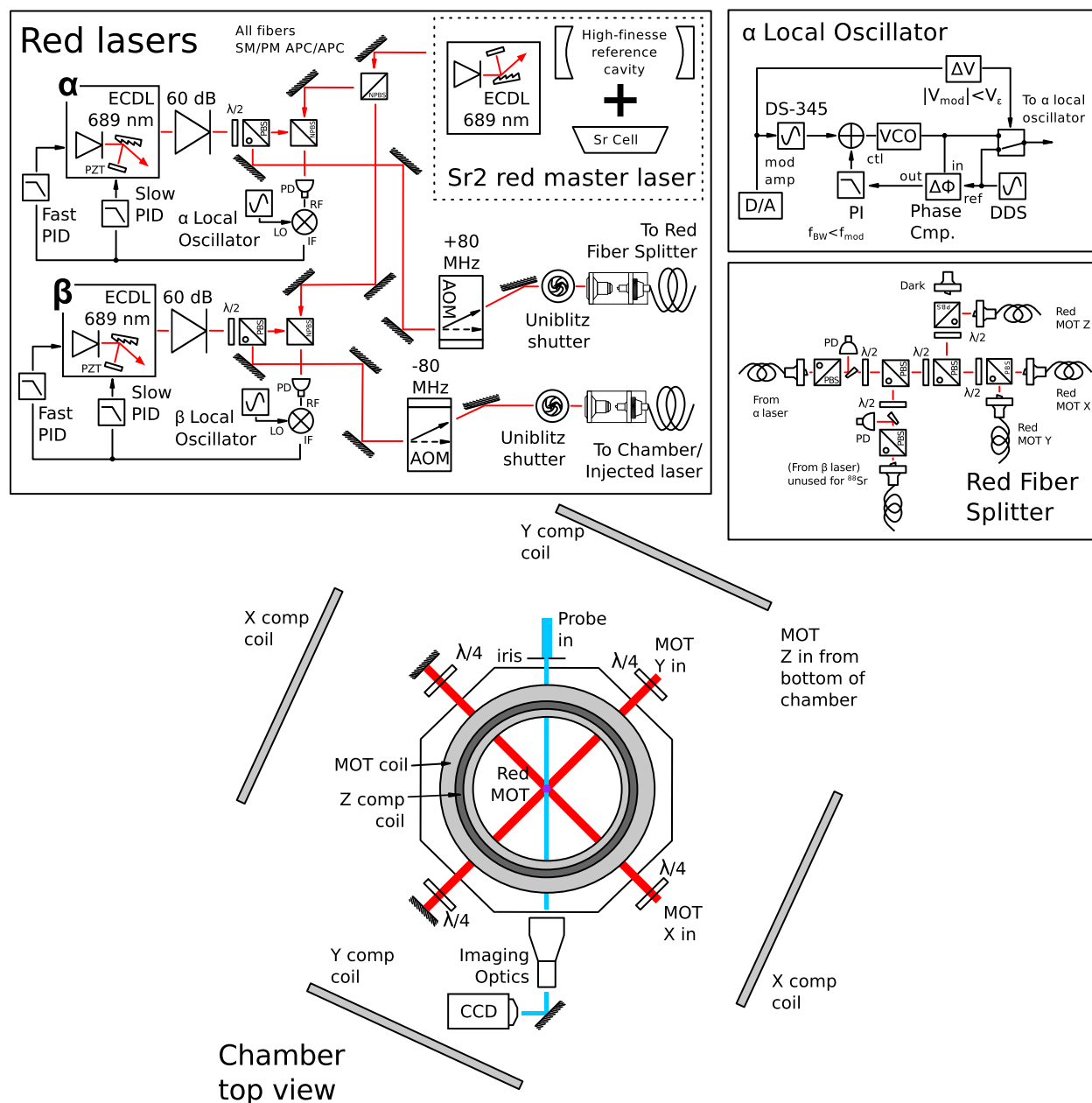
Figure 5.6.: Schematic overview of the 689 nm red laser system for cooling and trapping. See the main text for details. The top part of the figure shows a schematic of the phase locked diode lasers. The bottom part shows the magnetic coils and laser beams in a schematic top view of the vacuum chamber.

profile in the ~1 mK atoms released from the blue MOT. The modulation is produced by the setup shown in the top right part of Fig. 5.6. An SRS DS-345 oscillator produces a sinusoidal voltage at 36 kHz and its amplitude is controlled by an analog voltage from the control computer. The sinusoidal voltage is summed into the control voltage of a VCO at ~120 MHz. The mean frequency of the VCO is stabilized by slow PI feedback to the control voltage with a bandwidth that is smaller than the modulation frequency from the DS-345. The error signal for the feedback loop is generated by a digital phase detector that compares the output of the VCO to a DDS oscillator. The frequency of the DDS oscillator is controlled by the control computer and it is referenced to the lab frequency reference (a Wenzel crystal oscillator). A window comparator checks whether the modulation amplitude is small and switches between the DDS oscillator and the stabilized VCO automatically. In this way, the α local oscillator is a frequency-stabilized signal at 120.7 MHz with a kHz-level sinusoidal frequency modulation. If the modulation is small, the signal becomes a very clean digitally synthesized sine wave automatically.

As the magnetic field ramps between 3 and 10 Gauss/cm, the modulation peak-to-peak amplitude is decreased from 2.7 MHz and the center frequency is tuned closer to the atomic line so that the blue edge of the modulation spectrum is fixed at -700 kHz with respect to $^1S_0$-$^3P_1$. At the end of the magnetic field ramp, the modulation amplitude is zero and α remains at a single detuning of -700 kHz.

The second laser β is used for the photoassociation experiment described in this Chapter, but will function as a stirring laser in future experiments with ^{87}Sr [11, 20]. The local oscillator is derived from a referenced analog signal generator controlled by the control computer. The phase-lock easily supports local oscillator jumps on the 10 MHz level and we can tune β by about 1.5 GHz by slight adjustments to the PID gain. We find that tuning the local oscillator frequency is much more reliable than actuating on the AOM before the optical fiber.

5.4.4. Dipole trap & photoassociation lasers

The optical dipole trap is formed by two crossed laser beams at 1064 nm. The light is produced by a highly frequency-stable (kHz bandwidth) Innolight Mephisto. The setup is shown schematically in the top left part of Fig. 5.7. The Mephisto produces a linearly polarized beam and we use 30 dB of free-space optical isolation (OFR/Thorlabs) before coupling the beam into the input fiber of a Nufern fiber amplifier. When seeded with $\sim$100 mW of light, the amplifier produces up to 40 W cw light at 1064 nm and maintains a frequency bandwidth of 10 kHz. The output fiber is a large-mode-area armored optical fiber spliced to a water-cooled 30 dB fiber isolator. The setup produces a fairly good TEM_{00} with good linear polarization. The amplifier itself is contained in a water-cooled rack-mounted box. Due to space constraints and safety considerations, the laser system was built on an optical table enclosed in blackened aluminum sheeting removed from the main experiment.

The setup shown in Fig. 5.7 splits the amplifier's output into two optical beams that are controlled by two AOMs and coupled into two SM/PM APC/APC optical fibers that deliver the light to the vacuum chamber. The fiber coupling makes it necessary to add another 30 dB of free space isolation to prevent the amplifier from shutting down due to backreflections. The high optical power makes this system qualitatively different from all other laser systems in this experiment. The mirrors used are high-power Nd:YAG mirrors from Thorlabs that support both $0°$ and $45°$ incidence angles. All lenses and beam cubes are AR coated for 1064 nm and lenses made of fused silica are used when possible to prevent beam pointing drifts at high powers in BK7. Thermal power meters need to be used. Unfortunately, the amplifier mode shape depends on the amplifier current and we run the amplifier close to saturation at 40 A. After $\sim$8 months of everyday usage at this current, we found that the total output power has degraded to $\sim$32 W. Working with such high powers is impossible without having some way to adjust the power down to manageable levels. For this purpose, we added combinations of $\lambda/2$ waveplates, polarizing beam cubes and high power beam dumps to harmlessly divert power without changing the mode profile.

We use high efficiency IntraAction AOM-302AF3 glass AOMs at 30 MHz with opposite
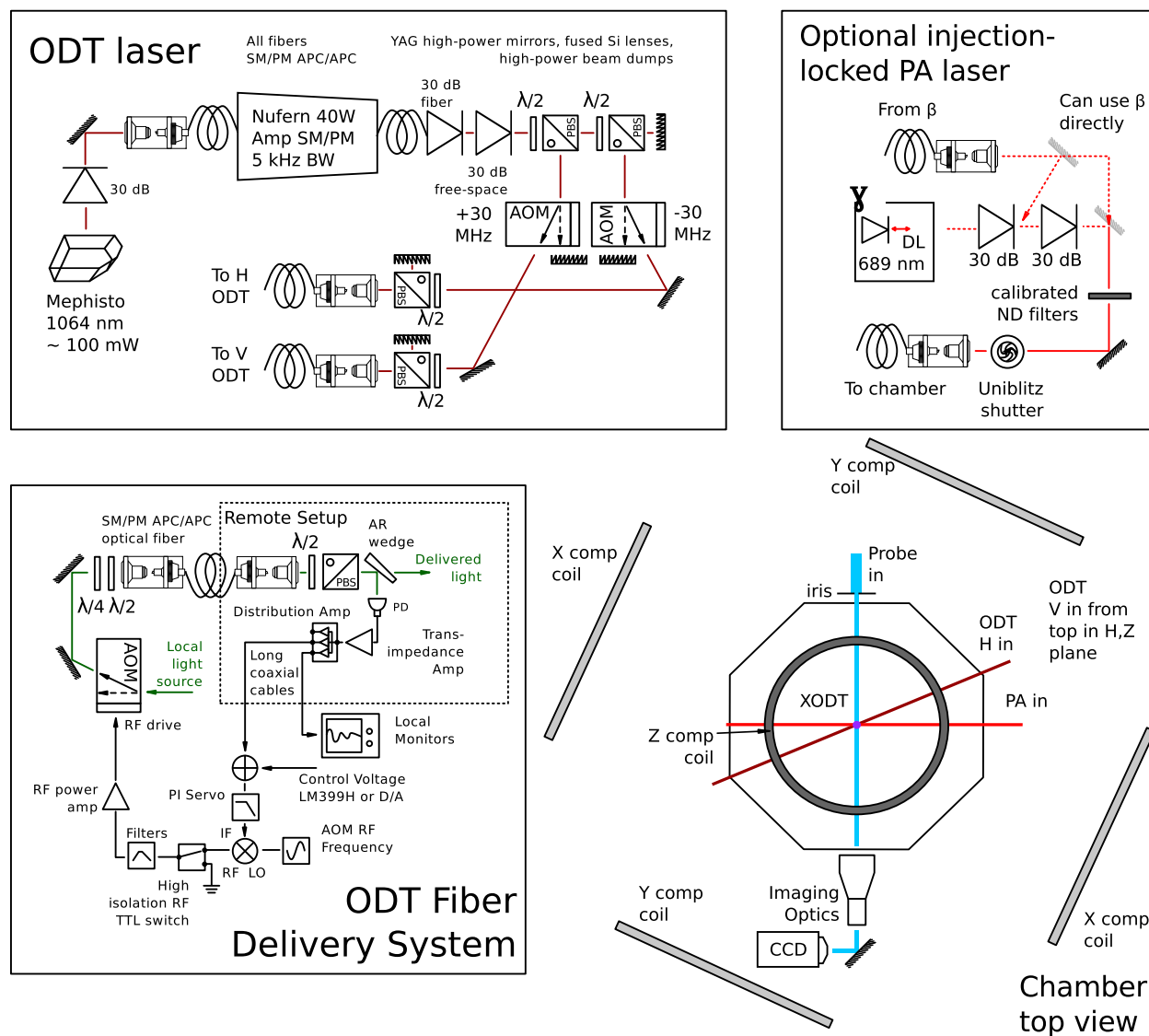
Figure 5.7.: Schematic overview of the 1064 nm infrared laser system for the optical dipole trap (ODT). See the main text for details. The left part of the figure describes the 1064 nm system and delivery system. The top right inset describes an optional injection-locked 689 nm laser to enhance the PA power available. The bottom right part shows a schematic top view of the vacuum chamber relevant for the OFR experiment.

orders to separate the optical frequency of both beams by 60 MHz. The AOMs are also used to switch off the dipole trap beams and stabilize the power transmission through the optical fibers. We have used these modulators very successfully for dipole traps at 914 nm and optical lattices at 813 nm and obtained diffraction efficiencies above 90%. However, we found that for high intensities, the diffraction efficiency tends to degrade on thermal timescales. We added water-cooled baseplates to the AOMs to counteract this effect. Even so, the AOM glass gets permanently damaged on timescales of several hours to days by optical powers above 15 W (even with $2-3$ mm beam diameters). Specialized YAG modulators that handle much higher intensities are available, but we found that other processes limit the usable power and continued to use the IntraAction AOMs.

Since free-space propagation to the experiment was not an option due to spatial constraints, we had to bridge the distance with optical fibers. We required single-mode and polarization-maintaining transmission to guarantee a well-defined and reproducible optical trap at the center of our chamber. This requirement limits the transmissible power severely. Power transmission through single-mode optical fibers is limited mostly by stimulated Brillouin scattering (SBS), where light is scattered off phonons in the optical fiber [164]. Above a certain threshold input intensity the transmitted power saturates and the rest is scattered back. The SBS threshold scales linearly with fiber length length and is inversely proportional to the mode area. Typical Panda SM/PM fiber for 1064 nm (e.g. Nufern PM980-XP) has an effective mode field diameter (MFD) of about 6 μm. We find that one can transmit about $5-6$ W through 5 m of this fiber. This is consistent with our finding that we could transmit about 1 W through 25 m of fiber when trying to transfer a beam from an adjacent lab. Forcing more power into the fiber can result in slow degradation of the core, making the fiber unusable. Specialized large-mode-area (LMA) fibers such as the one spliced to the output of the fiber amplifier support higher SBS thresholds. The mode area is limited by the desired spatial mode quality of the transmitted light. With larger mode area and longer fiber length, more light leaks into higher transverse modes. We have tried working with several LMA fibers from Nufern, and have transmitted up to 12 W through 5 m of several

fiber types with reasonable beam quality. At these powers, however, stable beam alignment into the fiber tip becomes extremely critical. Even with the fiber launch in the enclosure and careful alignment, thermal fluctuations cause the beam pointing to vary slightly. At these powers, any deviation from optimal alignment causes runaway heating in the fiber tip. Typical FC connectors are constructed by epoxying the fiber core into the connector which is then polished at the desired angle. With large heat load, the epoxy melts up to several cm along the fiber and flows over the fiber core at the tip. The fiber loses transmission and the epoxy burns the tip. We recleaved the fiber and machined a custom metal fiber holder without epoxy. However, thermal contact between fiber tip and holder is still important and in the subsequent test, the fiber tip itself melted. We decided to stay with the current setup for the present experiment, but would recommend setting up such high power laser sources with free-space coupling to the experiment if space allows. The great advantage of fiber delivery are the well-defined beam profile and the spatially defined delivery point with respect to the target at the center of the chamber. By rigidly mounting the fiber tip, pointing fluctuations can be very small.

The fiber delivery system is sketched in the bottom left part of Fig. 5.7. We find that adding both a $\lambda/4$ and $\lambda/2$ waveplate is necessary to compensate for slow changes in the fiber birefringence over time scales of several hours, even when the polarization was carefully aligned with the fiber axis. The polarization at the output of the fiber is defined by the mount, but we find it expedient to include another $\lambda/2$ waveplate to optimize transmission after the fiber was unplugged. A polarizing beam cube defines the polarization completely and allows servoing on the transmitted intensity independent of polarization drifts. An AR-coated wedge picks off a small fraction of the intensity which is detected on a photodetector (PD). The whole fiber launcher, waveplates, cube, photodetector, and beam diameter adjusting lenses (not shown) are built in a cage-mounted system for mechanical stability. On the local end, the photodetector voltage is compared against a stable reference and a PI servo feeds back on the amplitude of the RF signal that drives the AOM. We also include a high-isolation RF TTL switch for switching times limited only by the acoustic wave transfer time through

the AOM crystal. Most optical fibers shown in Figs. 5.5 and 5.6 have similar setups to the one shown here.

Finally, the delivered ODT beam has to be shaped to provide the desired focus at a given distance from the fiber tip. The beam shape can be measured and optimized easily with a USB CCD camera on a linear translation stage in combination with a program that displays and fits the mode in real time. To be useful for optimizing beams in a real experimental setup, it is important that the CCD chip is very small and lightweight; DataRay sells such a system. For almost the same price as the Thorlabs singlets, good 1 inch diameter singlets or achromats are available from Optosigma or Newport. Lens quality matters especially for good 461 nm beam quality over long distances. Lens quality becomes less crucial with larger diameter and longer wavelength, and we found that the 2 inch diameter IR achromats by Thorlabs produce reasonably aberration-free foci down to waists of 15 μm at the distances required to focus on the atomic cloud from outside the vacuum chamber.

We also built an additional 689 nm diode laser that can be injection-locked by the light delivered from β for higher PA intensities. The setup is shown schematically in the top right part of Fig. 5.7. The PA intensity is adjusted by placing neutral density filters before the final fiber transmission to the chamber. This setup allows changing the PA intensity by well-defined amounts over many orders of magnitude without changing the delivered PA beam pointing and transverse mode.

5.4.5. Dipole trap geometry

As discussed in section 5.4.3, we prepare ^{88}Sr atoms in a MOT operating on the ^{1}S$_0$-^{3}P$_1$ intercombination transition and obtain atomic clouds at typical temperatures of a few μK. While the MOT is operating, the atomic cloud is overlapped with the dipole trapping beams at $\lambda_{\text{XODT}} = 1064$ nm. After the MOT is switched off, $\sim 5 \times 10^4$ atoms remain in the crossed dipole trap (XODT). The trapping geometry is shown in Fig. 5.8, where the XODT is formed by a horizontal (H) and a vertical (V) beam which intercept in the $\hat{x} - \hat{z}$ plane. The trapping beams have $1/e^2$ waists $w_H = 63$ μm and $w_V = 53$ μm, respectively.
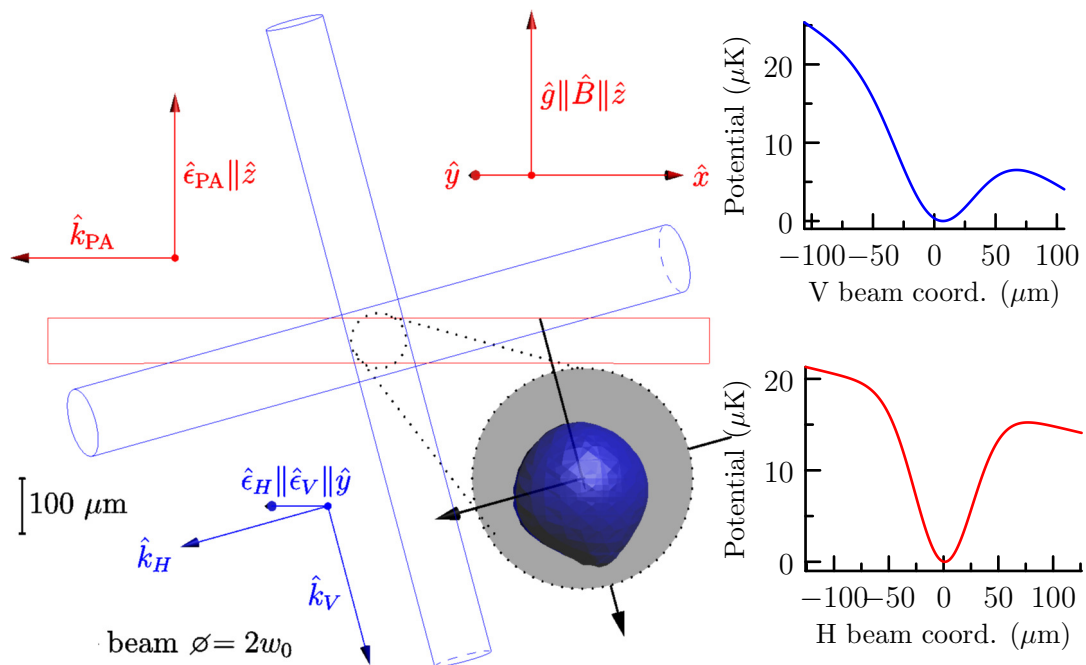
Figure 5.8.: Geometry of the experiment in the absorption image plane. The directions $\hat{x}$, $\hat{y}$, and $\hat{z}$ define the lab frame, where both gravity $\hat{g}$ and bias magnetic field $\hat{B}$ are parallel to $\hat{z}$. Symbols $\hat{k}$ are beam directions, and $\hat{\epsilon}$ are beam polarization vectors, where subscripts H, V, and PA indicate horizontal, vertical, and PA beams. H and V Gaussian beam profiles are shown in blue outline, PA Gaussian beam profile in red outline.

The drawing is shown in the focal plane of the absorption imaging system discussed in Sec. 5.4.2 and the H-V trap is always adjusted to the same spot with respect to the MOT before optimizing the loading from MOT to dipole trap for the day. Guaranteeing that the XODT forms at the foci of the H and V beams is not critical because of their large Rayleigh ranges $z_R^i \equiv \pi w_i^2 / \lambda_{\mathrm{XODT}} > 8$ mm, and the Gaussian beam isosurfaces at the beam waist are almost cylindrical (blue outlines).

Gravity points along $-\hat{z}$ and sets the trap depths of ~ 7 μK and ~ 15 μK along V and H. The two graphs on the right hand side show cuts through the model potential, which has been adjusted to match the trap frequencies measured via parametric resonance. An isosurface (dark blue) of the model potential at 7 μK is shown in the zoomed-out portion. The model potential is given by

$$U(\boldsymbol{x}) = U_H(\boldsymbol{x}) + U_V(\boldsymbol{x}) + m_{\mathrm{Sr}} g z, \tag{5.23}$$

where U_i are the Gaussian beam potentials in the lab frame, given by

$$U_i(\boldsymbol{x}) \equiv -U_T^i \exp\left\{ -\frac{2}{w_i^2} \left([\hat{\boldsymbol{\epsilon}}_i \cdot \boldsymbol{x}]^2 + [(\hat{\boldsymbol{k}}_i \times \hat{\boldsymbol{\epsilon}}_i) \cdot \boldsymbol{x}]^2 \right) \right\}. \tag{5.24}$$

The trapping beams point in the directions

$$\hat{\boldsymbol{k}}_H = -\cos\theta_H \hat{\boldsymbol{x}} - \sin\theta_H \hat{\boldsymbol{z}},$$
$$\hat{\boldsymbol{k}}_V = -\cos\theta_V \hat{\boldsymbol{z}} + \sin\theta_V \hat{\boldsymbol{x}}, \tag{5.25}$$

with $\theta_H = 16.0°$ and $\theta_V = 14.4°$. Both beams are linearly polarized along $\hat{\boldsymbol{\epsilon}}_H = \hat{\boldsymbol{\epsilon}}_V = \hat{\boldsymbol{y}}$, and their optical frequency differs by 60 MHz so that we can neglect any optical interference patterns distorting U. A bias magnetic field of $B_z \simeq 100$ mGauss defines the atomic quantization axis.

The absorption image plane is spanned by $\cos\frac{\pi}{8}\hat{\boldsymbol{x}} - \sin\frac{\pi}{8}\hat{\boldsymbol{y}}$ and $\hat{\boldsymbol{z}}$. The PA beam (red outline) propagates in the $\hat{\boldsymbol{x}} - \hat{\boldsymbol{y}}$ plane the along the horizontal axis of the absorption imaging system,

$$\hat{\boldsymbol{k}}_{\mathrm{PA}} = -\cos\theta_{\mathrm{PA}}\hat{\boldsymbol{x}} + \sin\theta_{\mathrm{PA}}\hat{\boldsymbol{y}}, \tag{5.26}$$

with $\theta_{\mathrm{PA}} = \pi/8$. The PA beam waist is $w_{\mathrm{PA}} = 41$ μm and it is linearly polarized along the atomic quantum axis $\hat{\boldsymbol{\epsilon}}_{\mathrm{PA}} = \hat{\boldsymbol{z}}$. Typical kinetic energies are 2-4 μK, and in-trap cloud FWHM are 45-55 μm. Although the PA beam FWHM $2\sqrt{2\ln 2} \times w_{\mathrm{PA}} \simeq 97$ μm is larger than the typical cloud FWHM, we use a density-averaged intensity $I_{\mathrm{av}} = \int d^3x\rho(\boldsymbol{x})I(\boldsymbol{x})/\int d^3x\rho(\boldsymbol{x})$ to characterize the PA intensity interacting with the atoms. Typical values are $I_{\mathrm{av}} \simeq (0.6 - 0.7) \times I_{\mathrm{pk}}$, where $I_{\mathrm{pk}} = \frac{2P}{\pi w_{\mathrm{PA}}^2}$ is the Gaussian beam peak intensity for total beam power P. The PA beam also adds to the optical trap slightly because of its relatively small detuning from the atomic transition. For large intensities and small w_{PA} and especially in a standing wave configuration, this effect can become important. The additional trap depth introduced by the PA beam here is typically < 0.1 μK and we neglect it.

5.5. Trap potential calibration

The ^{88}Sr sample is loaded from a thermalized distribution in the MOT into a conservative XODT potential. Although the sample is thermalized well by the MOT photons initially, the ^{88}Sr background scattering length is so small that the sample behaves as an ideal gas on experimental timescales. For this reason, inhomogeneities in kinetic energy persist and the ergodic gas dynamics are completely determined by the XODT potential. For the temperatures and typical trap depths considered here, the sample is trapped in the potential well defined by U. Nevertheless, the trap is not deep enough such that we can easily approximate it as harmonic. We calibrate the model potential by comparing its eigenfrequencies for measured beam powers against parametric resonance measurements for each axis.

The trap eigenaxes are determined by diagonalizing the symmetric curvature matrix (the Hessian) of the model potential around its minimum:

$$(\mathrm{Hess}\ U|_{\mathrm{min}})_{ij} = \frac{\partial^2 U}{\partial x_i \partial x_j}|_{\mathrm{min}}. \tag{5.27}$$

The eigenvalues of $(2\pi m_{\mathrm{Sr}})^{-1}\ \mathrm{Hess}\ U|_{\mathrm{min}}$ are the trap eigenfrequencies. The waists w_H and w_V used in the model potential are adjusted until the eigenfrequencies match the values obtained from parametric resonance measured along each beam axis. The waist values obtained

thus are consistent with the values measured outside the vacuum chamber when accounting for slight aberrations introduced by passing through the vacuum viewports. The vacuum viewports are anti-reflection coated for 461 nm, 690 nm, and 813 nm, since the vacuum chamber was designed for optical lattice clock experiments. The horizontal beam passes through a thin vacuum viewport at normal incidence and its intensity transmission coefficient at 1064 nm was measured as $T_H = 0.69$. The vertical viewport is made of much thicker fused silica than the horizontal viewport due to its large diameter. In addition, the vertical beam passes the viewport at θ_V and we measure $T_V = 0.58$. The beam powers entering the vacuum chamber are stabilized via feedback from photodetectors to acousto-optical modulators. The modulators are located before the optical fibers that transfer the 1064 nm light from the laser source to the vacuum chamber and are also used to switch off the trap to expand the atomic cloud for time-of-flight measurements. Typical optical powers before the vacuum chamber are $P_V = 1.15$ W and $P_H = 1.79$ W. The real part of the ${}^1S_0$ atomic polarizability when neglecting all but the ${}^1P_1$ contribution is Re $\alpha_{{}^1S_0}(1064 \text{ nm}) \simeq 239$ a.u. [11], where the atomic unit of polarizability is 1 a.u. $= 4\pi\epsilon_0 a_0^3$. The individual beam trap depth is then given by [165]

$$U_T^i = \frac{P_i}{\pi c \epsilon_0 w_i^2} \text{Re } \alpha_{{}^1S_0}(1064 \text{ nm}) \tag{5.28}$$

Taking the viewport transmission coefficients into account and using the typical beam powers and calibrated waists, we obtain

$$\hat{\boldsymbol{x}}_1 \simeq 0.984 \; \hat{\boldsymbol{x}} + 0.175 \; \hat{\boldsymbol{z}},$$
$$\hat{\boldsymbol{x}}_2 = \hat{\boldsymbol{y}}, \tag{5.29}$$
$$\hat{\boldsymbol{x}}_3 \simeq -0.175 \; \hat{\boldsymbol{x}} + 0.984 \; \hat{\boldsymbol{z}},$$

where we ordered the eigenaxes $\hat{\boldsymbol{x}}_i$ according to the lab frame axes they are closest to. The eigenfrequencies are

$$\{\nu_1, \nu_2, \nu_3\} \simeq \{219, 290, 187\} \text{ Hz}. \tag{5.30}$$

The potential along the 2-axis is the most harmonic since the transverse potential of both trapping beams adds to produce a very deep trap. The potential along the horizontal axis is

the next deepest, but becomes lopsided because of gravity. The potential along the vertical trap axis is very anharmonic and gravity introduces a single saddle point where atoms can escape (see Fig. 5.8). This asymmetry in trap depths along the trap axes produces a persistent inhomogeneity along the horizontal and vertical axes, even when loading the trap from a thermal sample in the MOT. Unless care is taken to align the XODT with respect to the MOT every day, the loading process does not prepare a comparable phase space distribution each day. The difference between potential minima in the MOT and the XODT determines the persistent kinetic energy inhomogeneities in the cloud. We developed a careful alignment procedure that set the relative position of MOT and XODT in the absorption image plane and then optimized the relative magnitudes of horizontal and vertical kinetic energies determined from time-of-flight measurements.

5.6. Modeling the phase-space distribution

To understand and model the initial atomic phase-space distribution, we performed Monte-Carlo simulations of loading the conservative model potential U with N classical particles from a thermal sample at a given temperature. Letting each atom in the sample evolve in the conservative trap for several trap oscillation cycles consistently produced inhomogeneous density distributions. For the relevant temperature range the resulting inhomogeneous density and momentum distributions consistently separated into symmetric distributions along each trap eigenaxis, since no thermalizing collisions were allowed to couple the different axes. We also find that each axial potential energy follows the corresponding axial kinetic energy faithfully and conclude that the trap is ergodic on timescales longer than a few trap oscillation cycles. The resulting phase space distributions fit well to independent Gaussian distributions along each trap eigenaxis. Nevertheless, it is not adequate to approximate harmonic confinement where the RMS axial cloud extent is proportional to the axial RMS velocity via the axial eigenfrequency. Even for typical temperatures of 3 μK, the cloud is large enough to explore the anharmonic parts of the trapping potential.

We model the density distribution as

$$n(\boldsymbol{x}) \equiv N f(\boldsymbol{x}), \tag{5.31}$$

with atom number $N = \int d^3x\, n(\boldsymbol{x})$, position distribution

$$f(\boldsymbol{x}) = \prod_i \frac{1}{\sqrt{2\pi\sigma_{x_i}^2}} \exp\left[-\frac{x_i^2}{2\sigma_{x_i}^2}\right], \tag{5.32}$$

and position variances $\sigma_{x_i}^2 \equiv \langle x_i^2 \rangle - \langle x_i \rangle^2$, where the angled brackets indicate an ensemble average. The in-trap momentum distribution is also modeled as Gaussian

$$g(\boldsymbol{p}) = \prod_i \frac{1}{\sqrt{2\pi\sigma_{p_i}^2}} \exp\left[-\frac{p_i^2}{2\sigma_{p_i}^2}\right], \tag{5.33}$$

with velocity variances $\sigma_{p_i}^2 \equiv \langle p_i^2 \rangle - \langle p_i \rangle^2$. Although we do not assume that there is a global temperature, the relationship between $\sigma_{x_i}^2$ and $\sigma_{p_i}^2$ is given by the (ergodic) trap and can be determined from the Monte Carlo simulation when assuming the correctness of our model potential. In this model, the expression for the phase space density becomes

$$\rho(\boldsymbol{x}, \boldsymbol{p}) = N h^3 f(\boldsymbol{x}) g(\boldsymbol{p}), \tag{5.34}$$

with Planck's constant $h = 2\pi\hbar$ and peak phase space density

$$\rho_0 \equiv \rho(\boldsymbol{0}, \boldsymbol{0}) = N \prod_i \frac{\hbar}{\sigma_{x_i}\sigma_{p_i}}. \tag{5.35}$$

Typically, we refer to the position and momentum variances as the widths w_{x_i} and per-axis temperatures T_i, defined as

$$w_{x_i} \equiv \sigma_{x_i},$$
$$k_B T_i / 2 \equiv \sigma_{p_i}^2 / (2m), \tag{5.36}$$

with Boltzmann's constant k_B and atomic mass m. In these terms, the peak density n_0 and peak phase space density ρ_0 become

$$n_0 \equiv n(\boldsymbol{0}) = \frac{N}{(2\pi)^{3/2} \prod_i w_{x_i}},$$
$$\rho_0 = N \prod_i \left(\frac{\hbar^2 m}{w_{x_i}^2 k_B T_i}\right)^{1/2}. \tag{5.37}$$

For comparison: in a harmonic trap with trap frequencies ω_i and interaxis thermal equilibrium at temperature $T_i \equiv T$, these expressions assume the forms

$$k_B T/2 = m\omega_i \sigma_{x_i}^2/2 = \sigma_{p_i}^2/(2m),$$

$$n_0 = N \prod_i \left(\frac{m\omega_i^2}{2\pi k_B T} \right)^{1/2} = N \prod_i m\omega_i \lambda_T/h, \tag{5.38}$$

$$\rho_0 = N \prod_i \frac{\hbar\omega_i}{k_B T},$$

with thermal wavelength $\lambda_T = h/\sqrt{2\pi m k_B T}$.

In summary, we find that both density and velocity distributions can be modeled as independent Gaussians along each trap eigenaxis. Because the trap is anharmonic, the connection between cloud extent and RMS velocity is not simply given by the axial eigenfrequencies. We need to measure both the spatial and the momentum distributions to obtain a full description of the atomic sample.

5.7. Measuring the phase-space distribution

We use an interleaved experimental sequence, where two runs of the same experiment are performed consecutively. At the end of the first experiment, the atomic cloud is imaged via absorption while the cloud is confined in the XODT potential. This image provides us with information about the density distribution at the end of the experiment. Appendix A summarizes some important effects that need to be taken into account to make in-situ imaging and its analysis reliable. At the end of the second experiment, the XODT potential is switched off and the atomic cloud is allowed to expand for typically 1.5 ms before we take the absorption image. The second image provides information about the kinetic energy distribution. The images determine the projection of the density distribution and the kinetic energy distribution into the absorption image plane. The atomic cloud is typically exposed for 50 μs of light on the $^1S_0$-$^1P_1$ transition with intensities of 10% of the saturation intensity $I_{\text{sat}} \simeq 40$ mW/cm^2.

5.8. Inelastic loss as relative momentum knife

In the regime of small optical length, we can neglect elastic scattering and view the inelastic loss as a "relative momentum knife". At a particular detuning, the inelastic loss only removes particle pairs with certain relative momenta. To investigate the effect on the single-particle momentum distribution, we need to find out which parts of the single-particle distribution contribute to a certain relative momentum class.

5.8.1. Single-particle and relative momentum distributions

The relative momentum $\boldsymbol{p}^r$ of particles 1 and 2 having individual momenta $\boldsymbol{p}^1$ and $\boldsymbol{p}^2$, respectively, is given by

$$\boldsymbol{p}^r \equiv \boldsymbol{p}^1 - \boldsymbol{p}^2. \tag{5.39}$$

We assume that both particles are distributed according to the same Gaussian probability distribution

$$\boldsymbol{p}^i \sim \mathcal{N}(\boldsymbol{\mu}, \boldsymbol{C}). \tag{5.40}$$

We will also assume zero mean $\boldsymbol{\mu} = 0$ and that the distribution is anisotropic but that the axes are decoupled, such that the covariance matrix $\boldsymbol{C}$ is diagonal and given by

$$\boldsymbol{C} = \begin{pmatrix} \langle p_1^2 \rangle & 0 & 0 \\ 0 & \langle p_2^2 \rangle & 0 \\ 0 & 0 & \langle p_3^2 \rangle \end{pmatrix}. \tag{5.41}$$

Then the differential probability for finding a single particle of momentum $\boldsymbol{p}^i$ can be written as

$$
\begin{aligned}
dP(\boldsymbol{p}^i) = f(\boldsymbol{p}^i)d^3p^i &= \frac{1}{(2\pi)^{3/2}\sqrt{\det \boldsymbol{C}}} \exp\left[-\frac{1}{2}(\boldsymbol{p}^i - \boldsymbol{\mu})^\top \boldsymbol{C}^{-1}(\boldsymbol{p}^i - \boldsymbol{\mu})\right] d^3p^i \\
&= \left(\prod_{j=1}^3 2\pi \langle p_j^2 \rangle\right)^{-1/2} \exp\left[-\frac{1}{2}\sum_{j=1}^3 \frac{(p_j^i)^2}{\langle p_j^2 \rangle}\right] d^3p^i.
\end{aligned}
\tag{5.42}
$$

Since the relative momentum is a sum of Gaussian-distributed momenta, the differential conditional probability $dP(\boldsymbol{p}^r | \boldsymbol{p}^1)$ of finding a relative momentum $\boldsymbol{p}^r$ when the momentum

of particle 1 is known is also Gaussian. Its mean as a function of $\boldsymbol{p}^1$ is

$$\langle \boldsymbol{p}^r \rangle = \langle \boldsymbol{p}^1 - \boldsymbol{p}^2 \rangle = \boldsymbol{p}^1 - \langle \boldsymbol{p}^2 \rangle = \boldsymbol{p}^1, \tag{5.43}$$

and its covariances are twice the single-particle covariances:

$$\langle p_i^r p_j^r \rangle - \langle p_i^r \rangle \langle p_j^r \rangle = 2\delta_{ij} \langle p_i^2 \rangle. \tag{5.44}$$

Thus the conditional probability is

$$dP(\boldsymbol{p}^r | \boldsymbol{p}^1) = f(\boldsymbol{p}^r | \boldsymbol{p}^1) d^3 p^r \propto \exp\left[-\frac{1}{2} \sum_j \frac{4}{\langle p_j^2 \rangle} (p_j^r - p_j^1/2)^2 \right] d^3 p^r. \tag{5.45}$$

By integrating over the marginal variable $\boldsymbol{p}^1$ we verify that the probability distribution function for the relative momentum $\boldsymbol{p}^r$ is

$$f(\boldsymbol{p}^r) = \int d^3 p^1 f(\boldsymbol{p}^r | \boldsymbol{p}^1) \propto \exp\left[-\sum_j \frac{(p_j^r)^2}{\langle p_j^2 \rangle} \right]. \tag{5.46}$$

To simplify the problem, we would like to find an expression for the conditional probability that only involves the magnitude of the relative and single-particle momenta. In the following, we will assume isotropy, such that

$$\langle p_j^2 \rangle \equiv \sigma^2. \tag{5.47}$$

We note that conditional and joint probabilities of variables A and B are generally related by [166]

$$P(A, B) = P(A|B)P(B). \tag{5.48}$$

Thus the joint probability for $\boldsymbol{p}^r$ and $\boldsymbol{p}^1$ is

$$dP(\boldsymbol{p}^r, \boldsymbol{p}^1) = dP(\boldsymbol{p}^r | \boldsymbol{p}^1) \times dP(\boldsymbol{p}^1) \tag{5.49}$$

and we integrate over momentum shells S and S' of radii p^r and p^1, respectively, to find the joint probability for the magnitudes:

$$\begin{aligned} dP(p^r, p^1) &= \int_S d^3 p^1 \int_{S'} d^3 p^r f(\boldsymbol{p}^r | \boldsymbol{p}^1) f(\boldsymbol{p}^1) \\ &\propto \int d\Omega^r \int d\Omega^1 (p^r p^1)^2 e^{-(p^r)^2/\sigma^2} \exp\left[-\frac{(\boldsymbol{p}^1 - \boldsymbol{p}^r)^2}{\sigma^2} \right] dp^1 dp^r \\ &\propto (p^1 p^r)^2 e^{-2(p^r)^2/\sigma^2} e^{-(p^1)^2/\sigma^2} \frac{\sinh \frac{2p^1 p^r}{\sigma^2}}{\frac{2p^1 p^r}{\sigma^2}} dp^1 dp^r, \end{aligned} \tag{5.50}$$

where $d\Omega^r$ and $d\Omega^1$ indicate the angular differentials corresponding to integration over S and S'. Since the single-particle probability is given by

$$dP(p^1)dp^1 = \int_S d^3p^1 f(\boldsymbol{p}^1) \propto (p^1)^2 e^{-\frac{(p^1)^2}{2\sigma^2}} dp^1, \tag{5.51}$$

we obtain the conditional probability of finding a particle pair with relative momentum of magnitude p^r for a given single collision partner momentum of magnitude p^1:

$$dP(p^r|p^1) \propto (p^r)^2 \exp\left[-\frac{2(p^r)^2}{\sigma^2} - \frac{(p^1)^2}{2\sigma^2}\right] \frac{\sinh\frac{2p^1 p^r}{\sigma^2}}{\frac{2p^1 p^r}{\sigma^2}} dp^r. \tag{5.52}$$

Figure 5.9 shows the relative momentum magnitude p^r distribution conditional to a known value of the single particle momentum magnitude p^1 in a thermal sample. For $p^1 \to 0$, the relative momentum distribution is Maxwell-Boltzmann with single particle temperature reduced by $\sqrt{2}$. For increasing p^1, the distribution approaches a Gaussian distribution around p^1. From this picture, we conclude that relative momenta for small single-particle momentum are determined by the second particle. For large single-particle momentum, the relative momentum increases. We can now use the conditional relative momentum distribution to predict the effect of relative-momentum dependent loss on the single-particle momentum distribution.

5.8.2. Effect of relative-momentum dependent loss

We are interested in a scenario where collision pairs with a given relative momentum p^r are removed from the sample and would like to predict the effect of such a removal on the single particle momentum distribution. In particular, we are interested in determining which single-particle momenta out of the initial distribution can contribute to a given relative momentum. We use Bayes' theorem [166] to invert the conditional probability:

$$dP(p^1|p^r)dP(p^r) = dP(p^r|p^1)dP(p^1) = dP(p^r, p^1). \tag{5.53}$$

This form can then be used to determine the conditional probability $dP(p^1|\text{loss})$ of finding a particle of momentum p^1 after removal of particles with momentum p^r. If we define the loss
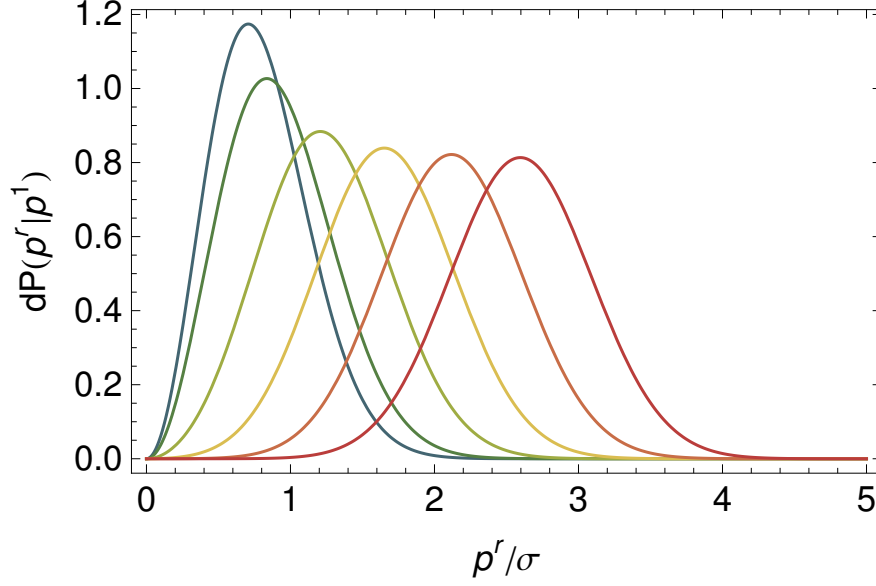
Figure 5.9.: Distribution of relative momentum magnitude p^r, conditional on value of single-particle momentum magnitude p^1 for an isotropic Maxwell-Boltzmann single-particle momentum distribution with $\sigma = \sqrt{mk_BT}$. The single particle momentum $p^1/\sigma = 0$ for the leftmost trace and increases in steps of 1 towards 5 (rightmost trace).

probability $f_{\text{loss}}(p^r)$, the survival probability of a particle with p^1 after relative momentum loss according to $f_{\text{loss}}(p^r)$ is

$$dP(p^1|\text{loss}) \propto \int dP(p^r|p^1)dP(p^1)[1 - f_{\text{loss}}(p^r)] = \int dP(p^r, p^1)[1 - f_{\text{loss}}(p^r)], \qquad (5.54)$$

where we integrate over the relative momentum p^r. If we normalize the left hand side of Eq. 5.54 with respect to p^1, we find

$$dP(x|\text{loss}) = \frac{xe^{-x^2}dx \ \int_0^\infty dy \ [1 - f_{\text{loss}}(y)]e^{-2y^2}y\sinh 2xy}{\int_0^\infty dx \ xe^{-x^2} \int_0^\infty dy \ [1 - f_{\text{loss}}(y)]e^{-2y^2}y\sinh 2xy}, \qquad (5.55)$$

with dimensionless momenta $x \equiv p^1/\sigma$ and $y \equiv p^r/\sigma$.

Figure 5.10(a) shows the effect of relative-momentum dependent loss on the single-particle momentum distribution. Here, we have assumed a Gaussian f_{loss} centered at different values of p^r/σ with a FWHM corresponding to 15 kHz in frequency units at a temperature of 3 μK. The single-particle distributions are renormalized after the loss process according to Eq. 5.55. The green trace shows the effect of loss when setting the center of the Gaussian loss at $p^r/\sigma =$

0. The initial single-particle distribution is almost unchanged, since particles are removed uniformly. The purple trace shows the effect of loss when $p^r/\sigma = 3$. The initial distribution is almost unchanged, but in this case, this is because there are not many single-particle momenta contributing to relative momenta of this magnitude. The red trace corresponds to $p^r/\sigma = 1$. Here, many particles are removed close to the most likely momentum, and the final distribution is shifted to higher momenta, corresponding to a higher average kinetic energy. The blue trace corresponds to $p^r/\sigma = 2$. Here, single-particle momenta larger than the most likely momentum are removed and the sample becomes colder.

The fractional change in the norm of the distribution in Eq. 5.55 with respect to having no loss process is equal to the fractional atom number change

$$\frac{N}{N_0} = 1 - \frac{8}{\pi} \int_0^\infty dx \, x e^{-x^2} \int_0^\infty dy \, f_{\text{loss}}(y) e^{-2y^2} y \sinh 2xy, \tag{5.56}$$

and moments of the distribution can be calculated as

$$\langle x^n \rangle \equiv \int_0^\infty x^n dP(x|\text{loss}). \tag{5.57}$$

However, it is more convenient to also define fractional changes of such moments with respect to having no loss process present:

$$\frac{\langle x^n \rangle}{\langle x^n \rangle_0} = \left[1 - \frac{\sqrt{\pi}}{2^{1+n/2}\Gamma(3+n/2)} \int_0^\infty dx \, x^{n+1} e^{-x^2} \int_0^\infty dy \, f_{\text{loss}}(y) e^{-2y^2} y \sinh 2xy \right] \times \left(\frac{N}{N_0} \right)^{-1} \tag{5.58}$$

For instance, the fractional change in temperature due to the relative momentum dependent loss process is

$$\frac{T}{T_0} = \frac{\langle x^2 \rangle}{\langle x^2 \rangle_0}. \tag{5.59}$$

Figure 5.10(b) shows the fractional atom number and temperature change under the same conditions as for panel (a), when scanning the mean target relative momentum p^r/σ. Most atoms are removed when p^r/σ targets the most likely single-particle momentum and the sample gets heated. For larger relative momentum, the sample becomes colder.

In conclusion: The relative momentum knife picture derived here describes removal of atoms with a given relative momentum magnitude. Depending on which class of atoms are
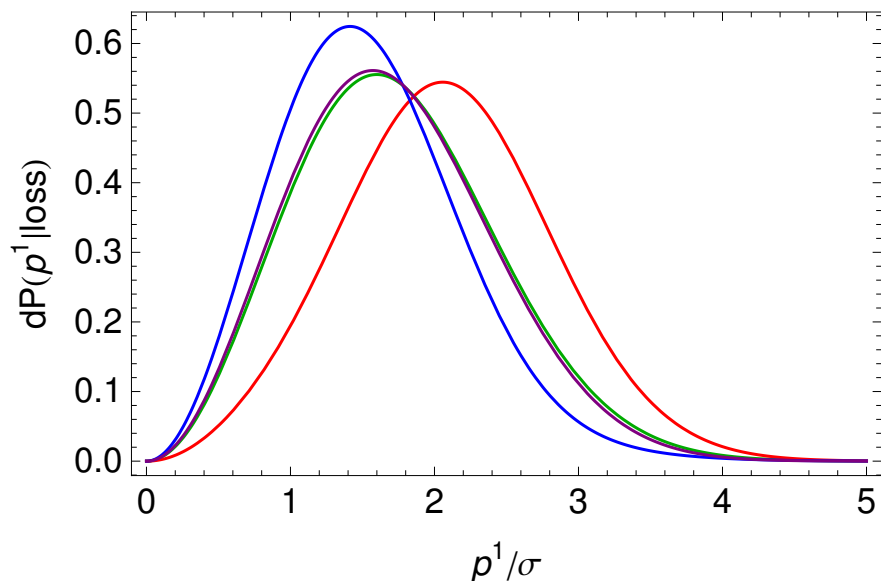
(a) Renormalized single-particle distribution after loss according to a Gaussian loss probability f_{loss} with FWHM corresponding to a frequency width of 15 kHz at 3 μK. The loss is centered at $p^r/\sigma = 0$, 1, 2, and 3 for the green, red, blue, and purple traces, respectively.
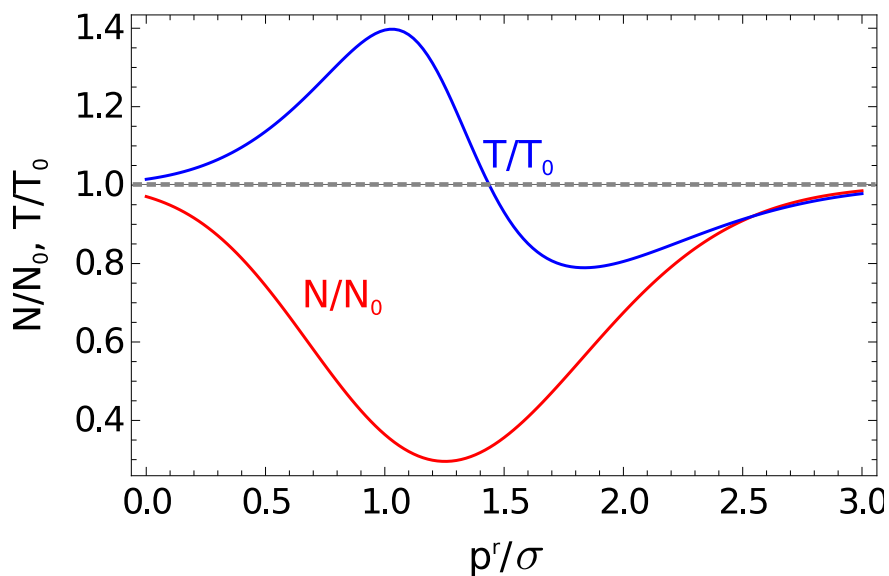
(b) Fractional atom number (temperature) change N/N_0 (T/T_0) shown as the red (blue) trace while scanning the loss center for the same conditions as in panel (a).

Figure 5.10.: Effect of relative-momentum dependent loss on the single-particle momentum distribution in an isotropic thermal sample.

removed, the sample gets heated or cooled. This simple static probabilistic model gives insight into the effect of instantaneous particle removal. However, it cannot describe the sample dynamics for time scales that are longer than the typical trap oscillation periods since the trap acts as a phase-space randomizer. To model the sample dynamics under relative-momentum dependent particle removal, we need a model that can account for the trapping potential.

5.9. Inelastic loss from a Gaussian distribution

The treatment here is an abbreviated version of unpublished notes by T. Nicholson; see also the online material of Ref. [10]. As argued in Sec. 5.1, we can describe the density evolution by a nonlinear differential equation involving the momentum-averaged inelastic collision rate constant

$$\dot{n} = -\bar{K}_{\mathrm{in}}n^2 - n/\tau_{\mathrm{bg}}, \tag{5.60}$$

where we have included a single-atom loss via the $1/e$ trap lifetime τ_{bg}. This equation can be integrated to obtain the density evolution with time t:

$$n(\boldsymbol{x}, t) = \frac{n_0(\boldsymbol{x})}{1 + \bar{K}_{\mathrm{in}}\tau_{\mathrm{eff}}n_0(\boldsymbol{x})}, \tag{5.61}$$

with effective time scale $\tau_{\mathrm{eff}} = \tau_{\mathrm{bg}}(e^{-t/\tau_{\mathrm{bg}}} - 1)$ and initial density distribution

$$n_0(\boldsymbol{x}) = N_0 \prod_{i=1}^{3} \frac{1}{\sqrt{2\pi\langle x_i^2 \rangle}} e^{-x_i^2/2\langle x_i^2 \rangle} \equiv n_{\mathrm{pk}} \prod_{i=1}^{3} e^{-x_i^2/2\langle x_i^2 \rangle}, \tag{5.62}$$

with peak density n_{pk}. The fractional atom number at time t is then

$$\begin{aligned}
\frac{N(t)}{N_0} &= \int d^3x \; n(\boldsymbol{x}, t) = N_0^{-1} \prod_{i=1}^{3} \sqrt{\langle x_i^2 \rangle} \int d\Omega_r \int_0^{\infty} dr \; r^2 n(r, t) \\
&\equiv \sqrt{\frac{2}{\pi}} n_{\mathrm{pk}}^{-1} \int_0^{\infty} dr \; r^2 n(r, t),
\end{aligned} \tag{5.63}$$

where we have defined rescaled coordinates $\xi_i \equiv x_i/\sqrt{\langle x_i^2 \rangle}$ and the rescaled radius $r \equiv \sqrt{\sum_i \xi_i^2}$. In terms of these coordinates, the fractional atom loss becomes

$$\frac{N(t)}{N_0} = \sqrt{\frac{2}{\pi}} \int_0^{\infty} dr \; \frac{r^2 e^{-r^2/2}}{1 + \bar{K}_{\mathrm{in}}\tau_{\mathrm{eff}}n_{\mathrm{pk}}e^{-r^2/2}} = \frac{2}{\sqrt{\pi}} \int_0^{\infty} du \; \frac{\sqrt{u}e^{-u}}{1 + \bar{K}_{\mathrm{in}}\tau_{\mathrm{eff}}n_{\mathrm{pk}}e^{-u}}, \tag{5.64}$$

with $u \equiv r^2/2$, which makes the integral more convenient for numerical calculations.

If we allow inhomogeneous kinetic energy distributions, the momentum-averaged inelastic rate can be quite complicated to calculate. To simplify the integrals to a point where fitting PA spectra becomes feasible, we have to assume a mean kinetic energy for the sample and perform the momentum average as if there were a single temperature describing the sample. Under this assumption, the thermally-averaged inelastic collision rate can be written as

$$
\bar{K}_{\text{in}}(\Delta, u, \ell_{\text{opt}}\gamma_m, T) = \frac{4h\ell_{\text{opt}}\gamma_m}{\sqrt{\pi}\mu} \int_0^\infty d\eta \, \frac{\gamma\sqrt{\eta} \, e^{-\eta}}{D^2 + \Gamma^2/4},
$$
$$
D \equiv \Delta + \frac{k_B T}{h}\eta - \nu_{\text{rec}} - \nu_s e^{-u/u_0}, \tag{5.65}
$$
$$
\Gamma \equiv \gamma + 2k_{\text{th}}\ell_{\text{opt}}\gamma_m\sqrt{\eta},
$$

with dimensionless relative momentum magnitude $\eta \equiv k^2/k_{\text{th}}^2$, thermal momentum $\hbar k_{\text{th}} = \sqrt{2\mu k_B T}$, center-of-mass PA photon recoil energy $h\nu_{\text{rec}}$, and trapping laser ac Stark shift at the center of the trap ν_s. The PA laser with optical frequency ν_l is detuned from the PA resonance by

$$
\Delta \equiv \nu_l - [\nu(^1\text{S}_0 - {}^3\text{P}_1) + \nu_n + \Delta\nu(I)], \tag{5.66}
$$

where $\nu(^1\text{S}_0 - {}^3\text{P}_1)$ is the atomic transition frequency, and $h\nu_n$ is the energy of state n with respect to the free threshold. The detuning term $\Delta\nu(I)$ accounts for the ac Stark shift of the molecular resonance with respect to I.

For the fitting routine, we approximated the integral in Eq. 5.64 (Eq. 5.65) as a 10-term (53-term) sum using Gauss-Laguerre quadrature [167, 168]. The quantities $(\ell_{\text{opt}}\gamma_m)$, T, u_0, and a term added to the detuning to represent the line center were allowed to vary. The parameter T is used as a check against the experimentally measured temperatures and agrees well with the average of the axial temperatures. The Stark shift term $\nu_s e^{-u/u_0}$ was included to account for the broadening of the atomic loss profile to the blue side of a molecular resonance due to the ac Stark shift induced by the trap.

5.10. Results for small optical length

A typical PA loss feature for small ℓ_{opt} is shown in Fig. 5.11(a), where the final atom number after application of PA light is shown with respect to PA detuning from $^1\mathrm{S}_0$-$^3\mathrm{P}_1$. The per-axis kinetic energies for this scan correspond to a horizontal (vertical) temperature $T_H(T_V) = 2~\mu\mathrm{K}$ ($3~\mu\mathrm{K}$) resulting in the typical thermal tail towards the red side of the resonance [169].

The solid line is a fit with the inelastic collision model derived in the last Section, for a vacuum-limited trap lifetime $\tau_{\mathrm{bg}} \simeq 1.3$ s. We extract ℓ_{opt} and the position of the line center. Panel (b) shows the time dependence of the same loss process. In the presence of resonant PA light, we clearly observe two-body loss. To fit the decay curve, however, it is necessary to perform the same thermal averaging process as for the lineshape to obtain a good match with the experimental data.

The measurements were performed for a range of optical lengths by adjusting the density profile averaged PA intensity I_{av}. Multiple molecular resonances were measured and results for $n = -2$ are shown in panel (c). The optical length data is fit with a linear function to extract $\ell_{\mathrm{opt}}/I_{\mathrm{av}}$, and the results are summarized in the table at the bottom. The fit coefficient $\ell_{\mathrm{opt}}/I_{\mathrm{av}}$ is given by the free-bound Franck-Condon factor and decreases drastically with decreasing n. Panel (d) exemplifies similar measurements done to determine the line shift $\Delta\nu$ of the same PA resonances with I_{av}. To obtain good signal-to-noise on these frequency shifts, we decreased the PA exposure time and increased I_{av} to maintain a constant pulse energy. Linear shift coefficients $\Delta\nu/I_{\mathrm{av}}$ and zero intensity line positions ν_n with respect to the atomic transition are also shown in the table. The sign and magnitude of $\Delta\nu/I_{\mathrm{av}}$ are consistent with the predictions in Ref. [144].

5.11. Elastic contributions to the cross section

For larger optical lengths, the elastic contribution to the scattering cross section becomes important. In this regime, the simple inelastic loss picture becomes insufficient to describe OFR spectra. Elastic collisions introduce cross-dimensional thermalization and (on longer

n	$\ell_{\mathrm{opt}}^{\mathrm{cc}}/I$ $\left(\frac{a_0}{\mathrm{W/cm^2}}\right)$	$\ell_{\mathrm{opt}}/I_{\mathrm{av}}$ $\left(\frac{a_0}{\mathrm{W/cm^2}}\right)$	$\frac{\gamma_m}{\gamma}\ell_{\mathrm{opt}}/I_{\mathrm{av}}$ $\left(\frac{a_0}{\mathrm{W/cm^2}}\right)$	ν_n (MHz)	$\Delta\nu/I_{\mathrm{av}}$ $\left(\frac{\mathrm{kHz}}{\mathrm{W/cm^2}}\right)$
-2	8.3×10^3	$15.8(8)\times10^3$	$5.9(3)\times10^3$	-23.98(1)	$-(251\pm67)$
-3	38	68(3)	26(1)	-222.18(5)	$+(29\pm2)$
-4	32	40(2)	15(1)	-1084.12(5)	$+(4\pm1)$
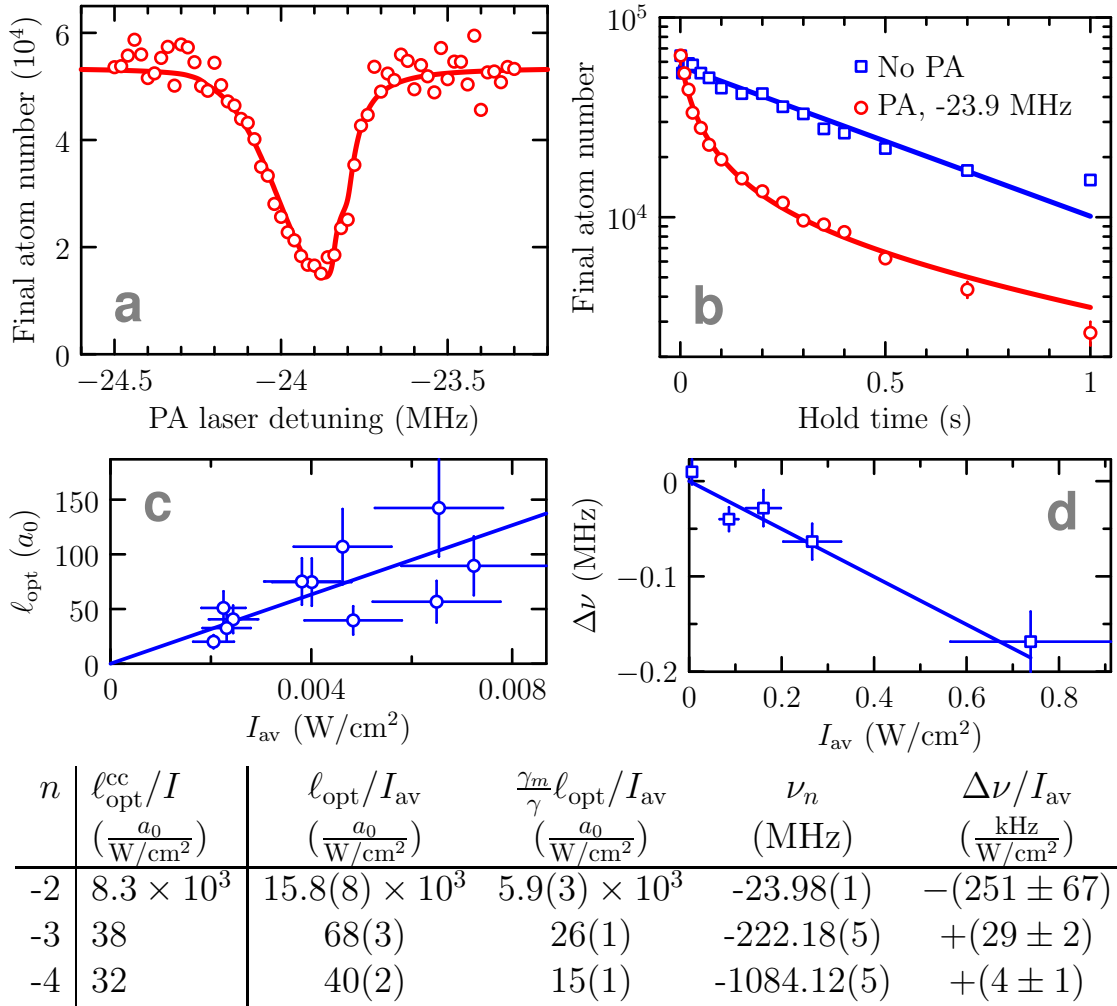
Figure 5.11.: Photoassociative spectroscopy for $n = -2$. **a**, Typical PA loss feature in the low intensity regime at $I_{\mathrm{av}} = 7$ mW/cm^2, with density-profile averaged PA intensity I_{av}. **b**, Time evolution of the trapped sample without PA light (blue squares) determines τ_{bg}. The dynamics with resonant PA light (red circles) show distinct two-body loss curves that can be fit with a thermally averaged model (solid red curve). **c**, Linear increase of the optical length ℓ_{opt} with increasing I_{av} for sufficiently small ℓ_{opt}. **d**, Molecular line center shift $\Delta\nu$ for large intensities. Both graphs are obtained by fitting loss spectra such as in panel a. For each n, OFR parameters from the coupled-channels calculation and the experiment are summarized in the table at the bottom. Here, $\ell_{\mathrm{opt}}^{\mathrm{cc}}$ indicates the theoretical result, ν_n is the zero-intensity molecular line center with respect to $^1\mathrm{S}_0$-$^3\mathrm{P}_1$, and $\Delta\nu/I_{\mathrm{av}}$ characterizes the molecular ac Stark shift with respect to I [144].

timescales) evaporation into the sample dynamics.

We show the atom loss with respect to PA laser detuning for $n = -2$ in Fig. 5.12(a). Both in-trap size and kinetic energy are measured by absorption imaging. Far detuned from the resonance, the gas is almost ideal, as shown by the persistent kinetic energy inhomogeneity along H and V in Fig. 5.12(b). In the center of the resonance (vertical dashed line), inelastic collisions dominate and cause heating. For red detuning from the molecular resonance, the temperatures approach each other.

The measured cloud widths w_H and w_V confirm that the potential energy follows the kinetic energy [see Fig. 5.12(c)] since particles oscillate in the trap many times between inelastic collisions. Similar measurements were performed for $n = -3$ and $n = -4$, and we find that the same dispersive behavior in temperatures and widths appears around $2\langle k \rangle \ell_{\mathrm{opt}} \gamma_m / \gamma \sim 30\%$ at 200 ms PA exposure times.

The data can be understood by a simple picture of competing elastic and inelastic collision rates. As discussed in Sec. 5.2, the elastic and inelastic rates average differently with k in a thermal sample, causing them to peak at different detunings from the molecular resonance. Elastic collisions cause cross-dimensional thermalization [170] and tend to equalize T_H and T_V. Since inelastic collisions predominantly remove cold atoms from the most dense part of the cloud, the resulting loss increases the system energy – a process referred to as anti-evaporation.

This behavior is confirmed by a Monte-Carlo simulation, where 5.5×10^4 classical particles are simulated and each particle undergoes elastic and inelastic collisions according to the cross sections in Sec. 5.2. The simulation is described in detail in Appendix B. The solid lines overlaid on the experimental data in Fig. 5.12 are the results of such a simulation. An average ratio of elastic to inelastic collisions per particle from the simulation is shown in Fig. 5.12(d). The dispersive shapes are sensitive to γ. Combined with the low ℓ_{opt} data in Fig. 5.11, the entire simulation reproduces the experimental data only when $\gamma = 2\pi \times 40(5)$ kHz $> 2\gamma_a = 15$ kHz without other free parameters. We have ruled out magnetic field or PA laser noise as a source of broadening. Instead, we conclude that this extra broadening is related to a
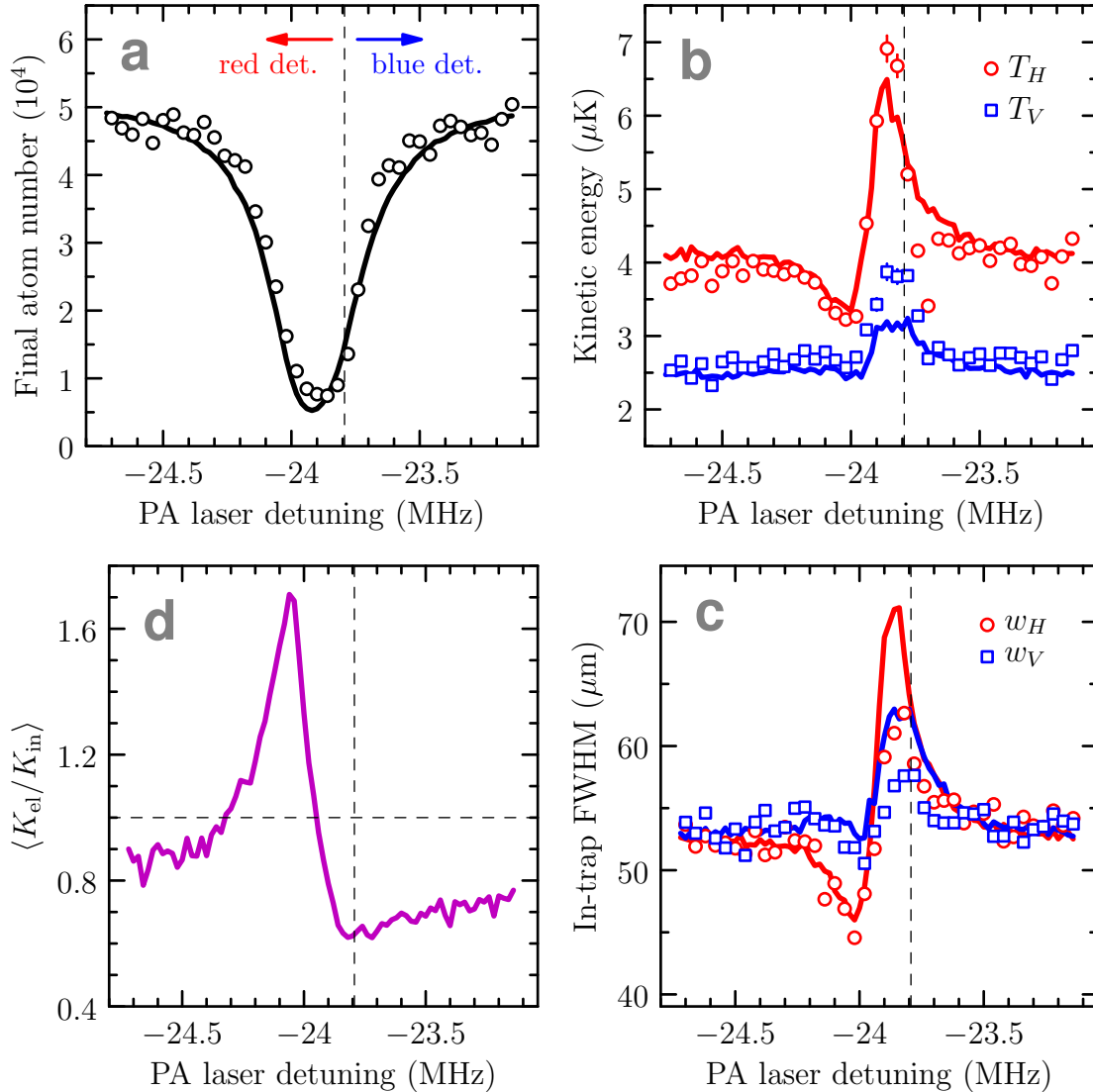
Figure 5.12.: Elastic contribution to the scattering cross section. Experimental data for $n = -2$ at $I_{av} = 22$ mW/cm^2 (open circles) and results of a Monte-Carlo simulation (solid lines) using the single-channel elastic and inelastic cross sections in a crossed Gaussian beam potential including gravity for $\ell_{opt}\gamma_m/\gamma = 140a_0$. (a) Atom loss as a function of PA laser detuning from the atomic $^1S_0$-$^3P_1$ resonance. In panels (b) and (c), blue (red) data points and solid lines indicate the corresponding quantities for the vertical (horizontal) trap axis. (b) Change in kinetic energy derived from time-of-flight images, and (c), potential energy change corresponding to varying in-trap density full widths at half maximum (FWHM). (d) Simulated ratio of elastic and inelastic collisions per particle, averaged over the PA exposure time.

faster molecular decay rate, which is consistent with our earlier measurements [137] and Rb results [133].

We conclude that the isolated resonance approximation universally describes OFR in the vicinity of each resonance. We have validated the linear line strength scaling and linear resonance shift with I and have observed a clear modification of both the inelastic and elastic parts of the scattering cross section.

5.12. Coupled-channels calculations

Our experimental work on optical Feshbach resonances was paralleled by detailed coupled-channels calculations by P. S. Julienne [10, 171]. The calculations predict the changes in real and imaginary parts of the scattering length using a model potential that only includes the natural radiative decay. Single-channel optical length expressions can be fit to the numerical results in the vicinity of each resonance. The optical length values extracted from these fits are shown as $\ell_{\mathrm{opt}}^{\mathrm{cc}}$ in the Table in Fig. 5.11. The agreement between our data and the theoretical predictions is fair; the theoretical value lies in between the experimentally determined values for ℓ_{opt} and $\ell_{\mathrm{eff}} = \ell_{\mathrm{opt}} \gamma_m / \gamma$.

As shown in the previous Sections, the single-channel theory has been very successfully used to describe both inelastic and elastic cross sections in the vicinity of three different molecular lines. The initial motivation for a more accurate description of the OFR process was to extend the theoretical description beyond the single-channel model into the far-detuned regime.

In addition to the vibrational levels investigated here, the $n = -1$ vibrational state exists at -0.4 MHz detuning from the free threshold, which leads to a PA resonance with a very large line strength ℓ_{opt}/I [137]. The isolated resonance theory indicates that operating with large I at $\mathcal{O}(10^5 \gamma_a)$ detuning from the $n = -1$ state should allow modifications to the scattering length of $\mathcal{O}(100 a_0)$ [136] with very low inelastic losses. However, with intensities up to 1 kW/cm^2 we did not observe changes to the thermodynamic properties of the gas,

in contrast to theory predictions. The theory proposal relied on extrapolating the large line strength of the $n = -1$ state to large detunings across multiple intermediate PA resonances. This assumption seemed valid since the $n = -1$ resonance is several orders of magnitude stronger than the intermediate resonances [137].

The discrepancy between theory and experiment stimulated a coupled-channels treatment of an atomic collision in a radiation field that properly switches between the short range molecular states and two field-dressed separated atoms [172, 173]. The two coupled excited potentials (0_u, 1_u) have the form of Ref. [137] and the decay of the excited state is treated by introducing an imaginary term $-i\hbar\gamma_m/2$ in the molecular potential. The ground state potential uses the dispersion coefficients of Ref. [174], has a scattering length of $-1.4\ a_0$, and reproduces the bound state data of Ref. [140] to better than 0.4%. The coupled-channels calculation does not assume isolated resonances, and all 0_u and 1_u molecular eigenstates emerge from the calculation as interfering, decaying scattering resonances [121]. The results of the coupled-channels calculation are shown in Fig. 5.13.

Figure 5.13(c) and (d) show that the coupled-channels model reproduces the isolated resonance expressions [121, 130] for the complex scattering length and the rate constants, as long as the detuning is small compared to the spacing between molecular levels. However, the elastic collision rate constant returns to its background value in between resonances regardless of their relative strengths, as indicated by the dotted line showing the background $K_{\mathrm{el}}^{\mathrm{bg}}$ at $E/k_B = 4\ \mu$K in Fig. 5.13(a). The same is true of the real part of the scattering length, as indicated by the dotted line for zero-energy a_{bg} in Fig. 5.13(d). These calculations show that the OFR effect does not extrapolate across an intermediate resonance, even a much weaker one, but that each molecular line behaves as an isolated resonance near its line center.

It is instructive to write the complex scattering length in the limit of large detuning, $|\Delta| \gg \gamma + \Gamma_s$, in the standard form for magnetic Feshbach resonances

$$\lim_{k \to 0} \alpha(k) = a_{\mathrm{bg}} \left(1 - \frac{w}{\Delta} + \frac{i}{2}\frac{w\gamma}{\Delta^2} \right), \tag{5.67}$$

where the resonance width $w \equiv -\ell_{\mathrm{opt}}\gamma_m/a_{\mathrm{bg}}$. To obtain a meaningful change in scattering
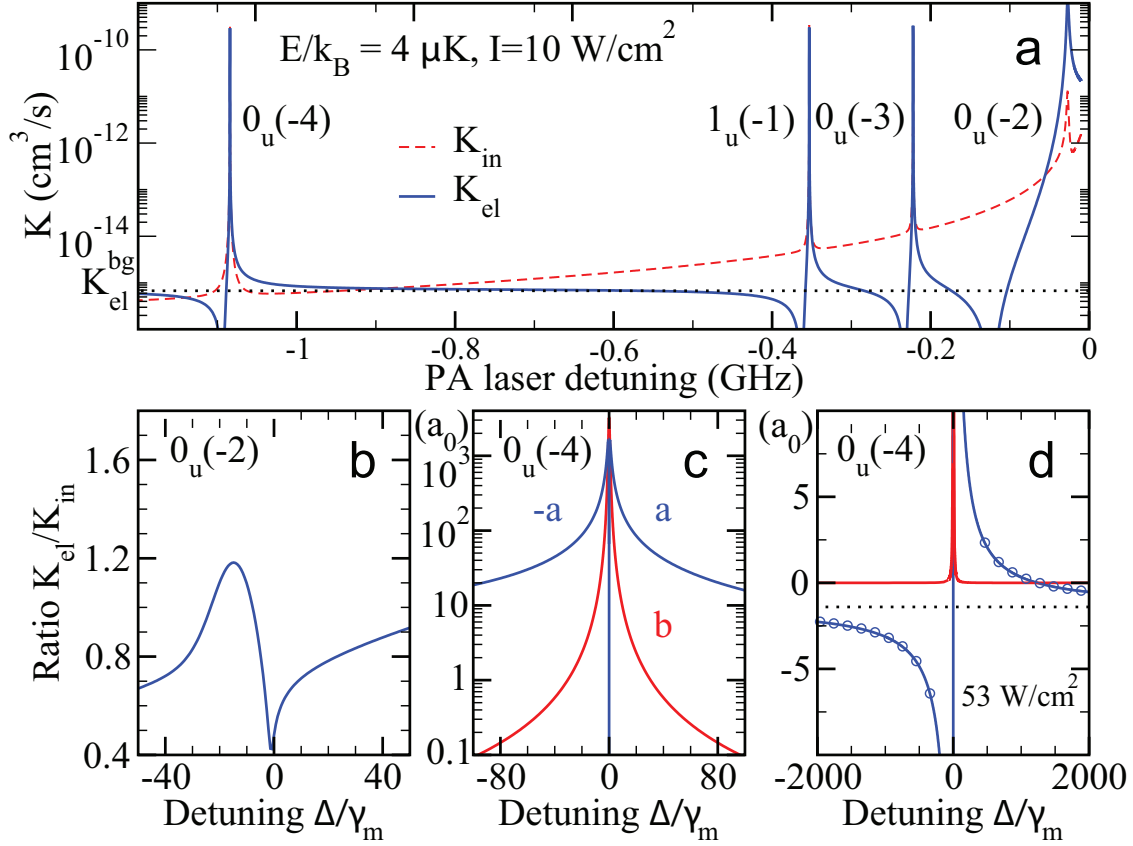
Figure 5.13.: Coupled channels calculations, Figure courtesy of P. S. Julienne. (a) Elastic and inelastic rate constants at $E/k_B = 4~\mu$K and $I = 10$ W/cm^2, versus PA laser detuning from atomic resonance. Each resonance peak is labeled by its electronic symmetry 0_u or 1_u and its vibrational quantum number. Between resonances, the coupled-channels K_{in} is only approximate. (b) Ratio of the thermally averaged rate constants at 2 μK for detuning Δ/γ_m near the $0_u(-2)$ feature. The intensity $I = 44$ mW/cm^2 to give the same $\ell_{opt} = 360a_0$ as for the conditions in Fig. 5.12(b). (c) Zero energy limit of real and imaginary parts of the scattering length for detuning near the $0_u(-4)$ feature. The intensity $I = 53.5$ W/cm^2 results in one PA photon scattering event during the typical exposure time of 200 ms. (d) Same calculation as in panel (c), except on a linear scale and large detuning. The circles show the coupled channels calculation, and the solid lines show the analytic isolated resonance formula. The analytic isolated resonance expressions are indistinguishable from the coupled channels results here.

length, $\ell_{\text{opt}}\gamma_m/\Delta$ needs to be sufficiently large, and the imaginary part $b = \frac{1}{2}\ell_{\text{opt}}\gamma_m\gamma/\Delta^2$ needs to be sufficiently small. Since $K_{\text{in}} \simeq (2 \times 10^{-12} \text{ cm}^3/\text{s}) \, (b/a_0)$, for a density of $\rho = 10^{12} \text{ cm}^{-3}$ and $b = 0.1a_0$, $K_{\text{in}}\rho$ gives the same loss rate $(200 \text{ ms})^{-1}$ as the atomic light scattering rate for the power $I = 53 \text{ W/cm}^2$ assumed for Figs. 5.13(c) and (d). Thus, the calculations predict that changes in the scattering length on the order of $10 \, a_0 \gg |a_{\text{bg}}|$ should be possible for detunings $\sim 100 \, \gamma_m$ for time periods $\sim 200 \text{ ms}$.

Chapter 6

Summary & Outlook

In this thesis, we have discussed several precision measurements related to an optical frequency standard based on neutral atomic Sr. We have presented detailed models that led to a deeper understanding of the underlying physical phenomena. A lot of the work on optical standards tries to realize a quantum system that is as clean and as simple as possible. All that should be required to understand the spectroscopic process is a driven two-level atomic system without spontaneous decay. Effects that mar this simple picture are considered systematic effects that need to be understood, measured, and controlled.

Because the aim of an optical frequency standard is to prepare the cleanest driven two-level system possible, the typical method of doing so is to consider the currently largest systematic effect and try to understand it. Once a particular effect is successfully understood, it can be modeled in a simple manner, and can be controlled and removed by careful system design. This process might take a while, especially as the effects become smaller and smaller, but it has been very successful so far in decreasing the frequency uncertainty towards the next order of magnitude.

The current main systematic under investigation is the density shift. As we have seen in Chapter 3, fairly good models have been put forward to understand its origins. These models have also led to new proposals on how to improve the system to suppress the density shift. By now, this suppression has also been shown experimentally [51, 67]. Although a full clock

evaluation exploiting the density shift suppression will need to be done, these results promise to get rid of one of the two limiting effects in the Sr uncertainty budget (see Sec. 1.2).

The second large uncertainty – the BBR shift – is currently under investigation in all major labs that work on Sr optical frequency standards. A better understanding of the theoretical model for the atomic polarizabilities will reduce the BBR uncertainty, but requires careful measurements of the key contributing electronic states [34]. Even with an improved polarizability model and a careful measurement of the environmental temperature, one cannot confidently quote a small BBR uncertainty because of the non-blackbody character of the vacuum chamber environment. For this reason, the most likely approach to measure the BBR shift is to build a specialized environment for the spectroscopic process. The most straightforward approach would be to simply heat and cool the environment and measure the clock frequency shift with respect to this parameter. The temperature range explored by this approach is too small, however, to obtain good uncertainties since typical vacuum chambers and experimental apparatuses cannot support temperature changes of more than a few 10 °C. For these reasons, the main approach for constructing a specialized environment has been to build a small in-vacuum enclosure that can be cooled using liquid nitrogen or helium [12, 36]. Atoms would then be transferred into such an enclosure using a moving optical lattice and spectroscopy could take place in a carefully constructed BBR environment at a controlled (and small) temperature. The main difficulties for building such a system are technical in nature. One has to carefully consider how the enclosure is built to avoid leakage of room temperature BBR into the enclosure. In addition, pumping speed limitations in small enclosures might be a considerable concern, even at cold temperatures. Characterization of the BBR shift will be a major step forward for optical lattice clocks, but it might take some time to settle on a reliable system design that does not impede clock operation in some other way.

Meanwhile, the high precision obtained in optical lattice clock experiments has led to interesting proposals for investigations of condensed-matter systems that could be realized with alkaline earth atoms [126–128]. In the last few years, all isotopes of Sr have been

used to produce quantum degenerate gases [142, 143, 175–178]. A long-standing goal for optical lattice clock experiments has been to operate with a sample in a Mott insulator state, trapped in a three-dimensional optical lattice. This idea is conceptually intriguing, because many-body effects would automatically be suppressed as long as the lattice is deep enough to prevent tunneling and all atoms would be prepared in the lowest motional state of each site. Such a sample would be a real equivalent of an array of identical ion traps, where a single particle is interrogated in a deep potential well. Even the very first experimental strontium lattice clock paper [1] contained a drawing that shows single atoms trapped in an eggcrate-shaped potential that can only be realized in a three-dimensional optical lattice.

Because of their conceptual attractiveness, these pictures can be very misleading. The main detractor for building a serious 3D optical lattice clock is the fact that optical lattice polarizations cannot be kept parallel to the bias magnetic field in three dimensions. Of necessity, one beam will have a polarization that is not colinear with the bias magnetic field. This configuration breaks the symmetry that allows clock frequency shifts related to the tensor polarizability in fermionic isotopes to be suppressed [22]. Although a bosonic optical lattice clock in three dimensions has been built [179, 180], its accuracy is not nearly as good as the systems realized with one-dimensional lattices. Bosonic isotopes require a large magnetic field to induce the clock transition which introduces a large uncertainty due to long-term magnetic field stability.

In addition, the Wannier-Stark ladder gravitational symmetry breaking between lattice sites (see Cha. 2) cannot be obtained in an optical lattice of dimension two or greater. The transverse harmonic confinement in an optical lattice beam will absorb the linear potential shift due to gravity, and the energy splitting between lattice sites becomes parabolic as a result. Because of the transverse harmonic confinement, sites at the center of the trap become much closer to being degenerate than would be the case in a vertical one-dimensional optical lattice [56]. Tunneling can become a concern even in two-dimensional optical lattices – see the online material for Ref. [51]. Care will have to be taken in finding a compromise between tunneling (for shallow lattices) and lattice-intensity related detrimental effects such as photon

scattering at the lattice wavelength (for deep lattices).

In addition, the individual sites in a 2D or 3D optical lattice are actually much more inhomogeneous than in a 1D optical lattice. Because of the transverse confinement, sites away from the center of the trap will have different trap depths and frequencies than the sites close to the center. These effects exacerbate the Rabi frequency inhomogeneities discussed in Cha. 2, and averages over the particle distribution across different lattice sites become much more important [51].

All of these effects will become even more important as laser coherence times become longer and narrower linewidths are obtained using the next generation of highly stable spectroscopy lasers. Preliminary investigations show that for long coherence times, new effects such as different collision channels and higher-order light scattering processes will also start to be significant [68, 181]. Finally, spectroscopy-induced dipole-dipole coupling between atoms in neighboring lattice sites [182] will become a concern when spectroscopic precisions approach the 10 mHz level with novel spectroscopy laser designs [183–185].

For these reasons, it currently seems unlikely that the accuracy achieved in 1D optical lattice clocks will be surpassed by 3D optical lattice clocks in the near future. In addition, operation of a 3D Mott insulator clock requires the preparation of a Mott insulating state on competitive time scales. Current 1D experimental cycles are on the order of 1 s, which already limits the optical clock precision via the optical Dick effect [186, 187] by aliasing spectroscopy laser noise at the duty cycle into the measurement bandwidth. This limitation has led to a lot of work on duty-cycle optimization and sample reuse by the Paris group [54, 187–189]. Evaporative cooling to quantum degeneracy currently takes at least several seconds [142, 143, 175–178], which would reduce the measurement precision even further and make laser stabilization very difficult. The cooling time scale is unlikely to improve much since evaporation is necessarily tied to the trap frequency of the optical potential in which the particles are cooled. Other cooling methods such as narrow-line laser cooling based on spontaneous Raman scattering might prove more useful, but significant experimental work will be necessary to decide whether they are feasible [190, 191]. The preparation

time required makes an optical lattice clock based on a quantum degenerate gas unfeasible unless some interleaved preparation scheme is employed where a second sample is prepared while the current sample is interrogated.

Nevertheless, most groups are working on building multiple Sr clock systems in the same lab to simplify the evaluation of systematic effects. Probing a condensed matter analog based on quantum degenerate Sr with another experiment set up as an optical lattice clock has many promising advantages. Such a setup could be used to realize novel and interesting alkaline earth quantum simulation schemes [126–128]. Probing such a system with the high precision afforded by the optical lattice clock will then enable investigations of the system dynamics at the Hz scale. Conversely, the understanding gained from careful investigation of the quantum degenerate gas system will help in furthering the optical lattice clock design and may enable construction of a degenerate gas optical lattice clock in the future.

One tool for studying and manipulating such quantum degenerate gases of alkaline earth atoms is the OFR effect. We investigated this effect in detail in a thermal gas of ^{88}Sr, but as we have seen in Chapter 5, the real application of the OFR would be as a tool to manipulate phase shifts or mean field energies in the degenerate gas regime. Because there are no magnetic Feshbach resonances in the (interesting) states of alkaline earths, the OFR is the sole candidate for manipulation of the interaction strength so far. The main result of our studies is that the elastic scattering length modification under the OFR effect is inseparable from inelastic losses and that the effect is reliable only in the vicinity of a vibrational resonance. But, we have also shown that it can still be usefully applied under a careful combination of parameters, even in a thermal gas. Whether the OFR could also be used to further the study and operation of optical lattice clocks remains to be seen. The relevant collision channel for the density shift is ^{1}S$_0$-^{3}P$_0$. One could, for instance, imagine that the interaction energy might be modified by coupling this channel to a vibrational state in ^{3}P$_1$-^{3}P$_0$.

Even though the optical lattice clock is the simplest spectroscopic system we can prepare, each gain in systematic uncertainty brings new effects to light. Studying and learning to con-

trol these effects is what keeps work on a seemingly simple spectroscopy system interesting. The benefit of pushing the accuracy to higher and higher levels is that novel effects unrelated to the atomic physics can be studied. The main candidate for these studies are the relativistic effects of gravity and their manifestation in the red shift. We have shown in Cha. 4 that optical clock experiments can easily be tied to investigations of large-scale fundamental physics. The red shift manifests as a frequency shift of 1×10^{-16} m^{-1}, and optical clocks are fast approaching the accuracy regime where gravity can be investigated on small length scales [192]. Projects for large scale investigations of gravity by placing optical standards on a space vehicle are also under development [113]. Any advancement in miniaturization and automation of the currently large, power-intensive, and manpower-hungry optical clock systems will help these projects. Replacing the microwave-standards used in satellite systems such as GPS with optical standards will enable precision mapping of gravity and improve position triangulation on Earth's surface from meters to millimeters or below. Astronomic applications include ranging at interplanetary distances [193] and building phase-coherent links between remote antenna arrays for very-long-baseline interferometry.

The atomic frequency standard of the future will not matter much for civil time keeping, but I believe that Sr based precision spectroscopy will remain interesting for years to come.

Appendix A

ABSORPTION IMAGING OF TRAPPED PARTICLES

THIS appendix summarizes the relevant physics of a probe beam scattering off a sample of trapped atoms. Absorption imaging of trapped particles is subject to many systematic effects. Nevertheless, in-situ absorption imaging can be made to work reliably provided that these effects are understood, measured, and accounted for.

A.1. Beer's law and classical scattering cross section

Assume that a probe beam of intensity I_{in} enters an absorbing medium and that the intensity after transmission has been reduced to I_{out}. Then the medium's optical depth (OD) is defined as

$$\text{OD} = -\ln \frac{I_{\text{out}}}{I_{\text{in}}} \tag{A.1}$$

If the medium absorbs with a constant probability per unit length, the medium has a linear absorption coefficient α and the intensity along the beam coordinate z attenuates exponentially according to Beer's law

$$I_{\text{out}}(z) = I_{\text{in}}e^{-\alpha z}. \tag{A.2}$$

Assuming that the medium consists of a dilute collection of identical scatterers, the absorption coefficient should be proportional to their density n and one can define a scattering cross section

$$\sigma = \alpha/n \tag{A.3}$$

that summarizes the scattering properties of an individual scatterer. For a dilute monatomic gas interacting with a resonant monochromatic field, the resonant scattering cross section can be calculated from the linear response of a two-level system consisting of ground state $|g\rangle$ and excited state $|e\rangle$. If the field's polarization is perfectly aligned with the two-level system's quantum axis, and the field is perfectly monochromatic, one finds from the equivalence principle that [194]

$$\sigma_{eg} = \frac{3\lambda_{eg}^2}{2\pi}, \tag{A.4}$$

where λ_{eg} is the wavelength of the atomic transition.

A.2. Polarization, selection rules, and atomic response function

We will argue that the quantum mechanical equivalent of Eq. A.4 essentially gives the same answer. The derivation follows the solid treatment in Ref. [195] and will be carried out in some detail to expose each assumption going into our final result. We would like to determine the numerical value of the factor $3^* \in [0, 3]$ as defined by Siegman [196] and check whether λ_{eg} in Eq. A.4 should be λ_{eg} or $\lambda_{eg}/(2\pi)$.

We start with a differential formulation of Fermi's Golden Rule for the transition rate per photon energy E from a combined light and atomic state $|i\rangle$ to another combined light and atomic state $|f\rangle$ under the perturbation H':

$$dW_{fi} = \frac{2\pi}{\hbar}|\langle f|H'|i\rangle|^2 S(E)P(E)dE, \tag{A.5}$$

where $P(E)$ describes the *atomic response* to the application of a photon of energy E, i.e. it is the probability of a successful absorption process at photon frequency $\omega \equiv E/\hbar$. The

energy distribution $S(E)$ is the area-normalized power spectrum applied to the atom.

A.2.1. Atomic matrix element

In the dipole approximation, the Hamiltonian H' coupling a two-level atom of mass m to a single-mode light field with vector potential $\boldsymbol{A}$, polarization $\hat{\boldsymbol{\epsilon}}$, wave vector $\boldsymbol{k}$, and frequency ω can be written as [195]

$$H' = \frac{e}{mc}\boldsymbol{p} \cdot \boldsymbol{A} = \frac{e}{m}\sqrt{\frac{2\pi\hbar}{V\omega}}\left[a(\boldsymbol{p} \cdot \hat{\boldsymbol{\epsilon}})e^{i\boldsymbol{k}\cdot\boldsymbol{r}} + a^{\dagger}(\boldsymbol{p} \cdot \hat{\boldsymbol{\epsilon}}^{*})e^{-i\boldsymbol{k}\cdot\boldsymbol{r}}\right], \tag{A.6}$$

where e is the electron charge, $\boldsymbol{p}$ $(\boldsymbol{x})$ is the atomic momentum (position) operator, and a $(a^{\dagger})$ is the photon mode annihilation (creation) operator in the quantization volume V. The first term describes the absorption of a photon and the second term describes the emission of a photon. Here, we will only consider first order perturbation theory for H', where a photon is absorbed and the two-level atom undergoes the corresponding transition of interest. We consider an initial state $|i\rangle \equiv |g\rangle \otimes |n\rangle \equiv |g, n\rangle$ of the combined system, where the atom is in ground state $|g\rangle$ and the photon field is in the n-photon Fock state $|n\rangle$. One photon is absorbed and the atom undergoes a transition to excited state $|e\rangle$ such that the final state is $|f\rangle \equiv |e\rangle \otimes |n-1\rangle \equiv |e, n-1\rangle$. The transition matrix element becomes

$$\langle f|H'|i\rangle = \frac{e}{m}\sqrt{\frac{2\pi\hbar}{V\omega}}\langle e, n-1|a(\boldsymbol{p} \cdot \hat{\boldsymbol{\epsilon}})e^{i\boldsymbol{k}\cdot\boldsymbol{r}}|g, n\rangle = \frac{e}{m}\sqrt{\frac{2\pi\hbar n}{V\omega}}\langle e|(\boldsymbol{p} \cdot \hat{\boldsymbol{\epsilon}})e^{i\boldsymbol{k}\cdot\boldsymbol{r}}|g\rangle. \tag{A.7}$$

As long as the particle motion can be treated classically (beyond the Lamb-Dicke regime), we can ignore the operator character of the phase factor and separate it from the electronic degree of freedom. We find

$$\langle f|H'|i\rangle \simeq \frac{e}{m}\sqrt{\frac{2\pi\hbar n}{V\omega}}e^{i\boldsymbol{k}\cdot\boldsymbol{r}}\langle e|\boldsymbol{p} \cdot \hat{\boldsymbol{\epsilon}}|g\rangle, \tag{A.8}$$

and we can write down the Heisenberg equation for the position operator $\boldsymbol{r}$ and atomic Hamiltonian H_a:

$$[\boldsymbol{r}, H_a] = i\hbar\frac{d\boldsymbol{r}}{dt} = \frac{i\hbar\boldsymbol{p}}{m}. \tag{A.9}$$

We use that $|e\rangle$ and $|g\rangle$ are eigenstates of H_a and find

$$\langle e|\boldsymbol{p} \cdot \hat{\boldsymbol{\epsilon}}|g\rangle = im\omega_{eg}\langle e|\boldsymbol{r} \cdot \hat{\boldsymbol{\epsilon}}|g\rangle \equiv -\frac{im}{e}\omega_{eg}\langle e|\boldsymbol{D} \cdot \hat{\boldsymbol{\epsilon}}|g\rangle, \tag{A.10}$$

for the bare transition frequency ω_{eg} defined as the eigenenergy difference between the atomic states $|e\rangle$ and $|g\rangle$, and the dipole operator $\boldsymbol{D} \equiv -e\boldsymbol{r}$. Thus Eq. (A.7) becomes

$$\langle f|H'|i\rangle = -i\sqrt{\frac{2\pi\hbar n}{V\omega}}\omega_{eg}\langle e|\boldsymbol{D}\cdot\hat{\boldsymbol{\epsilon}}|g\rangle. \tag{A.11}$$

Note that we have not assumed that the driving photon at frequency ω is exactly at the bare transition frequency ω_{eg}.

We proceed by assuming that the atomic states are well described by a total angular momentum J and magnetic quantum number m, so that

$$|g\rangle \equiv |J_g m_g\rangle$$
$$|e\rangle \equiv |J_e m_e\rangle. \tag{A.12}$$

In this case, the dipole matrix element Eq. (A.11) can be separated into spherical tensor components. The scalar product between dipole operator and polarization vector separates into [195]

$$\boldsymbol{D}\cdot\hat{\boldsymbol{\epsilon}} = \sum_{q=-1}^{+1}(-)^q(\hat{\boldsymbol{\epsilon}}\cdot\hat{\boldsymbol{e}}_{-q})D_q^1, \tag{A.13}$$

with polarization quantum number q corresponding to a spherical tensor basis

$$\hat{\boldsymbol{e}}_0 \equiv \hat{\boldsymbol{z}}$$
$$\hat{\boldsymbol{e}}_{\pm 1} \equiv \mp(\hat{\boldsymbol{x}} \pm i\hat{\boldsymbol{y}})/\sqrt{2} \tag{A.14}$$

with quantum axis along $\hat{\boldsymbol{z}}$. In the spherical tensor basis, the dipole matrix elements can be further simplified via the Wigner-Eckart theorem[1]

$$\langle J_e m_e|D_q^1|J_g m_g\rangle = (2J_e + 1)^{-1/2}\langle J_g 1 m_g q|J_e m_e\rangle\langle J_e\|D^1\|J_g\rangle. \tag{A.15}$$

---

[1]The numerical and phase factors in front of the reduced matrix element in the Wigner-Eckart theorem have various definitions in the literature. It is important to use the definition of the Wigner-Eckart theorem, the Clebsch-Gordan coefficient in terms of $3j$-symbols and the reduced matrix element from the same reference to get consistent results. We follow Ref. [195] here which is consistent with Refs. [194, 197–200] in both Wigner-Eckart theorem and definition of Clebsch-Gordan coefficients in terms of $3j$-symbols. Sakurai [71] uses a different phase prefactor but that might be a misprint. Other books use a different factorization of the Wigner-Eckart theorem and are not consistent with the presentation here [57, 201–204].

with radial integral $\langle J_e \| D^1 \| J_g \rangle$ (called the reduced matrix element) and Clebsch-Gordan coefficient

$$\langle J_g 1 m_g q | J_e m_e \rangle = (-)^{m_e} \sqrt{2J_e + 1} \begin{pmatrix} J_g & 1 & J_e \\ m_g & q & -m_e \end{pmatrix}. \tag{A.16}$$

For a given combination of quantum numbers, the Clebsch-Gordan coefficient enforces the dipole selection rules $|J_e - J_g| \leq 1$, $m_g + q = m_e$, and $J_e = J_g \Rightarrow q \neq 0$. In particular, this means that for a given combination of quantum numbers, there is only one polarization component $q = m_e - m_g$ with $|q| \leq 1$ that can drive the dipole transition.

Combining Eqs. A.15-A.16, we find

$$\langle J_e m_e | D_q^1 | J_g m_g \rangle = \delta_{q,m_e-m_g} (\hat{e}_{-q} \cdot \hat{\epsilon}) (-)^{m_e+q} \begin{pmatrix} J_g & 1 & J_e \\ m_g & q & -m_e \end{pmatrix} \langle J_e \| D^1 \| J_g \rangle. \tag{A.17}$$

The reduced matrix element can be related to the Einstein A coefficient of the particular transition [195]

$$A_{eg} = \frac{4\omega_{eg}^3}{3\hbar c^3} \frac{|\langle J_e \| D^1 \| J_g \rangle|^2}{2J_e + 1}. \tag{A.18}$$

For the transition rate Eq. (A.5), we only require the magnitude-squared of the atomic dipole matrix element. We find

$$\begin{aligned}
\frac{2\pi}{\hbar} |\langle f | H' | i \rangle|^2 &= \frac{4\pi^2 n}{V\omega} \omega_{eg}^2 \times |\langle e | \boldsymbol{D} \cdot \hat{\boldsymbol{\epsilon}} | g \rangle|^2 \\
&= \frac{4\pi^2 n}{V\omega} \omega_{eg}^2 \times \delta_{q,m_e-m_g} |\hat{e}_{-q} \cdot \hat{\boldsymbol{\epsilon}}|^2 \begin{pmatrix} J_g & 1 & J_e \\ m_g & q & -m_e \end{pmatrix}^2 \times \\
&\quad \times \frac{3\hbar c^3}{4\omega_{eg}^3} (2J_e + 1) A_{eg}.
\end{aligned} \tag{A.19}$$

The Fermi's Golden Rule differential transition rate for absorption of photons with energy $E = \hbar\omega$ while the atom undergoes the transition $|g\rangle \rightarrow |e\rangle$ becomes

$$\begin{aligned}
dW_{eg} &= \Phi \times 3(\pi\hbar c)^2 \frac{A_{eg}}{\omega_{eg}} \times \\
&\quad \times \delta_{q,m_e-m_g} |\hat{e}_{-q} \cdot \hat{\boldsymbol{\epsilon}}|^2 (2J_e + 1) \begin{pmatrix} J_g & 1 & J_e \\ m_g & q & -m_e \end{pmatrix}^2 \times \\
&\quad \times \frac{1}{E} S(E) P(E) dE,
\end{aligned} \tag{A.20}$$

where we have defined the photon flux $\Phi \equiv cn/V$ as the density of photons in the quantization volume traveling at the speed of light. To obtain a useful expression for the scattering rate, we have to assume a particular form of the atomic response $P(E)$.

A.2.2. Atomic response and laser spectrum

In the case of a (homogeneously broadened) Lorentzian line centered at ω_{eg} with linewidth γ_e, we have an area-normalized response

$$P(E = \hbar\omega) = \frac{\hbar\gamma_e/(2\pi)}{(\hbar\omega - \hbar\omega_{eg})^2 + (\hbar\gamma_e/2)^2} = \frac{2}{\pi\hbar\gamma_e}\frac{1}{1 + 4(\omega - \omega_{eg})^2/\gamma_e^2} \tag{A.21}$$

Note that the homogeneous linewidth γ_e includes decay to other levels. If the lineshape is dominated by the transition's natural linewidth, $\gamma_e = A_e = \sum_j A_{ej}$, with Einstein coefficient A_e and branching ratios A_{ej}/A_e to all other levels $|j\rangle$.

In the limit of a monochromatic spectrum at the transition frequency the spectrum becomes $S(E) \to S_0(E) \equiv \delta(E - \hbar\omega_{eg})$ and we retrieve a total transition rate

$$W_{eg} = \Phi\frac{3\lambda_{eg}^2}{2\pi}\frac{A_{eg}}{\gamma_e}\delta_{q,m_e-m_g}|\hat{e}_{-q} \cdot \hat{\epsilon}|^2(2J_e + 1)\begin{pmatrix} J_g & 1 & J_e \\ m_g & q & -m_e \end{pmatrix}^2. \tag{A.22}$$

If the probe laser spectrum is broadened with respect to $S_0(E)$, the transition rate W_{eg} will be diluted by a factor

$$\xi \equiv \frac{\int_0^\infty dE S(E)P(E)/E}{\int_0^\infty dE S_0(E)P(E)/E} = \int_0^\infty d\omega S(\omega)\frac{\omega_{eg}/\omega}{1 + 4(\omega - \omega_{eg})^2/\gamma_e^2}, \tag{A.23}$$

where the laser spectrum is area-normalized to $\int_0^\infty d\omega S(\omega) = 1$. Figure A.1 shows the dilution factor ξ for several power spectral density shapes assuming that the laser spectrum is centered around ω_{eg} but broadened. Detuning from resonance is easily included in ξ by shifting $S(\omega)$.
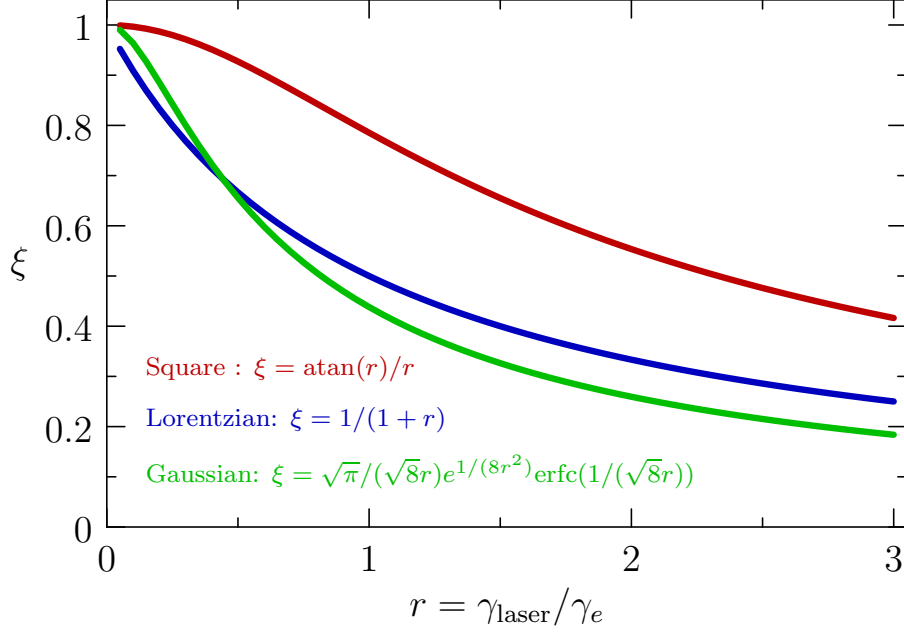
Figure A.1.: Transition rate dilution factor ξ from laser spectrum for square spectrum (red), Lorentzian spectrum (blue), and Gaussian spectrum (green).

A.2.3. Scattering cross section

The scattering cross section for the atomic transition $|g\rangle \to |e\rangle$ is defined as the ratio of scattering rate W_{eg} to photon flux Φ. From Eq. (A.22), we find

$$\sigma_{eg} \equiv W_{eg}/\Phi = \frac{3\lambda_{eg}^2}{2\pi}\frac{A_{eg}}{\gamma_e}\xi\delta_{q,m_e-m_g}|\hat{\boldsymbol{e}}_{-q}\cdot\hat{\boldsymbol{\epsilon}}|^2(2J_e+1)\begin{pmatrix} J_g & 1 & J_e \\ m_g & q & -m_e \end{pmatrix}^2. \tag{A.24}$$

In our case, the atomic states under investigation are $|g\rangle = 5s^2\ {}^1\mathrm{S}_0$ and $|e\rangle = 5s5p\ {}^1\mathrm{P}_1$ in ^{88}Sr. The quantum axis is provided by a magnetic field of several hundred mGauss along the vertical axis in the lab frame. The ground state is spinless ($J = 0$) and the excited state has three magnetic substates ($J = 1$), so that there are three different transitions to consider. The transitions are not quite closed, since $5s5p\ {}^1\mathrm{P}_1$ decays to $5s4d\ {}^1\mathrm{D}_2$ which decays to the metastable $5s5p\ {}^3\mathrm{P}_2$. However, the branching ratio from ${}^3\mathrm{P}_1$ to ${}^1\mathrm{D}_2$ is on the order of 10^{-5} so that we will ignore losses to ${}^1\mathrm{D}_2$ for the photon numbers per atom considered here. The natural linewidth is $A_e = 2\pi \times 30$ MHz which dominates the line profile at μK temperatures. For these reasons, we only consider radiative decay and set $\gamma_e = A_e = A_{eg}$.

In addition, we have $J_g = 0$, $m_g = 0$, and $J_e = 1$, such that

$$(2J_e + 1) \begin{pmatrix} J_g & 1 & J_e \\ m_g & q & -m_e \end{pmatrix}^2 \mapsto 1 \ \forall \ q. \tag{A.25}$$

If we apply an arbitrary (but pure) polarization $\hat{\boldsymbol{\epsilon}}$ with $\hat{\boldsymbol{\epsilon}}^* \cdot \hat{\boldsymbol{\epsilon}} = 1$, then

$$\sum_{q=-1}^{+1} |\hat{\boldsymbol{e}}_{-q} \cdot \hat{\boldsymbol{\epsilon}}|^2 = 1, \tag{A.26}$$

and the scattering cross section becomes

$$\sigma_{eg} = \frac{3\lambda_{eg}^2}{2\pi} \xi, \tag{A.27}$$

in agreement with the classical expression Eq. (A.4).

A.3. Atomic saturation

When the light intensity approaches the saturation intensity

$$I_{\text{sat}} = \frac{\pi h c}{3\lambda_{eg}^3} \gamma, \tag{A.28}$$

the atomic system does not absorb linearly anymore. Instead, a full treatment based on the Maxwell-Bloch equations becomes necessary to describe pulse propagation in a saturable medium. In the present case, we operate at a few ten percent of I_{sat} and would like to calculate first order corrections to the linear response. The treatment in this section follows Ref. [205, 206].

As in section A.1, we assume pulse propagation along z and find an equation for the saturation parameter

$$s_0(z) \equiv I(z)/I_{\text{sat}} = 2\Omega^2/\gamma^2, \tag{A.29}$$

on resonance as [205]

$$\frac{ds_0}{dz} = -\alpha_{\text{Beer}} \frac{s_0}{1 + s_0}. \tag{A.30}$$

This equation can be integrated by separation of variables [206]

$$\int_{s_{\text{in}}}^{s_{\text{out}}} ds_0 \, \frac{1 + s_0}{s_0} = -\alpha_{\text{Beer}} \int_0^z dz$$

$$\ln \frac{s_{\text{out}}}{s_{\text{in}}} + (s_{\text{out}} - s_{\text{in}}) = -\alpha_{\text{Beer}} z \equiv -\text{OD}_{\text{Beer}}. \tag{A.31}$$

The left hand side can be related to the measured optical depth $\text{OD}_{\text{exp}} \equiv -\ln(s_{\text{out}}/s_{\text{in}})$, which allows us to correct for the effect of atomic saturation:

$$\text{OD}_{\text{Beer}} = \text{OD}_{\text{exp}} + (1 - e^{-\text{OD}_{\text{exp}}}) s_{\text{in}}, \tag{A.32}$$

if we know the probe intensity interacting with the atoms. Detuning and laser spectrum is accounted for by the factor ξ we derived in the previous Section.

A.4. Time evolution of sample with probe pulse

To obtain large signal-to-noise from the trapped sample, it is necessary to scatter many photons from each individual atom. For each absorbed photon, an atom gets a momentum kick in the direction of the probe beam with the photon recoil momentum $p_{\text{rec}} = h/\lambda_{eg}$, corresponding to a recoil velocity $v_{\text{rec}} = h/(m\lambda_{eg})$. In addition the atom will receive a random momentum kick when the photon gets reemitted. In this Section, we derive a compromise for the number of photons scattered per atom that still gives good signal-to-noise, but does not influence the sample too much.

A.4.1. Photon rescattering

The response of the atomic cloud to the rescattering process amounts to a random walk in momentum space, overlaid with linear acceleration along the probe beam direction. The random walk can be modeled using a multivariate Ornstein-Uhlenbeck process [207], where the position and momentum of each particle is a random variable influenced by the trapping potential and the white momentum noise. For a particle in a one-dimensional harmonic trap with trap frequency ω, the Itô stochastic differential equation for position x and velocity v

is

$$\begin{pmatrix} dx \\ dv \end{pmatrix} = \begin{pmatrix} 0 & 1 \\ -\omega^2 & 0 \end{pmatrix} \begin{pmatrix} x \\ v \end{pmatrix} dt + \begin{pmatrix} 0 & 0 \\ 0 & \sqrt{D} \end{pmatrix} \begin{pmatrix} dw_x \\ dw_v \end{pmatrix} \tag{A.33}$$

with velocity diffusion constant D, which is the mean-square velocity change per unit time, and zero-mean white noise increments dw_x and dw_v. The equation is of the form

$$d\boldsymbol{x} = \boldsymbol{A}\boldsymbol{x}\,dt + \boldsymbol{B}\,d\boldsymbol{w}, \tag{A.34}$$

with constant system matrix $\boldsymbol{A}$ and constant noise covariance matrix $\boldsymbol{B}$. The equation can be solved for the mean $\langle \boldsymbol{x}_t \rangle$ and the covariance matrix $\mathrm{Cov}(\boldsymbol{x}_t)$ [207]. We obtain

$$\begin{aligned} \langle \boldsymbol{x}_t \rangle &= e^{-\boldsymbol{A}t}\langle \boldsymbol{x}(0) \rangle \\ \mathrm{Cov}(\boldsymbol{x}_t) &= e^{-\boldsymbol{A}t}\mathrm{Cov}(\boldsymbol{x}_0)e^{-\boldsymbol{A}^\top t} + \int_0^t dt'\, e^{-\boldsymbol{A}(t-t')}\boldsymbol{B}\boldsymbol{B}^\top e^{-\boldsymbol{A}^\top(t-t')}. \end{aligned} \tag{A.35}$$

This form allows us to find equations for the position and velocity variances under the influence of the probe pulse in a harmonic trap (assuming that $\sigma_{xv}^2(0) = \sigma_{vx}^2(0) = 0$),

$$\begin{aligned} \sigma_x^2(t) &= \sigma_x^2(0)\cos^2\omega t + \frac{\sigma_v^2(0)}{\omega^2}\sin^2\omega t + D\frac{2\omega t - \sin 2\omega t}{4\omega^3} \\ \sigma_v^2(t) &= \sigma_x^2(0)\omega^2\sin^2\omega t + \sigma_v^2(0)\cos\omega t + D\frac{2\omega t + \sin 2\omega t}{4\omega}. \end{aligned} \tag{A.36}$$

For long times $\omega t \gg 1$, this result amounts to a linear increase in both position and velocity uncertainty with superposed oscillations at the trap frequency.

For a three-dimensional anisotropic harmonic trap (without anharmonic corrections or interaxis coupling) and trap frequencies ω_i, the above results hold true for each pair of position and velocity coordinates (x_i, v_i) and per-axis diffusion constant D_i.

The overall system energy E can then be calculated as

$$\begin{aligned} E(t) &= \sum_i \frac{m}{2}\sigma_{v_i}^2(t) + \frac{m\omega_i^2}{2}\sigma_{x_i}^2(t) \\ &= E(0) + \frac{m}{2}t\sum_i D_i. \end{aligned} \tag{A.37}$$

The rate of energy gain is

$$\Gamma_E \equiv \frac{dE}{dt} = \frac{m}{2}\sum_i D_i, \tag{A.38}$$

reemphasizing the role of the diffusion constants D_i as the per-axis mean square velocity gain per unit time. If we define the total diffusion constant D, we can write it as the product of a scattering rate times the square of the recoil velocity

$$D \equiv \sum_i D_i \equiv \Gamma_{\text{sc}} v_{\text{rec}}^2 = \Gamma_{\text{sc}} \frac{h^2}{m^2 \lambda_{eg}^2}. \tag{A.39}$$

In this context, we are interested in the short term behavior of the atomic cloud under the influence of photon scattering with rate Γ_{sc}. In the limit $\omega t \ll 1$, the above equations become independent of the trapping frequency and we obtain the free space random walk results

$$\sigma_{x_i}^2(t) \simeq \sigma_{x_i}^2(0) + \frac{D_i t^3}{3}$$
$$\sigma_{v_i}^2(t) \simeq \sigma_{v_i}^2(0) + D_i t \tag{A.40}$$

We are interested in having a constant number of photons $N_p \equiv \Gamma_{\text{sc}} t_p$ interact with the atoms during the probe time t_p to obtain a certain signal size on the camera. However, we would also like to minimize size changes of the cloud. Under these conditions, comparing the per-axis cloud size change

$$\frac{\delta \sigma_{x_i}^2(t_p')}{\delta \sigma_{x_i}^2(t_p)} = \frac{N_p(t_p')^2}{N_p t_p^2} = \left(\frac{t_p'}{t_p} \right)^2, \tag{A.41}$$

tells us that we should work with low exposure times and high probe intensities, as long as atomic transition saturation does not cause too many problems.

If we assume that photons are rescattered isotropically, we have $D_i = D/3 = \Gamma_{\text{sc}} v_{\text{rec}}^2 / 3$ and

$$\sigma_{x_i}^2(t) = \sigma_{x_i}^2(0) + N_p \left(\frac{v_{\text{rec}} t_p}{3} \right)^2 = \sigma_{x_i}^2(0) + N_p \left(3.28 \text{ nm} \times \frac{t_p}{\mu s} \right)^2. \tag{A.42}$$

A.4.2. Doppler shift

So far, we have only treated the probe photon reemission, but have ignored the linear acceleration of the atomic cloud along the probe direction due to the absorption of the probe photon. The continual absorption of probe photons along the probe direction results in a linear increase in each atom's mean velocity along the probe direction

$$\langle v(t) \rangle = v_{\text{rec}} \Gamma_{\text{sc}} t_p = v_{\text{rec}} N_p. \tag{A.43}$$

In the low saturation limit, the photon scattering rate is dependent on the probe detuning δ_p via

$$\Gamma_{sc} = \Gamma_{sc}^0/[1 + (2\delta_p/\gamma)^2], \tag{A.44}$$

for on-resonance scattering rate Γ_{sc}^0 and atomic linewidth γ. The Doppler effect changes the detuning during the course of the probe pulse via

$$2\delta_p/\gamma = \frac{4\pi}{\lambda_{eg}\gamma}\langle v(t)\rangle = \frac{2\pi h}{m\lambda_{eg}^2\gamma}N_p \equiv \beta N_p, \tag{A.45}$$

with $\beta \equiv 1.422 \times 10^{-3}$. Assuming that the atoms are at rest initially ($\delta = 0$), the corresponding fractional change in per-axis diffusion constant D_i is

$$\frac{\delta D_i}{D_i} = \frac{\Gamma_{sc}(0) - \Gamma_{sc}(t_p)}{\Gamma_{sc}(0)} = \frac{(\beta N_p)^2}{1 + (\beta N_p)^2} \simeq \beta^2 N_p^2 \simeq \left(\frac{N_p}{700}\right)^2. \tag{A.46}$$

In summary: relying on the free-space diffusion formalism above necessitates scattering much less than 700 photons from each atom.

A.4.3. Cloud displacement

Each atom's mean position along the probe direction z is given by

$$\langle z(t)\rangle = \Gamma_{sc}v_{rec}\frac{t_p^2}{2} = N_p v_{rec}\frac{t_p}{2}. \tag{A.47}$$

This means that we can neglect the cloud displacement as long as $\langle z\rangle \ll \sqrt{\sigma_z^2(0)}$, or

$$N_p \ll \frac{2\sigma_z(0)}{v_{rec}t_p} \simeq (203 \ \mu s/\mu m)\frac{\sigma_z(0)}{t_p}. \tag{A.48}$$

A.4.4. Radiation trapping

If a photon gets scattered in a region of high atomic density, the surrounding atoms are likely to rescatter the scattered photon. In this way, radiation can be trapped within a sample of high density and photon energy can be stored.

The reabsorption probability of the spherical wave emanating from an atomic scatterer can be estimated by imagining a sphere of radius r around the scattering atom. This sphere

contains $N_a = \frac{4\pi}{3}r^3\bar{n}$ atoms, where $\bar{n}$ is the average atomic density within the sphere. Each atom within the sphere contributes a resonant rescattering cross section $\sigma = 3\lambda_{eg}^2/(2\pi)$ to the total rescattering cross section $N_a\sigma$. As soon as the total rescattering cross section becomes comparable to the surface of the sphere, the rescattering probability approaches unity. Using this argument, we can define a mean-free radius

$$
\begin{aligned}
4\pi r_{\text{free}}^2 &\equiv \sigma N_a = \sigma\frac{4\pi}{3}r_{\text{free}}^3\bar{n} \\
\Rightarrow r_{\text{free}} &= \frac{2\pi}{\bar{n}\lambda_{eg}^2} \simeq (29.6~\mu\text{m}) \times \left(\frac{\bar{n}}{10^{12}~\text{cm}^{-3}}\right)^{-1}.
\end{aligned}
\tag{A.49}
$$

If the mean free radius is much smaller than the cloud size, probe photons will be scattered multiple times within the cloud and enhance the photon scattering rate Γ_{sc} and thus the detrimental effects of size changes.

Appendix B

Monte-Carlo Collision Simulation

WITH current processor speeds, it has become feasible to simulate the thermodynamics of a dilute thermal gas of ultracold atoms directly. The main problem remains the simultaneous evolution of $N = 10^4 - 10^5$ particles, since even the simulation of two-particle interactions requires $\mathcal{O}(N^2)$ checks at each time step. A popular method for simulations in the collisionless flow regime due to Bird [208] reduces this complexity by discretizing space into small volumes and only handling local interactions. Among other applications, it has been successfully used to model evaporative cooling [209, 210], particle evolution in non-harmonic traps [211], and cross-dimensional thermalization [170, 212].

In the following, we will briefly describe the algorithm, analyze a few simple test cases, and show results for the full OFR interaction model including both elastic and inelastic collision processes.

B.1. Bird's method

The application of Bird's method to ultracold atom systems has been described in many theses; good discussions can be found in [170, 211]. The program used here is implemented in `C++` and makes extensive use of the GNU Scientific Library (GSL).

The algorithm proceeds in time steps of length τ. Between each time step, the particles of mass m are evolved in the trapping potential $U(\boldsymbol{x})$ according to the classical equations of

motion:

$$\dot{\boldsymbol{x}} = \boldsymbol{v}$$
$$\dot{\boldsymbol{v}} = -\nabla U(\boldsymbol{x})/m.$$

(B.1)

Convenient units for the simulation are ms, μm, and recoil energy, for time, position, and potential, respectively. The particles are propagated using an embedded Runge-Kutta method [98, 213], using analytical derivatives of U. Implemented potentials include anisotropic harmonic traps and arbitrary superpositions of Gaussian beams (excluding interference effects). Including gravity in the potential is optional.

After each time step, space is discretized into a grid of spacing d. The coordinate system's origin lies close to the center of the trap, and each site is indexed by a tuple $(i, j, k) \in \mathbb{Z}^3$. Each particle at position $\boldsymbol{x}$ is associated with the closest grid site

$$(i, j, k) = [\boldsymbol{x}/d],$$

(B.2)

where the brackets indicate rounding to the closest integer. We define a spherical volume

$$V = \frac{4\pi}{3} \left(\frac{d}{2}\right)^3$$

(B.3)

around each grid point and the grid spacing d is automatically adjusted such that the sample-average of the occupation number (mean particle number per cell in the trap volume) is

$$\langle N_{\text{occ}} \rangle = 0.01,$$

(B.4)

which is well below 10% [170].

To simplify the collision checks, a list of particle identifiers is sorted according to the particles' associated grid indices. After the sorting operation, the particles at the same grid point are consecutive in the index list to enable quick access. Using quicksort [98], reusing the sorted list from time-step to time-step to reduce the number of sort operations, and sorting only once per time step allows the algorithm to be fairly fast.

Within each sphere, a list of $N_{\text{occ}}(N_{\text{occ}} - 1)/2$ potential collision pairs is made. For each distinguishable pair of atoms with velocities $\boldsymbol{v}_1$ and $\boldsymbol{v}_2$, the collision probability is calculated

as

$$P_{\text{coll}} = |\boldsymbol{v}_1 - \boldsymbol{v}_2|\sigma\tau/V, \tag{B.5}$$

where σ is the total collision cross section for the process under consideration. A random number q is then drawn uniformly from $[0, 1]$, and if $P_{\text{coll}} > q$, the collision happens. For successful elastic collisions, the particle velocities are rotated with a random Euler rotation matrix. For successful inelastic collisions, both particles are removed from the simulation. The corresponding collisional cross sections σ_{el} and σ_{in} can be velocity dependent or can be made to depend on other external parameters. The OFR effect is simulated by inserting the cross sections from the Bohn and Julienne theory [121, 130].

Finally, the time step τ is servoed using a simple integrating feedback loop such that the sample averaged collision probability during τ remains small, typically $\langle P_{\text{coll}} \rangle \simeq \langle N_{\text{occ}} \rangle \times 0.05 \simeq 5 \times 10^{-4}$. These numerical parameters have been found to make the method reliable and stable [170]. When simulating velocity-dependent cross sections in a thermal distribution of atoms, it is hard to predict what the actual collision rate per time step is. With feedback, the simulation becomes a factor of 5-10 faster by checking for collisions only as often as required.

The remaining important point is that the simulation obviously works with distinguishable particles. To mimic results for indistinguishable thermal bosons in the same spin state ($J = 0$), we have to modify the corresponding cross sections. The simulation is based on distinguishable particles identified by an id tag. To translate the simulation results to thermalization of identical bosons in the same spin state, we need to include a bosonic enhancement factor in the elastic scattering cross section. Simulating thermalization of indistinguishable bosons requires using a scattering cross section $\sigma_{\text{el}} = g_\alpha 4\pi a^2$ with $g_\alpha = 2$ for s-wave scattering length a. The same bosonic enhancement factor g_α appears in the inelastic cross section. A thorough and careful discussion of the origin of these factors can be found in Ref. [119].

However, many authors make no clean distinction between the inelastic scattering event cross section and the inelastic collision rate. Even such basic terminology as *event rate* and

collision rate is not uniquely defined. This confusion arises from different factors of two canceling in the final equations for the density evolution under inelastic loss. The density evolution equation generally used is of the form of Eq. 5.12:

$$\dot{n} = -K_{\text{in}}n^2 = -\sigma_{\text{in}}v_{\text{rel}}n^2. \tag{B.6}$$

Unless this full definition is given, the meaning of K_{in} can be ambiguous. Cross sections σ are always related to the probability of a collision *event* in the sense of Eqs. 5.6 or B.5. Multiplication by the relative velocity thus gives a collision event rate for a collision pair at a given relative velocity. Particle pairs are thus lost at rate K_{in}, but particles are lost at a rate $2K_{\text{in}}$, since two particles are lost per collision event. But, since there are only $N(N-1)/2$ possible distinguishable collision pairs (see Eq. 5.9), the final rate coefficient appearing in the evolution equation for the *single-particle* density (Eq. B.6) is equal to the *pair-loss* rate.

For the same reason, we need to be careful in comparing simulation results for elastic collisions to common statements like: "It takes about three elastic collisions to thermalize a particle." [162, 170, 211, 212] The meaning of this statement is that each of N particles participates in roughly $\kappa = 3$ collisions during the $1/e$ time $\Gamma_{\text{therm}}^{-1}$ it takes for kinetic energy inhomogeneities to equilibrate. If we fit an exponential decay to the disappearance of a thermal inhomogeneity, we can count the number of elastic collision events $N_{\text{event}}^{\text{el}}$ during an exposure time of τ_{PA} and obtain a rough estimate for κ from

$$\kappa \simeq \frac{2N_{\text{event}}^{\text{el}}}{N} \times \frac{1}{\tau_{\text{PA}}\Gamma_{\text{therm}}}. \tag{B.7}$$

B.2. Inelastic collisions

The inelastic collisions were calibrated against the analytical model of Sec. 5.9 in a simplified test. The optical trap was replaced by an isotropic harmonic oscillator with trap frequencies $(\nu_x, \nu_y, \nu_z) = (200, 200, 200)$ Hz, to make the problem as simple as possible. Gravity was removed and the trap was cut off at a radial distance of 200 μm corresponding to a trap depth >1 mK along each axis. An initial distribution containing 50,000 atoms was synthesized, assuming Maxwell-Boltzmann statistics with both velocity and position variances

corresponding to a temperature of 3 μK along each of the three trap axes. Both the velocity and position variances are stationary if the simulation is run without allowing any collision processes.

We then allow inelastic collisions with a constant (relative velocity independent) cross section and turn off any elastic collisions in the simulation. To make comparisons between elastic and inelastic collisions more obvious, we parametrize the inelastic cross section by an artificial "inelastic length" b and set $\sigma_{\mathrm{in}} = 8\pi b^2$. The simulation is run for 500 ms with $b = 100$ a$_0$, and the position and velocity variances along each trap axis are calculated at each time step. Figure B.1(a) shows the increasing position variances along x, y, and z as red, blue, and green traces, respectively. Similarly, panel (b) shows the increase in velocity variances with time. Panel (c) shows the fractional atom loss as the solid black trace. A fit with the thermally averaged model in Sec. 5.9 (dashed red trace) shows fair agreement and returns a collision rate that is about 10% larger than what is used in the simulation. This overestimation is consistent with the slight overestimation (underestimation) of the black curve at times shorter (longer) than 70 ms (150 ms).

The analytical model does not describe the effect of inelastic loss on the momentum distribution, but only includes density-dependent loss from a Gaussian distribution. Similar levels of agreement are obtained when fitting the simulated mean density as a function of time with the solution of $\dot{\bar{n}} = -K_{\mathrm{in}}\bar{n}^2$. In contrast, the Monte-Carlo simulation calculates the effect of inelastic losses on the full phase-space distribution in the presence of a particular trapping potential. We conclude that the agreement between model and simulation is good enough to extract optical lengths from inelastic loss data at the 10-20% level. Typical experimental error bars are much larger (see Fig. 5.11) and we use many PA spectra to reduce the statistical error on $\ell_{\mathrm{opt}}/I_{\mathrm{av}}$. The same level of agreement between the analytical model and the Monte-Carlo simulation is achieved when modeling the full model potential in the simulation and fitting the resulting atom loss traces.

Panel (d) emphasizes the fact that potential and kinetic energies follow each other. The slope of lines fitted to the velocity variances as a function of the position variances is pro-
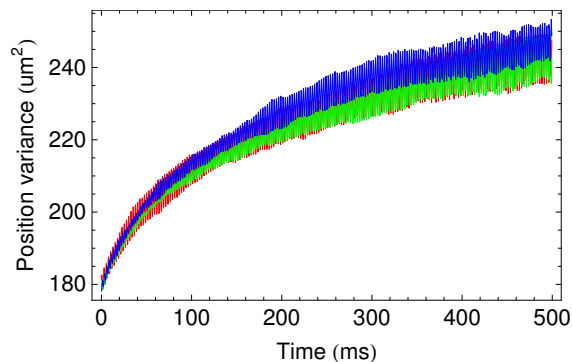
(a) Sample potential energy increases with inelastic loss.
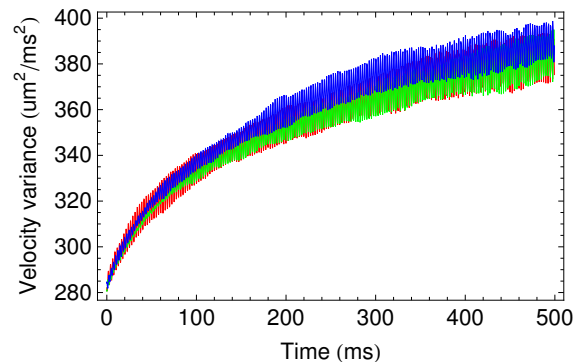
(b) Sample kinetic energy increases with inelastic loss.
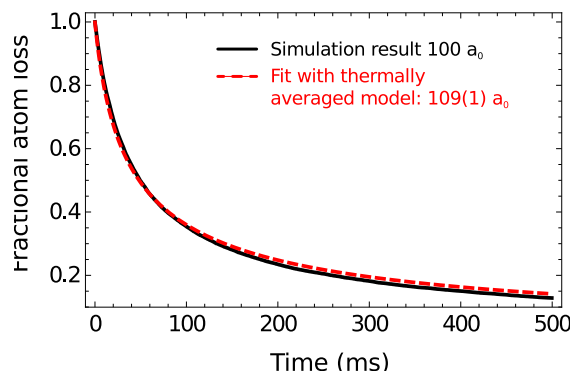
(c) Inelastic particle loss (black) and fit with thermally averaged model from Sec. 5.9.
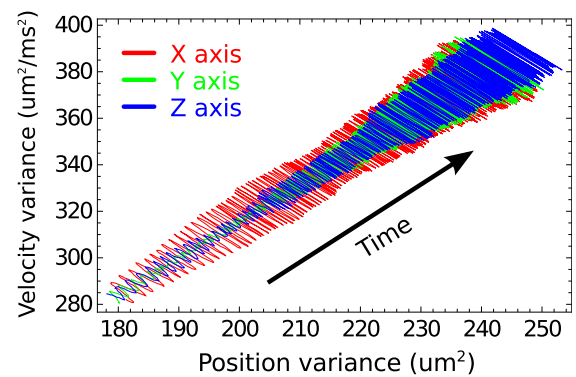
(d) Potential and Kinetic energy are tied together on average over time scales longer than a few trap oscillation cycles.

Figure B.1.: Simulation of inelastic loss in a harmonic trap using an initial Maxwell-Boltzmann distribution at 3 μK.

portional to the square of the axial trap frequencies, as expected in a harmonic trap. Comparisons against more realistic anisotropic harmonic traps and the full model potential were also performed. Agreements between the analytical model and the simulation are similar.

B.3. Elastic collisions

To calibrate the Monte-Carlo simulation against known behavior under elastic collisions, the trap was changed to an anisotropic harmonic oscillator with trap frequencies close to the model potential eigenfrequencies at the bottom of the trap $(\nu_x, \nu_y, \nu_z) = (240, 310, 180)$ Hz. We introduce an anisotropy in both position and momentum space and let the X and Y axes have a Boltzmann distribution with $T_x^0 = T_y^0 = 3\,\mu$K. The Z axis is initially set to $T_z^0 = 5\,\mu$K. By the initial axial temperatures T_i^0 we mean that both the potential energy $m(2\pi\nu_i)^2\langle x_i^2\rangle/2$ and kinetic energy $m\langle v_i^2\rangle/2$ is set to $k_B T_i^0/2$ along each axis initially. Elastic collisions tend to equilibrate the temperature and from a treatment based on Enskog's equation, we expect that the axial temperatures T_i approach each other exponentially [162]. This thermalization process can be modeled as

$$\dot{T}_i = -\sum_{j\neq i} \frac{\Gamma_{\text{therm}}}{3}(T_i - T_j), \tag{B.8}$$

with solution

$$T_i(t) = \bar{T}(0) + e^{-\Gamma_{\text{therm}}t}[T_i(0) - \bar{T}(0)], \tag{B.9}$$

and mean temperature $\bar{T} \equiv \sum_j T_j$. The thermalization constant Γ_{therm} is then related to the number of collision events required for thermalization κ via [162]

$$\Gamma_{\text{therm}} = \frac{2\bar{n}\sigma_{\text{el}}\langle v_{\text{rel}}\rangle_{\bar{T}}}{\kappa}, \tag{B.10}$$

with mean density $\bar{n}$ and thermally averaged relative velocity

$$\langle v_{\text{rel}}\rangle_{\bar{T}} = \sqrt{\frac{8k_B\bar{T}}{\pi\mu}}. \tag{B.11}$$

Since these quantities are thermally averaged and the initial distribution is not thermalized, we expect Γ_{therm} to be time-dependent and also depend on the initial inhomogeneity. Following Ref. [212], we can define an initial inhomogeneity parameter as the ratio of axial energies

E_i (valid for an anisotropic harmonic trap):

$$\Omega = \left.\frac{E_{x,y}}{E_z}\right|_{t=0} = \frac{\langle v_x^2 \rangle + (2\pi\nu_x)^2 \langle x_x^2 \rangle}{\langle v_z^2 \rangle + (2\pi\nu_z)^2 \langle x_z^2 \rangle} = \frac{\langle v_x^2 \rangle}{\langle v_z^2 \rangle} = \frac{T_x^0}{T_z^0} = 0.6. \tag{B.12}$$

For this value of Ω, we find a prediction of $\kappa \simeq 2.5$ from the analytical model in Ref. [212].

The simulation results for $\sigma_{\text{el}} = 8\pi(100a_0)^2$ are shown in Fig. B.2. As seen in panel (a), no atoms are lost due to evaporation or inelastic losses. However, the mean density decreases by about 5% because the density along X and Y dilutes slightly as the Z distribution concentrates. The axial kinetic energies equilibrate towards $\bar{T} = \frac{3+3+5}{3}\ \mu\text{K} = 3.67\ \mu\text{K}$ and we extract $\Gamma_{\text{therm}}^{-1} \simeq 65$ ms from fitting Eq. B.10 to the data in panel (c).

The axial potential energies in panel (d) follow the kinetic energies and equilibrate at the levels given by the individual trap frequencies, as shown by panel (e). As argued above, the collision event rate changes slightly as the sample equilibrates [see panel (f)]. Initially, the rate of collision events is about $\Gamma_{\text{el}}(0) \simeq 860\ \text{ms}^{-1}$ and then settles towards $\Gamma_{\text{el}}(\infty) \simeq 840\ \text{ms}^{-1}$ as the sample thermalizes. From Eq. B.10, we find $\kappa_\infty \simeq 2.23$. Rescaling towards the value at short times [212] we find

$$\kappa_0 = \kappa_\infty \frac{\Gamma_{\text{el}}(0)}{\Gamma_{\text{el}}(\infty)} \simeq 2.3, \tag{B.13}$$

which is in fair agreement with the prediction $\kappa \simeq 2.5$ [212].

We conclude that the Monte-Carlo simulation agrees reasonably well with what we expect from the known results for both elastic and inelastic collision processes in harmonic traps for constant cross sections. We then use it in the main text to model the collisional dynamics of the OFR effect in the full model potential and with the full detuning- and velocity-dependent cross section expressions.
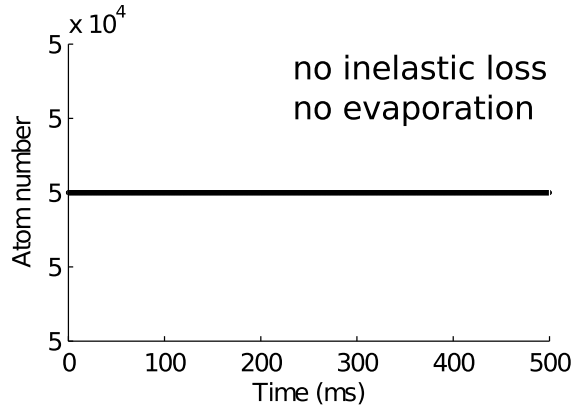
(a) The atom number stays constant throughout the simulation.
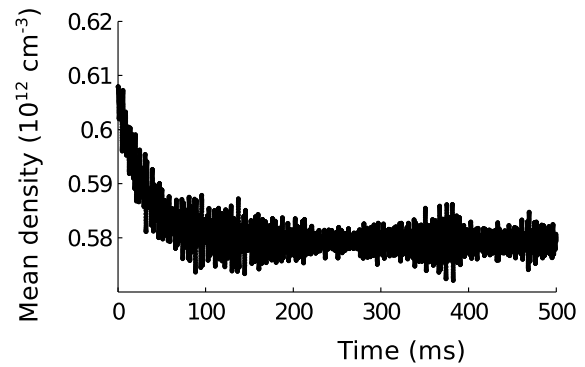
(b) The mean density decreases because the X and Y distributions are heated.
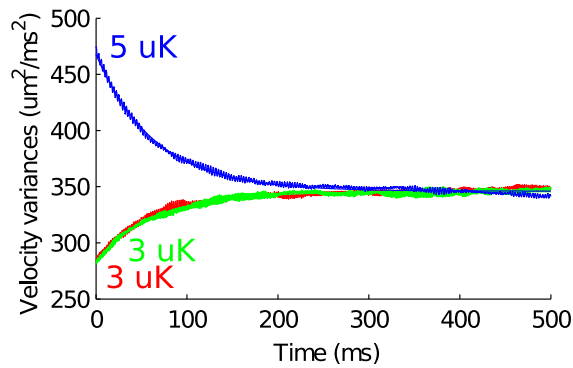
(c) The kinetic energy equilibrates to the mean over all axes.
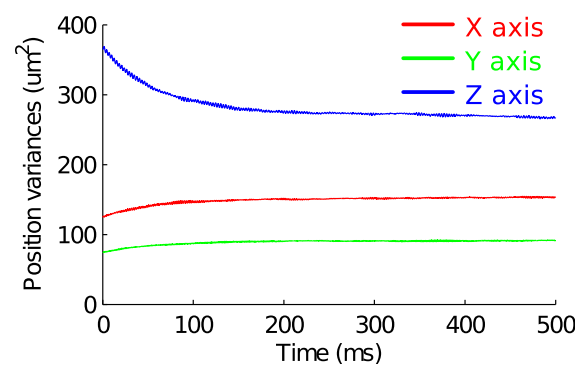
(d) The cloud widths settle according to the axial trap frequency and the kinetic energy.
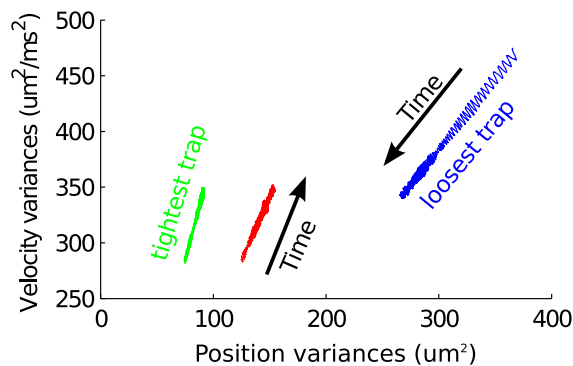
(e) The potential energy follows the kinetic energy on timescales longer than a few trap oscillations.
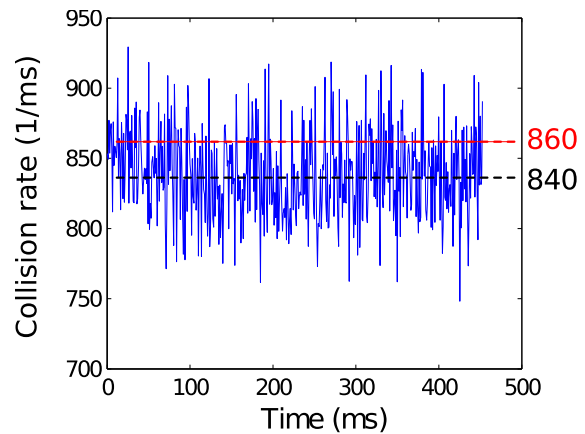
(f) The collision event rate decreases since the mean density goes down.

Figure B.2.: Simulation of cross-dimensional thermalization in an anisotropic harmonic trap. The initial potential and kinetic energy along the X and Y axes are $\frac{k_B}{2} \times (3 \ \mu\text{K})$, the Z axis distributions are heated to $5 \ \mu\text{K}$.

RELATED PUBLICATIONS

B Y now, the first generation of graduate students in optical lattice clock experiments has graduated and the interested reader is referred to the many excellent and publicly available theses on high-resolution laser spectroscopy, absolute frequency measurements, remote optical comparison of frequency standards, and the relevant atomic physics and technology.

Publicly available theses on optical lattice clocks:

- JILA Sr clock: [11–14]
- LNE SYRTE Sr clock: [52, 53, 147] (French), [54] (English)
- LENS Sr clock: [214] (English)
- NIST Yb clock: [215]
- LNE SYRTE Hg lattice spectroscopy: [216] (English)

List of publications related to this work:

- S. Blatt, T. L. Nicholson, B. J. Bloom, J. R. Williams, J. W. Thomsen, P. S. Julienne, and J. Ye, *Thermodynamics of the Optical Feshbach Resonance Effect*, arXiv:1104.0210v1, submitted to Physical Review Letters [10].

- M. D. Swallows, M. Bishof, Y. Lin, S. Blatt, M. J. Martin, A. M. Rey, and J. Ye, *Suppression of Collisional Shifts in a Strongly Interacting Lattice Clock*, Science **331**, 1043 (2011) [51].

- M. D. Swallows, G. K. Campbell, A. D. Ludlow, M. M. Boyd, J. W. Thomsen, M. J. Martin, S. Blatt, T. L. Nicholson, and J. Ye, *Precision measurement of fermionic collisions using*

an ^{87}Sr optical lattice clock with 1×10^{-16} inaccuracy, IEEE Transactions on Ultrasonics, Ferroelectrics and Frequency Control **57**, 574 (2010) [186].

- S. Blatt, J. W. Thomsen, G. K. Campbell, A. D. Ludlow, M. D. Swallows, M. J. Martin, M. M. Boyd, and J. Ye, *Rabi spectroscopy and excitation inhomogeneity in a one-dimensional optical lattice clock*, Physical Review A **80**, 052703 (2009) [9].

- G. K. Campbell, M. M. Boyd, J. W. Thomsen, M. J. Martin, S. Blatt, M. D. Swallows, T. L. Nicholson, T. Fortier, C. W. Oates, S. A. Diddams, N. D. Lemke, P. Naidon, P. Julienne, Jun Ye, and A. D. Ludlow, *Probing Interactions Between Ultracold Fermions*, Science **324**, 360 (2009) [46].

- G. K. Campbell, A. D. Ludlow, S. Blatt, J. W. Thomsen, M. J. Martin, M. H. G. de Miranda, T. Zelevinsky, M. M. Boyd, J. Ye, S. A. Diddams, T. P. Heavner, T. E. Parker, and S. R. Jefferts, *The absolute frequency of the ^{87}Sr optical clock transition*, Metrologia **45**, 539 (2008) [7].

- A. D. Ludlow, S. Blatt, T. Zelevinsky, G. K. Campbell, M. J. Martin, J. W. Thomsen, M. M. Boyd, and J. Ye, *Ultracold strontium clock: Applications to the measurement of fundamental constant variations*, The European Physical Journal Special Topics **163**, 9 (2008) [31].

- S. Blatt, A. D. Ludlow, G. K. Campbell, J. W. Thomsen, T. Zelevinsky, M. M. Boyd, J. Ye, X. Baillard, M. Fouché, R. Le Targat, A. Brusch, P. Lemonde, M. Takamoto, F.-L. Hong, H. Katori, and V. V. Flambaum, *New Limits on Coupling of Fundamental Constants to Gravity Using ^{87}Sr Optical Lattice Clocks*, Physical Review Letters **100**, 140801 (2008) [8].

- A. D. Ludlow, T. Zelevinsky, G. K. Campbell, S. Blatt, M. M. Boyd, M. H. G. de Miranda, M. J. Martin, J. W. Thomsen, S. M. Foreman, Jun Ye, T. M. Fortier, J. E. Stalnaker, S. A. Diddams, Y. Le Coq, Z. W. Barber, N. Poli, N. D. Lemke, K. M. Beck, and C. W. Oates, *Sr Lattice Clock at 1×10^{-16} Fractional Uncertainty by Remote Optical Evaluation with a Ca Clock*, Science **319**, 1805 (2008) [31].

- T. Zelevinsky, S. Blatt, M. M. Boyd, G. K. Campbell, A. D. Ludlow, and J. Ye, *Highly Coherent Spectroscopy of Ultracold Atoms and Molecules in Optical Lattices*, ChemPhysChem **9**, 375 (2008) [217].

- J. Ye, S. Blatt, M. M. Boyd, S. M. Foreman, E. R. Hudson, T. Ido, B. Lev, A. D. Ludlow, B. C. Sawyer, B. Stuhl, and T. Zelevinsky, *Precision measurement based on ultracold atoms and cold molecules*, International Journal of Modern Physics D **16**, 2481 (2007) [218].

- M. M. Boyd, T. Zelevinsky, A. D. Ludlow, S. Blatt, T. Zanon-Willette, S. M. Foreman, and J. Ye, *Nuclear spin effects in optical lattice clocks*, Physical Review A **76**, 022510 (2007) [94].

- T. Zelevinsky, M. M. Boyd, A. D. Ludlow, S. M. Foreman, S. Blatt, T. Ido, and J. Ye, *Optical clock and ultracold collisions with trapped strontium atoms*, Hyperfine Interactions **174**, 55 (2007) [219].

- A. D. Ludlow, X. Huang, M. Notcutt, T. Zanon-Willette, S. M. Foreman, M. M. Boyd, S. Blatt, and J. Ye, *Compact, thermal-noise-limited optical cavity for diode laser stabilization at 1×10^{-15}*, Optics Letters **32**, 641 (2007) [27].

- M. M. Boyd, A. D. Ludlow, S. Blatt, S. M. Foreman, T. Ido, T. Zelevinsky, and J. Ye, ^{87}Sr *Lattice Clock with Inaccuracy below* 10^{-15}, Physical Review Letters **98**, 083002 (2007) [94].

- T. Zanon-Willette, A. D. Ludlow, S. Blatt, M. M. Boyd, E. Arimondo, and J. Ye, *Cancellation of Stark Shifts in Optical Lattice Clocks by Use of Pulsed Raman and Electromagnetically Induced Transparency Techniques*, Physical Review Letters **97**, 233001 (2006) [220].

- M. M. Boyd, T. Zelevinsky, A. D. Ludlow, S. M. Foreman, S. Blatt, T. Ido, and J. Ye, *Optical Atomic Coherence at the 1-Second Time Scale*, Science **314**, 1430 (2006) [43].

- A. D. Ludlow, M. M. Boyd, T. Zelevinsky, S. M. Foreman, S. Blatt, M. Notcutt, T. Ido, and J. Ye, *Systematic Study of the* ^{87}Sr *Clock Transition in an Optical Lattice*, Physical Review Letters **96**, 033003 (2006) [2].

Bibliography

[1] Masao Takamoto, Feng-Lei Hong, Ryoichi Higashi, and Hidetoshi Katori.
   An optical lattice clock.
   Nature **435**, 321, 2005.
   doi:10.1038/nature03541.

[2] Andrew D. Ludlow, Martin M. Boyd, Tanya Zelevinsky, Seth M. Foreman, Sebastian Blatt, Mark Notcutt, Tetsuya Ido, and Jun Ye.
   Systematic study of the ^{87}Sr clock transition in an optical lattice.
   Physical Review Letters **96**, 033003, 2006.
   doi:10.1103/PhysRevLett.96.033003.

[3] Rodolphe Le Targat, Xavier Baillard, Mathilde Fouché, Anders Brusch, Olivier Tcherbakoff, Giovanni Rovera, and Pierre Lemonde.
   Accurate optical lattice clock with ^{87}Sr atoms.
   Physical Review Letters **97**, 130801, 2006.
   doi:10.1103/PhysRevLett.97.130801.

[4] N. Lemke, A. Ludlow, Z. Barber, T. Fortier, S. Diddams, Y. Jiang, S. Jefferts, T. Heavner, T. Parker, and C. Oates.
   Spin-1/2 optical lattice clock.
   Physical Review Letters **103**, 063001, 2009.
   doi:10.1103/PhysRevLett.103.063001.

[5] Xavier Baillard, Mathilde Fouché, Rodolphe Le Targat, Philip G. Westergaard, Arnaud Lecallier, Yann Le Coq, Giovanni D. Rovera, Sebastien Bize, and Pierre Lemonde.
   Accuracy evaluation of an optical lattice clock with bosonic atoms.
   Optics Letters **32**, 1812, 2007.
   doi:10.1364/OL.32.001812.

[6] Ch. Lisdat, J. S. R. Vellore Winfred, T. Middelmann, F. Riehle, and U. Sterr.
   Collisional losses, decoherence, and frequency shifts in optical lattice clocks with bosons.
   Physical Review Letters **103**, 090801, 2009.
   doi:10.1103/PhysRevLett.103.090801.

[7] Gretchen K. Campbell, Andrew D. Ludlow, Sebastian Blatt, Jan W. Thomsen, Michael J. Martin, Marcio H. G. de Miranda, Tanya Zelevinsky, Martin M. Boyd, Jun Ye, Scott A. Diddams, Thomas P. Heavner, Thomas E. Parker, and Steven R. Jefferts.
   The absolute frequency of the ^{87}Sr optical clock transition.
   Metrologia **45**, 5, 539, 2008.
   doi:10.1088/0026-1394/45/5/008.

[8] S. Blatt, A. Ludlow, G. Campbell, J. Thomsen, T. Zelevinsky, M. Boyd, J. Ye, X. Baillard, M. Fouché, R. Le Targat, A. Brusch, P. Lemonde, M. Takamoto, F.-L. Hong, H. Katori, and V. Flambaum.
   New limits on coupling of fundamental constants to gravity using ^{87}Sr optical lattice clocks.
   Physical Review Letters **100**, 140801, 2008.
   doi:10.1103/PhysRevLett.100.140801.

[9] S. Blatt, J. W. Thomsen, G. K. Campbell, A. D. Ludlow, M. D. Swallows, M. J. Martin, M. M. Boyd, and J. Ye.
   Rabi spectroscopy and excitation inhomogeneity in a one-dimensional optical lattice clock.
   Physical Review A **80**, 052703, 2009.
   doi:10.1103/PhysRevA.80.052703.

[10] S. Blatt, T. L. Nicholson, B. J. Bloom, J. R. Williams, J. W. Thomsen, P. S. Julienne, and J. Ye.
Thermodynamics of the optical Feshbach resonance effect.
arXiv:1104.0210v1 2011.

[11] Martin M. Boyd.
High Precision Spectroscopy of Strontium in an Optical Lattice: Towards a New Standard for Frequency and Time.
PhD thesis, University of Colorado, 2007.
URL `http://jilawww.colorado.edu/yelabs/pubs/theses.html`.

[12] Andrew D. Ludlow.
The Strontium Optical Lattice Clock: Optical Spectroscopy with Sub-Hertz Accuracy.
PhD thesis, University of Colorado, 2008.
URL `http://jilawww.colorado.edu/yelabs/pubs/theses.html`.

[13] Seth M. Foreman.
Femtosecond Frequency Combs for Optical Clocks and Timing Transfer.
PhD thesis, University of Colorado, 2007.
URL `http://jila.colorado.edu/thesis`.

[14] Sebastian Blatt.
Precision Spectroscopy in 1D Optical Lattices.
Masters thesis, Leopold-Franzens-Universität Innsbruck, 2005.

[15] Xinye Xu, Thomas Loftus, Matthew Smith, John Hall, Alan Gallagher, and Jun Ye.
Dynamics in a two-level atom magneto-optical trap.
Physical Review A **66**, 011401, 2002.
doi:10.1103/PhysRevA.66.011401.

[16] Xinye Xu, Thomas H. Loftus, John L. Hall, Alan Gallagher, and Jun Ye.
Cooling and trapping of atomic strontium.
Journal of the Optical Society of America B **20**, 968, 2003.
doi:10.1364/JOSAB.20.000968.

[17] Xinye Xu, Thomas Loftus, Josh Dunn, Chris Greene, John Hall, Alan Gallagher, and Jun Ye.
Single-stage sub-Doppler cooling of alkaline earth atoms.
Physical Review Letters **90**, 193002, 2003.
doi:10.1103/PhysRevLett.90.193002.

[18] Thomas H. Loftus, Tetsuya Ido, Martin M. Boyd, Andrew D. Ludlow, and Jun Ye.
Narrow line cooling and momentum-space crystals.
Physical Review A **70**, 063413, 2004.
doi:10.1103/PhysRevA.70.063413.

[19] Thomas Loftus, Tetsuya Ido, Andrew Ludlow, Martin Boyd, and Jun Ye.
Narrow line cooling: Finite photon recoil dynamics.
Physical Review Letters **93**, 073003, 2004.
doi:10.1103/PhysRevLett.93.073003.

[20] Takashi Mukaiyama, Hidetoshi Katori, Tetsuya Ido, Ying Li, and Makoto Kuwata-Gonokami.
Recoil-limited laser cooling of ^{87}Sr atoms near the Fermi temperature.
Physical Review Letters **90**, 113002, 2003.
doi:10.1103/PhysRevLett.90.113002.

[21] J. Ye, H. J. Kimble, and H. Katori.
Quantum state engineering and precision metrology using state-insensitive light traps.
Science **320**, 1734, 2008.
doi:10.1126/science.1148259.

[22] Martin Boyd, Tanya Zelevinsky, Andrew Ludlow, Sebastian Blatt, Thomas Zanon-Willette, Seth Foreman, and Jun Ye.
Nuclear spin effects in optical lattice clocks.
Physical Review A **76**, 022510, 2007.
doi:10.1103/PhysRevA.76.022510.

[23] A. V. Taichenachev, V. I. Yudin, C. W. Oates, C. W. Hoyt, Z. W. Barber, and L. Hollberg.
Magnetic field-induced spectroscopy of forbidden optical transitions with application to lattice-based optical atomic clocks.
Physical Review Letters **96**, 083001, 2006.
doi:10.1103/PhysRevLett.96.083001.

[24] N. Poli, Z. W. Barber, N. D. Lemke, C. W. Oates, L. S. Ma, J. E. Stalnaker, T. M. Fortier, S. A. Diddams, L. Hollberg, J. C. Bergquist, A. Brusch, S. Jefferts, T. Heavner, and T. Parker.
Frequency evaluation of the doubly forbidden $^1S_0 \rightarrow{}^3P_0$ transition in bosonic ^{174}Yb.
Physical Review A **77**, 050501, 2008.
doi:10.1103/PhysRevA.77.050501.

[25] D. Wineland and Wayne Itano.
Laser cooling of atoms.
Physical Review A **20**, 1521, 1979.
doi:10.1103/PhysRevA.20.1521.

[26] D. Leibfried, R. Blatt, C. Monroe, and D. Wineland.
Quantum dynamics of single trapped ions.
Reviews of Modern Physics **75**, 281, 2003.
doi:10.1103/RevModPhys.75.281.

[27] A. D. Ludlow, X. Huang, M. Notcutt, T. Zanon-Willette, S. M. Foreman, M. M. Boyd, S. Blatt, and J. Ye.
Compact, thermal-noise-limited optical cavity for diode laser stabilization at 1×10^{-15}.
Optics Letters **32**, 641, 2007.
doi:10.1364/OL.32.000641.

[28] Seth M. Foreman, Kevin W. Holman, Darren D. Hudson, David J. Jones, and Jun Ye.
Remote transfer of ultrastable frequency references via fiber networks.
Review of Scientific Instruments **78**, 021101, 2007.
doi:10.1063/1.2437069.

[29] Seth M. Foreman, Andrew D. Ludlow, Marcio H. G. de Miranda, Jason E. Stalnaker, Scott A. Diddams, and Jun Ye.
Coherent optical phase transfer over a 32-km fiber with 1 s instability at 10^{-17}.
Physical Review Letters **99**, 153601, 2007.
doi:10.1103/PhysRevLett.99.153601.

[30] T. Fortier, N. Ashby, J. Bergquist, M. Delaney, S. Diddams, T. Heavner, L. Hollberg, W. Itano, S. Jefferts, K. Kim, F. Levi, L. Lorini, W. Oskay, T. Parker, J. Shirley, and J. Stalnaker.
Precision atomic spectroscopy for improved limits on variation of the fine structure constant and local position invariance.
Physical Review Letters **98**, 070801, 2007.
doi:10.1103/PhysRevLett.98.070801.

[31] A. D. Ludlow, T. Zelevinsky, G. K. Campbell, S. Blatt, M. M. Boyd, M. H. G. de Miranda, M. J. Martin, J. W. Thomsen, S. M. Foreman, J. Ye, T. M. Fortier, J. E. Stalnaker, S. A. Diddams, Y. Le Coq, Z. W. Barber, N. Poli, N. D. Lemke, K. M. Beck, and C. W. Oates.
Sr lattice clock at 1×10^{-16} fractional uncertainty by remote optical evaluation with a Ca clock.
Science **319**, 1805, 2008.
doi:10.1126/science.1153341.

[32] Wayne M. Itano, L. L. Lewis, and D. J. Wineland.
Shift of $^2S_{1/2}$ hyperfine splittings due to blackbody radiation.
Physical Review A **25**, 1233, 1982.
doi:10.1103/PhysRevA.25.1233.

[33] Sergey Porsev and Andrei Derevianko.
Multipolar theory of blackbody radiation shift of atomic energy levels and its implications for optical lattice clocks.
Physical Review A **74**, 020502, 2006.
doi:10.1103/PhysRevA.74.020502.

[34] S. Porsev, Andrew Ludlow, Martin Boyd, and Jun Ye.
Determination of Sr properties for a high-accuracy optical clock.
Physical Review A **78**, 032508, 2008.
doi:10.1103/PhysRevA.78.032508.

[35] M. S. Safronova, Dansha Jiang, M. G. Kozlov, and U. I. Safronova.
Blackbody radiation shifts and magic wavelengths for atomic clock research.
In *2010 IEEE International Frequency Control Symposium (FCS)*, p. 59. 2010.
doi:10.1109/FREQ.2010.5556374.

[36] Thomas Middelmann, Christian Lisdat, Stephan Falke, Joseph S. R. Vellore Winfred, Fritz Riehle, and Uwe Sterr.
Tackling the blackbody shift in a strontium optical lattice clock.
arXiv:1009.2017v1 2010.

[37] H. Katori.
In P. Gill, editor, *Proceedings of the 6th Symposium on Frequency Standards and Metrology*, pp. 323–330 (World Scientific, Singapore), 2002.

[38] Hidetoshi Katori, Masao Takamoto, V. Pal'chikov, and V. Ovsiannikov.
Ultrastable optical clock with neutral atoms in an engineered light shift trap.
Physical Review Letters **91**, 173005, 2003.
doi:10.1103/PhysRevLett.91.173005.

[39] H. J. Kimble, C. J. Hood, T. W. Lynn, H. Mabuchi, D. W. Vernooy, and J. Ye.
The quantum internet.
In R. Blatt, J. Eschner, D. Leibfried, and F. Schmidt-Kaler, editors, *Proceedings of the Fourteenth International Conference on Laser Spectroscopy (ICOLS99), Innsbruck*, pp. 80–99 (World Scientific, Singapore), 1999.

[40] Irène Courtillot, Audrey Quessada, Richard Kovacich, Anders Brusch, Dmitri Kolker, Jean-Jacques Zondy, Giovanni Rovera, and Pierre Lemonde.
Clock transition for a future optical frequency standard with trapped atoms.
Physical Review A **68**, 030501, 2003.
doi:10.1103/PhysRevA.68.030501.

[41] Masao Takamoto and Hidetoshi Katori.
Spectroscopy of the $^1S_0$-$^3P_0$ clock transition of ^{87}Sr in an optical lattice.
Physical Review Letters **91**, 223001, 2003.
doi:10.1103/PhysRevLett.91.223001.

[42] Masao Takamoto, Feng-Lei Hong, Ryoichi Higashi, Yasuhisa Fujii, Michito Imae, and Hidetoshi Katori.
Improved frequency measurement of a one-dimensional optical lattice clock with a spin-polarized fermionic ^{87}Sr isotope.
Journal of the Physics Society Japan **75**, 104302, 2006.
doi:10.1143/JPSJ.75.104302.

[43] M. M. Boyd, T. Zelevinsky, A. D. Ludlow, S. M. Foreman, S. Blatt, T. Ido, and J. Ye.
Optical atomic coherence at the 1-second time scale.
Science **314**, 1430, 2006.
doi:10.1126/science.1133732.

[44] Anders Brusch, Rodolphe Le Targat, Xavier Baillard, Mathilde Fouché, and Pierre Lemonde.
Hyperpolarizability effects in a Sr optical lattice clock.
Physical Review Letters **96**, 103003, 2006.
doi:10.1103/PhysRevLett.96.103003.

[45] X. Baillard, M. Fouché, R. Le Targat, P. G. Westergaard, A. Lecallier, F. Chapelet, M. Abgrall, G. D. Rovera, P. Laurent, P. Rosenbusch, S. Bize, G. Santarelli, A. Clairon, P. Lemonde, G. Grosche, B. Lipphardt, and H. Schnatz.
An optical lattice clock with spin-polarized ^{87}Sr atoms.
The European Physical Journal D **48**, 11, 2007.
doi:10.1140/epjd/e2007-00330-3.

[46] G. K. Campbell, M. M. Boyd, J. W. Thomsen, M. J. Martin, S. Blatt, M. D. Swallows, T. L. Nicholson, T. Fortier, C. W. Oates, S. A. Diddams, N. D. Lemke, P. Naidon, P. Julienne, J. Ye, and A. D. Ludlow.
Probing interactions between ultracold fermions.
Science **324**, 360, 2009.
doi:10.1126/science.1169724.

[47] A. M. Rey, A. V. Gorshkov, and C. Rubbo.
Many-body treatment of the collisional frequency shift in fermionic atoms.
Physical Review Letters **103**, 260402, 2009.
doi:10.1103/PhysRevLett.103.260402.

[48] Kurt Gibble.
Decoherence and collisional frequency shifts of trapped bosons and fermions.
Physical Review Letters **103**, 113202, 2009.
doi:10.1103/PhysRevLett.103.113202.

[49] Zhenhua Yu and C. J. Pethick.
Clock shifts of optical transitions in ultracold atomic gases.
Physical Review Letters **104**, 010801, 2010.
doi:10.1103/PhysRevLett.104.010801.

[50] Y. B. Band and I. Osherov.
Collisionally induced atomic clock shifts and correlations.
arXiv:1011.3311v1 2010.

[51] M. D. Swallows, M. Bishof, Y. Lin, S. Blatt, M. J. Martin, A. M. Rey, and J. Ye.
Suppression of collisional shifts in a strongly interacting lattice clock.
Science **331**, 1043, 2011.
doi:10.1126/science.1196442.

[52] Rodolphe Le Targat.
Horloge à réseau optique au Strontium: une 2ème génération d'horloges à atomes froids.
PhD thesis, LNE-SYRTE, 2007.
URL http://tel.archives-ouvertes.fr/tel-00170038.

[53] Xavier Baillard.
Horloge à réseau optique à atomes de Strontium.
PhD thesis, Université de Paris VI, 2008.
URL http://tel.archives-ouvertes.fr/docs/00/26/73/09/PDF/These_X_Baillard.pdf.

[54] Philip G. Westergaard.
Horloge à réseau optique au Strontium: en quête de la performance ultime.
PhD thesis, L'Edite de Paris, 2010.
URL http://tel.archives-ouvertes.fr/tel-00541420/en/.

[55] K. E. Cahill and R. J. Glauber.
Ordered expansions in boson amplitude operators.
Physical Review **177**, 1857, 1969.
doi:10.1103/PhysRev.177.1857.

[56] Pierre Lemonde and Peter Wolf.
Optical lattice clock with atoms confined in a shallow trap.
Physical Review A **72**, 033409, 2005.
doi:10.1103/PhysRevA.72.033409.

[57] R. Shankar.
Principles of Quantum Mechanics (Springer, New York), second edition, 1994.
ISBN 0-306-44790-8.

[58] Milton Abramowitz and Irene A. Stegun, editors.
Handbook of Mathematical Functions (Dover, Mineola, New York), 1972.
ISBN 0-486-61272-4.

[59] Pradip K. Ghosh.
Ion Traps (Clarendon Press, Oxford), 1995.
ISBN 0-19-853995-9.

[60] J. Slater.
A soluble problem in energy bands.
Physical Review **87**, 807, 1952.
doi:10.1103/PhysRev.87.807.

[61] W. Kohn.
Analytic properties of Bloch waves and Wannier functions.
Physical Review **115**, 809, 1959.
doi:10.1103/PhysRev.115.809.

[62] M. Glück, A. R. Kolovsky, H. J. Korsch, and N. Moiseyev.
Calculation of Wannier-Bloch and Wannier-Stark states.
The European Physical Journal D - Atomic, Molecular and Optical Physics **4**, 239, 1998.
doi:10.1007/s100530050205.

[63] Markus Glück, Andrey R. Kolovsky, and Hans Jürgen Korsch.
Wannier-Stark resonances in optical and semiconductor superlattices.
Physics Reports **366**, 103, 2002.
doi:10.1016/S0370-1573(02)00142-4.

[64] Ana Maria Rey.
    Ultracold bosonic atoms in optical lattices.
    PhD thesis, University of Maryland, Department of Physics, 2004.
    URL `http://jila.colorado.edu/~arey/papers/thesis.pdf`.

[65] Quentin Beaufils, Gunnar Tackmann, Xiaolong Wang, Bruno Pelle, Sophie Pelisson, Peter Wolf, and Franck Pereira Dos
    Santos.
    Laser controlled tunneling in a vertical optical lattice.
    arXiv:1102.5326v1 2011.

[66] Ana Maria Rey.
    Collisional frequency shifts in 1D bosonic atoms.
    unpublished 2010.

[67] Michael Bishof, Yige Lin, Matthew D. Swallows, Alexey V. Gorshkov, Jun Ye, and Ana Maria Rey.
    Resolved atomic interaction sidebands in an optical clock transition.
    arXiv:1102.1016v2 2011.

[68] N. D. Lemke, A. D. Ludlow, J. von Stecher, J. A. Sherman, A. M. Rey, and C. W. Oates.
    p-Wave cold collisions in a Yb lattice clock.
    arXiv:1105.2014v1 2011.

[69] T. Holstein and H. Primakoff.
    Field dependence of the intrinsic domain magnetization of a ferromagnet.
    Physical Review **58**, 1098, 1940.
    doi:10.1103/PhysRev.58.1098.

[70] L. Childress, M. V. Gurudev Dutt, J. M. Taylor, A. S. Zibrov, F. Jelezko, J. Wrachtrup, P. R. Hemmer, and M. D. Lukin.
    Coherent dynamics of coupled electron and nuclear spin qubits in diamond.
    Science **314**, 281, 2006.
    doi:10.1126/science.1131871.

[71] J. J. Sakurai.
    Modern Quantum Mechanics (Addison-Wesley, Reading, Massachusetts), second edition, 1994.
    ISBN 0-201-53929-2.

[72] T. L. Gilbert.
    Classics in magnetics A phenomenological theory of damping in ferromagnetic materials.
    IEEE Transactions on Magnetics **40**, 3443, 2004.
    doi:10.1109/TMAG.2004.836740.

[73] Massimiliano d'Aquino.
    Nonlinear Magnetization Dynamics in Thin-films and Nanoparticles.
    PhD thesis, Università degli studi di Napoli "Federico II", Facoltà di Ingegneria, 2004.
    URL `http://www.fedoa.unina.it/148/`.

[74] Ivan Cimrák.
    On the Landau-Lifshitz Equation of Ferromagnetism.
    PhD thesis, Ghent University, Faculty of Applied Sciences, Faculty of Mathematical Analysis, 2005.
    URL `http://biblio.ugent.be/input/download?func=downloadFile&fileOId=494022`.

[75] J. Webb, M. Murphy, V. Flambaum, V. Dzuba, J. Barrow, C. Churchill, J. Prochaska, and A. Wolfe.
    Further evidence for cosmological evolution of the fine structure constant.
    Physical Review Letters **87**, 091301, 2001.
    doi:10.1103/PhysRevLett.87.091301.

[76] R. Srianand, H. Chand, P. Petitjean, and B. Aracil.
    *Limits on the time variation of the electromagnetic fine-structure constant in the low energy limit from absorption lines
    in the spectra of distant quasars.*
    Physical Review Letters **92**, 121302, 2004.
    doi:10.1103/PhysRevLett.92.121302.

[77] Thibault Damour and Freeman Dyson.
    The Oklo bound on the time variation of the fine-structure constant revisited.
    Nuclear Physics B **480**, 37, 1996.
    doi:10.1016/S0550-3213(96)00467-1.

[78] S. G. Karshenboim.
Some possibilities for laboratory searches for variations of fundamental constants.
Canadian Journal of Physics **78**, 2000.
doi:10.1139/cjp-78-7-639.

[79] S. G. Karshenboim, V. V. Flambaum, and E. Peik.
Atomic clocks and constraints on variation of fundamental constants.
In G. W. F. Drake, editor, *Handbook of Atomic, Molecular and Optical Physics*, pp. 455–463 (Springer), 2005.
ISBN 0-387-20802-X.

[80] S. N. Lea.
Limits to time variation of fundamental constants from comparisons of atomic frequency standards.
Reports on Progress in Physics **70**, 1473, 2007.
doi:10.1088/0034-4885/70/9/R01.

[81] Savely G. Karshenboim and Ekkehard Peik, editors.
Lecture Notes in Physics: Astrophysics, Clocks and Fundamental Constants, volume 648 (Springer, Berlin), 2004.
ISBN 3-540-21967-6.

[82] E. Peik, B. Lipphardt, H. Schnatz, T. Schneider, Chr. Tamm, and S. Karshenboim.
Limit on the present temporal variation of the fine structure constant.
Physical Review Letters **93**, 170801, 2004.
doi:10.1103/PhysRevLett.93.170801.

[83] M. Fischer, N. Kolachevsky, M. Zimmermann, R. Holzwarth, Th. Udem, T. W. Hänsch, M. Haas, U. D. Jentschura, and C. H. Keitel.
New limits on the drift of fundamental constants from laboratory measurements.
Physical Review Letters **92**, 230802, 2004.
doi:10.1103/PhysRevLett.92.230802.

[84] M. Zimmermann, M. Fischer, N. Kolachevsky, R. Holzwarth, T. Udem, T. W. Hänsch, M. Abgrall, J. Grünert, I. Maksimovic, S. Bize, H. Marion, F. Pereira Dos Santos, P. Lemonde, G. Santarelli, P. Laurent, A. Clairon, and C. Salomon.
High-resolution laser spectroscopy and time variation of fundamental constants.
Laser Physics **15**, 997, 2005.

[85] E. Peik, B. Lipphardt, H. Schnatz, C. Tamm, S. Weyers, and R. Wynands.
Laboratory limits on temporal variations of fundamental constants: An update.
In H. Kleinert, R. T. Jantzen, and R. Ruffini, editors, *Proceedings of the 11th Marcel Grossmann Meeting on General Relativity*, pp. 941–951. 2008.

[86] John Turneaure, Clifford Will, Brian Farrell, Edward Mattison, and Robert Vessot.
Test of the principle of equivalence by a null gravitational red-shift experiment.
Physical Review D **27**, 1705, 1983.
doi:10.1103/PhysRevD.27.1705.

[87] John Prestage, Robert Tjoelker, and Lute Maleki.
Atomic clocks and variations of the fine structure constant.
Physical Review Letters **74**, 3511, 1995.
doi:10.1103/PhysRevLett.74.3511.

[88] A. Bauch and S. Weyers.
New experimental limit on the validity of local position invariance.
Physical Review D **65**, 081101, 2002.
doi:10.1103/PhysRevD.65.081101.

[89] N. Ashby, T. P. Heavner, S. R. Jefferts, T. E. Parker, A. G. Radnaev, and Y. O. Dudin.
Testing local position invariance with four cesium-fountain primary frequency standards and four NIST hydrogen masers.
Physical Review Letters **98**, 070802, 2007.
doi:10.1103/PhysRevLett.98.070802.

[90] Th. Schmidt.
Über die magnetischen Momente der Atomkerne.
Zeitschrift für Physik **106**, 358, 1937.
doi:10.1007/BF01338744.

[91] H. Kopfermann.
Nuclear Moments (Academic Press, New York, New York), 1958.

[92] V. V. Flambaum and A. F. Tedesco.
Dependence of nuclear magnetic moments on quark masses and limits on temporal variation of fundamental constants from atomic clock experiments.
Physical Review C **73**, 055501, 2006.
doi:10.1103/PhysRevC.73.055501.

[93] E. J. Angstmann, V. A. Dzuba, and V. V. Flambaum.
Atomic clocks and the search for variation of the fine structure constant.
arXiv:physics/0407141v1 2004.

[94] Martin M. Boyd, Andrew D. Ludlow, Sebastian Blatt, Seth M. Foreman, Tetsuya Ido, Tanya Zelevinsky, and Jun Ye.
^{87}Sr *lattice clock with inaccuracy below* 10^{-15}.
Physical Review Letters **98**, 083002, 2007.
doi:10.1103/PhysRevLett.98.083002.

[95] T. Rosenband, D. B. Hume, P. O. Schmidt, C. W. Chou, A. Brusch, L. Lorini, W. H. Oskay, R. E. Drullinger, T. M. Fortier, J. E. Stalnaker, S. A. Diddams, W. C. Swann, N. R. Newbury, W. M. Itano, D. J. Wineland, and J. C. Bergquist.
Frequency ratio of Al^+ *and* Hg^+ *single-ion optical clocks; metrology at the 17th decimal place.*
Science **319**, 1808, 2008.
doi:10.1126/science.1154622.

[96] Philip R. Bevington and D. Keith Robinson.
Data Reduction and Error Analysis for the Physical Sciences (McGraw-Hill, New York, New York), third edition, 2003.
ISBN 0-07-247227-8.

[97] Matthew Lybanon.
A better least-squares method when both variables have uncertainties.
American Journal of Physics **52**, 22, 1984.
doi:10.1119/1.13822.

[98] William H. Press, Saul A. Teukolsky, William T. Vetterling, and Brian P. Flannery.
Numerical Recipes in `C++` (Cambridge University Press, Cambridge), second edition, 2002.
ISBN 0-521-75033-4.

[99] R. J. Carroll, D. Ruppert, and L. A. Stefanski.
Measurement Error in Nonlinear Models (Chapman & Hall, London), 1995.
ISBN 0-412-04721-7.

[100] Norman A. Draper and Harry Smith.
Applied Regression Analysis (Wiley, New York, New York), third edition, 1998.
ISBN 9812530347.

[101] David R. Williams.
NASA planetary factsheet 2005.
URL `http://nssdc.gsfc.nasa.gov/planetary/factsheet/`.

[102] M. R. House.
Orbital forcing timescales: an introduction.
Geological Society, London, Special Publications **85**, 1, 1995.
doi:10.1144/GSL.SP.1995.085.01.01.

[103] P. Bretagnon and G. Francou.
Planetary theories in rectangular and spherical variables. VSOP87 solutions.
Astronomy and Astrophysics **202**, 309, 1988.

[104] W. M. Smart.
Celestial Mechanics (Wiley, New York), 1953.

[105] David W. Allan, Neil Ashby, and Clifford C. Hodge.
The science of timekeeping.
Hewlett-Packard Application Notes **1289**, 1997.

[106] T. M. Fortier, N. Ashby, J. C. Bergquist, M. J. Delaney, S. A. Diddams, T. P. Heavner, L. Hollberg, W. M. Itano, S. R. Jefferts, K. Kim, W. H. Oskay, T. E. Parker, J. Shirley, J. E. Stalnaker, F. Levi, and L. Lorini.
Improved limits on variation of the fine structure constant and violation of local position invariance.
In *Frequency Control Symposium, 2007 Joint with the 21st European Frequency and Time Forum*, p. 663 (IEEE International), 2007.

ISBN 9781-424-4064-7-0.
doi:10.1109/FREQ.2007.4319157.

[107] Thomas Dent.
Eötvös bounds on couplings of fundamental parameters to gravity.
Physical Review Letters **101**, 041102, 2008.
doi:10.1103/PhysRevLett.101.041102.

[108] Thomas Dent, Steffen Stern, and Christof Wetterich.
Competing bounds on the present-day time variation of fundamental constants.
Physical Review D **79**, 083533, 2009.
doi:10.1103/PhysRevD.79.083533.

[109] Holger Müller, Achim Peters, and Steven Chu.
A precision measurement of the gravitational redshift by the interference of matter waves.
Nature **463**, 926, 2010.
doi:10.1038/nature08776.

[110] Michael A. Hohensee and Holger Müller.
Redshift anomalies with universal free-fall.
arXiv:1008.0611v2 2010.

[111] Peter Wolf, Luc Blanchet, Christian J. Bordé, Serge Reynaud, Christophe Salomon, and Claude Cohen-Tannoudji.
Atom gravimeters and gravitational redshift.
Nature **467**, E1, 2010.
doi:10.1038/nature09340.

[112] Peter Wolf, Luc Blanchet, Christian J. Bordé, Serge Reynaud, Christophe Salomon, and Claude Cohen-Tannoudji.
Does an atom interferometer test the gravitational redshift at the Compton frequency?
arXiv:1012.1194v3 2010.

[113] P. Wolf, Ch. J. Bordé, A. Clairon, L. Duchayne, A. Landragin, P. Lemonde, G. Santarelli, W. Ertmer, E. Rasel, F. S. Cataliotti, M. Inguscio, G. M. Tino, P. Gill, H. Klein, S. Reynaud, C. Salomon, E. Peik, O. Bertolami, P. Gil, J. Páramos, C. Jentsch, U. Johann, A. Rathke, P. Bouyer, L. Cacciapuoti, D. Izzo, P. Natale, B. Christophe, P. Touboul, S. G. Turyshev, J. Anderson, M. E. Tobar, F. Schmidt-Kaler, J. Vigué, A. A. Madej, L. Marmet, M.-C. Angonin, P. Delva, P. Tourrenc, G. Metris, H. Müller, R. Walsworth, Z. H. Lu, L. J. Wang, K. Bongs, A. Toncelli, M. Tonelli, H. Dittus, C. Lämmerzahl, G. Galzerano, P. Laporta, J. Laskar, A. Fienga, F. Roques, and K. Sengstock.
Quantum physics exploring gravity in the outer solar system: the SAGAS project.
Experimental Astronomy **23**, 651, 2008.
doi:10.1007/s10686-008-9118-5.

[114] E. Tiesinga, B. J. Verhaar, and H. T. C. Stoof.
Threshold and resonance phenomena in ultracold ground-state collisions.
Physical Review A **47**, 4114, 1993.
doi:10.1103/PhysRevA.47.4114.

[115] S. Inouye, M. R. Andrews, J. Stenger, H.-J. Miesner, D. M. Stamper-Kurn, and W. Ketterle.
Observation of Feshbach resonances in a Bose-Einstein condensate.
Nature **392**, 151, 1998.
doi:10.1038/32354.

[116] Ugo Fano.
Sullo spettro di assorbimento dei gas nobili presso il limite dello spettro d'arco.
Il Nuovo Cimento **12**, 154, 1935.
doi:10.1007/BF02958288.

[117] Ugo Fano.
On the absorption spectrum of noble gases at the arc spectrum limit.
arXiv:cond-mat/0502210v1 2005.

[118] Herman Feshbach.
A unified theory of nuclear reactions. II.
Annals of Physics **19**, 287, 1962.
doi:10.1016/0003-4916(62)90221-X.

[119] James Patrick Burke, Jr.
Theoretical Investigation of Cold Alkali Atom Collisions.
PhD thesis, University of Colorado, 1999.
URL `http://jila.colorado.edu/thesis/`.

[120] C. J. Pethick and H. Smith.
Bose-Einstein Condensation in Dilute Gases (Cambridge University Press, Cambridge), second edition, 2008.
ISBN 9780-521-84651-6.

[121] C. Chin, R. Grimm, P. S. Julienne, and E. Tiesinga.
Feshbach resonances in ultracold gases.
Reviews of Modern Physics **82**, 1225, 2010.
doi:10.1103/RevModPhys.82.1225.

[122] Chris H. Greene.
Universal insights from few-body land.
Physics Today **63**, 40, 2010.
doi:10.1063/1.3366239.

[123] Francesca Ferlaino and Rudolf Grimm.
Forty years of Efimov physics: How a bizarre prediction turned into a hot topic.
Physics **3**, 2010.
doi:10.1103/Physics.3.9.

[124] Wolfgang Ketterle and Martin W. Zwierlein.
Making, probing and understanding ultracold Fermi gases.
In M. Inguscio, W. Ketterle, and C. Salomon, editors, *Ultracold Fermi Gases, Proceedings of the International School of Physics "Enrico Fermi", Course CLXIV, Varenna, 20 - 30 June 2006*, p. 95. 2008.

[125] Immanuel Bloch, Jean Dalibard, and Wilhelm Zwerger.
Many-body physics with ultracold gases.
Reviews of Modern Physics **80**, 885, 2008.
doi:10.1103/RevModPhys.80.885.

[126] Michael Hermele, Victor Gurarie, and Ana Maria Rey.
Mott insulators of ultracold fermionic alkaline earth atoms: Underconstrained magnetism and chiral spin liquid.
Physical Review Letters **103**, 135301, 2009.
doi:10.1103/PhysRevLett.103.135301.

[127] A. V. Gorshkov, M. Hermele, V. Gurarie, C. Xu, P. S. Julienne, J. Ye, P. Zoller, E. Demler, M. D. Lukin, and A. M. Rey.
Two-orbital SU(N) magnetism with ultracold alkaline-earth atoms.
Nature Physics **6**, 289, 2010.
doi:10.1038/nphys1535.

[128] Michael Foss-Feig, Michael Hermele, and Ana Maria Rey.
Probing the Kondo lattice model with alkaline-earth-metal atoms.
Physical Review A **81**, 051603, 2010.
doi:10.1103/PhysRevA.81.051603.

[129] P. Fedichev, Yu. Kagan, G. Shlyapnikov, and J. Walraven.
Influence of nearly resonant light on the scattering length in low-temperature atomic gases.
Physical Review Letters **77**, 2913, 1996.
doi:10.1103/PhysRevLett.77.2913.

[130] John Bohn and P. Julienne.
Semianalytic theory of laser-assisted resonant cold collisions.
Physical Review A **60**, 414, 1999.
doi:10.1103/PhysRevA.60.414.

[131] Kevin Jones, Eite Tiesinga, Paul Lett, and Paul Julienne.
Ultracold photoassociation spectroscopy: Long-range molecules and atomic scattering.
Reviews of Modern Physics **78**, 483, 2006.
doi:10.1103/RevModPhys.78.483.

[132] F. Fatemi, K. Jones, and P. Lett.
Observation of optically induced Feshbach resonances in collisions of cold atoms.
Physical Review Letters **85**, 4462, 2000.
doi:10.1103/PhysRevLett.85.4462.

[133] M. Theis, G. Thalhammer, K. Winkler, M. Hellwig, G. Ruff, R. Grimm, and J. Hecker Denschlag.
Tuning the scattering length with an optically induced Feshbach resonance.
Physical Review Letters **93**, 123001, 2004.
doi:10.1103/PhysRevLett.93.123001.

[134] Gregor Thalhammer, Matthias Theis, Klaus Winkler, Rudolf Grimm, and Johannes Hecker Denschlag.
Inducing an optical Feshbach resonance via stimulated Raman coupling.
Phys. Rev. A **71**, 033403, 2005.
doi:10.1103/PhysRevA.71.033403.

[135] Matthias Theis.
Optical Feshbach Resonances in a Bose-Einstein Condensate.
PhD thesis, Fakultät für Mathematik, Informatik und Physik, Leopold-Franzens-Universität Innsbruck, 2005.
URL `http://pc150-c704.uibk.ac.at/ultracold/doc/thesis_matthias_theis/thesis_matthias_theis.pdf`.

[136] R. Ciuryło, E. Tiesinga, and P. S. Julienne.
Optical tuning of the scattering length of cold alkaline-earth-metal atoms.
Physical Review A **71**, 030701, 2005.
doi:10.1103/PhysRevA.71.030701.

[137] T. Zelevinsky, M. M. Boyd, A. D. Ludlow, T. Ido, J. Ye, R. Ciuryło, P. Naidon, and P. S. Julienne.
Narrow line photoassociation in an optical lattice.
Physical Review Letters **96**, 203201, 2006.
doi:10.1103/PhysRevLett.96.203201.

[138] K. Enomoto, K. Kasa, M. Kitagawa, and Y. Takahashi.
Optical Feshbach resonance using the intercombination transition.
Physical Review Letters **101**, 203201, 2008.
doi:10.1103/PhysRevLett.101.203201.

[139] Rekishu Yamazaki, Shintaro Taie, Seiji Sugawa, and Yoshiro Takahashi.
Submicron spatial modulation of an interatomic interaction in a Bose-Einstein condensate.
Physical Review Letters **105**, 050405, 2010.
doi:10.1103/PhysRevLett.105.050405.

[140] Y. Martinez de Escobar, P. Mickelson, P. Pellegrini, S. Nagel, A. Traverso, M. Yan, R. Côté, and T. Killian.
Two-photon photoassociative spectroscopy of ultracold ^{88}Sr.
Physical Review A **78**, 062708, 2008.
doi:10.1103/PhysRevA.78.062708.

[141] A. Stein, H. Knöckel, and E. Tiemann.
The 1S+1S asymptote of Sr_2 studied by Fourier-transform spectroscopy.
European Physical Journal D **57**, 171, 2010.
doi:10.1140/epjd/e2010-00058-y.

[142] Simon Stellmer, Meng Tey, Bo Huang, Rudolf Grimm, and Florian Schreck.
Bose-Einstein condensation of strontium.
Physical Review Letters **103**, 200401, 2009.
doi:10.1103/PhysRevLett.103.200401.

[143] Y. de Escobar, P. Mickelson, M. Yan, B. DeSalvo, S. Nagel, and T. Killian.
Bose-Einstein condensation of ^{84}Sr.
Physical Review Letters **103**, 200402, 2009.
doi:10.1103/PhysRevLett.103.200402.

[144] R. Ciuryło, E. Tiesinga, and P. S. Julienne.
Stationary phase approximation for the strength of optical Feshbach resonances.
Physical Review A **74**, 022710, 2006.
doi:10.1103/PhysRevA.74.022710.

[145] Jeremy M. Hutson.
Feshbach resonances in ultracold atomic and molecular collisions: threshold behaviour and suppression of poles in scattering lengths.
New Journal of Physics **9**, 152, 2007.
doi:10.1088/1367-2630/9/5/152.

[146] Paul S. Julienne.
Notes on ^{88}Sr optical Feshbach resonances.
unpublished 2010.

[147] Irène Courtillot.
   Première observation de la transition fortement interdite $^1S_0$-$^3P_0$ du strontium, pour une horloge optique à atomes piégés.
   PhD thesis, Université de Paris VI, 2003.
   URL http://tel.archives-ouvertes.fr/tel-00004039/en/.

[148] Eric Wille.
   Preparation of an optically trapped Fermi-Fermi mixture of ^6Li and ^{40}K atoms and characterization of the interspecies interactions by Feshbach spectroscopy.
   PhD thesis, Universität Innsbruck, Fakultät für Mathematik, Informatik und Physik, 2009.
   URL http://ultracold.at.

[149] I. I. Rabi, J. M. B. Kellogg, and J. R. Zacharias.
   The magnetic moment of the proton.
   Physical Review **46**, 157, 1934.
   doi:10.1103/PhysRev.46.157.

[150] Norman F. Ramsey.
   Molecular Beams (Oxford University Press, London), 1956.

[151] Jacques Vanier and Claude Audoin.
   The Quantum Physics of Atomic Frequency Standards (Adam Hilger, Bristol), 1989.
   ISBN 0-85274-434-X.

[152] Bruce G. Klappauf, Yannick Bidel, David Wilkowski, Thierry Chanelière, and Robin Kaiser.
   Detailed study of an efficient blue laser source by second-harmonic generation in a semimonolithic cavity for the cooling of strontium atoms.
   Applied Optics **43**, 2510, 2004.
   doi:10.1364/AO.43.002510.

[153] R. Le Targat, J.-J. Zondy, and P. Lemonde.
   75%-efficiency blue generation from an intracavity PPKTP frequency doubler.
   Optics Communications **247**, 471, 2005.
   doi:10.1016/j.optcom.2004.11.081.

[154] B. Boulanger, M. M. Fejer, R. Blachman, and P. F. Bordui.
   Study of $KTiOPO_4$ gray-tracking at 1064, 532, and 355 nm.
   Applied Physics Letters **65**, 2401, 1994.
   doi:10.1063/1.112688.

[155] R. Blachman, P. F. Bordui, and M. M. Fejer.
   Laser-induced photochromic damage in potassium titanyl phosphate.
   Applied Physics Letters **64**, 1318, 1994.
   doi:10.1063/1.111920.

[156] Benoît Boulanger, Jean-Philippe Fève, and Yannick Guillien.
   Thermo-optical effect and saturation of nonlinear absorption induced by gray tracking in a 532-nm-pumped KTP optical parametric oscillator.
   Optics Letters **25**, 484, 2000.
   doi:10.1364/OL.25.000484.

[157] Zhi M. Liao, Stephen A. Payne, Jay Dawson, Alex Drobshoff, Chris Ebbers, Dee Pennington, and Luke Taylor.
   Thermally induced dephasing in periodically poled KTP frequency-doubling crystals.
   Journal of the Optical Society of America B **21**, 2191, 2004.
   doi:10.1364/JOSAB.21.002191.

[158] S. Wang, V. Pasiskevicius, and F. Laurell.
   Dynamics of green light-induced infrared absorption in $KTiOPO_4$ and periodically poled $KTiOPO_4$.
   Journal of Applied Physics **96**, 2023, 2004.
   doi:10.1063/1.1738528.

[159] A. Skliar (Raicol).
   private communication 2008.
   URL http://www.raicol.com.

[160] Daisuke Akamatsu, Masami Yasuda, Takuya Kohno, Atsushi Onae, and Feng-Lei Hong.
   A compact light source at 461 nm using a periodically poled $LiNbO_3$ waveguide for strontium magneto-optical trapping.
   Optics Express **19**, 2046, 2011.
   doi:10.1364/OE.19.002046.

[161] W. Ketterle, D. S. Durfee, and D. M. Stamper-Kurn.
Making, probing and understanding Bose-Einstein condensates.
arXiv:cond-mat/9904034v2 1999.

[162] Jacob Lyman Roberts.
Bose-Einstein Condensates with Tunable Atom-atom Interactions: The First Experiments with ^{85}Rb BECs.
PhD thesis, University of Colorado, Department of Physics, 2001.
URL http://jilawww.colorado.edu/yelabs/pubs/theses.html.

[163] Jeff Conrad.
Depth of field in depth 2006.
URL http://www.largeformatphotography.info/articles/DoFinDepth.pdf.

[164] Andrey Kobyakov, Michael Sauer, and Dipak Chowdhury.
Stimulated Brillouin scattering in optical fibers.
Advances in Optics and Photonics **2**, 1, 2009.
doi:10.1364/AOP.2.000001.

[165] Rudolf Grimm, Matthias Weidemüller, and Yurii B. Ovchinnikov.
Optical dipole traps for neutral atoms.
arXiv:physics/9902072v1 1999.

[166] Edwin T. Jaynes.
Probability Theory (Cambridge University Press, Cambridge), 2003.
ISBN 0-521-59271-2.

[167] Vladimir Ivanovich Krylov.
Approximate Calculation of Integrals (Dover Publications, Mineola, New York), 2005.
ISBN 0-486-44579-8.

[168] Philip J. Davis and Philip Rabinowitz.
Methods of Numerical Integration (Dover Publications, Mineola, New York), 2007.
ISBN 0-486-45339-1.

[169] R. Ciuryło, E. Tiesinga, S. Kotochigova, and P. Julienne.
Photoassociation spectroscopy of cold alkaline-earth-metal atoms near the intercombination line.
Physical Review A **70**, 1, 2004.
doi:10.1103/PhysRevA.70.062710.

[170] Jonathan Michael Goldwin.
Quantum Degeneracy and Interactions in the ^{87}Rb-^{40}K Bose-Fermi Mixture.
PhD thesis, University of Colorado, 2005.
URL http://jila.colorado.edu/thesis/.

[171] P. S. Julienne.
to be published 2011.

[172] P. S. Julienne and F. H. Mies.
Nonadiabatic theory of atomic line broadening: Redistribution calculations for $Sr(^1P \to ^1S)$+Ar.
Physical Review A **34**, 3792, 1986.
doi:10.1103/PhysRevA.34.3792.

[173] Reginaldo Napolitano, John Weiner, and Paul S. Julienne.
Theory of optical suppression of ultracold-collision rates by polarized light.
Physical Review A **55**, 1191, 1997.
doi:10.1103/PhysRevA.55.1191.

[174] S. G. Porsev and A. Derevianko.
High-accuracy calculations of dipole, quadrupole, and octupole electric dynamic polarizabilities and van der Waals coefficients C_6, C_8, and C_{10} for alkaline-earth dimers.
Journal of Experimental and Theoretical Physics **102**, 195, 2006.
doi:10.1134/S1063776106020014.

[175] Meng Khoon Tey, Simon Stellmer, Rudolf Grimm, and Florian Schreck.
Double-degenerate Bose-Fermi mixture of strontium.
Physical Review A **82**, 011608, 2010.
doi:10.1103/PhysRevA.82.011608.

[176] Simon Stellmer, Meng Khoon Tey, Rudolf Grimm, and Florian Schreck.
Bose-Einstein condensation of ^{86}Sr.
Physical Review A **82**, 041602, 2010.
doi:10.1103/PhysRevA.82.041602.

[177] B. DeSalvo, M. Yan, P. Mickelson, Y. Martinez de Escobar, and T. Killian.
Degenerate Fermi gas of ^{87}Sr.
Phys. Rev. Lett. **105**, 030402, 2010.
doi:10.1103/PhysRevLett.105.030402.

[178] P. G. Mickelson, Y. N. Martinez de Escobar, M. Yan, B. J. DeSalvo, and T. C. Killian.
Bose-Einstein condensation of ^{88}Sr through sympathetic cooling with ^{87}Sr.
Phys. Rev. A **81**, 051601, 2010.
doi:10.1103/PhysRevA.81.051601.

[179] Tomoya Akatsuka, Masao Takamoto, and Hidetoshi Katori.
Optical lattice clocks with non-interacting bosons and fermions.
Nature Physics **4**, 954, 2008.
doi:10.1038/nphys1108.

[180] Tomoya Akatsuka, Masao Takamoto, and Hidetoshi Katori.
Three-dimensional optical lattice clock with bosonic ^{88}Sr atoms.
Physical Review A **81**, 023402, 2010.
doi:10.1103/PhysRevA.81.023402.

[181] M. Bishof *et al.*
in preparation 2011.

[182] D. Chang, Jun Ye, and M. Lukin.
Controlling dipole-dipole frequency shifts in a lattice-based optical atomic clock.
Physical Review A **69**, 023810, 2004.
doi:10.1103/PhysRevA.69.023810.

[183] D. Meiser, Jun Ye, D. Carlson, and M. Holland.
Prospects for a millihertz-linewidth laser.
Physical Review Letters **102**, 163601, 2009.
doi:10.1103/PhysRevLett.102.163601.

[184] D. Meiser and M. J. Holland.
Steady-state superradiance with alkaline-earth-metal atoms.
Physical Review A **81**, 033847, 2010.
doi:10.1103/PhysRevA.81.033847.

[185] M. J. Martin, D. Meiser, J. W. Thomsen, Jun Ye, and M. J. Holland.
Extreme non-linear response of ultra-narrow optical transitions in cavity QED for laser stabilization.
arXiv:1105.2373v1 2011.

[186] Matthew Swallows, Gretchen Campbell, Andrew Ludlow, Martin Boyd, Jan Thomsen, Michael Martin, Sebastian Blatt, Travis Nicholson, and Jun Ye.
Precision measurement of fermionic collisions using an ^{87}Sr optical lattice clock with 1×10^{-16} inaccuracy.
IEEE Transactions on Ultrasonics, Ferroelectrics and Frequency Control **57**, 574, 2010.
doi:10.1109/TUFFC.2010.1449.

[187] Philip Westergaard, Jerome Lodewyck, and Pierre Lemonde.
Minimizing the Dick effect in an optical lattice clock.
IEEE Transactions on Ultrasonics, Ferroelectrics and Frequency Control **57**, 623, 2010.
doi:10.1109/TUFFC.2010.1457.

[188] Jérôme Lodewyck, Philip Westergaard, and Pierre Lemonde.
Nondestructive measurement of the transition probability in a Sr optical lattice clock.
Physical Review A **79**, 061401, 2009.
doi:10.1103/PhysRevA.79.061401.

[189] Jérôme Lodewyck, Philip G Westergaard, Arnaud Lecallier, Luca Lorini, and Pierre Lemonde.
Frequency stability of optical lattice clocks.
New Journal of Physics **12**, 065026, 2010.
doi:10.1088/1367-2630/12/6/065026.

[190] J. I. Cirac, M. Lewenstein, and P. Zoller.
Collective laser cooling of trapped atoms.
Europhysics Letters **35**, 647, 1996.
doi:10.1209/epl/i1996-00165-4.

[191] S. Blatt.
Feasibility of narrow line laser cooling of Sr in optical dipole traps by spontaneous Raman scattering.
unpublished 2009.

[192] C. W. Chou, D. B. Hume, T. Rosenband, and D. J. Wineland.
Optical clocks and relativity.
Science **329**, 1630, 2010.
doi:10.1126/science.1192720.

[193] Jun Ye.
Absolute measurement of a long, arbitrary distance to less than an optical fringe.
Optics Letters **29**, 1153, 2004.
doi:10.1364/OL.29.001153.

[194] B. H. Bransden and C. J. Joachain.
Physics of Atoms and Molecules (Pearson Education, Edinburgh), second edition, 2003.
ISBN 0-582-35692-X.

[195] D. Budker, D. F. Kimball, and D. P. DeMille.
Atomic Physics : an exploration through problems and solutions (Oxford University Press, Oxford), 2004.
ISBN 0-19-850950-2.

[196] A. E. Siegman.
Lasers (University Science Books), 1986.
ISBN 0-935702-11-3.

[197] A. R. Edmonds.
Angular Momentum in Quantum Mechanics (Princeton University Press, Princeton, New Jersey), second edition, 1960.

[198] A. Messiah.
Quantum Mechanics (Dover, Mineola, New York), 1999.
ISBN 0-486-40924-4.

[199] I. I. Sobel'man.
Introduction to the Theory of Atomic Spectra (Pergamon Press, Oxford), 1972.

[200] D. A. Varshalovich, A. N. Moskalev, and V. K. Khersonskii.
Quantum Theory of Angular Momentum (World Scientific, Singapore), 1988.
ISBN 9971509962.

[201] D. M. Brink and G. R. Satchler.
Angular Momentum (Clarendon Press, Oxford), second edition, 1968.

[202] M. E. Rose.
Elementary Theory of Angular Momentum (Dover, New York), 1995.
ISBN 0-486-68480-6.

[203] H. Friedrich.
Theoretical Atomic Physics (Springer, Berlin), second edition, 1998.
ISBN 3-540-64124-6.

[204] E. Merzbacher.
Quantum Mechanics (Wiley, New York), third edition, 1998.
ISBN 0-471-88702-1.

[205] L. Allen and J. H. Eberly.
Optical Resonance and Two-Level Atoms (Dover, New York), 1987.
ISBN 0-486-65533-4.

[206] T. Cumby.
Notes on OD saturation 2010.

[207] C. W. Gardiner.
       Handbook of Stochastic Methods for Physics, Chemistry and the Natural Sciences (Springer, Berlin), third edition, 2004.
       ISBN 3-540-20882-8.

[208] G. A. Bird.
       Molecular gas dynamics and the direct simulation of gas flows (Clarendon Press, Oxford), 1994.
       ISBN 0-19-856195-4.

[209] Huang Wu and Christopher J. Foot.
       Direct simulation of evaporative cooling.
       Journal of Physics B: Atomic, Molecular and Optical Physics **29**, L321, 1996.
       doi:10.1088/0953-4075/29/8/003.

[210] Huang Wu, Ennio Arimondo, and Christopher Foot.
       Dynamics of evaporative cooling for Bose-Einstein condensation.
       Physical Review A **56**, 560, 1997.
       doi:10.1103/PhysRevA.56.560.

[211] Michael Eric Gehm.
       Preparation of an optically-trapped degenerate Fermi gas of ^6Li: Finding the route to degeneracy.
       PhD thesis, Duke University, 2003.
       URL http://www.phy.duke.edu/research/photon/qoptics/theses/.

[212] J. Goldwin, S. Inouye, M. Olsen, and D. Jin.
       Cross-dimensional relaxation in Bose-Fermi mixtures.
       Physical Review A **71**, 043408, 2005.
       doi:10.1103/PhysRevA.71.043408.

[213] J. Stoer and R. Bulirsch.
       Introduction to Numerical Analysis (Springer, New York), third edition, 2002.
       ISBN 0-387-95452-X.

[214] Marco Giacinto Tarallo.
       Development of a Strontium optical lattice clock.
       PhD thesis, Univesità degli Studi di Pisa, Facoltà di Scienze Matematiche Fisiche e Naturali, 2009.
       URL http://etd.adm.unipi.it/theses/available/etd-05182009-164852/.

[215] Zeb Barber.
       Ytterbium Optical Lattice Clock.
       PhD thesis, University of Colorado, 2007.
       URL https://jilawww.colorado.edu/pubs/thesis/barber/.

[216] Michael Petersen.
       Laser-cooling of Neutral Mercury and Laser-spectroscopy of the $^1S_0$-$^3P_0$ optical clock transition.
       PhD thesis, Université Pierre et Marie Curie, Paris VI, 2009.
       URL http://tel.archives-ouvertes.fr/tel-00405200/en/.

[217] Tanya Zelevinsky, Sebastian Blatt, Martin M. Boyd, Gretchen K. Campbell, Andrew D. Ludlow, and Jun Ye.
       Highly coherent spectroscopy of ultracold atoms and molecules in optical lattices.
       ChemPhysChem **9**, 375, 2008.
       doi:10.1002/cphc.200700713.

[218] J. Ye, S. Blatt, M. M. Boyd, S. M. Foreman, E. R. Hudson, T. Ido, B. Lev, A. D. Ludlow, B. C. Sawyer, B. Stuhl, and
           T. Zelevinsky.
       Precision measurement based on ultracold atoms and cold molecules.
       International Journal of Modern Physics D **16**, 2481, 2007.
       doi:10.1142/S0218271807011826.

[219] T. Zelevinsky, M. M. Boyd, A. D. Ludlow, S. M. Foreman, S. Blatt, T. Ido, and J. Ye.
       Optical clock and ultracold collisions with trapped strontium atoms.
       Hyperfine Interactions **174**, 55, 2007.
       doi:10.1007/s10751-007-9564-x.

[220] Thomas Zanon-Willette, Andrew Ludlow, Sebastian Blatt, Martin Boyd, Ennio Arimondo, and Jun Ye.
       *Cancellation of Stark shifts in optical lattice clocks by use of pulsed Raman and electromagnetically induced transparency
           techniques.*
       Physical Review Letters **97**, 233001, 2006.
       doi:10.1103/PhysRevLett.97.233001.